Modelling incomplete fusion dynamics of complex nuclei at Coulomb energies: Superheavy element formation

Rafael Van den Bossche
Supervisor: Alexis Diaz-Torres
Co-Supervisor: Paul Stevenson

Submitted for the Degree of
Doctor of Philosophy
from the
University of Surrey

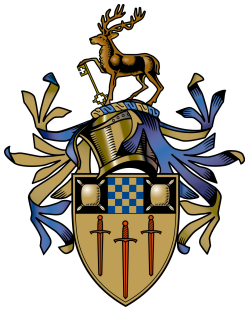

Department of Physics
Faculty of Engineering and Physical Sciences
University of Surrey
Guildford, Surrey GU2 7XH, U.K.

June 2021

© Rafael Van den Bossche 2021

Summary

The incomplete fusion dynamics of various target-projectile collisions at energies above the Coulomb barrier are investigated using a novel semi-classical dynamical model which combines a classical trajectory model with stochastic breakup, as implemented in the PLATYPUS code, with a dynamical fragmentation theory treatment of two-body clusterisation and decay of a projectile. Studied in this work are the projectiles ^{20}Ne and ^{40,48}Ca, the targets ^{248,250}Cm, ^{252,254}Cf and ^{254,256}Es, at incident energies equal to, 5% above and 10% above the Coulomb barrier. Results are compared with published experimental values to indicate the success of this new model and to calibrate it for the subsequently presented novel predictions for superheavy element formation. Evaporation residue cross-sections are also calculated and presented for selected primary incomplete fusion products. The results are crucial for planning experiments for the production of new superheavy isotopes exploiting the incomplete fusion reaction mechanism.

Key words: Nuclear reactions, Incomplete fusion, Coulomb energies, Superheavy elements, Charge asymmetry, Evaporation residue cross-sections.

Email: r.vandenbossche@surrey.ac.uk

Acknowledgements

I would like to thank my parents Michael and Katty, for providing me with every opportunity over the last 27 years that would go on to culminate in the undertaking of this work, and for all their support throughout it. I would also like to thank my supervisor Alexis, for providing me with his laudable guidance, expertise and patience over the last four years. Thank you all for helping me to make this a reality.

Contents

Chapter 1

Introduction

1.1 Superheavy element background

"Superheavy elements" (SHEs) often refers to the transactinide elements, which have an atomic number $104 \leq Z \leq 120$, and sometimes to the superactinide elements ($121 \leq Z \leq 157$) and beyond [1]. In some cases the term has been used to refer to elements located in or near the theoretically predicted "island of stability", which have atomic and mass numbers (Z, N) $\cong$ (114 or 120 or 126, 184) [2, 3], and in 1990 Seaborg and Loveland suggested that the term SHE should be associated with "an element whose lifetime is strikingly longer than its neighbors in the chart of the nuclides" [4]. Typically, the heavier the system the faster the Coulomb repulsion between the increasing number of protons outgrows the attractive nuclear forces. The aforementioned island of stability is a predicted set of heavy nuclides with a near magic number of protons and neutrons that temporarily reverses the trend of decreasing stability (with increasing atomic and neutron numbers) in elements heavier than uranium [5]. In the context of this work, the term SHEs refers to the transactinide elements, which includes elements located in or near the island of stability.

SHEs were predicted using the nuclear shell model in the 1960s [2, 7–9], and their production is very challenging (due to very small cross-sections in the range of a few picobarns or less), with complete fusion (CF) of heavy ions being one of the most successful ways of producing SHEs [10]. The CF mechanism predominantly produces

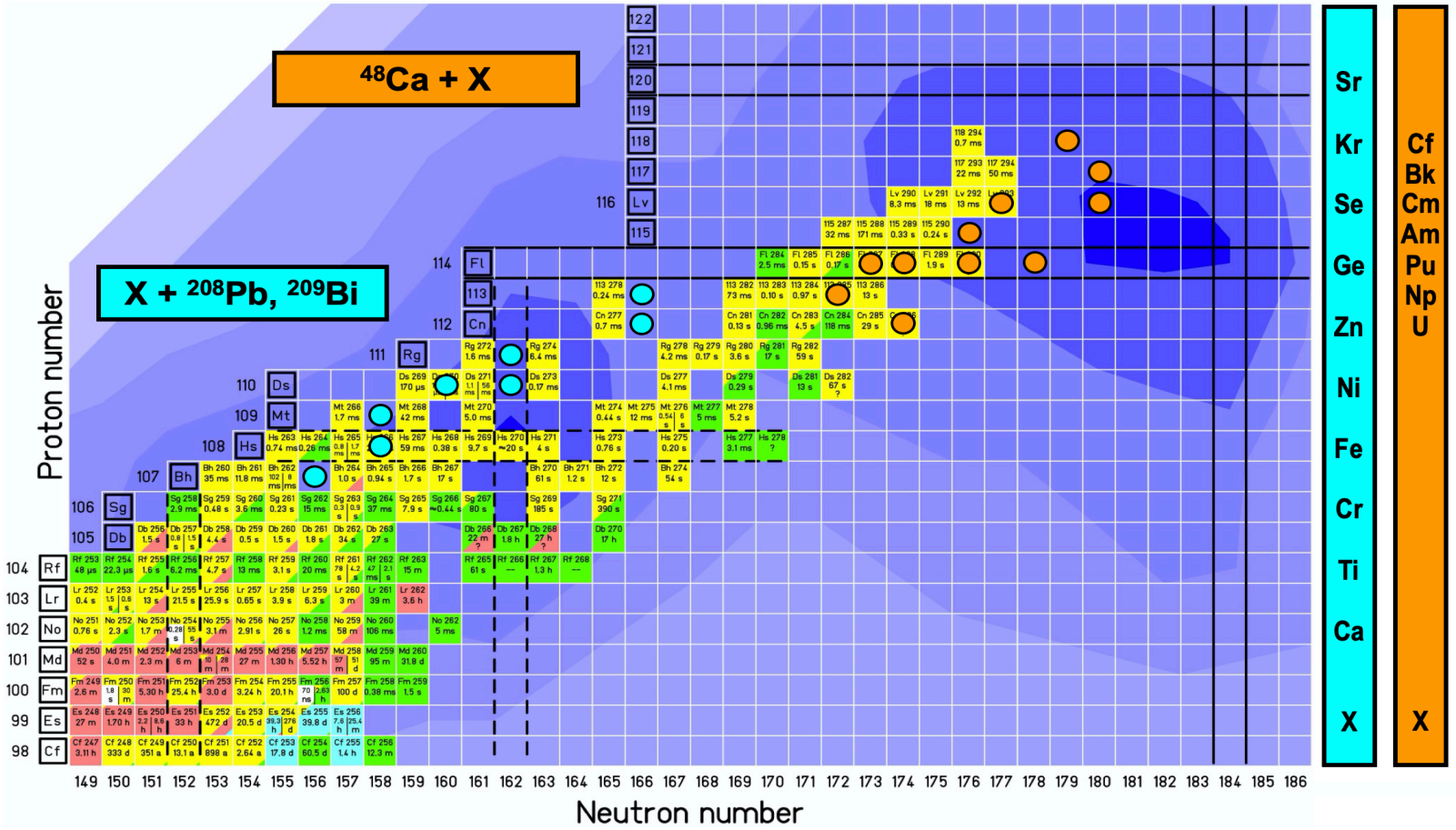

Figure 1.1: Courtesy of the GSI Helmholtz Centre for Heavy Ion Research [6]. CF of heavy ions has been successfully used for producing SHEs in laboratories: Cold CF involving heavy ions on ^{209}Bi or ^{208}Pb targets typically leads to compound nuclei with 10-20 MeV of excitation energy, whilst hot CF involving heavy ions (e.g. ^{48}Ca) on actinide targets typically results in compound nuclei with 40-60 MeV of excitation energy.

neutron-deficient SHEs, as corroborated by the large number of CF products lying to the left of the darker blue 'island of stability' in the table of nuclides shown in Fig. 1.1. This makes investigation into new methods of production crucial for further progress in SHE research.

1.2 Incomplete fusion review

An alternative method of SHE production to the CF mechanism can be found in the incomplete fusion (ICF) mechanism. ICF differs from CF in that (typically after projectile breakup) at least one, but not all, of the fragments of a projectile fuse with the target as opposed to the projectile wholly fusing with the target (with or without undergoing breakup).

In order to understand the underlying dynamics, numerous dynamical models were proposed following the first experimental observation of projectile-like fragments associated with ICF [11, 12]. A 'break-up fusion' model [13] based on the distorted-wave Born approximation was proposed by Udagawa and Tamura wherein the projectile is assumed to break up into α-clusters within the nuclear field of the target, one of which fuses with target nucleus. The production of these breakup fragments was described by a simple plane-wave-projectile-breakup model [14, 15] proposed by Wu and Lee wherein the (fast) breakup process is governed by the projectile's nucleon momenta distribution, and the coupling of Fermi-momentum and the centre-of-mass momentum is assumed to result in the production of these quick fragments. A sum-rule model [16] proposed by Wilczyński *et al.* that concluded that ICF mainly originates from peripheral collisions and is confined to the l-space above the l_{crit} for CF was later extended by Brâncuş *et al.* [17]. Bondorf *et al.* proposed a promptly-emitted-particles model [18] in which it was explained that the nucleons transferred to the target nucleus from the projectile nucleus may obtain extra velocity to escape before equilibration as a consequence of being accelerated in the nuclear field of the target. Fermi-jet [19, 20], moving-source [21], exciton [22, 23], and overlap [24, 25] models, as well as dynamical models for ICF and projectile breakup [26, 27], were also proposed. The probability of ICF was correlated with the mass asymmetry of interacting partners by Morgenstern *et al.* [28], a

supplement for which was presented by Gupta *et al.* [29] and Singh *et al.* [30]. The particle-γ coincidence measurements by Inamura *et al.* [31–33] and Zolnowski *et al.* [34] resulted in the advancement of understanding of ICF dynamics. Geoffroy *et al.* investigated the origin of projectile fragments from undamped peripheral interactions at high l-values, and measured the γ multiplicity as well as the correlation of energies and angles of charged particles [35]. Trautmann *et al.* [36] and Inamura *et al.* [31–33] also emphasised the peripheral nature of ICF. It was inferred in Gerschel's review of ICF [37] that target deformation also has an effect on localisation of the l-window. The emission of projectile-like fragments was suggested to originate from l-values smaller than 0.5 l_{crit} [38, 39] based on results with semi-magic targets obtained by Tricoire *et al.* [20], however this emission was found to originate from high l-values for rare-earth targets [16, 31, 35, 40]. Despite the aforementioned studies, ICF dynamics are still not very well understood at energies around 4-7 MeV/A [41, 42].

In order to address low-energy fusion dynamics of weakly bound nuclei, new types of models ranging from classical to quantum-mechanical methods have been used [43], with new studies on the inclusive non-elastic breakup cross-section potentially leading to the calculation of the ICF cross-section of weakly bound nuclei via a quantum-mechanical route [44, 45]. An alternative quantum-mechanical framework in the form of the time-dependent wave-packet (TDWP) method [46, 47] is capable of calculating ICF and CF cross-sections unambiguously [47], which would otherwise be a challenge using the continuum discretised coupled-channels (CDCC) method [48–50], however the approach is currently under development for implementation using a three-dimensional reaction model. The three-dimensional classical dynamical model [51–53] implemented by the PLATYPUS code [53], which uses classical trajectories in conjunction with stochastic breakup [51, 52], can overcome some of the challenges posed by the quantum-mechanical models. PLATYPUS treats the dynamics of ICF and provides a number of differential cross-sections that are critical for understanding exclusive experimental data [54], in contrast to most existing models for ICF.

1.3 Motivation

This work is experimentally motivated: the observation of energetic α-particles at forward angles in reactions induced by heavy-ions at Coulomb energies [55–58] indicates the existence of a reaction mechanism in which, following projectile breakup, the α-particle carries away most of the bombarding energy of the projectile, leaving the other remaining projectile fragment to be captured by the target resulting in a colder fusion product than would typically be achieved via the CF mechanism (with higher excitation energy). The newly formed nucleus may possess high angular momentum. In particular, at $E_\alpha = E_\alpha^{max}$ the excitation of the nucleus is determined basically by rotation and this can lead to the formation of fast rotating cold nuclei [55]. The low excitation energy of these cold products from ICF reactions results in both a higher survivability against fission and fewer neutrons evaporated, indicating that this mechanism could be a successful way of producing relatively stable SHE isotopes.

Unfortunately not much work has been done in the field of heavy-ion fusion to address the aforementioned reaction mechanism. According to the review of theoretical approaches for understanding the ICF process in [59], it is apparent that whilst there are models available to explain CF and to explain ICF at energies $E \geq 10.5$ MeV/A or so (and ICF at energies below that threshold for weakly-bound nuclei [52, 53]) there is currently no theoretical model available to predict ICF at lower energies ($E \approx 4 - 7$ MeV/A) for complex nuclei. As this mechanism has not been thoroughly explored yet, and could prove to be an effective way of producing neutron-rich SHE isotopes with low excitation energies [57], the focus of this work is to investigate ICF reaction dynamics of complex nuclei at Coulomb energies. Broadly, this reaction mechanism can also be useful for producing new isotopes throughout the periodic table [60]. According to Ref. [61] it can be inferred that the ICF process makes a greater contribution to the total fusion cross-section at low projectile energies, and that projectile structure has a strong effect on the total ICF cross-section.

To this aim, a semi-classical dynamical model has been developed [62, 63] by combining a classical trajectory model with stochastic breakup, as implemented in the PLATYPUS code [52, 53], with the quantum-mechanical fragmentation theory [64] treatment of

two-body clusterisation and decay of a projectile. A 'complex nucleus' is a nucleus wherein it is not clear that there is one dominant cluster structure, as opposed to a weakly bound light nucleus (such as ^{6}Li, ^{7}Li and ^{9}Be for example) which has a single dominant cluster structure. A complex nucleus can be viewed as a superposition of many simple cluster structures, and this is why fragmentation theory (illustrated in Fig. 3.1) is useful for this work.

Fragmentation theory was developed by the Frankfurt school of Theoretical Nuclear Physics [65–67]. This theory provides a sound framework for a unified and consistent description of the treatment of two-body and many-body breakup channels in fission, fusion, cluster radioactivity and heavy ion scattering [68]. This theory properly takes into account nuclear shell effects as it is based on the two-center shell model (TCSM) [69]. The basic idea of fragmentation theory is the introduction of collective mass and charge fragmentation co-ordinates, η and η_Z respectively, which allow one to describe the incomplete fusion of a complex projectile in a unified way. The dynamics of the fragmentation degree of freedom are described in Chapter 3.1. In the past, the collective description of a nuclear system has proven to be extremely successful [70], the main advantage of which being the clear physical picture behind the various collective Hamiltonians, allowing for a rather simple description of complicated many-body phenomena such as fusion, fission, and cluster decay amongst others. The collective phenomena form only a part of the full picture of the nucleus, but they are often the most striking and interesting aspect, and many theories for nucleus-nucleus collisions also have in common the fact that they describe the complex many-body problem in semi-classical pictures with a few important collective degrees of freedom [68].

1.4 Goals of this work and its structure

In concise terms, the main goals of this work are as follows:

(i) To develop a semi-classical dynamical model comprised of a classical trajectory model and the quantum-mechanical fragmentation theory.

(ii) To test the resultant predictions of the aforementioned model against published experimental results in order to calibrate the model and validate its accuracy.

(iii) To use the calibrated model to make new predictions for SHE formation in ICF reactions at Coulomb energies.

In the current chapter introductions to SHE research and fragmentation theory have been presented along with a brief review of studies of the ICF mechanism and the motivation for carrying out this work. Chapter 2 details the classical trajectory model upon which this work is built and the refinements that have been made to it, and Chapter 3 covers this work's key addition to that foundation; the quantum-mechanical fragmentation theory. In Chapter 4 the potential and inertia parameters are detailed, and in Chapter 5 model test case results are evaluated and compared with published experimental data for calibration. Chapter 6 presents novel model predictions for SHEs along with discussions, with associated evaporation residues (EVRs) provided in Chapter 7. Chapter 8 concludes with a summary of this work and future outlooks.

Chapter 2

Classical Trajectory Model

2.1 PLATYPUS implementation

PLATYPUS is a self-contained Fortran-90 program based on a classical trajectory model [51, 52] with stochastic breakup and is a powerful tool for quantifying complete and incomplete fusion, as well as breakup in reactions induced by weakly bound two-body projectiles near the Coulomb barrier, which for this work has been extended for the reactions of complex nuclei.

The program calculates a wide range of observables including integrated CF and ICF cross-sections and their spin distribution, as well as breakup observables such as the angle, kinetic energy, and relative energy distributions of the fragments. All of the observables are calculated using a three-dimensional classical dynamical model merged with Monte-Carlo sampled probability-density distributions [52].

The main features of the model are as follows:

(i) In the origin of the laboratory frame, the weakly-bound (two-body) projectile P with incident energy E_0 and orbital angular momentum L_0 approaches the initially-at-rest target T along the z-axis. An ensemble of N incident projectiles is considered for each integer number of $\hbar$, chosen to represent L_0. An orbit with a definite distance of closest approach $R_{min}(E_0,\ L_0)$ is determined by classical

equations of motion (see Appendix A) including the P-T mutual Coulomb and nuclear forces.

(ii) A local breakup probability density, a function of the projectile-target separation R, namely $\mathcal{P}^L_{BU}(R)$, empirically encodes the complexity of the projectile dissociation. Consequently, $\mathcal{P}^L_{BU}(R)\mathrm{d}R$ is the probability of breakup in the interval R to $R + \mathrm{d}R$ (see Appendix B). An important feature is that the integral of this breakup probability density along a given classical orbit is an exponential function of its distance of closest approach, $R_{min}(E_0, L_0)$ for a given projectile-target combination, as indicated by both measurements [71, 72] and continuum-discretised coupled channels (CDCC) calculations [51]:

$$P_{BU}(R_{min}) = 2\int_{R_{min}}^{\infty} \mathcal{P}^L_{BU}(R)dR = e^{-\alpha R_{min}+\beta}. \tag{2.1}$$

$\mathcal{P}^L_{BU}(R)$ has the same exponential form, $\mathcal{P}^L_{BU}(R) \propto e^{-\alpha R}$, as a consequence, with the factor of 2 indicating that breakup may occur along either the trajectory's entrance branch or exit branch, although the the maximum probability of breakup is placed at R_{min} by the exponential form. The position of projectile breakup in the orbit discussed in (i) is determined by sampling this function, in which the projectile is instantaneously separated into fragments F_1 and F_2, which interact with each other and with the target T through real central two-body potentials having Coulomb barriers V^{ij}_B at separations R^{ij}_B $(i, j = 1, 2, T,\ i \neq j)$. The constants α and β are determined from experimental results that vary for different systems [73, 74].

(iii) At breakup, the excited projectile's total internal energy ε_{12}, its angular momentum $\vec{\ell}_{12}$ and the separation of the fragments $\vec{d}_{12}$ are all Monte Carlo sampled. The radial and angular probability distributions of the projectile ground-state wave function are sampled to determine the initial separation d_{12} between the fragments and its orientation $\vec{d}_{12}$, respectively. A very good approximation for calculating d_{12} for a two-body projectile with 0^+ ground state is through a Gaussian sampling function in the classically allowed region of the fragments, with the orientation of $\vec{d}_{12}$ being isotropic. The orientation of $\vec{\ell}_{12}$ is chosen ran-

domly from all directions orthogonal to $\vec{d}_{12}$. When there is no barrier between F_1 and F_2 for high ℓ_{12} excitations, d_{12} is equated with their external turning point. An exponentially decreasing function for energies between the top of the barrier (V_B^{12}) and a chosen maximum ε_{max} is sampled to determine ε_{12}, whilst ℓ_{12} is sampled uniformly in the interval [0,ℓ_{max}]. Both ε_{max} and ℓ_{max} are increased until convergence of the observables occur.

(iv) The instantaneous velocities of the particles F_1, F_2 and T are determined by conservation of energy, linear momentum and angular momentum in the overall centre-of-mass frame (see appendix A), given that the position and dynamical variables of the excited projectile fragments at the moment of breakup have now been fixed. The three bodies are propagated in time upon transforming these breakup initial conditions to the laboratory frame. The number of ICF, CF and non-capture breakup (NCBU) events are determined by the calculated trajectories of F_1, F_2 and T, with a given fragment F_j being assumed to be captured if the classical trajectories take it within the fragment-target barrier radius R_B^{jT}.

(v) For each projectile angular momentum L_0, N breakup events are sampled, with the numbers of events N_i in which $i = 0$ (NCBU), 1 (ICF), or 2 (CF) fragments are captured determining the relative yields $\tilde{P}_i = N_i/N$ of these three reaction processes after breakup, with the sum total of these relative yields being equal to 1 ($\tilde{P}_0 + \tilde{P}_1 + \tilde{P}_2 = 1$). The relative yields and the integrated breakup probability over the whole trajectory $P_{BU}(R_{min})$ are used to express the absolute probabilities $P_i(E_0, L_0)$ of these processes:

$$P_0(E_0, L_0) = P_{BU}(R_{min})\tilde{P}_0, \tag{2.2a}$$

$$P_1(E_0, L_0) = P_{BU}(R_{min})\tilde{P}_1, \tag{2.2b}$$

$$P_2(E_0, L_0) = [1 - P_{BU}(R_{min})]H(L_{cr} - L_0) + P_{BU}(R_{min})\tilde{P}_2, \tag{2.2c}$$

where L_{cr} is the critical partial wave for projectile fusion and $H(x)$ is the Heaviside step function. The cross-sections are calculated using:

$$\sigma_i(E_0) = \pi\lambda^2 \sum_{L_0} (2L_0 + 1) P_i(E_0, L_0), \tag{2.3}$$

where μ is the reduced mass ($\frac{m_P m_T}{m_P + m_T}$) and $\lambda^2 = \frac{\hbar^2}{2\mu E_0}$. Asymptotic observables, such as the angular, kinetic energy and relative energy distributions of the fragments from NCBU events, are calculated alongside the absolute cross-sections by tracking their trajectories to a large distance from the target.

(vi) Incorporated into this model for the ICF events are the time propagation of the ICF product and the surviving breakup fragment. After overcoming the Coulomb barrier V_B^{jT}, the fragment F_j reaches the target radius, forming the ICF product, while the remaining fragment travels away. This is the moment when the three-body propagation becomes a two-body propagation, with definite interaction potentials and initial conditions determined by the position and velocity of the three particles at the moment of ICF product formation. The spin and excitation energy distributions of the *primary* ICF product are also yielded by these two-body interaction potentials and initial conditions, with the asymptotic angular distribution of the ICF product and the surviving breakup fragment being calculated in terms of their trajectories.

A major limitation of using the PLATYPUS code to model the ICF of complex nuclei is that it requires the binary fragmentation configuration of the projectile as an input; in effect it addresses the ICF of a single binary fragmentation configuration. Whilst the code provides the probability of a given projectile breaking up into a specific binary configuration of fragments (as a function of R_{min}), it does not mean that the projectile would necessarily break up into those two specific fragments in reality as many other competing binary fragmentation configurations are possible with a complex nucleus (see Fig. 3.1). This shortcoming is the motivation for adopting a dynamical fragmentation theory [64] treatment of two-body clusterisation and decay of a projectile.

2.2 Projectile friction

An extension of the classical trajectory model described in Chapter 2.1 that has been implemented here consists of the addition of friction terms [75] to the target-projectile's Newtonian equations of motion as shown in Eqs. (2.4) and (2.6):

$$\frac{d}{dt}(\mu\dot{r}) - \mu r\dot{\varphi}^2 - \frac{dV_{NC}}{dr} + K_r\dot{r} = 0. \tag{2.4}$$

μ is the reduced mass ($\frac{m_P m_T}{m_P+m_T}$), $\dot{r}$ is the radial velocity, $\dot{\varphi}$ is the angular velocity, V_{NC} is the interaction potential consisting of nuclear and Coulomb parts, and K_r is the radial friction coefficient, which is proportional to the square of the nuclear force [75]:

$$K_r = K_r^0(\nabla V_N)^2, \tag{2.5}$$

where $K_r^0 = 4 \times 10^{-23}$s/MeV [75]. Included here is only radial friction, causing radial kinetic energy dissipation. The last term in Eq. (2.4) accounts for such a radial kinetic energy dissipation along a projectile-target trajectory. The loss of radial kinetic energy due to the last term in Eq. (2.4) produces the full energy loss along a projectile-target trajectory and directly determines the excitation energy of the projectile, and by extension the number of summed excited states considered in the calculation of the total probability density function of the projectile's fragmentation in the charge asymmetry co-ordinate in Chapter 3.4. This energy loss, ΔE, as a function of distance between target and projectile, R, is shown in Fig. 2.1a for the reaction ^{20}Ne+^{208}Pb with the projectile incident energy being 10% above the Coulomb barrier. With increasing orbital angular momentum, L, the energy lost to friction as a function of distance decreases. The arrow marks the location of the Coulomb barrier, and the energy loss at the point of projectile breakup in terms of R is taken to determine the excitation energy of the projectile. In this case the taken excitation energy does not exceed ~ 8 MeV for $L = 0$-$100\hbar$.

Similarly, the loss of orbital angular momentum due to the tangential friction term in Eq. (2.6) has been considered to account for the full angular momentum loss along a

projectile-target trajectory and directly determines the intrinsic angular momentum of the projectile:

$$\frac{d}{dt}(\mu r^2\dot{\varphi}) + K_\varphi r^2\dot{\varphi} = 0. \tag{2.6}$$

where K_φ is the tangential friction coefficient, which is also proportional to the square of the nuclear force [75]:

$$K_\varphi = K_\varphi^0(\nabla V_N)^2, \tag{2.7}$$

where $K_\varphi^0 = 0.01 \times 10^{-23}$s/MeV [75]. This angular momentum loss, ΔL, due to tangential friction is shown in Fig. 2.1b for the reaction ^{20}Ne+^{208}Pb with the projectile incident energy being 10% above the Coulomb barrier. With increasing L, ΔL as a function of distance increases. The arrow marks the location of the Coulomb barrier, and the orbital angular momentum loss at the point of projectile breakup in terms of R is taken to determine the the initial, maximal angular momentum between the two fragments, L_{12}. In this case the taken L_{12} is negligible for $L = 0$-$100\hbar$.

For the sake of simplicity, the tangential angular momentum loss has not been considered in subsequent calculations. The approximation has instead been made that the intrinsic angular momentum of the projectile is equal to zero.

In this chapter the classical trajectory model, as implemented in the PLATYPUS code, has been detailed along with the additional consideration of projectile friction, which means that two former inputs of the model are now intrinsically determined, making for a more realistic and self-contained model. Chapter 3 will take this approach further with the consideration of fragmentation theory.

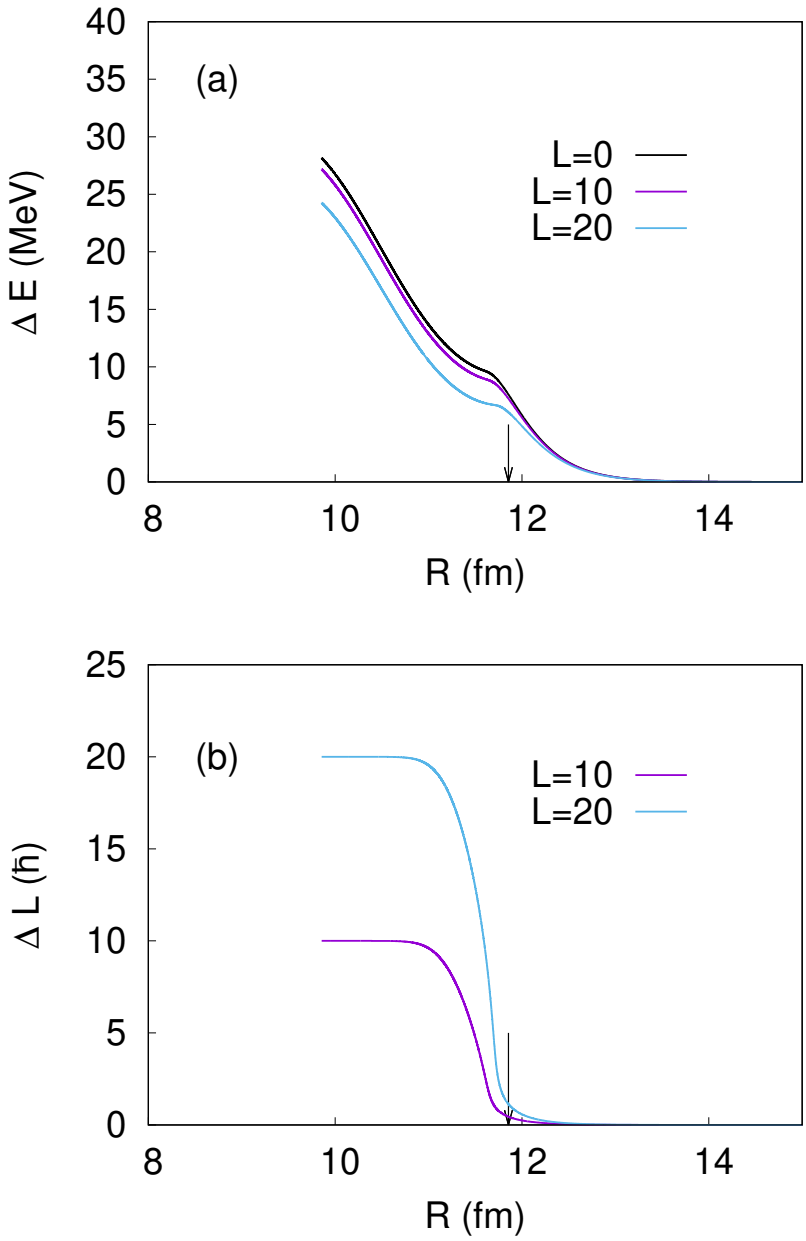

Figure 2.1: Loss of: (a) radial kinetic energy, (b) orbital angular momentum, due to projectile friction as a function of distance between target and projectile for the reaction ^{20}Ne+^{208}Pb with the projectile incident energy being 10% above the Coulomb barrier. Each line represents a different partial wave and the arrow marks the location of the Coulomb barrier.

Chapter 3

Fragmentation Theory

3.1 The charge asymmetry coordinate

In 2012 Kuklin et al. presented a model [64] that makes use of the charge asymmetry co-ordinate, η_Z, which stems from the mass asymmetry co-ordinate, η, first proposed by the Frankfurt School for Theoretical Nuclear Physics in the 1970s [66, 67], and is equal to the continuous volume asymmetry co-ordinate when the two nuclei overlap [66, 67]. Take, for example, a complex projectile undergoing fragmentation in order to incompletely fuse with an actinide target, as shown in Fig. 3.1.

In the centre of Fig. 3.1 there are three binary configurations shown for the fragmentation of the projectile in the charge asymmetry coordinate, to demonstrate the concept. η_Z is defined as the difference in the charges of the two fragments divided by the sum total of their charges, as per Eq. (3.1).

$$\eta_Z = \frac{(Z_1 - Z_2)}{(Z_1 + Z_2)}, \tag{3.1}$$

where Z_1 and Z_2 are the charges of fragments 1 and 2 respectively. In the case of $\eta_Z = 0$, the fragmentation is symmetric ($Z_1 = Z_2$), as per the middle configuration in Fig. 3.1. At the extremes, where $\eta_Z = \pm 1$, there is no fragmentation (as one of the would-be fragments has charge $Z = 0$). The charge asymmetry co-ordinate is similar

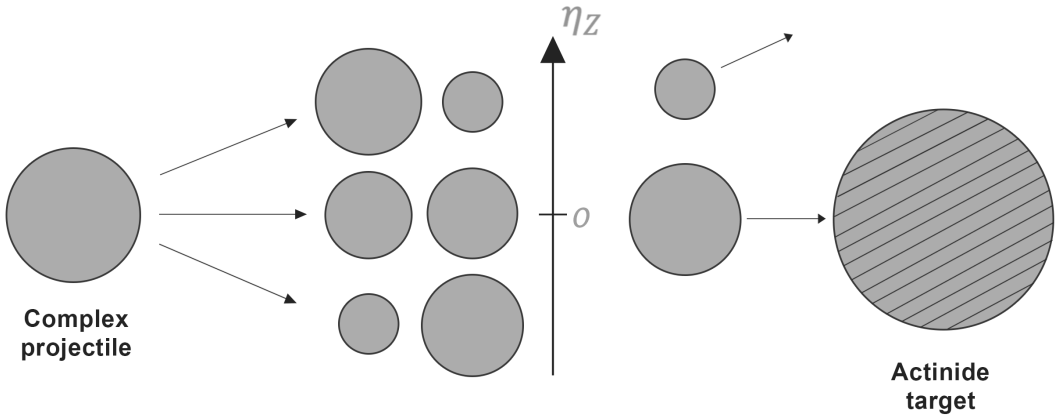

Figure 3.1: A diagram representing ICF of a complex projectile (undergoing fragmentation in the charge asymmetry co-ordinate) and an inert target.

to the mass asymmetry co-ordinate [65–67], but it concerns charge distribution rather than mass distribution:

$$\eta = \frac{(A_1 - A_2)}{(A_1 + A_2)}. \tag{3.2}$$

3.2 The time-independent Schrödinger equation

The determination of the state of a dinuclear system for a given parent nucleus is made by solving the time-independent Schrödinger equation in the charge asymmetry co-ordinate with periodic boundary conditions at $\eta_Z = \pm 1$ [64]:

$$\hat{H}\Psi_n(\eta_Z) = E_n\Psi_n(\eta_Z), \tag{3.3}$$

where Ψ is the wavefunction, E is the energy, n is the eigenstate quantum number, η_Z is the charge asymmetry co-ordinate, and $\hat{H}$ is the collective Hamiltonian:

$$\hat{H} = -\frac{\hbar^2}{2}\frac{\partial}{\partial\eta_Z}(B^{-1})_{\eta_Z\eta_Z}\frac{\partial}{\partial\eta_Z} + V(\eta_Z), \tag{3.4}$$

where $(B^{-1})_{\eta_Z\eta_Z}$ is the inverse inertia coefficient (a mass parameter for the co-ordinate η_Z) (units: nucleon mass^{-1} fm^{-2}) [64, 76] and $V(\eta_Z)$ is the driving potential as a function of η_Z. This condenses to:

$$\left[-\frac{\hbar^2}{2}\frac{\partial}{\partial\eta_Z}(B^{-1})_{\eta_Z\eta_Z}\frac{\partial}{\partial\eta_Z}+V(\eta_Z)\right]\psi(\eta_Z)=E\psi(\eta_Z). \tag{3.5}$$

The numerical method for solving Eq. (3.5) is explained in detail in Chapter 3.3. The calculation of the ingredients of this equation, the driving potential and the inverse inertia coefficient, are presented in Chapters 4.2 and 4.3, respectively. The inverse inertia coefficient in the charge asymmetry coordinate is strongly connected with the inertia coefficient in the mass asymmetry coordinate, as discussed in Refs. [64, 76, 77]. The latter inertia coefficient depends on the number of nucleons in the neck between the two touching fragments, whose determination requires a 3D spatial integration (Eq. (4.10)). Values of the inverse inertia coefficients and the driving potentials for projectiles considered in this work are presented in Chapter 4.4.

3.3 Finite-difference method

A finite-difference method solution to the time-independent Schrödinger equation that incorporates periodic boundary conditions is presented in Ref. [78]. The premise of the method is to discretise the continuous variable (in this case, x) into a series of points with a finite difference Δ in such a manner that $x_i = x_0 + i\Delta$, where i is the step number ($i = 0, 1, 2, 3, ..., N$).

Starting with the time-independent Schrödinger equation, the mass, m, is also taken as a function of the co-ordinate x as well as the potential, V, and the wavefunction, ψ [79]:

$$-\frac{\hbar^2}{2}\frac{d}{dx}\left(\frac{1}{m(x)}\frac{d}{dx}\right)\psi(x)+V(x)\psi(x)=E\psi(x). \tag{3.6}$$

Taking $m(x) = m_0B(x)$ and multiplying by $\frac{2m_0}{\hbar^2}$:

$$-\frac{d}{dx}\left(\frac{1}{B(x)}\frac{d}{dx}\psi(x)\right)+\frac{2m_0}{\hbar^2}V(x)\psi(x)=\frac{2m_0}{\hbar^2}E\psi(x). \tag{3.7}$$

Introducing the terms $v(x)=\frac{2m_0}{\hbar^2}V(x)$ and $\mathcal{E}=\frac{2m_0}{\hbar^2}E$:

$$-\frac{d}{dx}\left(\frac{1}{B(x)}\frac{d}{dx}\psi(x)\right)+v(x)\psi(x)=\mathcal{E}\psi(x). \tag{3.8}$$

Rewriting the derivatives using the finite difference method:

$$-\frac{1}{\Delta x^2}\left(\frac{\psi_{i+1}-\psi_i}{B_{i+1/2}}-\frac{\psi_i-\psi_{i-1}}{B_{i-1/2}}\right)+v_i\psi_i=\mathcal{E}\psi_i, \tag{3.9}$$

where the intermediate points $(i\pm 1/2)$ are the mean values of the two adjacent points:

$$\begin{aligned} B_{i+1/2}&=\frac{1}{2}\left(B_{i+1}+B_i\right),\\ B_{i-1/2}&=\frac{1}{2}\left(B_i+B_{i-1}\right). \end{aligned} \tag{3.10}$$

Here the periodic boundary condition $\psi_0=\psi_N$ is enforced [80]. With this boundary condition the domain of definition of our wavefunction can formally be extended from the interval $x\in[0,L]$ to the whole number axis, with the requirement that the function be periodic with the period L:

$$\psi(x+L)=\psi(x). \tag{3.11}$$

The co-ordinate space x is related to the charge asymmetry co-ordinate by:

$$x=1-\eta_Z, \tag{3.12}$$

and as the range of η_Z is 2, the range of x (and therefore L in Eq. (3.11)) must also be 2.

In order to enforce this periodic boundary condition the tridiagonal Hamiltonian matrix must be amended by setting the top-right (1,N) and bottom-left (N,1) elements equal to the sub-diagonal elements, as per Eq. (3.13).

$$\begin{pmatrix} -2c+v_1 & a & 0 & \cdots & b \\ b & -2c+v_2 & a & \cdots & 0 \\ 0 & b & -2c+v_3 & \cdots & 0 \\ 0 & 0 & b & \cdots & 0 \\ \vdots & \vdots & \vdots & \ddots & \vdots \\ a & 0 & 0 & \cdots & -2c+v_N \end{pmatrix} \times \begin{pmatrix} \psi_1 \\ \psi_2 \\ \psi_3 \\ \vdots \\ \psi_N \end{pmatrix} = \mathcal{E} \begin{pmatrix} \psi_1 \\ \psi_2 \\ \psi_3 \\ \vdots \\ \psi_N \end{pmatrix}, \quad (3.13)$$

where v_i is the potential of the ith step, $\mathcal{E}$ is the eigenenergy, $a = -\frac{1}{\Delta^2}\frac{1}{B_{i+1/2}}$ for elements above the diagonal, $b = -\frac{1}{\Delta^2}\frac{1}{B_{i-1/2}}$ for elements below the diagonal and $c = -\frac{1}{2}\left(\frac{1}{\Delta^2}\left(\frac{1}{B_{i+1/2}} + \frac{1}{B_{i-1/2}}\right)\right)$ for elements on the diagonal (for which B is the mass parameter). Eq. (3.13) is the practical application of Eq. (3.5) in the code, however an additional approximation has been made: the values of top-right (1,N) and bottom-left (N,1) elements have been changed to their combined average value, $(a+b)/2$ (or simply, c). In doing so, the matrix has been symmetrised, ensuring compatibility with the very efficient LAPACK subroutine *dsyevx* [81], which is used to diagonalise this tridiagonal matrix. The consequence of this approximation for the results is numerically negligible. The advantage of having a symmetric matrix is that it allows one to avoid using a time-consuming generic algorithm of matrix diagonalisation. The resultant eigenvectors are subsequently normalised so that the probability density function (PDF) ψ^2 can be computed and plotted as shown in Fig. 3.2. The Fortran-90 implementation of this method is included in Appendix C.

In this example, ^{20}Ne is used as a test case because this nucleus has been used as a complex projectile in several ICF experiments [55–58]. Figs. 3.2(a), 3.2(b) and 3.2(c) represent the PDF associated with the first, second and third energy eigenvalues, respectively, for the fragmentation of ^{20}Ne in the charge asymmetry coordinate. These three energy eigenvalues correspond to six degenerate eigenvectors. This degeneracy arises from the symmetry of the potential about $\eta_Z = 0$ in Fig. 4.1. For the first and third

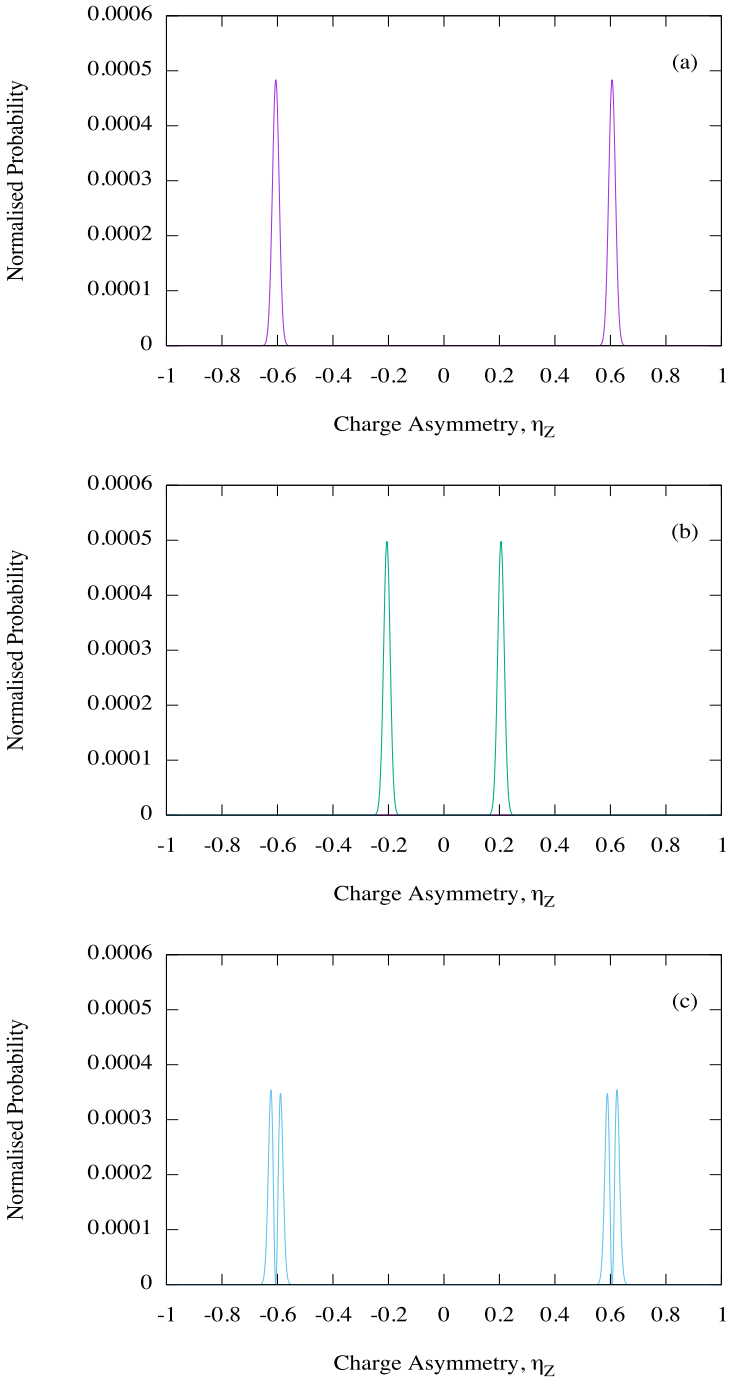

Figure 3.2: Normalised PDF representing the fragmentation for the first three energy eigenvalues of ^{20}Ne in the charge asymmetry coordinate, with the potential energy and inertia coefficients of Fig. 4.1: (a) -5.38 MeV, (b) -5.34 MeV, and (c) -4.76 MeV. The inertia coefficients and potentials of Fig. 4.1 have been interpolated here using $\Delta\eta_Z = 0.001$.

eigenvalues there are clear peaks at $\eta_Z = \pm 0.6$, which arise from fragment charges Z_1 and Z_2 of 8 and 2, corresponding to $^{16}_{8}$O and $^{4}_{2}$He. Similarly for the second eigenvalue there are clear peaks at $\eta_Z = \pm 0.2$, which arise from fragment charges Z_1 and Z_2 of 6 and 4, corresponding to $^{12}_{6}$C and $^{8}_{4}$Be. This shows that this method can successfully distinguish between the different binary configurations of fragmentation. The splitting of the peaks in Fig. 3.2(c) is due to the increased number of nodes in this higher excited state of ^{20}Ne.

3.4 Summing states via a Boltzmann factor

A given projectile excitation energy range encompasses a certain number of eigenstates, and so in order to account for each state's contribution to the total fragmentation PDF they are summed using a Boltzmann factor [68]:

$$|\Psi(\eta_Z)|^2 = \frac{\sum_{i=0}^{N} e^{-E_i/T} |\psi_i(\eta_Z)|^2}{\sum_{i=0}^{N} e^{-E_i/T}}, \tag{3.14}$$

where E_i is the eigenenergy of the i-th state and T is the temperature in MeV given by:

$$T = \sqrt{\frac{E^*_{max}}{a}}, \tag{3.15}$$

where E^*_{max} is the maximum excitation energy of the projectile, given by the loss of the radial kinetic energy of the projectile (due to the last term in Eq. (2.4)) over the course of the projectile-target trajectory until the point of breakup, relative to the height of the Coulomb barrier between the two fragments. As the breakup radius, R_{BU}, of the projectile is sampled, E^*_{max} is treated here as a dynamical variable that changes for different internuclear distances, and consequently the number of summed eigenstates varies from sample to sample.

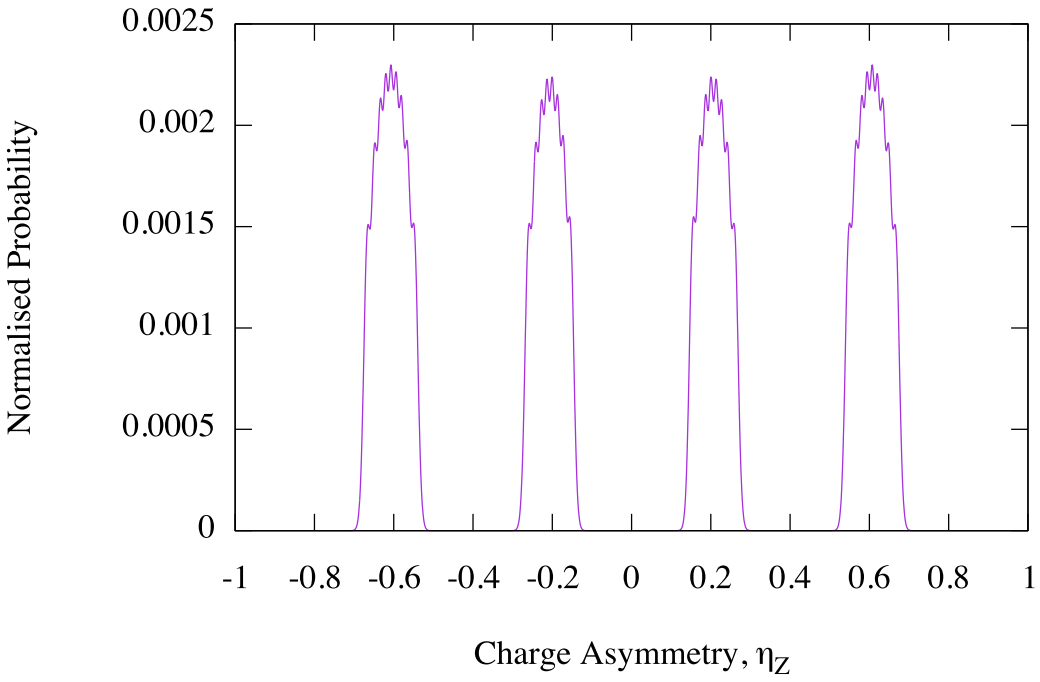

Figure 3.3: Normalised total PDF representing the fragmentation for all 34 eigenvalues that lie within a 5 MeV excitation energy range of ^{20}Ne in the charge asymmetry coordinate, with the potential energy and inertia coefficients of Fig. 4.1. The inertia coefficients and potentials of Fig. 4.1 have been interpolated here using $\Delta\eta_Z = 0.001$.

The constant a in MeV^{-1} in Eq. (3.15) is given by the Fermi gas model [68]:

$$a = \frac{A_P}{10 \text{ MeV}}, \tag{3.16}$$

where A_P is the nucleon number of the projectile nucleus.

The resulting total PDF for ^{20}Ne of Eq. (3.14) with $E^*_{max} = 5$ MeV is shown in Fig. 3.3 as an example. This PDF is then turned into a cumulative distribution function (CDF) and Monte-Carlo sampled in order to select a binary fragmentation configuration. This is achieved via direct inversion of the CDF [82], a process explained in Appendix D.

In this chapter the major addition to the classical trajectory model described in Chapter 2 has been detailed. A major input of the original model, namely the determination of binary configuration of the projectile, is now also intrinsically determined, making the model substantially more self-contained than before. Chapter 4 will round out the model with the determination of potential and inertia parameters used throughout.

Chapter 4

Driving Potentials and Inertia Coefficients in the Charge Asymmetry Coordinate

4.1 The Broglia-Winther nuclear potential

The nuclear interaction potentials used in this model were calculated using the Broglia-Winther approach [83], wherein the real part of the nucleus-nucleus optical potential is assumed to have a Woods-Saxon shape:

$$V_N(r) = -\frac{V_0}{1 + \exp\left(\frac{r-R_0}{a}\right)}, \tag{4.1}$$

where

$$V_0 = 16\pi \frac{R_1 R_2}{R_1 + R_2}\gamma a, \quad a = 0.63fm, \tag{4.2}$$

and

$$R_0 = R_1 + R_2 + 0.29 \text{ fm}, \;\; R_i = 1.233A_i^{1/3} - 0.98A_i^{-1/3}, \tag{4.3}$$

with surface energy constant γ:

$$\gamma = \gamma_0 \left[1 - k_s \left(\frac{N_1 - Z_1}{A_1}\right)\left(\frac{N_2 - Z_2}{A_2}\right)\right], \tag{4.4}$$

where γ_0 and k_s are assumed to be 0.95 MeV/fm^2 and 1.8 respectively [83]. The Broglia-Winther potential has been used as a real nuclear potential to systematically explain the elastic differential cross-sections of many heavy-ion systems [83].

4.2 Projectile driving potential

The proposed solution to the time-independent Schrödinger equation (Eq. (3.5)) postulates that each binary configuration of fragmentation has its own associated driving potential energy $V(\eta_Z)$, as exemplified by Fig. 4.1.

In the present work binary configurations of spherical fragments are considered. Both the inverse inertia coefficients and the driving potentials are determined at the contact distance between the fragments which is the sum of their radii, i.e., $R_c = R_1 + R_2$, with R_i given by Eq. (4.3). Whilst binary configurations of deformed fragments in the ^{20}Ne projectile were considered in Ref. [62], the present dynamical reaction model also considers isotropic orientation of the segment joining the two fragments relative to the segment between the centre of mass of the projectile and the target. Since this assumption of 'isotropic orientation' diminishes the role of the fragment deformation in the ICF process, it is considered that the use of spherical fragments is simpler and a good approximation. The total driving potential, $V(\eta_Z)$ is taken as the sum of the nuclear and Coulomb potentials, V_N and V_C respectively, in addition to the binding energies of the two fragments, BE_1 and BE_2, relative to the binding energy of the compound nucleus, BE_{CN}:

$$V(\eta_Z) = V_N + V_C + BE_1 + BE_2 - BE_{CN}. \tag{4.5}$$

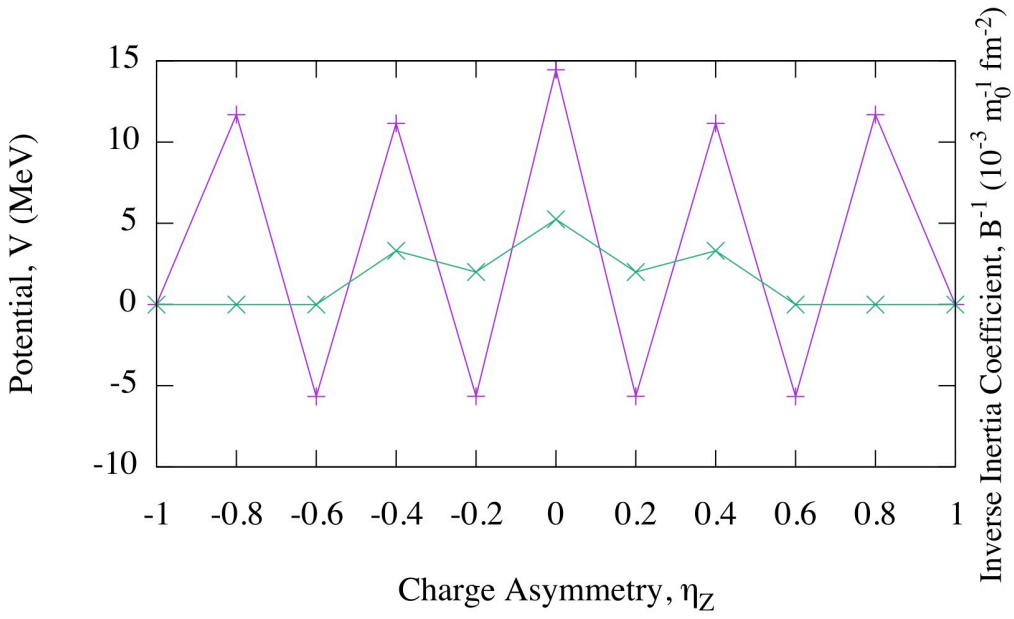

Figure 4.1: Inverse inertia coefficient (×) / potential (+) plot for the fragmentation of $^{20}_{10}$Ne in the charge asymmetry coordinate, with the potential energy of the compound nucleus $U_0 = 0$ MeV. m_0 is the nucleon mass (938 MeV/c^2). Markers denote values calculated, whilst intermediate values can be interpolated. These values have been used in the calculation of Figs. 3.2 and 3.3.

The nuclear interaction potentials are calculated using the Broglia-Winther approach as described in Chapter 4.1. The Coulomb interaction potentials are calculated using Eq. (4.6):

$$V_C = \frac{Z_1 Z_2 e^2}{R_c}, \tag{4.6}$$

where Z_1 and Z_2 are the charges of fragments 1 and 2, respectively, e^2 is the elementary charge (1.43997 MeV fm) and R_c is the contact distance between the fragments. Binding energies for the projectile and its constituent fragments were taken from Ref. [84], whilst binding energies for exotic targets and ICF products were taken from Ref. [85]. The strong variations in binding energy for different fragments give rise to the large energy fluctuations among the dinuclear configurations in Fig. 4.1. The driving potentials and inverse inertia coefficients shown in Fig. 4.1 were calculated using a double-folding nuclear interaction potential and considered deformed fragments [86]. The inertia coefficient plot has been extrapolated from $\eta_Z = \pm 0.6$ to ± 1 due to insufficient data, and so the actual inertia coefficient points for $\eta_Z = \pm 0.8$ are also expected to be local maxima. Fig. 4.1 here serves as a demonstration, representing the inputs for the calculation of the fragmentation PDFs in Figs. 3.2 and 3.3. For the results in Chapters 5 and 6, the driving potentials and inverse inertia coefficients presented in the following subchapters (summarised and tabulated in Chapter 4.4) are used, which are calculated using the Broglia-Winther nuclear interaction potential and consider spherical fragments. Another good reason to consider spherical fragments over deformed fragments is one of uniformity, as the underlying PLATYPUS code already considers spherical fragments.

4.2.1 ^{20}Ne driving potentials

Fig. 4.2 presents the driving potentials for the fragmentation of of ^{20}Ne in the charge asymmetry coordinate. The potential wells at $\eta_Z = \pm 0.6$ and ± 0.4 indicate that the pairings of O+He and C+Be are the most and second-most energetically favourable fragmentations respectively.

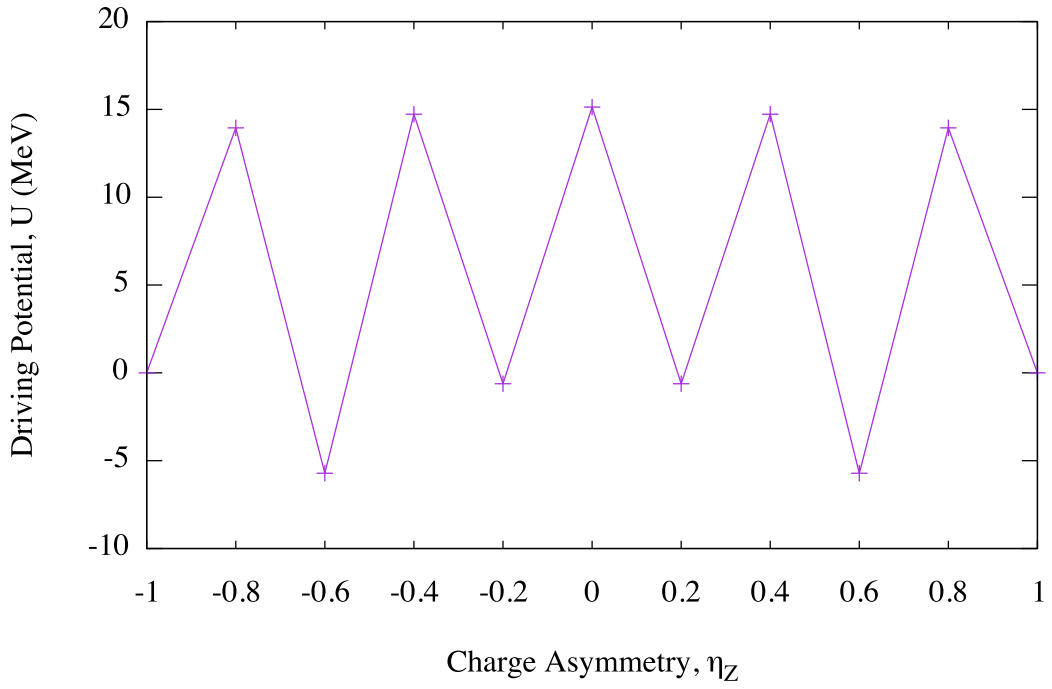

Figure 4.2: Driving potential plot for the fragmentation of ^{20}Ne in the charge asymmetry coordinate. The fragments are considered at the contact distance, i.e., $R_c = R_1 + R_2$, with R_i given by Eq. (4.3). Markers denote values calculated, whilst intermediate values can be interpolated. These values are tabulated in Table 4.1.

4.2.2 ^{40}Ca driving potentials

Fig. 4.3 presents the driving potentials for the fragmentation of of ^{40}Ca in the charge asymmetry coordinate. The potential wells at $\eta_Z = \pm 0.8, \pm 0.4, \pm 0.2$ and 0 indicate that the pairings of Ar+He, Si+C, Mg+O and Ne+Ne are the most energetically favourable fragmentations, in descending order.

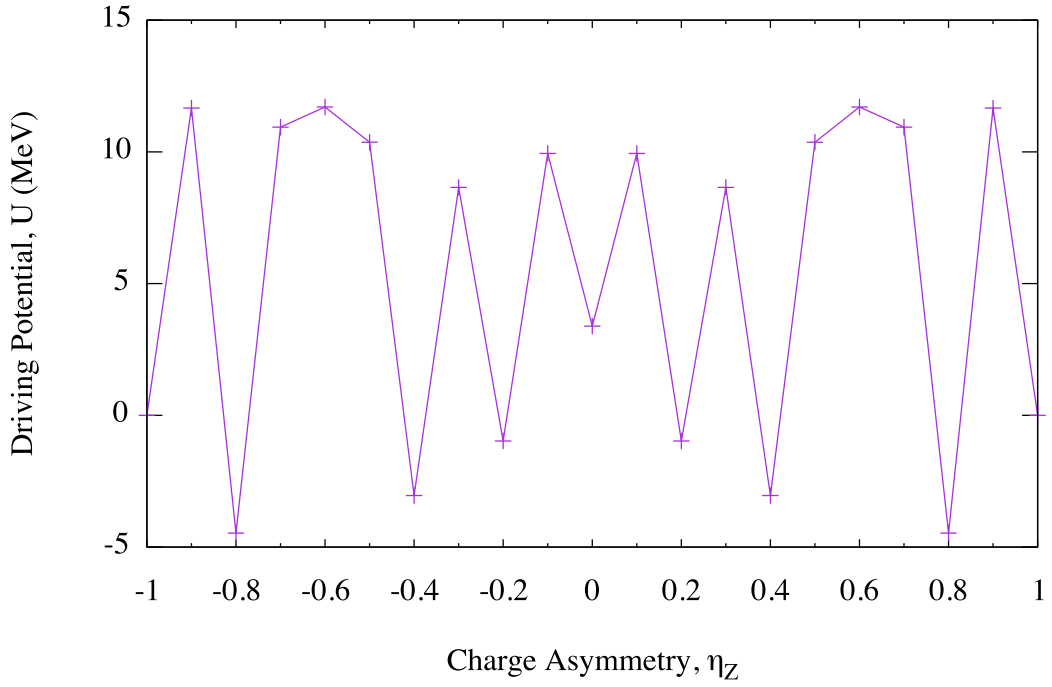

Figure 4.3: As Fig. 4.2 but for ^{40}Ca. These values are tabulated in Table 4.2.

4.2.3 ^{48}Ca driving potentials

Fig. 4.4 presents the driving potentials for the fragmentation of of ^{48}Ca in the charge asymmetry coordinate. The potential wells at $\eta_Z = \pm 0.8$ and ± 0.4 indicate that the pairings of Ar+He and Si+C are the most and second-most energetically favourable fragmentations, respectively. Whilst potential wells also reside at $\eta_Z = \pm 0.6, \pm 0.2$ and 0, it appears that the potential hill at $\eta_Z = \pm 0.9$ is yet more energetically favourable.

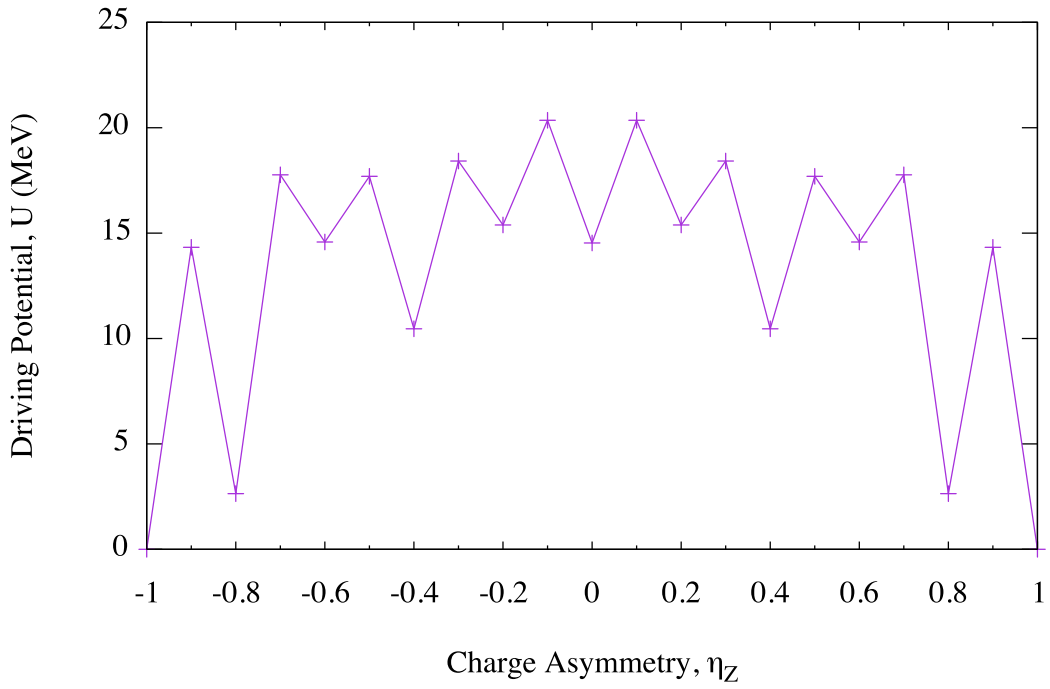

Figure 4.4: As Fig. 4.2 but for ^{48}Ca. These values are tabulated in Table 4.3.

4.3 Inverse inertia coefficient

The inverse inertia coefficient mentioned in Chapter 3.2 is used as the mass parameter for a given binary fragmentation configuration of the projectile and is calculated using a macroscopic, geometrical model explained in Refs. [64, 76]:

$$(B^{-1})_{\eta_Z\eta_Z} = \left(\frac{\partial\eta}{\partial\eta_Z}\right)^{-2} \frac{1}{m_0} \frac{A_{neck}}{2\sqrt{2\pi}b^2A^2}, \tag{4.7}$$

where A is the total nucleon number of the projectile, A_{neck} is the number of nucleons in the neck between the two projectile fragments, m_0 is the nucleon mass and b is a parameter that characterises the size of the 'neck', a region of overlap between the intranuclear nucleon-distribution tails, as visualised by Fig. 4.5. $\frac{\partial\eta}{\partial\eta_Z}$ is equivalent to $\frac{Z}{A}$, and A_{neck} is given by:

$$A_{neck} = \int d^3\mathbf{r}\,[\rho_1(\mathbf{r}) + \rho_2(\mathbf{R}-\mathbf{r})] \exp\left(-\frac{(z-z_0)^2}{b^2}\right), \tag{4.8}$$

where $\rho_1(\mathbf{r})$ and $\rho_2(\mathbf{R}-\mathbf{r})$ are the nucleon densities of the two fragments as functions of the distance from the centre of mass of each fragment. $\mathbf{R}$ is the distance between the centres of mass of the two fragments, z is the z-axis component of $\mathbf{r}$, and z_0 is the point where these two fragments densities are equal ($\rho_1(z_0) = \rho_2(z_0)$). This is because $\mathbf{r}$ and $\mathbf{R}-\mathbf{r}$ are the vectors from the centre of mass of fragments 1 and 2, respectively. There is no single vector as the two fragments are displaced by $\mathbf{R}$. The origin of the coordinate system is the centre of mass of fragment 1, and the z-axis is along $\mathbf{R}$. The nucleon densities of the fragments are given by:

$$\begin{aligned} \rho_1(\mathbf{r}) &= \frac{\rho_0}{1+\exp\left(\frac{\sqrt{x^2+y^2+z^2}-r_{0_1}A_1^{1/3}}{a_{0_1}}\right)}, \\ \rho_2(\mathbf{R}-\mathbf{r}) &= \frac{\rho_0}{1+\exp\left(\frac{\sqrt{x^2+y^2+(R-z)^2}-r_{0_2}A_2^{1/3}}{a_{0_2}}\right)}. \end{aligned} \tag{4.9}$$

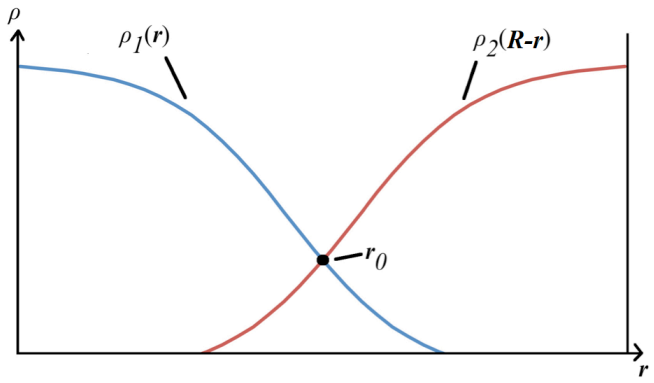

Figure 4.5: Schematic diagram representing the overlap between intranuclear nucleon-distribution tails of the two fragments (the 'neck') of a dinuclear system.

where ρ_0 is the central density of the spherical fragments, A is the corresponding mass number, a_0 denotes diffuseness parameters for the two densities and x, y, z are Cartesian co-ordinates. These parameters have been set as follows: $\rho_0 = 0.16$ fm^{-3}, r_{0_1} and r_{0_2} = 1.1 fm, a_{0_1} and a_{0_2} = 0.5 fm, and $b = 0.45$ fm. Using cylindrical co-ordinates, Eq. (4.8) can be rewritten as:

$$A_{neck} = 2\pi\rho_0 \int_0^\infty r dr \int_{-\infty}^\infty dz \exp\left(-\frac{(z-z_0)^2}{b^2}\right) \times \left[\frac{1}{1+\exp\left(\frac{\sqrt{r^2+z^2}-r_{0_1}A_1^{1/3}}{a_{0_1}}\right)} + \frac{1}{1+\exp\left(\frac{\sqrt{r^2+(R-z)^2}-r_{0_2}A_2^{1/3}}{a_{0_2}}\right)}\right]. \tag{4.10}$$

z_0 is derived from the relation:

$$\frac{z_0 - r_{0_1}A_1^{1/3}}{a_{0_1}} = \frac{(R-z_0) - r_{0_2}A_2^{1/3}}{a_{0_2}}, \tag{4.11}$$

which gives:

$$z_0 = \frac{a_{0_2}r_{0_1}A_1^{1/3} + a_{0_1}(R - r_{0_2}A_2^{1/3})}{a_{0_1} + a_{0_2}}. \tag{4.12}$$

In the method suggested in Ref. [76] for calculating the inertia coefficients, the phenomenological parameter b controls the size of the neck between two touching fragments. With the standard, adopted values of all the parameters contained in Eq. (4.10), the number of nucleons in the neck is approximately 2-3 over the range of values of the charge asymmetry coordinate. The standard, adopted value of b has been used in many applications of a dinuclear system model for describing alpha decay, cluster radioactivity and spontaneous fission [64, 77]. The Fortran-90 code used to solve Eq. (4.7) is given in Appendix E. The integral in Eq. (4.10) is solved numerically by making use of the adaptive multidemensional integration subroutine for a vector of integrals known as DCUHRE [87].

4.3.1 ^{20}Ne inertia coefficients

Fig. 4.6 presents the inverse inertia coefficients for the fragmentation of of ^{20}Ne in the charge asymmetry coordinate. The trend shown in this case is that the more symmetrical the fragmentation in the charge asymmetry co-ordinate, the greater the the value of the inverse inertia coefficient.

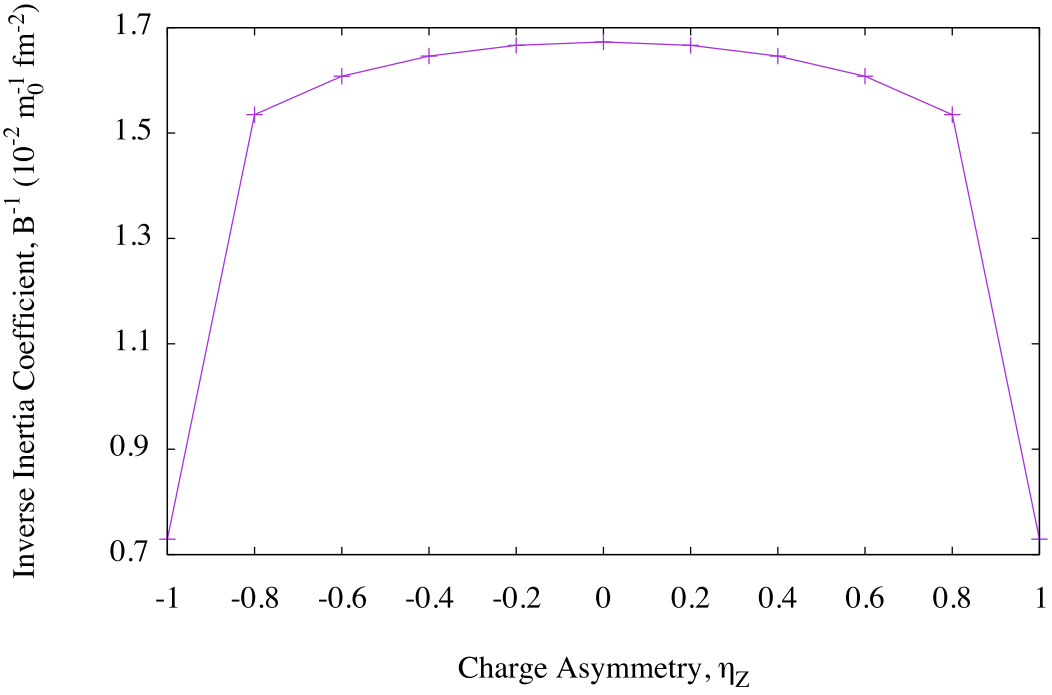

Figure 4.6: Inverse inertia coefficient plot for the fragmentation of ^{20}Ne in the charge asymmetry coordinate. The fragments are considered at the contact distance, i.e., $R_c = R_1 + R_2$, with R_i given by Eq. (4.3). Markers denote values calculated, whilst intermediate values can be interpolated. This data is presented in tabular form in Table 4.1.

As a comparison, Fig. 4.7 presents the total PDFs for the fragmentation of ^{20}Ne in the charge asymmetry coordinate; one considering deformed fragments as in Fig. 4.1 and Ref. [62], and the other considering spherical fragments as in Fig. 4.6 and Ref. [63], with the energy loss due to projectile friction determining the excitation energy range of the projectile as discussed in Chapter 2.2. The decision as to whether to consider

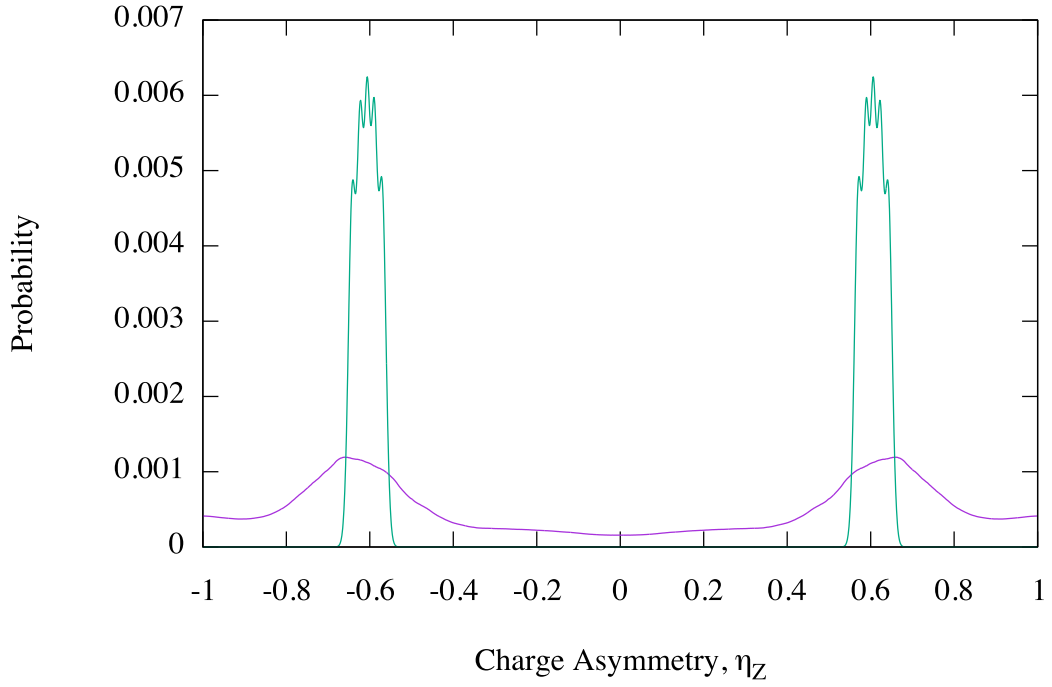

Figure 4.7: Normalised total PDF representing the fragmentation of ^{20}Ne in the charge asymmetry coordinate, with the driving potentials of Fig. 4.2, the deformed fragment inverse inertia coefficients of Fig. 4.1 (−) and the spherical fragment inverse inertia coefficients of Fig. 4.6 (−). The excitation energy range of the projectile in both cases is determined by the energy loss due to projectile friction as discussed in Chapter 2.2. The inverse inertia coefficients and driving potentials have been interpolated here using $\Delta\eta_Z = 0.001$.

spherical fragments or deformed fragments plays a significant role in the outcome of the fragmentation of ^{20}Ne in the charge asymmetry coordinate here. In the case of deformed fragments, effectively only fragmentations where $\eta_Z = \pm 0.6$ are permitted, which means ^{20}Ne would only fragment into O and He. In the case of spherical fragments, all other fragmentation pairings of ^{20}Ne are permitted, with fragmentations where $\eta_Z = \pm 0.6$ being the most common. The inverse inertia coefficients considering deformed fragments provided by Ref. [86] and the inverse inertia coefficients considering spherical fragments calculated using the code in Appendix E differ by more than three orders of magnitude, which appears to be the cause of the differences between the two total PDFs.

By artificially reducing the inverse inertia coefficients considering spherical fragments by three orders of magnitude to more closely match the inverse inertia coefficients considering deformed fragments from Ref. [76], the resultant normalised total PDF considering spherical fragments very closely resembles the restrictive normalised total PDF considering deformed fragments of Fig. 4.7 (−). The resultant expanded range of ICF products made possible by the consideration of spherical fragments is considered to be more realistic, and therefore another good reason to treat the fragments as spherical throughout these calculations.

4.3.2 ^{40}Ca inertia coefficients

Fig. 4.8 presents the inverse inertia coefficients for the fragmentation of of ^{40}Ca in the charge asymmetry coordinate. The trend shown in this case is also that the more symmetrical the fragmentation in the charge asymmetry co-ordinate, the greater the the value of the inverse inertia coefficient, with the exception of the pairings P+B and Si+C.

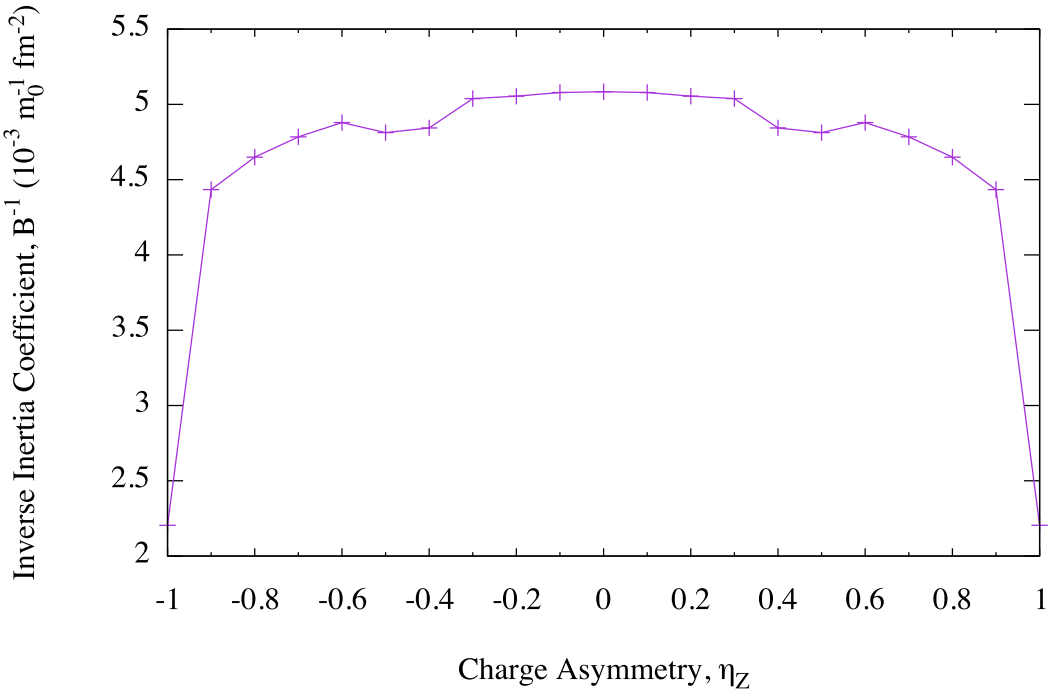

Figure 4.8: As Fig. 4.6 but for ^{40}Ca. This data is presented in tabular form in Table 4.2.

4.3.3 ^{48}Ca inertia coefficients

Fig. 4.9 presents the inverse inertia coefficients for the fragmentation of of ^{48}Ca in the charge asymmetry coordinate. The trend shown in this case follows the trend of Fig. 4.8, however the perceived dip in inverse inertia coefficient extends up from two pairings to four pairings: P+B and Si+C are joined by Al+N and Mg+O.

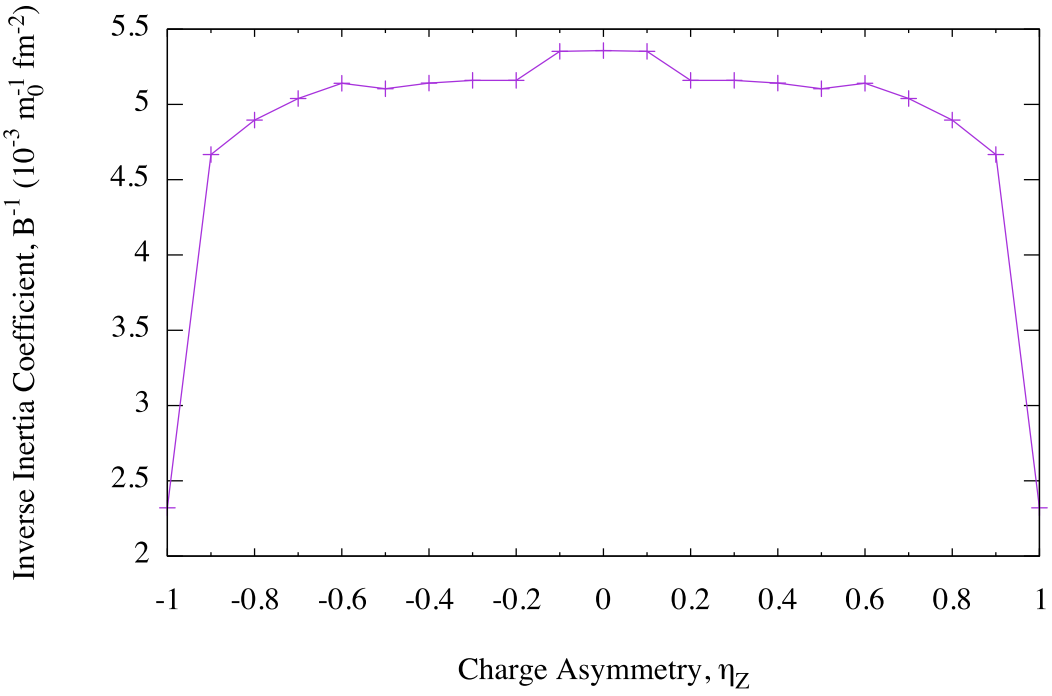

Figure 4.9: As Fig. 4.6 but for ^{48}Ca. This data is presented in tabular form in Table 4.3.

4.4 Binary configurations of the projectile

Using the aforedescribed methods, the projectile fragmentation parameters for ^{20}Ne were calculated and are shown in Table 4.1. The isotopic composition of the binary fragments has been chosen with the condition of a N/Z-equilibrium in the dinuclear system model [88–93]. As in Table 4.1, Tables 4.2 and 4.3 show calculated projectile fragmentation parameters for ^{40}Ca and ^{48}Ca respectively.

Table 4.1: ^{20}Ne projectile fragmentation variables. m_0 is the nucleon mass (938 MeV/c^2). The fragments are considered at the contact distance, i.e., $R_c = R_1 + R_2$, with R_i given by Eq. (4.3).

η_Z	Fragment 1	Fragment 2	$(B^{-1})_{\eta_Z\eta_Z}$ ($10^{-2}m_0^{-1}$fm^{-2})	$V(\eta_z)$ (MeV)
-0.8	^{2}H	^{18}F	1.5349	13.9502
-0.6	^{4}He	^{16}O	1.6078	-5.7166
-0.4	^{7}Li	^{13}N	1.6460	14.7268
-0.2	^{8}Be	^{12}C	1.6665	-0.6184
0	^{11}B	^{9}B	1.6728	15.1328
+0.2	^{12}C	^{8}Be	1.6665	-0.6184
+0.4	^{13}N	^{7}Li	1.6460	14.7268
+0.6	^{16}O	^{4}He	1.6078	-5.7166
+0.8	^{18}F	^{2}H	1.5349	13.9502

Table 4.2: As Table 4.1, but for ^{40}Ca.

η_Z	Fragment 1	Fragment 2	$(B^{-1})_{\eta_Z\eta_Z}$ $(10^{-3}m_0^{-1}\mathrm{fm}^{-2})$	$V(\eta_z)$ (MeV)
-0.9	^{2}H	^{38}K	4.4340	11.6644
-0.8	^{4}He	^{36}Ar	4.6494	-4.4696
-0.7	^{6}Li	^{34}Cl	4.7842	10.9375
-0.6	^{9}Be	^{31}S	4.8793	11.7028
-0.5	^{11}B	^{29}P	4.8124	10.3664
-0.4	^{12}C	^{28}Si	4.8435	-3.0442
-0.3	^{14}N	^{26}Al	5.0384	8.6515
-0.2	^{16}O	^{24}Mg	5.0547	-0.9725
-0.1	^{17}F	^{23}Na	5.0790	9.9393
0	^{20}Ne	^{20}Ne	5.0839	3.3850
+0.1	^{23}Na	^{17}F	5.0790	9.9393
+0.2	^{24}Mg	^{16}O	5.0547	-0.9725
+0.3	^{26}Al	^{14}N	5.0384	8.6515
+0.4	^{28}Si	^{12}C	4.8435	-3.0442
+0.5	^{29}P	^{11}B	4.8124	10.3664
+0.6	^{31}S	^{9}Be	4.8793	11.7028
+0.7	^{34}Cl	^{6}Li	4.7842	10.9375
+0.8	^{36}Ar	^{4}He	4.6494	-4.4696
+0.9	^{38}K	^{2}H	4.4340	11.6644

Table 4.3: As Table 4.1, but for ^{48}Ca.

η_Z	Fragment 1	Fragment 2	$(B^{-1})_{\eta_Z\eta_Z}$ $(10^{-3}m_0^{-1}\mathrm{fm}^{-2})$	$V(\eta_z)$ (MeV)
-0.9	^{2}H	^{46}K	4.6673	14.3263
-0.8	^{4}He	^{44}Ar	4.8961	2.6401
-0.7	^{7}Li	^{41}Cl	5.0394	17.7645
-0.6	^{10}Be	^{38}S	5.1404	14.5781
-0.5	^{11}B	^{37}P	5.1042	17.6953
-0.4	^{14}C	^{34}Si	5.1416	10.4599
-0.3	^{15}N	^{33}Al	5.1597	18.4195
-0.2	^{20}O	^{28}Mg	5.1598	15.3886
-0.1	^{23}F	^{25}Na	5.3526	20.3533
0	^{24}Ne	^{24}Ne	5.3578	14.5334
+0.1	^{25}Na	^{23}F	5.3526	20.3533
+0.2	^{28}Mg	^{20}O	5.1598	15.3886
+0.3	^{33}Al	^{15}N	5.1597	18.4195
+0.4	^{34}Si	^{14}C	5.1416	10.4599
+0.5	^{37}P	^{11}B	5.1042	17.6953
+0.6	^{38}S	^{10}Be	5.1404	14.5781
+0.7	^{41}Cl	^{7}Li	5.0394	17.7645
+0.8	^{44}Ar	^{4}He	4.8961	2.6401
+0.9	^{46}K	^{2}H	4.6673	14.3263

In this chapter the potential and inertia parameters of the model have been detailed, rounding out the theoretical basis of the upcoming calculations in subsequent chapters. Chapter 5 reveals test cases of the model, their comparison with experimental data, and the resultant calibration of the breakup function parameters.

Chapter 5

Model Test Cases and Calibration

5.1 Breakup function parameters

The breakup function parameters of Eq. (2.1), α and β, strongly influence resultant cross-sections, and consequently must be carefully selected. Fig. 5.1 illustrates cross-section sensitivity to the parameter α in the angular distribution for the transfer reaction of ^{4}He (^{20}Ne + ^{208}Pb $\rightarrow$ ^{212}Po + ^{16}O). In this instance a 10% decrease in α results in a $\sim$200% increase in the cross-section peak value.

Fig. 5.2 illustrates cross-section sensitivity to the parameter β in the angular distribution for the transfer reaction of ^{4}He (^{20}Ne + ^{208}Pb $\rightarrow$ ^{212}Po + ^{16}O). In this instance a 17% increase in β results in an $\sim$800% increase in the cross-section peak value. As well as on the magnitude, β appears to have a greater influence on the width of the peaks than α does, suggesting β should be tweaked primarily to match the peak shape, followed by α to further match the peak magnitude.

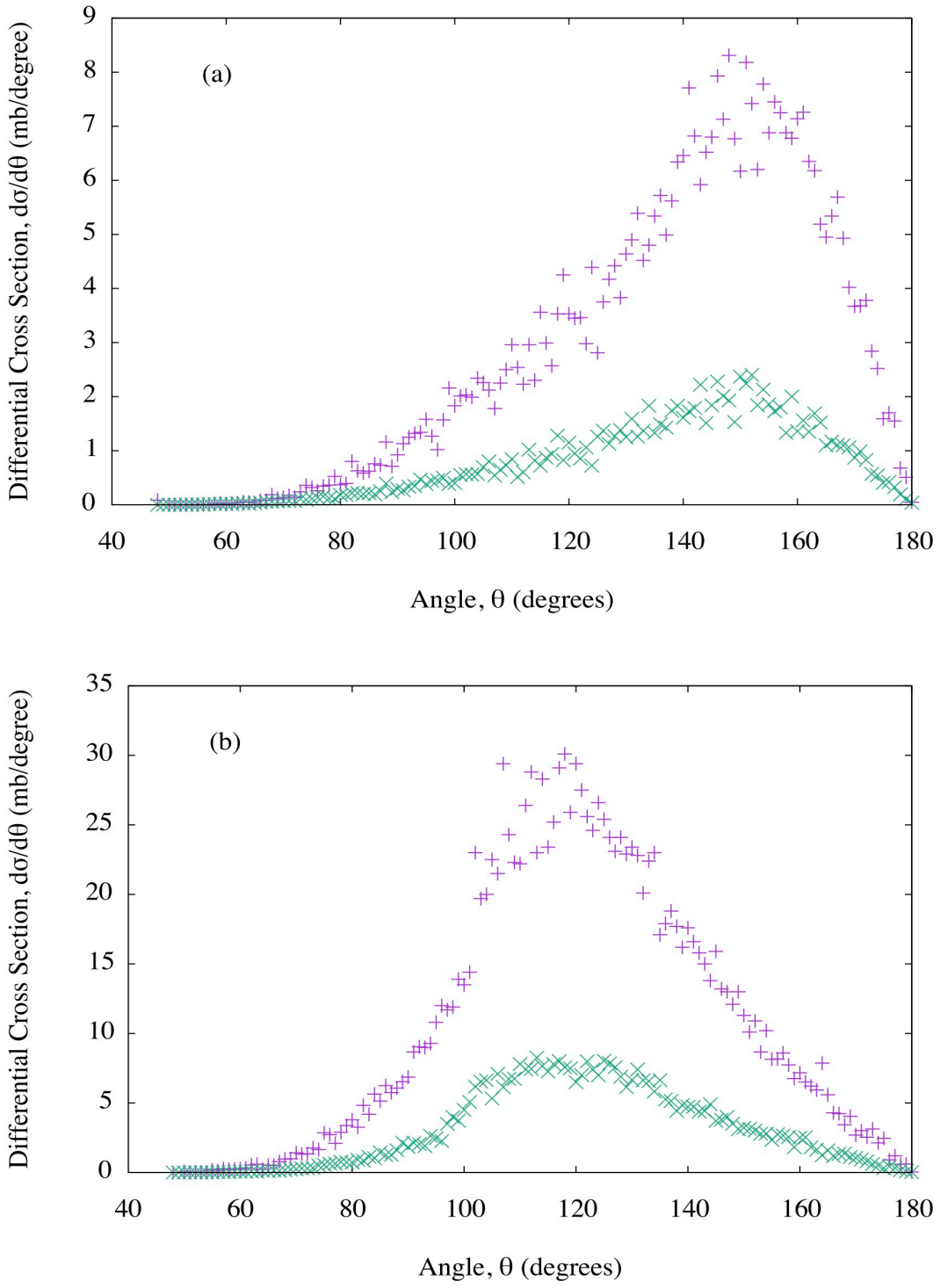

Figure 5.1: Angular distributions for the transfer reaction of ^{4}He (^{20}Ne + ^{208}Pb $\rightarrow$ ^{212}Po + ^{16}O) with $\alpha = 0.9$ (+) and $\alpha = 1.0$ ($\times$): (a) for projectile incident energies of 105 MeV, (b) for projectile incident energies of 115 MeV. β is fixed at 13.

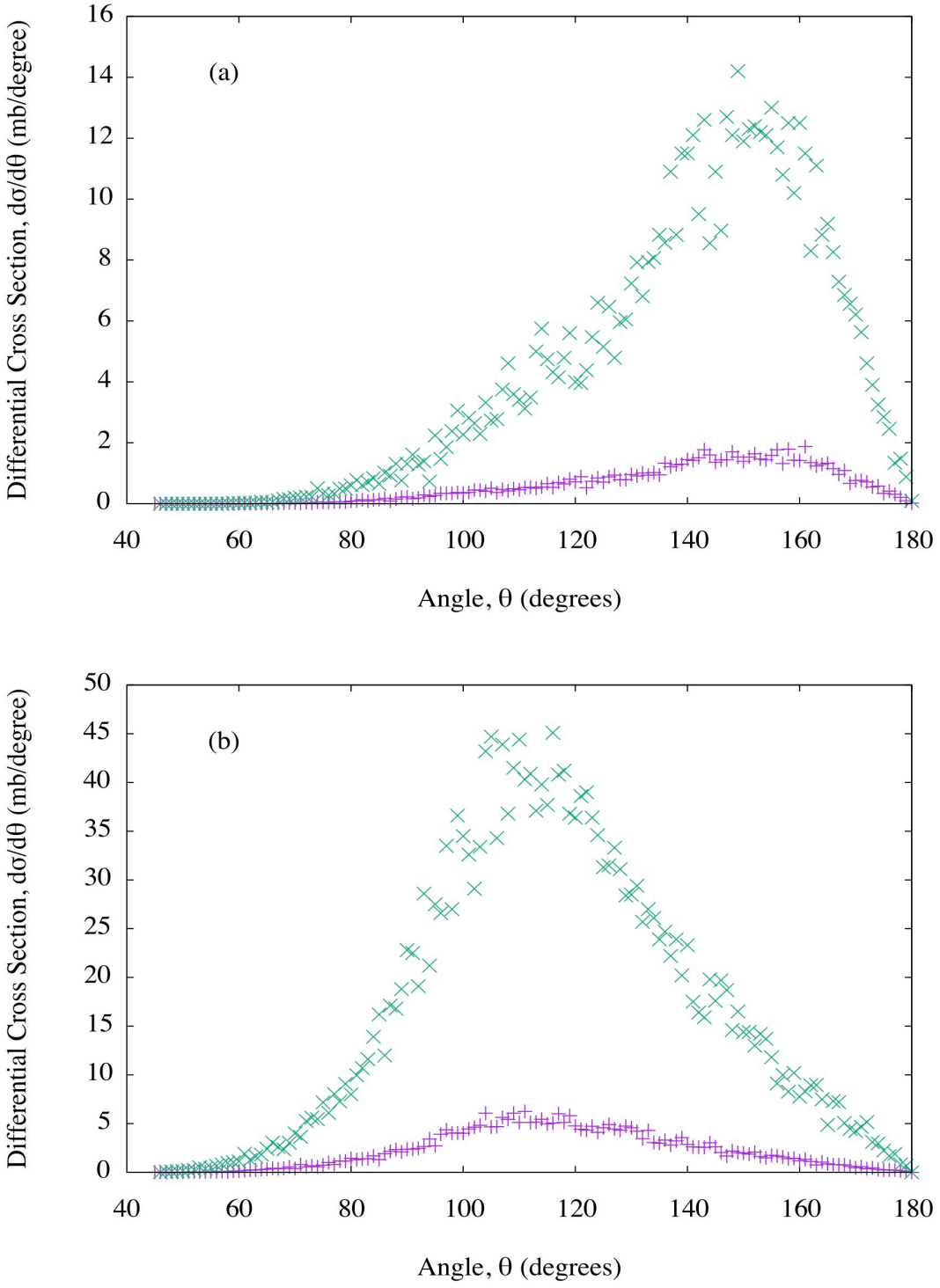

Figure 5.2: Angular distributions for the transfer reaction of ^{4}He (^{20}Ne + ^{208}Pb $\rightarrow$ ^{212}Po + ^{16}O) with $\beta = 12$ (+) and $\beta = 14$ ($\times$): (a) for projectile incident energies of 105 MeV, (b) for projectile incident energies of 115 MeV. α is fixed at 0.95.

5.2 Test case: ^{20}Ne+^{208}Pb

Values of $\alpha = 0.94$ and $\beta = 15$ were selected for the ^{20}Ne projectile because cross-sections borne from them match experimental results closely, as shown by the angular distributions for the transfer reaction of ^{4}He (^{20}Ne + ^{208}Pb $\rightarrow$ ^{212}Po + ^{16}O) in Fig. 5.3. These values of α and β were not chosen with the intention of perfectly matching the experimental results, but rather to demonstrate a qualitative agreement. Comparing the model results from Fig. 5.3(b) to the experimental results of Fig. 5.3(a) [94], differential cross-sections for an incident energy $E_0 = 115$ MeV are of a very similar magnitude. For $E_0 = 105$ MeV the magnitudes of differential cross-sections are less alike but still comparable. These results are tabulated in Table 5.1.

The main difference between these two figures is that the centroids of the distributions lie at vastly different angles, however, this can be explained as having arisen due to the global Broglia-Winther potential used to simulate the interaction between the three bodies. Additionally, as the present semi-classical model is based on a breakup-fusion picture, it cannot treat the quantum-mechanical α-stripping process [95], which might also play a part in explaining the discrepancies between the data of Figs. 5.3(a) and 5.3(b). The maximal orbital angular momentum between projectile and target considered here is $L_{TP} = 75\hbar$, with 1000 sampled fragmentations per orbital angular momentum.

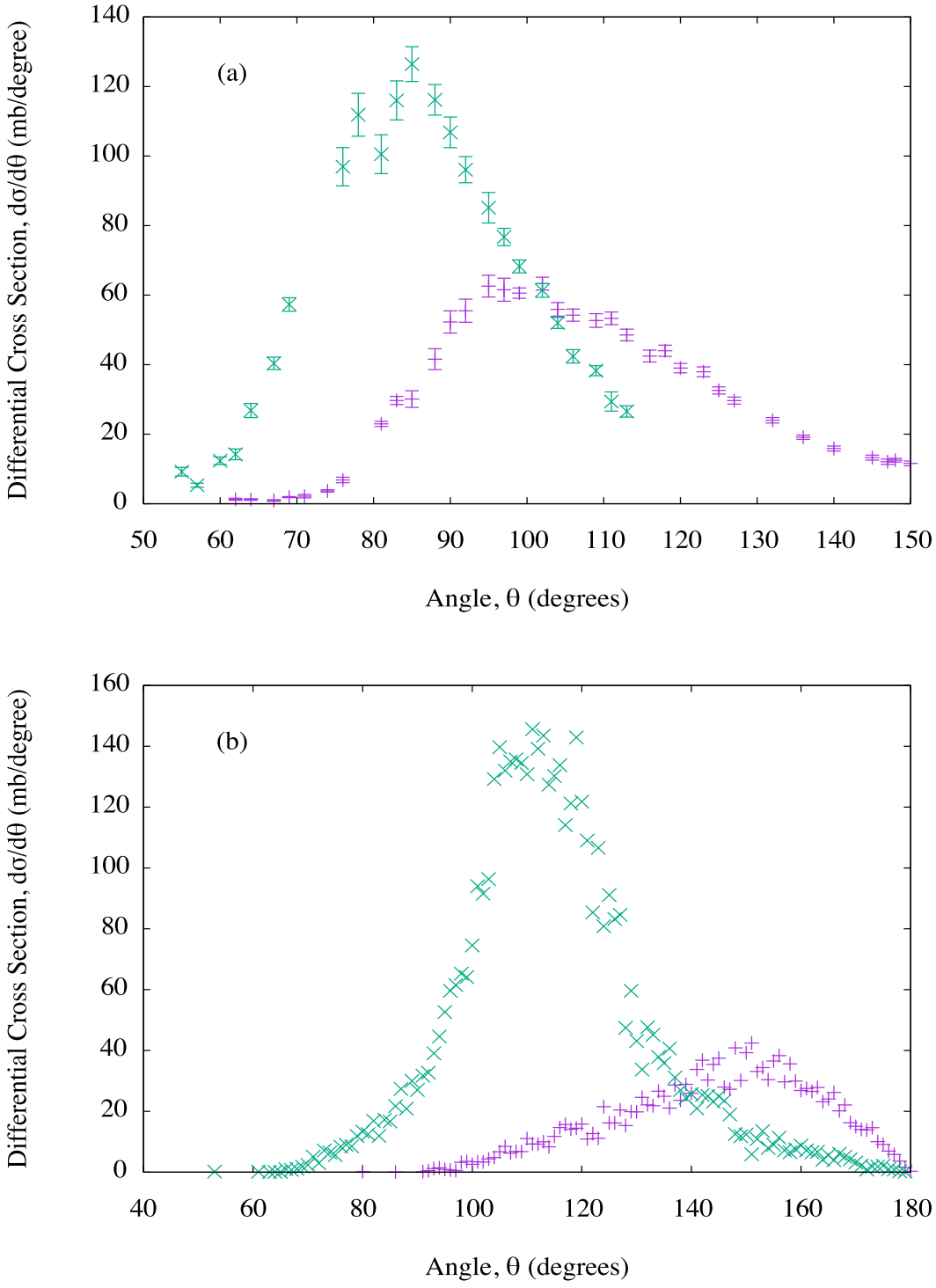

Figure 5.3: Angular distributions for the transfer reaction of ^{4}He (^{20}Ne + ^{208}Pb $\rightarrow$ ^{212}Po + ^{16}O) for projectile incident energies of 105 MeV (+) and 115 MeV ($\times$): (a) from experiment [94], (b) from present model calculations using $\alpha = 0.94$ and $\beta = 15$.

5.3 Test case: ^{40}Ca+^{248}Cm

For the ^{40}Ca and ^{48}Ca projectiles, parameters were determined by matching present model results for the reactions ^{40}Ca+^{248}Cm and ^{48}Ca+^{248}Cm respectively with experimental data in Ref. [96]. As the isotopic composition of the fragments has been chosen with the condition of a N/Z-equilibrium in the dinuclear system model [88–93], the resultant ICF products are restricted to one isotope per element and so could be considered representatives for all isotopes of their element combined. Therefore it is reasonable in this case to compare the present model ICF product cross-sections with the aforementioned combined experimental cross-sections for the purpose of determining meaningful parameter values for α and β. For these calculations, the initial, maximal angular momentum between the two fragments was set at $L_{12} = 0\hbar$, as approximated by the consideration of projectile orbital angular momentum loss in Chapter 2.2. The maximal orbital angular momentum between projectile and target considered here is $L_{TP} = 100\hbar$, with 1000 sampled fragmentations per orbital angular momentum.

The combined cross-sections for ICF products of the reaction ^{40}Ca+^{248}Cm at projectile incident energies not exceeding 259 MeV in Ref. [96] for the production of all reported Bk isotopes amount to 7.47 mb, and for the production of all reported Cf isotopes the total amounts to 2.12 mb. Using the present model calculations at a projectile incident energy of 259 MeV, parameter values of $\alpha = 0.95$ and $\beta = 12$ yield production cross-sections of 2.84 mb for ^{250}Bk and 7.75 mb for ^{252}Cf. As any change to α and β affects cross-sections in the same manner for both ^{250}Bk and ^{252}Cf (*i.e.* cross-sections would either both increase or both decrease), these values for α and β (to the stated precision) give the best averaged agreement across both of the compared element groups. These results are tabulated in Table 5.1.

5.4 Test case: ^{48}Ca+^{248}Cm

The combined cross-sections for ICF products of the reaction ^{48}Ca+^{248}Cm at projectile incident energies not exceeding 263 MeV in Ref. [96] for the production of all reported Bk isotopes amount to 5.82 mb, and for the production of all reported Cf isotopes the total amounts to 2.88 mb. Using the present model calculations at a projectile incident energy of 263 MeV, the same parameter values of $\alpha = 0.95$ and $\beta = 12$ yield production cross-sections of 2.05 mb for ^{250}Bk and 5.78 mb for ^{252}Cf. By coincidence these same values for α and β as for the ^{40}Ca projectile give the best averaged agreement across both of the compared element groups. This could in part be due to both projectiles resulting in the same Bk and Cf ICF products, courtesy of the N/Z-equilibrium consideration. These results are tabulated in Table 5.1.

Table 5.1: Comparison of experimental and calculated cross-sections, and the associated breakup function parameters.

Projectile	Incident energy (MeV)	ICF product	Experimental cross-section (mb)	Theoretical cross-section (mb)	α	β
^{20}Ne	105 MeV	^{16}O	60	40	0.94	15
^{20}Ne	115 MeV	^{16}O	130	150	0.94	15
^{40}Ca	259 MeV	(^{250})Bk	7.47	2.84	0.95	12
^{40}Ca	259 MeV	(^{252})Cf	2.12	7.75	0.95	12
^{48}Ca	263 MeV	(^{250})Bk	5.82	2.05	0.95	12
^{48}Ca	263 MeV	(^{252})Cf	2.88	5.78	0.95	12

In this chapter the final inputs of the model, the breakup function parameters α and β from Eq. (2.1), have been have been determined, paving the way for the upcoming novel model predictions in Chapter 6, and the resultant EVR cross-sections in Chapter 7.

Chapter 6

Model Results

In this chapter, results of ICF reactions induced by ^{20}Ne, ^{40}Ca and ^{48}Ca projectiles on several heavy actinide targets, ranging from ^{248}Cm to ^{256}Es, are presented and discussed. All 18 presented reactions were studied at three different incident energies each: that of the Coulomb barrier for a given projectile-target pairing, and up to 10% above the Coulomb barrier in increments of 5% ($E_{0_{c.m.}}/V_{CB}$ = 1.00, 1.05, 1.10, where $E_{0_{c.m.}}$ is the incident energy in the centre-of-mass frame and V_{CB} is the Coulomb barrier). Standard deviations are taken as the square root of the difference between the square of the weighted mean of a distribution and the weighted mean of the squares of a distribution. The weighting factors used are the differential cross sections associated with the corresponding physical quantities.

6.1 ^{20}Ne-induced incomplete fusion reactions

Total integrated cross-sections, angular, excitation energy and angular momentum distributions and their associated standard deviations were calculated for the primary ICF products of ^{20}Ne-induced incomplete fusion reactions with chains of Cm, Cf and Es targets at varying incident energies. The targets chosen were ^{248}Cm (Table 6.1), ^{250}Cm (Table 6.2), ^{252}Cf (Table 6.3), ^{254}Cf (Table 6.4), ^{254}Es (Table 6.5) and ^{256}Es (Table 6.6). These targets were chosen because (i) they are expected to have several primary ICF products in common, allowing for plenty of comparisons to be drawn, (ii) most of them

have already been used in experiments [97, 98], and (iii) they have relatively long half-lives (^{248}Cm: 348 kiloyears, ^{250}Cm: 8.3 kiloyears, ^{252}Cf: 2.645 years, ^{254}Cf: 60.5 days, ^{254}Es: 275.7 days, ^{256}Es: 25.4 minutes) [99]. The maximal orbital angular momentum between projectile and target considered here is $L_{TP} = 45\hbar$, with 1000 sampled fragmentations per orbital angular momentum. Results have been shown only for the ICF of the heavy fragment and target (with the exception of transactinide primary ICF products resulting from the ICF of the light fragment and Es targets) primarily because lighter primary ICF products such as actinides are not the focus of this study. Also presented are the angular distributions of all tabulated primary ICF products (Figs. 6.1-6.6).

6.1.1 ^{20}Ne+^{248}Cm

Fig. 6.1 contains the angular distributions of the heaviest primary ICF products of the reaction ^{20}Ne+^{248}Cm. At all studied incident energies, all differential cross-sections are found between 0-26 degrees. The closer the incident energy is to the Coulomb barrier, the more dominant the products ^{259}Md and ^{260}No are, most prominently found at 10 and 7 degrees respectively at $E_{0_{c.m.}}/V_{CB} = 1.00$. However, at $E_{0_{c.m.}}/V_{CB} = 1.05$ and above the SHE ICF products ^{264}Rf and ^{266}Db begin to dominate, especially at more forward angles than the other heavy ICF products (most prominently at 8 and 7 degrees respectively). At $E_{0_{c.m.}}/V_{CB} = 1.10$, the differential cross-sections of ^{264}Rf and ^{266}Db strongly eclipse those of the neighbouring heavy products (most prominently at 10 and 8 degrees respectively). Table 6.1 contains the total cross-sections and the means of the angular, excitation energy and angular momentum distributions of those same ICF products. The total cross-sections of the ICF products follow the same trend as the angular distributions in Fig. 6.1. As a general trend, the higher the projectile incident energy is, the higher the ICF product mean angle, mean excitation energy, mean angular momentum and their respective associated standard deviations are. Other apparent trends at all studied incident energies are that the heavier the ICF product is, (i) the more forward the mean angle is and the lower the associated standard deviation is; (ii) the higher the mean excitation energy is; and (iii) the lower the mean angular momentum and associated standard deviations are (with the exception of ^{264}Rf and

^{266}Db at $E_{0_{c.m.}}/V_{CB} = 1.10$). The ICF products ^{259}Md, ^{260}No and ^{261}Lr have rather high standard deviations associated with their mean excitation energies, whereas the SHE ICF products ^{264}Rf and ^{266}Db in contrast have much smaller associated standard deviations.

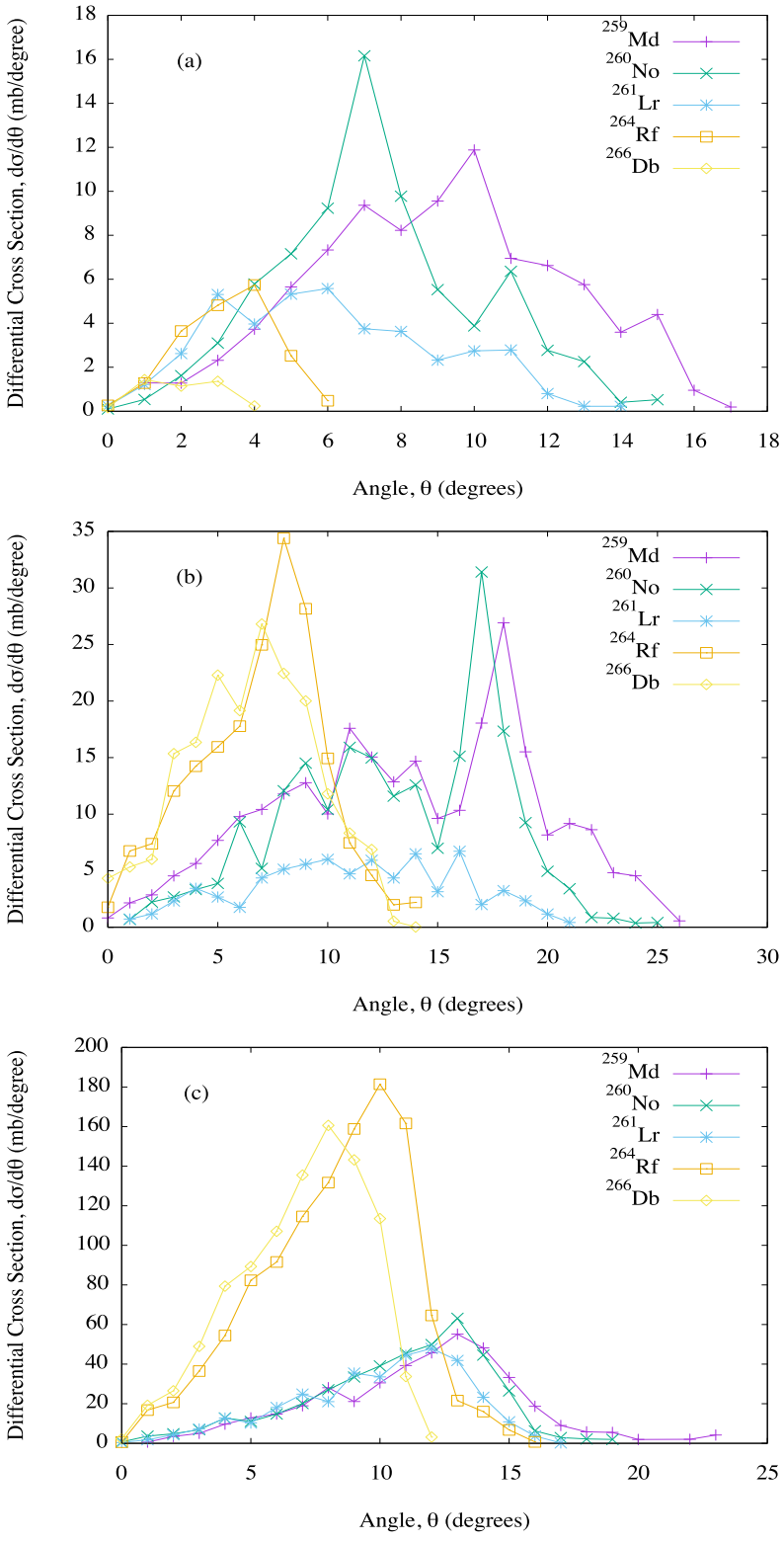

Figure 6.1: Angular distributions of the heaviest primary ICF products of the reaction ^{20}Ne+^{248}Cm, with: (a) $E_{0_{c.m.}}/V_{CB} = 1.00$, (b) $E_{0_{c.m.}}/V_{CB} = 1.05$, and (c) $E_{0_{c.m.}}/V_{CB} = 1.10$.

Table 6.1: Results for the heaviest primary ICF products of the reaction ^{20}Ne+^{248}Cm.

ICF product	Total cross section (mb)	Mean angle (degrees)	Mean exc. energy (MeV)	Mean angular momentum ($\hbar$)
$E_{0_{c.m.}}/V_{CB}$=1.00				
$^{259}_{101}$Md	89.10	8.98 ± 3.39	13.61 ± 10.01	12.56 ± 4.82
$^{260}_{102}$No	75.20	7.36 ± 2.75	34.13 ± 9.20	11.34 ± 4.84
$^{261}_{103}$Lr	40.74	6.10 ± 2.96	35.63 ± 11.39	11.41 ± 6.60
$^{264}_{104}$Rf	18.75	3.28 ± 1.26	45.31 ± 0.73	7.03 ± 3.85
$^{266}_{105}$Db	4.346	2.02 ± 1.01	53.97 ± 0.69	4.89 ± 2.23
$E_{0_{c.m.}}/V_{CB}$=1.05				
$^{259}_{101}$Md	255.0	13.52 ± 5.65	18.62 ± 9.85	15.61 ± 6.72
$^{260}_{102}$No	210.3	13.06 ± 4.71	35.53 ± 8.06	16.33 ± 6.13
$^{261}_{103}$Lr	73.73	11.18 ± 4.64	36.76 ± 11.03	14.75 ± 5.95
$^{264}_{104}$Rf	194.6	6.92 ± 2.88	47.37 ± 1.97	12.41 ± 4.93
$^{266}_{105}$Db	185.6	6.47 ± 2.88	55.84 ± 1.55	11.64 ± 4.87
$E_{0_{c.m.}}/V_{CB}$=1.10				
$^{259}_{101}$Md	413.8	11.55 ± 3.86	22.66 ± 8.54	17.49 ± 7.69
$^{260}_{102}$No	417.2	10.65 ± 3.46	44.99 ± 5.75	17.59 ± 7.73
$^{261}_{103}$Lr	342.0	9.94 ± 3.23	45.46 ± 7.59	17.50 ± 7.77
$^{264}_{104}$Rf	1161	8.28 ± 2.84	50.44 ± 3.14	18.60 ± 7.41
$^{266}_{105}$Db	962.3	6.95 ± 2.45	59.51 ± 2.30	18.84 ± 7.20

6.1.2 ^{20}Ne+^{250}Cm

Fig. 6.2 contains the angular distributions of the heaviest primary ICF products of the reaction ^{20}Ne+^{250}Cm. At all studied incident energies, all differential cross-sections are found between 0-26 degrees. The closer the incident energy is to the Coulomb barrier, the more dominant the products ^{261}Md and ^{262}No are, most prominently found at 13 and 11 degrees respectively at $E_{0_{c.m.}}/V_{CB} = 1.00$. However, at $E_{0_{c.m.}}/V_{CB} = 1.05$ and above the SHE ICF products ^{266}Rf and ^{268}Db begin to dominate, especially at more forward angles than the other heavy ICF products (most prominently at 7 and 6 degrees respectively). ^{263}Lr also catches up to ^{261}Md and ^{262}No in terms of maximum differential cross-section, with its peak nestled right in-between the already close peaks of ^{261}Md and ^{262}No.

Table 6.2 contains the total cross-sections and the means of the angular, excitation energy and angular momentum distributions of those same ICF products. The total cross-sections of the ICF products follow the same trend as the angular distributions in Fig. 6.2. As a general trend, the higher the projectile incident energy is, the higher the ICF product mean angle, mean excitation energy, mean angular momentum and their respective associated standard deviations are. Other apparent trends at all studied incident energies are that the heavier the ICF product is, (i) the more forward the mean angle is and the lower the associated standard deviation is; (ii) the higher the mean excitation energy is; and (iii) the lower the mean angular momentum and associated standard deviations are (with the exception of ^{268}Db at $E_{0_{c.m.}}/V_{CB} = 1.10$). The ICF products ^{261}Md, ^{262}No and ^{263}Lr have rather high standard deviations associated with their mean excitation energies, whereas the SHE ICF products ^{266}Rf and ^{268}Db in contrast have much smaller associated standard deviations, as is the case with ^{264}Rf and ^{266}Db from the reaction ^{20}Ne+^{248}Cm. This more consistent transfer of excitation energy to the ICF product in the case of these SHEs may perhaps be related to high charge asymmetry of the projectile fragments involved in those ICF reactions (namely ^{18}F+^{2}H and ^{16}O+^{4}He).

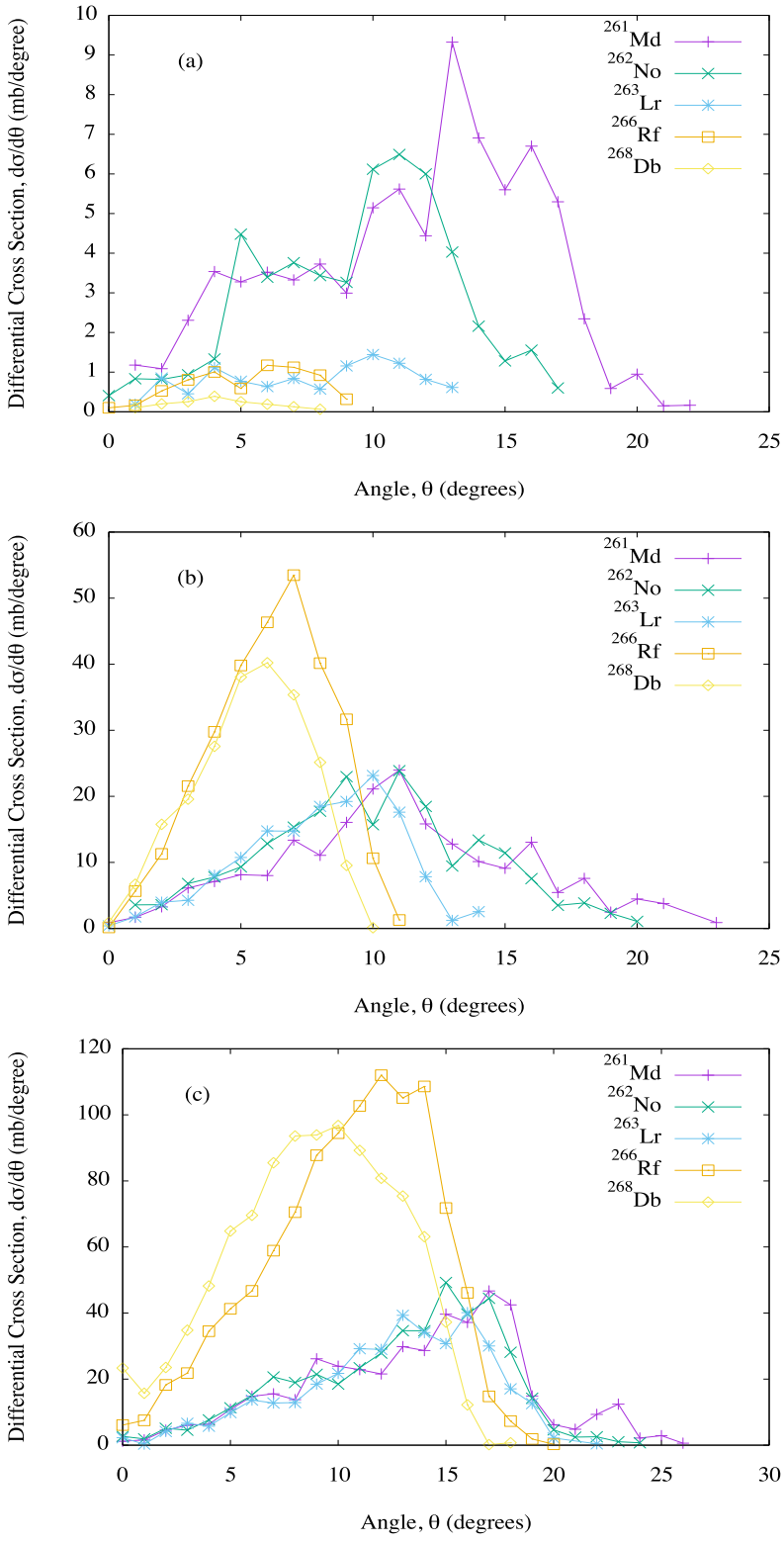

Figure 6.2: The same results as in Fig. 6.1, but for the reaction ^{20}Ne+^{250}Cm, with: (a) $E_{0_{c.m.}}/V_{CB} = 1.00$, (b) $E_{0_{c.m.}}/V_{CB} = 1.05$, and (c) $E_{0_{c.m.}}/V_{CB} = 1.10$.

Table 6.2: The same results as in Table 6.1, but for the reaction ^{20}Ne+^{250}Cm.

ICF product	Total cross section (mb)	Mean angle (degrees)	Mean exc. energy (MeV)	Mean angular momentum ($\hbar$)
		$E_{0_{c.m.}}/V_{CB}$=1.00		
$^{261}_{101}$Md	78.19	11.34 ± 4.58	15.31 ± 10.25	11.96 ± 4.89
$^{262}_{102}$No	50.90	9.39 ± 3.63	32.51 ± 9.32	10.18 ± 4.11
$^{263}_{103}$Lr	10.68	7.67 ± 3.42	30.86 ± 12.91	8.85 ± 3.51
$^{266}_{104}$Rf	6.721	5.31 ± 2.20	47.30 ± 0.70	6.18 ± 3.42
$^{268}_{105}$Db	1.576	4.20 ± 1.79	55.83 ± 0.37	3.78 ± 1.72
		$E_{0_{c.m.}}/V_{CB}$=1.05		
$^{261}_{101}$Md	206.4	10.92 ± 4.62	20.84 ± 9.02	15.14 ± 6.56
$^{262}_{102}$No	210.6	9.88 ± 4.06	41.58 ± 7.42	15.55 ± 5.86
$^{263}_{103}$Lr	148.7	8.01 ± 2.81	44.73 ± 7.21	14.86 ± 6.31
$^{266}_{104}$Rf	291.8	6.13 ± 2.17	49.80 ± 1.91	12.67 ± 5.76
$^{268}_{105}$Db	218.9	5.36 ± 2.04	58.06 ± 1.59	10.93 ± 5.05
		$E_{0_{c.m.}}/V_{CB}$=1.10		
$^{261}_{101}$Md	446.9	13.60 ± 5.02	25.47 ± 9.16	18.22 ± 8.19
$^{262}_{102}$No	435.6	12.75 ± 4.55	46.88 ± 6.30	18.37 ± 7.74
$^{263}_{103}$Lr	373.2	12.40 ± 4.22	47.34 ± 7.84	18.41 ± 8.41
$^{266}_{104}$Rf	1058	10.43 ± 3.79	52.43 ± 3.41	18.19 ± 7.81
$^{268}_{105}$Db	1009	8.77 ± 3.80	61.45 ± 2.45	18.67 ± 7.67

6.1.3 ^{20}Ne+^{252}Cf

Fig. 6.3 contains the angular distributions of the heaviest primary ICF products of the reaction ^{20}Ne+^{252}Cf. At all studied incident energies, all differential cross-sections are found between 0-25 degrees. The closer the incident energy is to the Coulomb barrier, the more dominant the products ^{263}Lr and ^{264}Rf are, most prominently found at 12 and 10 degrees respectively at $E_{0_{c.m.}}/V_{CB} = 1.00$. However, at $E_{0_{c.m.}}/V_{CB} = 1.05$ and above the SHE ICF products ^{268}Sg and ^{270}Bh begin to dominate, especially at more forward angles than the other heavy ICF products (most prominently at 9 and 7 degrees respectively). ^{265}Db also catches up to ^{263}Lr and ^{264}Rf in terms of maximum differential cross-section, with their peaks ranging from ∼10-15 degrees.

Table 6.3 contains the total cross-sections and the means of the angular, excitation energy and angular momentum distributions of those same ICF products. The total cross-sections of the ICF products follow the same trend as the angular distributions in Fig. 6.3. As a general trend, the higher the projectile incident energy is, the higher the ICF product mean angle, mean excitation energy, mean angular momentum and their respective associated standard deviations are. Other apparent trends at all studied incident energies are that the heavier the ICF product is, (i) the more forward the mean angle is and the lower the associated standard deviation is; (ii) the higher the mean excitation energy is; and (iii) the lower the mean angular momentum and associated standard deviations are (with the exception of ^{268}Sg and ^{270}Bh at $E_{0_{c.m.}}/V_{CB} = 1.10$). The ICF products ^{263}Lr, ^{264}Rf and ^{265}Db have rather high standard deviations associated with their mean excitation energies, whereas the ICF products ^{268}Sg and ^{270}Bh in contrast have much smaller associated standard deviations, as is the case with ^{264}Rf and ^{266}Db from the reaction ^{20}Ne+^{248}Cm and with ^{266}Rf and ^{268}Db from the reaction ^{20}Ne+^{250}Cm. This more consistent transfer of excitation energy to the ICF product in the case of these ICF products lends further credence to the notion that it is perhaps related to high charge asymmetry of the projectile fragments involved in those ICF reactions, especially now that the pattern has repeated with fragment charge asymmetry rather than with the atomic number of the ICF product (i.e. Rf and Db).

Comparing like ICF products from different reactions, ^{264}Rf yields higher total cross-

sections at $E_{0_{c.m.}}/V_{CB}$ = 1.00 and 1.05, yet a lower total cross-section at $E_{0_{c.m.}}/V_{CB}$ = 1.10, from the reaction ^{20}Ne+^{248}Cm than from ^{20}Ne+^{252}Cf. ^{264}Rf produced in the reaction ^{20}Ne+^{248}Cm is typically found at more forward angles, with higher excitation energies and less angular momentum than ^{264}Rf produced in the reaction ^{20}Ne+^{252}Cf. This makes the reaction ^{20}Ne+^{252}Cf the preferable choice to the reaction ^{20}Ne+^{248}Cm for the production of colder, more stable ^{264}Rf at the Coulomb barrier, however at 10% above the Coulomb barrier the reaction ^{20}Ne+^{248}Cm yields three times the total cross-section for only an 11% increase in excitation energy.

Similarly, ^{263}Lr yields higher total cross-sections from the reaction ^{20}Ne+^{252}Cf than from ^{20}Ne+^{250}Cm. ^{263}Lr produced in the reaction ^{20}Ne+^{250}Cm is typically found at more forward angles, with higher excitation energies and less angular momentum than ^{263}Lr produced in the reaction ^{20}Ne+^{252}Cf. This makes the reaction ^{20}Ne+^{252}Cf the all-round preferable choice to the reaction ^{20}Ne+^{250}Cm for the production of colder, more stable ^{263}Lr at the studied incident energies.

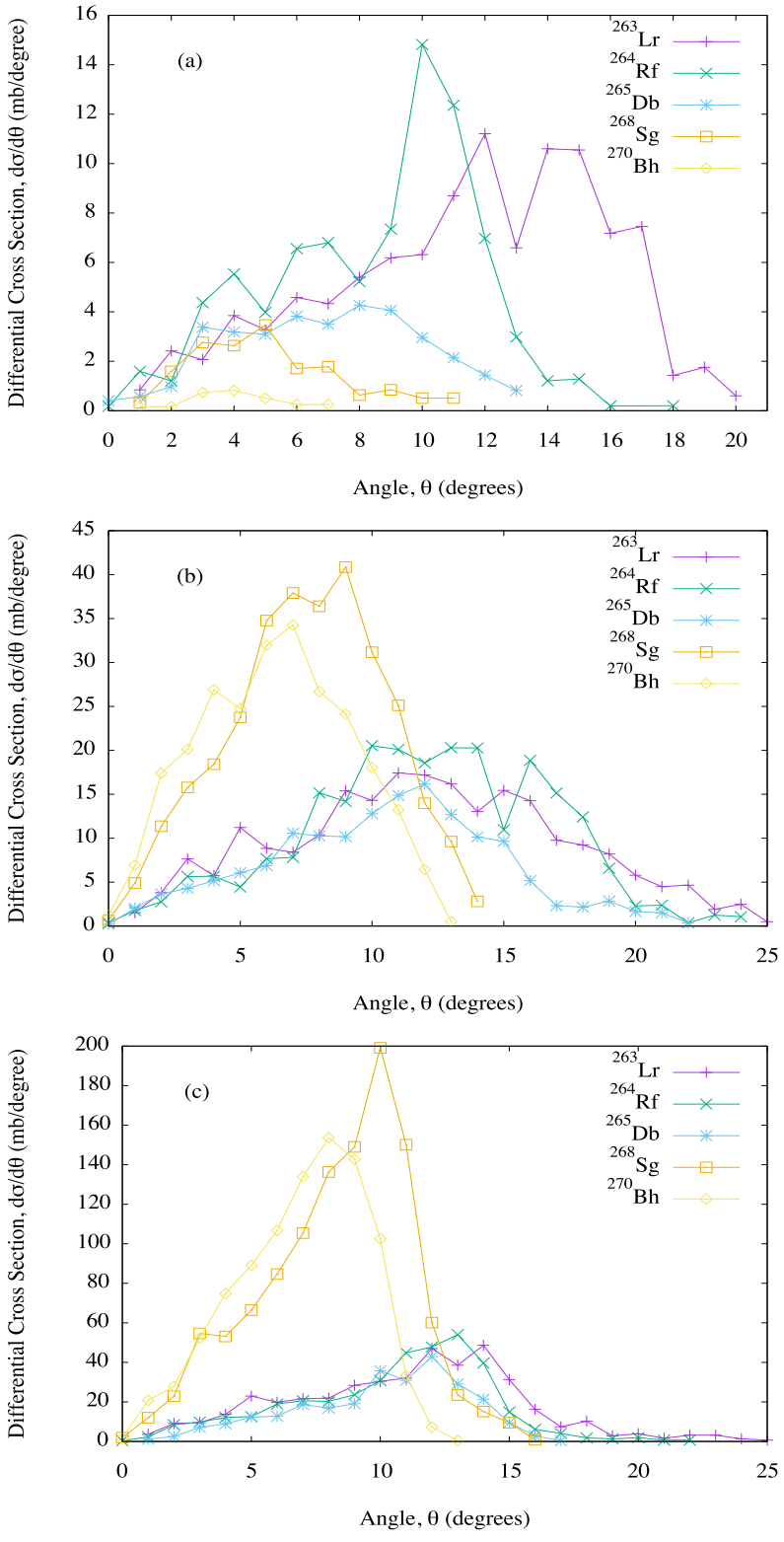

Figure 6.3: The same results as in Fig. 6.1, but for the reaction ^{20}Ne+^{252}Cf, with: (a) $E_{0_{c.m.}}/V_{CB} = 1.00$, (b) $E_{0_{c.m.}}/V_{CB} = 1.05$, and (c) $E_{0_{c.m.}}/V_{CB} = 1.10$.

Table 6.3: The same results as in Table 6.1, but for the reaction ^{20}Ne+^{252}Cf.

ICF product	Total cross section (mb)	Mean angle (degrees)	Mean exc. energy (MeV)	Mean angular momentum ($\hbar$)
$E_{0_{c.m.}}/V_{CB}$=1.00				
$^{263}_{103}$Lr	105.3	11.38 ± 4.30	11.86 ± 10.44	12.19 ± 4.83
$^{264}_{104}$Rf	82.82	8.50 ± 3.26	31.29 ± 8.78	10.47 ± 4.65
$^{265}_{105}$Db	34.63	6.93 ± 3.00	34.76 ± 11.25	9.54 ± 3.85
$^{268}_{106}$Sg	16.77	5.11 ± 2.34	45.63 ± 0.90	8.48 ± 4.01
$^{270}_{107}$Bh	2.922	4.07 ± 1.52	53.90 ± 0.52	8.57 ± 2.47
$E_{0_{c.m.}}/V_{CB}$=1.05				
$^{263}_{103}$Lr	227.8	12.09 ± 5.26	20.21 ± 9.44	14.80 ± 6.69
$^{264}_{104}$Rf	236.6	12.03 ± 4.53	40.31 ± 7.17	15.01 ± 6.19
$^{265}_{105}$Db	151.7	10.47 ± 4.34	39.81 ± 10.50	14.89 ± 5.94
$^{268}_{106}$Sg	307.5	7.55 ± 2.94	48.17 ± 2.08	13.79 ± 6.02
$^{270}_{107}$Bh	252.6	6.36 ± 2.82	55.96 ± 1.53	11.38 ± 5.32
$E_{0_{c.m.}}/V_{CB}$=1.10				
$^{263}_{103}$Lr	429.2	11.00 ± 4.47	22.35 ± 9.18	17.91 ± 8.17
$^{264}_{104}$Rf	377.6	10.43 ± 3.73	45.48 ± 6.17	17.59 ± 7.71
$^{265}_{105}$Db	272.2	10.00 ± 3.24	45.10 ± 7.98	17.65 ± 8.13
$^{268}_{106}$Sg	1145	8.28 ± 2.90	50.52 ± 3.29	18.51 ± 7.34
$^{270}_{107}$Bh	947.2	6.92 ± 2.49	59.43 ± 2.38	18.91 ± 7.39

6.1.4 ^{20}Ne+^{254}Cf

Fig. 6.4 contains the angular distributions of the heaviest primary ICF products of the reaction ^{20}Ne+^{254}Cf. At all studied incident energies, all differential cross-sections are found between 0-31 degrees. The closer the incident energy is to the Coulomb barrier, the more dominant the products ^{265}Lr and ^{266}Rf are, most prominently found at 12 and 8 degrees respectively at $E_{0_{c.m.}}/V_{CB} = 1.00$. However, at $E_{0_{c.m.}}/V_{CB} = 1.05$ and above the SHE ICF products ^{270}Sg and ^{272}Bh begin to dominate, especially at more forward angles than the other heavy ICF products (most prominently at 9 and 8 degrees respectively). At $E_{0_{c.m.}}/V_{CB} = 1.10$ the more clearly-defined peaks of ^{265}Lr, ^{266}Rf and ^{267}Db lie in the ∼15-20 degree region, whilst the ^{270}Sg and ^{272}Bh peaks have shifted and broadened to encompass the ∼7-16 degree region.

Table 6.4 contains the total cross-sections and the means of the angular, excitation energy and angular momentum distributions of those same ICF products. The total cross-sections of the ICF products follow the same trend as the angular distributions in Fig. 6.4, in that ^{270}Sg and ^{272}Bh start with the lowest yields at the Coulomb barrier, but at 5% and 10% above the barrier they stand tall with the highest yields by some margin. The same general trends of the table are observed here as with the previous three reactions.

Comparing like ICF products from different reactions, ^{266}Rf yields a lower total cross-section at $E_{0_{c.m.}}/V_{CB} = 1.00$, yet higher total cross-sections at $E_{0_{c.m.}}/V_{CB} = 1.05$ and 1.10, from the reaction ^{20}Ne+^{250}Cm than from ^{20}Ne+^{254}Cf. ^{266}Rf produced in the reaction ^{20}Ne+^{250}Cm is typically found at more forward angles, with higher excitation energies and less angular momentum than ^{266}Rf produced in the reaction ^{20}Ne+^{254}Cf. This makes the reaction ^{20}Ne+^{254}Cf the preferable choice to the reaction ^{20}Ne+^{250}Cm for the production of colder, more stable ^{266}Rf at the Coulomb barrier, albeit with lower yields.

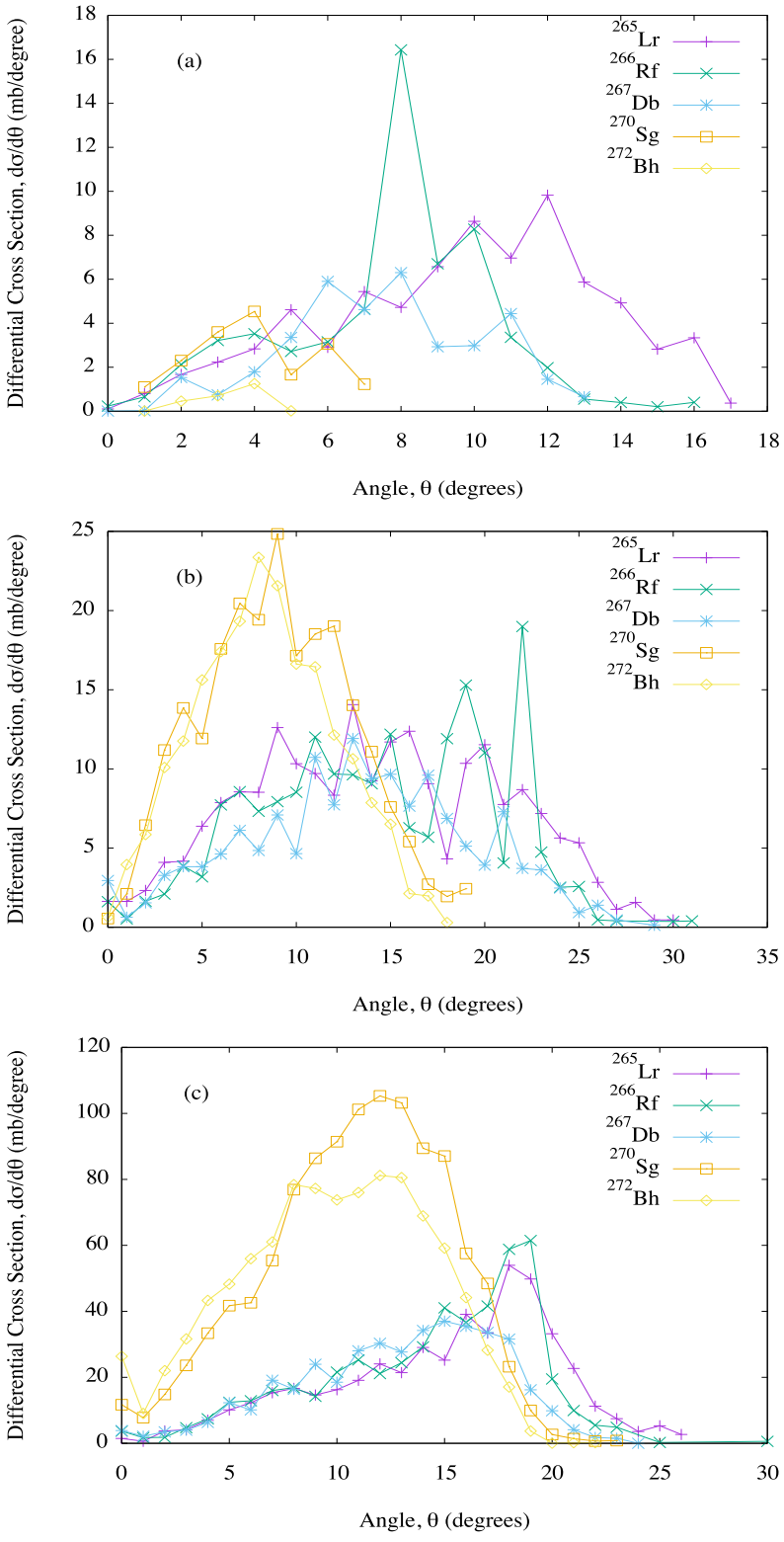

Figure 6.4: The same results as in Fig. 6.1, but for the reaction ^{20}Ne+^{254}Cf, with: (a) $E_{0_{c.m.}}/V_{CB} = 1.00$, (b) $E_{0_{c.m.}}/V_{CB} = 1.05$, and (c) $E_{0_{c.m.}}/V_{CB} = 1.10$.

Table 6.4: The same results as in Table 6.1, but for the reaction ^{20}Ne+^{254}Cf.

ICF product	Total cross section (mb)	Mean angle (degrees)	Mean exc. energy (MeV)	Mean angular momentum ($\hbar$)
$E_{0_{c.m.}}/V_{CB}$=1.00				
$^{265}_{103}$Lr	74.66	9.72 ± 3.68	12.78 ± 9.84	11.83 ± 4.73
$^{266}_{104}$Rf	58.58	7.70 ± 2.81	30.03 ± 7.90	10.55 ± 4.70
$^{267}_{105}$Db	36.76	7.58 ± 2.61	24.05 ± 12.30	9.95 ± 3.72
$^{270}_{106}$Sg	17.50	4.00 ± 1.65	42.49 ± 0.58	9.81 ± 3.25
$^{272}_{107}$Bh	2.442	3.33 ± 0.80	50.11 ± 0.31	8.61 ± 1.94
$E_{0_{c.m.}}/V_{CB}$=1.05				
$^{265}_{103}$Lr	209.9	14.17 ± 6.53	16.69 ± 9.76	15.36 ± 6.65
$^{266}_{104}$Rf	190.3	14.46 ± 6.04	37.87 ± 7.10	16.66 ± 5.94
$^{267}_{105}$Db	146.0	13.34 ± 5.94	35.74 ± 10.95	16.69 ± 6.64
$^{270}_{106}$Sg	228.2	9.02 ± 3.96	44.66 ± 2.81	13.53 ± 6.05
$^{272}_{107}$Bh	204.2	8.34 ± 3.65	52.26 ± 1.67	11.49 ± 5.55
$E_{0_{c.m.}}/V_{CB}$=1.10				
$^{265}_{103}$Lr	483.5	14.95 ± 5.22	18.27 ± 9.90	19.13 ± 8.71
$^{266}_{104}$Rf	493.7	14.24 ± 4.93	41.72 ± 6.84	18.82 ± 7.89
$^{267}_{105}$Db	411.6	12.81 ± 4.63	42.82 ± 8.67	18.47 ± 8.24
$^{270}_{106}$Sg	1117	10.88 ± 4.16	47.66 ± 3.34	18.70 ± 7.64
$^{272}_{107}$Bh	986.4	9.80 ± 4.39	55.78 ± 2.59	18.38 ± 7.56

6.1.5 ^{20}Ne+^{254}Es

Fig. 6.5 contains the angular distributions of the heaviest primary ICF products of the reaction ^{20}Ne+^{254}Es. At all studied incident energies, all differential cross-sections are found between 0-34 degrees. The closer the incident energy is to the Coulomb barrier, the more dominant the products ^{265}Rf and ^{266}Db are, most prominently found at 8 and 7 degrees respectively at $E_{0_{c.m.}}/V_{CB} = 1.00$. However, at $E_{0_{c.m.}}/V_{CB} = 1.05$ and above the SHE ICF products ^{270}Bh and ^{272}Hs begin to dominate, especially at more forward angles than the other SHE ICF products (most prominently at 9 and 7 degrees respectively). At $E_{0_{c.m.}}/V_{CB} = 1.10$ the peaks of ^{263,265}Rf, ^{266}Db and ^{267}Sg lie in the ∼15-20 degree region, whilst the ^{270}Bh and ^{272}Hs peaks have shifted to encompass the ∼8-16 degree region. Table 6.5 contains the total cross-sections and the means of the angular, excitation energy and angular momentum distributions of those same ICF products. The total cross-sections of the ICF products follow the same trend as the angular distributions in Fig. 6.5, in that ^{270}Bh and ^{272}Hs start with the lowest yields at the Coulomb barrier, but at 5% and 10% above the barrier they stand tall with the highest yields by some margin. The same general trends of the table are observed here as with the previous four reactions.

Comparing like ICF products from different reactions, ^{266}Db yields lower total cross-sections at $E_{0_{c.m.}}/V_{CB} = 1.00$ and 1.05, yet a higher total cross-section at $E_{0_{c.m.}}/V_{CB} = 1.10$, from the reaction ^{20}Ne+^{248}Cm than from ^{20}Ne+^{254}Es. ^{266}Db produced in the reaction ^{20}Ne+^{248}Cm is typically found at more forward angles, with higher excitation energies and less angular momentum than ^{266}Db produced in the reaction ^{20}Ne+^{254}Es. This makes the reaction ^{20}Ne+^{254}Es the preferable choice to the reaction ^{20}Ne+^{250}Cm for the production of colder, more stable ^{266}Db at the Coulomb barrier, albeit with lower yields at $E_{0_{c.m.}}/V_{CB} = 1.10$. Similarly, ^{270}Bh yields higher total cross-sections from the reaction ^{20}Ne+^{254}Es than from ^{20}Ne+^{252}Cf. ^{270}Bh produced in the reaction ^{20}Ne+^{252}Cf is typically found at more forward angles, with higher excitation energies than ^{270}Bh produced in the reaction ^{20}Ne+^{252}Cf. This makes the reaction ^{20}Ne+^{254}Es the all-round preferable choice to the reaction ^{20}Ne+^{252}Cf for the production of colder, more stable ^{270}Bh at the studied incident energies.

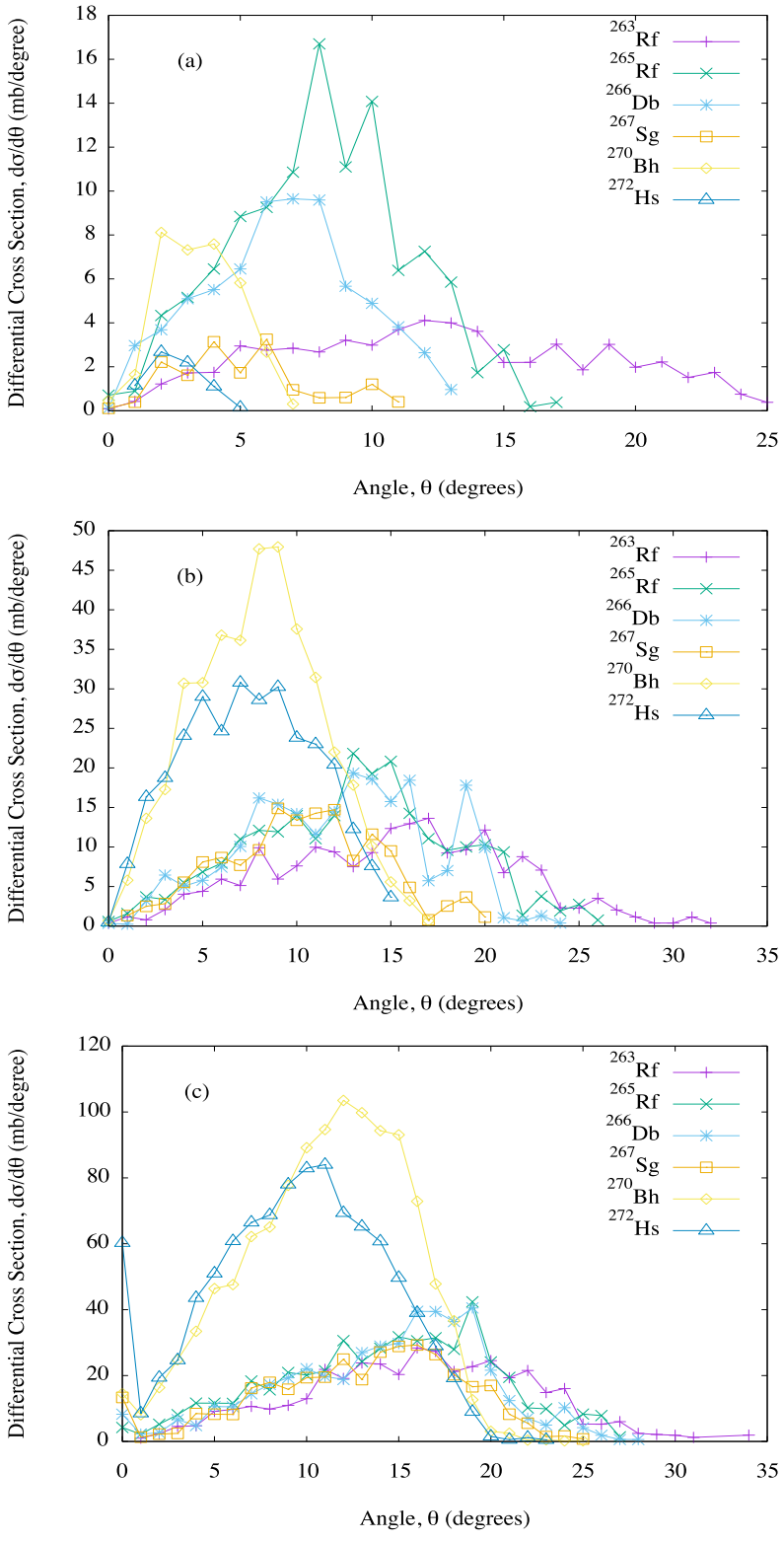

Figure 6.5: The same results as in Fig. 6.1, but for the reaction ^{20}Ne+^{254}Es, with: (a) $E_{0_{c.m.}}/V_{CB} = 1.00$, (b) $E_{0_{c.m.}}/V_{CB} = 1.05$, and (c) $E_{0_{c.m.}}/V_{CB} = 1.10$.

Table 6.5: The same results as in Table 6.1, but for the reaction ^{20}Ne+^{254}Es.

ICF product	Total cross section (mb)	Mean angle (degrees)	Mean exc. energy (MeV)	Mean angular momentum ($\hbar$)
$E_{0_{c.m.}}/V_{CB}$=1.00				
$^{263}_{104}$Rf	58.92	12.50 ± 5.87	51.50 ± 11.79	9.12 ± 3.76
$^{265}_{104}$Rf	113.0	8.05 ± 3.30	15.46 ± 10.19	12.17 ± 4.89
$^{266}_{105}$Db	70.55	6.62 ± 2.91	32.55 ± 9.81	10.34 ± 4.20
$^{267}_{106}$Sg	16.19	5.16 ± 2.54	34.15 ± 12.19	8.77 ± 3.68
$^{270}_{107}$Bh	33.91	3.46 ± 1.45	45.65 ± 0.90	8.31 ± 3.80
$^{272}_{108}$Hs	7.280	2.51 ± 1.00	56.51 ± 0.60	7.88 ± 3.85
$E_{0_{c.m.}}/V_{CB}$=1.05				
$^{263}_{104}$Rf	189.6	15.04 ± 6.20	55.99 ± 11.10	12.65 ± 5.44
$^{265}_{104}$Rf	240.6	13.02 ± 5.32	19.24 ± 8.79	14.79 ± 6.43
$^{266}_{105}$Db	226.5	12.28 ± 4.84	40.10 ± 7.59	14.98 ± 6.18
$^{267}_{106}$Sg	146.0	10.30 ± 4.07	42.09 ± 8.27	13.92 ± 6.11
$^{270}_{107}$Bh	395.8	7.97 ± 3.32	48.23 ± 1.99	13.29 ± 5.59
$^{272}_{108}$Hs	301.5	7.49 ± 3.45	58.52 ± 1.65	12.53 ± 5.61
$E_{0_{c.m.}}/V_{CB}$=1.10				
$^{263}_{104}$Rf	406.7	15.95 ± 6.13	60.14 ± 10.44	14.20 ± 5.86
$^{265}_{104}$Rf	484.6	14.22 ± 5.83	23.84 ± 9.70	19.55 ± 8.51
$^{266}_{105}$Db	462.4	14.19 ± 5.51	45.65 ± 6.53	18.96 ± 8.44
$^{267}_{106}$Sg	360.1	12.85 ± 5.36	47.28 ± 8.41	20.00 ± 9.17
$^{270}_{107}$Bh	1148	11.01 ± 4.34	51.25 ± 3.53	18.24 ± 8.07
$^{272}_{108}$Hs	993.4	9.44 ± 4.71	61.82 ± 2.56	18.17 ± 7.64

6.1.6 ^{20}Ne+^{256}Es

Fig. 6.6 contains the angular distributions of the heaviest primary ICF products of the reaction ^{20}Ne+^{256}Es. At all studied incident energies, all differential cross-sections are found between 0-39 degrees. The closer the incident energy is to the Coulomb barrier, the more dominant the products ^{267}Rf and ^{268}Db are, most prominently found at 11 and 9 degrees respectively at $E_{0_{c.m.}}/V_{CB} = 1.00$. ^{269}Sg and ^{272}Bh closely follow with peaks at 5 and 4 degrees respectively. However, at $E_{0_{c.m.}}/V_{CB} = 1.05$ and above the SHE ICF products ^{272}Bh and ^{274}Hs begin to dominate, especially at more forward angles than the other SHE ICF products (most prominently at 5 and 4 degrees respectively). At $E_{0_{c.m.}}/V_{CB} = 1.10$ the peaks of ^{267}Rf, ^{268}Db and ^{269}Sg lie in the ∼10-15 degree region, whilst the ^{272}Bh and ^{274}Hs peaks have shifted and broadened to encompass the ∼5-12 degree region. Table 6.6 contains the total cross-sections and the means of the angular, excitation energy and angular momentum distributions of those same ICF products. The total cross-sections of the ICF products follow the same trend as the angular distributions in Fig. 6.6, in that ^{270}Bh and ^{272}Hs start with the lowest yields at the Coulomb barrier, but at 5% and 10% above the barrier they have the highest yields by some margin. The same general trends of the table are observed here as with the previous five reactions.

Comparing like ICF products from different reactions, ^{272}Bh yields higher total cross-sections from the reaction ^{20}Ne+^{256}Es than from ^{20}Ne+^{254}Cf. ^{272}Bh produced in the reaction ^{20}Ne+^{256}Es is typically found at more forward angles, with lower excitation energies and slightly more angular momentum than ^{272}Bh produced in the reaction ^{20}Ne+^{254}Es. This makes the reaction ^{20}Ne+^{256}Es the all-round preferable choice to the reaction ^{20}Ne+^{254}Cf for the production of colder, more stable ^{272}Bh at the studied incident energies. Similarly, ^{265}Rf yields higher total cross-sections from the reaction ^{20}Ne+^{254}Es than from ^{20}Ne+^{256}Es. ^{265}Rf produced in the reaction ^{20}Ne+^{254}Es is typically found at more forward angles, with much lower excitation energies and slightly more angular momentum than ^{265}Rf produced in the reaction ^{20}Ne+^{256}Es. This makes the reaction ^{20}Ne+^{254}Es the all-round preferable choice to the reaction ^{20}Ne+^{256}Es for the production of colder, more stable ^{265}Rf at the studied incident energies.

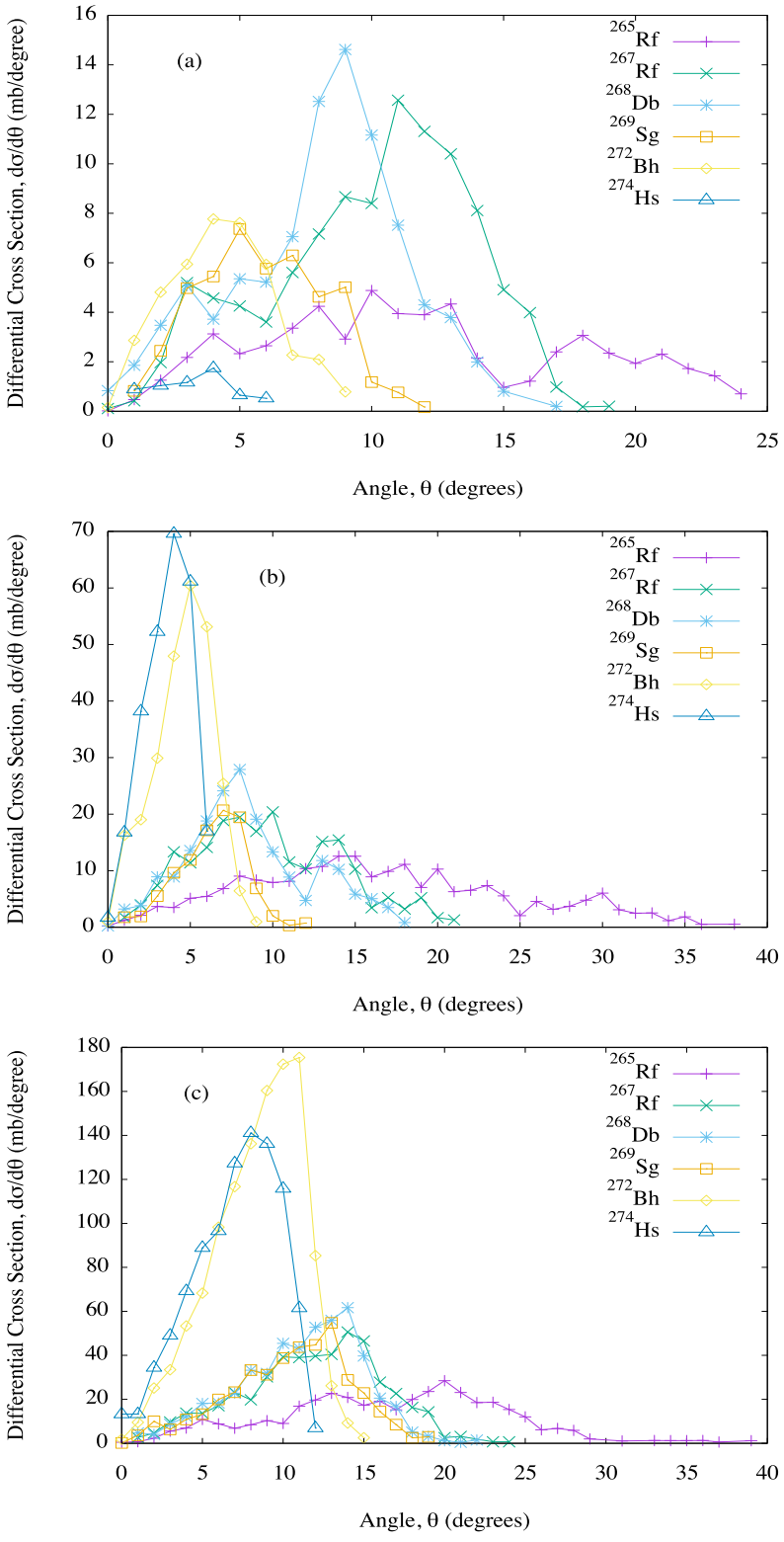

Figure 6.6: The same results as in Fig. 6.1, but for the reaction ^{20}Ne+^{256}Es, with: (a) $E_{0_{c.m.}}/V_{CB} = 1.00$, (b) $E_{0_{c.m.}}/V_{CB} = 1.05$, and (c) $E_{0_{c.m.}}/V_{CB} = 1.10$.

Table 6.6: The same results as in Table 6.1, but for the reaction ^{20}Ne+^{256}Es.

ICF product	Total cross section (mb)	Mean angle (degrees)	Mean exc. energy (MeV)	Mean angular momentum ($\hbar$)
$E_{0_{c.m.}}/V_{CB}$=1.00				
$^{265}_{104}$Rf	59.84	11.83 ± 5.86	54.68 ± 11.26	8.43 ± 3.99
$^{267}_{104}$Rf	102.6	9.97 ± 3.78	15.10 ± 10.11	12.73 ± 5.16
$^{268}_{105}$Db	89.49	8.01 ± 3.26	34.33 ± 9.56	10.68 ± 4.49
$^{269}_{106}$Sg	44.86	5.85 ± 2.34	37.58 ± 9.90	8.94 ± 3.75
$^{272}_{107}$Bh	40.23	4.34 ± 1.95	46.43 ± 0.85	8.84 ± 3.79
$^{274}_{108}$Hs	6.000	3.30 ± 1.48	56.84 ± 0.47	7.27 ± 3.10
$E_{0_{c.m.}}/V_{CB}$=1.05				
$^{265}_{104}$Rf	217.4	16.53 ± 7.98	56.83 ± 10.97	12.40 ± 5.24
$^{267}_{104}$Rf	210.5	9.75 ± 4.38	19.45 ± 9.50	15.40 ± 6.75
$^{268}_{105}$Db	192.8	8.53 ± 3.75	40.54 ± 8.39	14.62 ± 6.03
$^{269}_{106}$Sg	97.98	6.31 ± 2.00	43.44 ± 7.43	12.90 ± 5.75
$^{272}_{107}$Bh	260.5	4.59 ± 1.76	48.82 ± 1.95	13.68 ± 5.64
$^{274}_{108}$Hs	256.6	3.65 ± 1.37	58.65 ± 1.56	11.62 ± 5.46
$E_{0_{c.m.}}/V_{CB}$=1.10				
$^{265}_{104}$Rf	390.2	16.64 ± 6.79	60.97 ± 10.39	14.12 ± 6.14
$^{267}_{104}$Rf	478.2	11.78 ± 4.25	24.69 ± 9.99	19.02 ± 8.55
$^{268}_{105}$Db	501.3	11.13 ± 3.80	48.22 ± 6.94	19.38 ± 8.59
$^{269}_{106}$Sg	413.9	10.44 ± 3.70	48.41 ± 8.89	19.87 ± 8.70
$^{272}_{107}$Bh	1174	8.38 ± 2.77	51.96 ± 3.50	18.53 ± 8.19
$^{274}_{108}$Hs	953.3	7.02 ± 2.66	62.37 ± 2.53	17.73 ± 7.59

6.2 ^{40}Ca-induced incomplete fusion reactions

Total integrated cross-sections, angular, excitation energy and angular momentum distributions and their associated standard deviations were calculated for the primary ICF products of ^{40}Ca-induced incomplete fusion reactions with chains of Cm, Cf and Es targets at varying incident energies. The same targets were chosen here as with the ^{20}Ne-induced reactions: ^{248}Cm (Table 6.7), ^{250}Cm (Table 6.8), ^{252}Cf (Table 6.9), ^{254}Cf (Table 6.10), ^{254}Es (Table 6.11) and ^{256}Es (Table 6.12). The maximal orbital angular momentum between projectile and target considered here is $L_{TP} = 50\hbar$, with 1000 sampled fragmentations per orbital angular momentum. Results have been shown only for SHE primary ICF products. Also presented are the angular distributions of all tabulated primary ICF products (Figs. 6.7-6.12).

6.2.1 ^{40}Ca+^{248}Cm

Fig. 6.7 contains the angular distributions of primary SHE ICF products of the reaction ^{40}Ca+^{248}Cm. At all studied incident energies, all differential cross-sections are found between 0-35 degrees. The closer the incident energy is to the Coulomb barrier, the more dominant the lighter SHE ICF products, such as ^{264}Rf and ^{265}Db, are, maintaining among the highest cross-sections at all three incident energies. At $E_{0_{c.m.}}/V_{CB} = 1.05$, ^{271}Bh and ^{272}Hs have the highest peaks, and at $E_{0_{c.m.}}/V_{CB} = 1.10$ they have similar peak heights to ^{264}Rf and ^{265}Db, though the peaks are narrower and found at more forward angles. Most notably at $E_{0_{c.m.}}/V_{CB} = 1.10$, the heavier SHE ICF products have a greater presence, with ^{286}Mc and ^{284}Fl having over double the peak height of all other primary SHE ICF products.

Table 6.7 contains the total cross-sections and the means of the angular, excitation energy and angular momentum distributions of those same ICF products. The total cross-sections of the ICF products follow the same trend as the angular distributions in Fig. 6.7, in that ^{264}Rf and ^{265}Db have among the highest yields at all three incident energies, with ^{286}Mc and ^{284}Fl contending with them at 10% above the barrier. Similar general trends of the table are observed here as with the ^{20}Ne-induced reactions, namely

that the heavier the ICF product the more forward the angle and the higher the angular momentum, and the lower the total cross-section with exceptions for the heaviest two ICF products at higher energies.

Comparing like ICF products from different reactions, ^{264}Rf, ^{265}Db, ^{268}Sg and ^{272}Hs yield far lower total cross-sections, and with higher excitation energies, here than from the studied ^{20}Ne-induced reactions, suggesting that the ^{20}Ne-induced reactions are the preferable choices for production of more stable SHE ICF products that are shared with the ^{40}Ca-induced reactions.

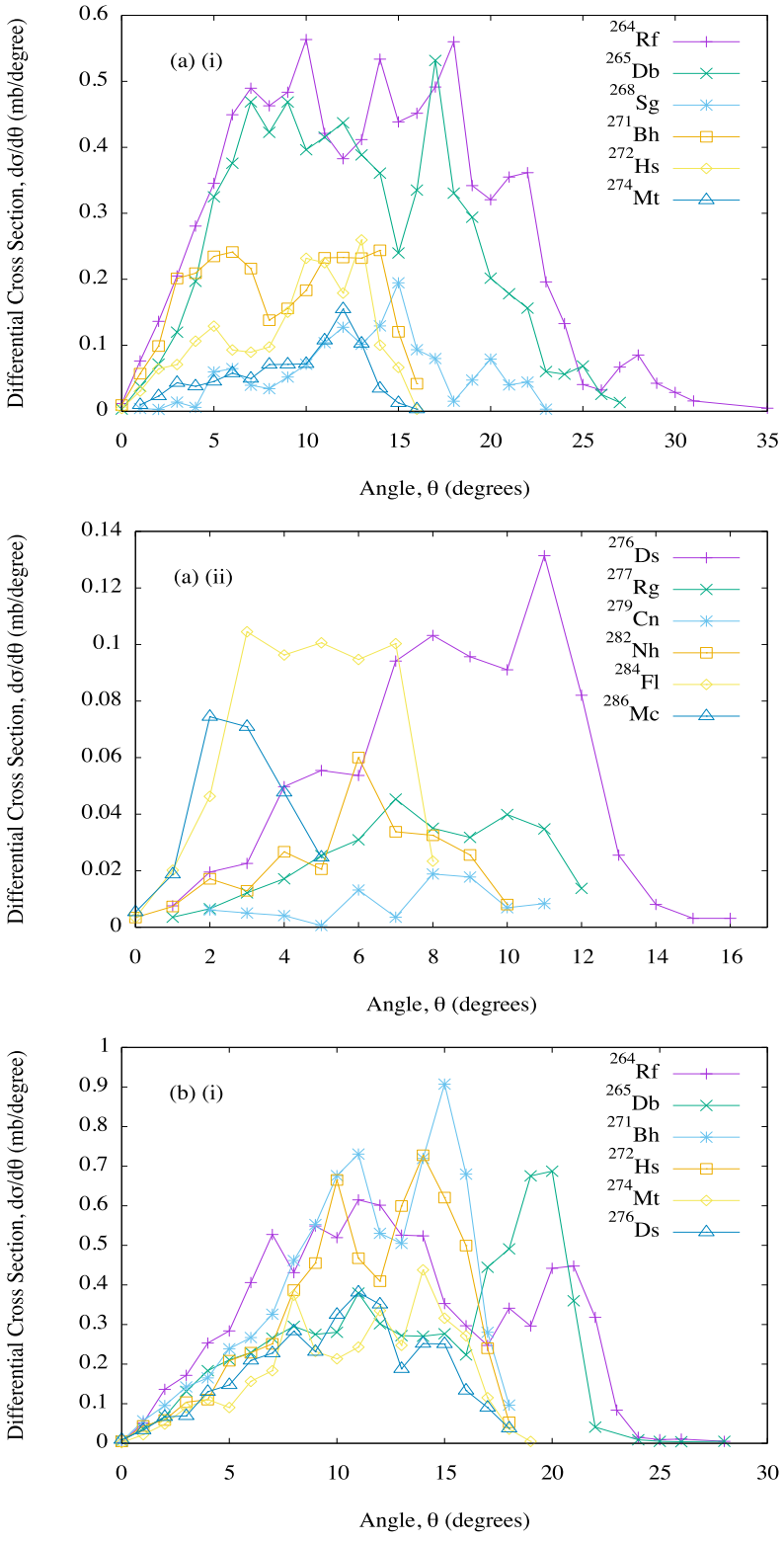

Figure 6.7: Angular distributions of SHE primary ICF products of the reaction ^{40}Ca+^{248}Cm, with: (a) $E_{0_{c.m.}}/V_{CB} = 1.00$, (b) $E_{0_{c.m.}}/V_{CB} = 1.05$, and (c) $E_{0_{c.m.}}/V_{CB} = 1.10$. Subfigures are further separated into parts (i) and (ii) to enhance readability.

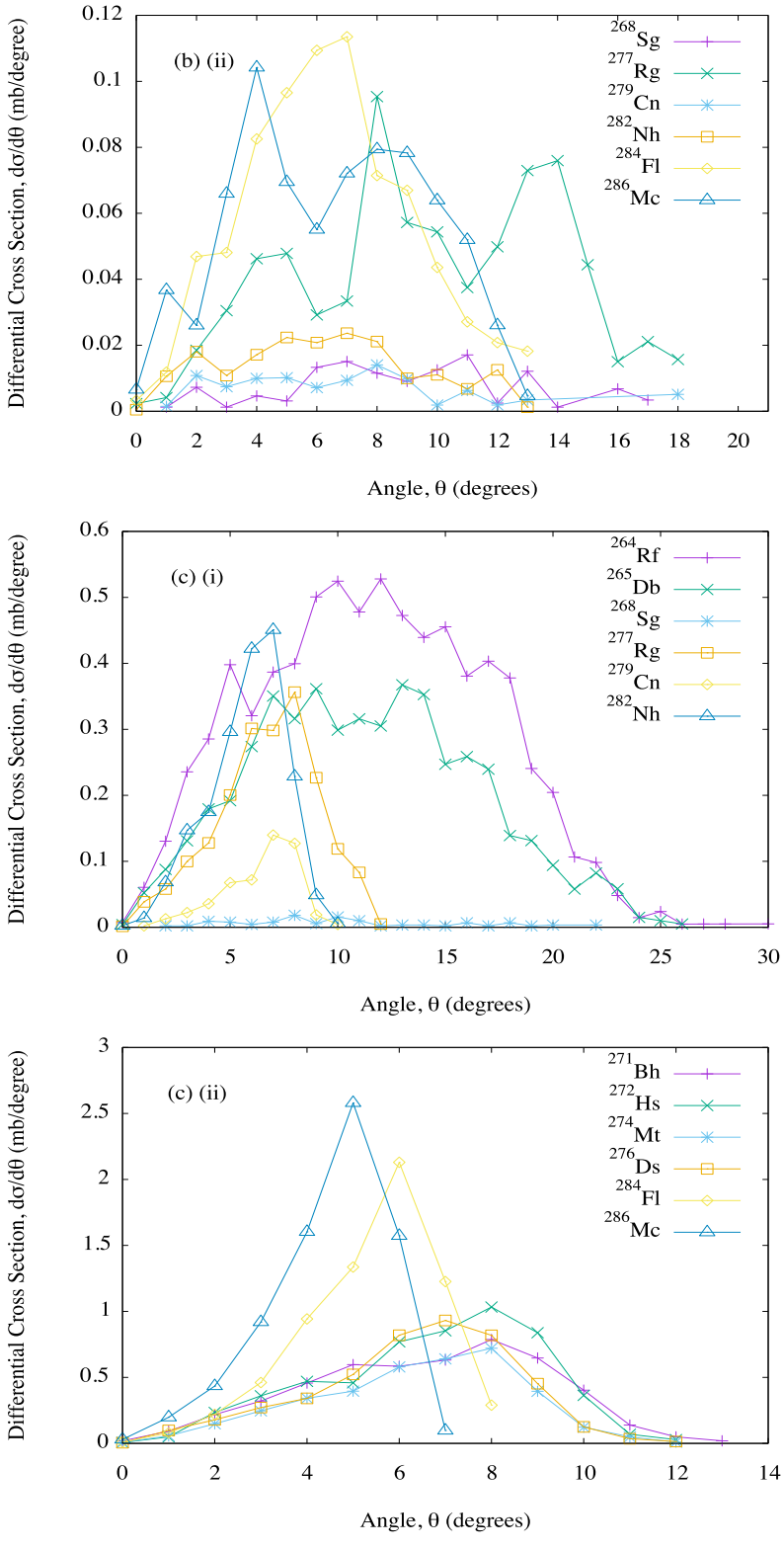

Continuation of Fig. 6.7.

Table 6.7: Results for SHE primary ICF products of the reaction ^{40}Ca+^{248}Cm.

ICF product	Total cross section (mb)	Mean angle (degrees)	Mean exc. energy (MeV)	Mean angular momentum ($\hbar$)
$E_{0_{c.m.}}/V_{CB}$=1.00				
$^{264}_{104}$Rf	9.218	13.31 ± 6.37	46.90 ± 12.57	15.90 ± 9.09
$^{265}_{105}$Db	6.980	12.35 ± 5.55	73.23 ± 21.80	15.48 ± 9.23
$^{268}_{106}$Sg	1.406	13.29 ± 4.57	53.14 ± 7.13	17.72 ± 7.37
$^{271}_{107}$Bh	2.848	8.58 ± 4.09	36.49 ± 22.58	24.80 ± 15.05
$^{272}_{108}$Hs	1.900	9.22 ± 3.69	65.70 ± 12.26	26.16 ± 14.31
$^{274}_{109}$Mt	0.8942	9.25 ± 3.46	71.59 ± 11.27	29.76 ± 13.20
$^{276}_{110}$Ds	0.8459	8.44 ± 2.94	68.34 ± 9.05	32.52 ± 13.45
$^{277}_{111}$Rg	0.2963	7.64 ± 2.65	73.73 ± 24.29	35.54 ± 12.23
$^{279}_{112}$Cn	0.08452	7.37 ± 2.58	79.08 ± 23.51	36.53 ± 11.07
$^{282}_{113}$Nh	0.2480	5.87 ± 2.33	67.91 ± 3.15	29.19 ± 11.93
$^{284}_{114}$Fl	0.5897	4.70 ± 1.84	63.23 ± 2.30	24.78 ± 11.25
$^{286}_{115}$Mc	0.2418	2.87 ± 1.19	62.02 ± 1.26	20.77 ± 7.76
$E_{0_{c.m.}}/V_{CB}$=1.05				
$^{264}_{104}$Rf	8.464	12.45 ± 5.56	50.35 ± 6.98	20.19 ± 8.21
$^{265}_{105}$Db	6.428	13.71 ± 5.58	82.18 ± 18.81	19.50 ± 8.09
$^{268}_{106}$Sg	0.1221	8.98 ± 3.75	65.97 ± 4.69	21.57 ± 9.02
$^{271}_{107}$Bh	7.437	11.28 ± 3.91	36.21 ± 22.92	21.69 ± 9.50
$^{272}_{108}$Hs	6.135	11.30 ± 3.78	68.52 ± 8.19	21.05 ± 9.06
$^{274}_{109}$Mt	3.530	10.92 ± 3.96	72.04 ± 6.98	21.68 ± 9.23
$^{276}_{110}$Ds	3.416	10.12 ± 3.89	65.42 ± 7.18	21.81 ± 8.94
$^{277}_{111}$Rg	0.7516	9.79 ± 4.17	74.00 ± 24.00	20.52 ± 9.25
$^{279}_{112}$Cn	0.09887	7.00 ± 3.95	65.14 ± 26.29	18.95 ± 8.93
$^{282}_{113}$Nh	0.1866	6.22 ± 3.11	62.28 ± 2.79	19.69 ± 10.71
$^{284}_{114}$Fl	0.7602	6.46 ± 2.78	60.50 ± 2.59	20.24 ± 8.78
$^{286}_{115}$Mc	0.7405	6.50 ± 3.09	62.75 ± 2.37	18.77 ± 8.56

Continuation of Table 6.7.

ICF product	Total cross section (mb)	Mean angle (degrees)	Mean exc. energy (MeV)	Mean angular momentum ($\hbar$)
$E_{0_{c.m.}}/V_{CB}$=1.10				
$^{264}_{104}$Rf	7.542	11.65 ± 5.26	54.45 ± 6.82	25.03 ± 9.53
$^{265}_{105}$Db	4.928	11.35 ± 5.14	84.30 ± 18.64	24.96 ± 9.76
$^{268}_{106}$Sg	0.1198	10.39 ± 4.97	69.54 ± 7.42	26.98 ± 10.27
$^{271}_{107}$Bh	4.964	6.60 ± 2.55	38.15 ± 24.20	26.28 ± 11.05
$^{272}_{108}$Hs	5.534	6.67 ± 2.31	72.51 ± 10.30	26.21 ± 11.64
$^{274}_{109}$Mt	3.714	6.35 ± 2.21	75.99 ± 10.44	26.70 ± 11.89
$^{276}_{110}$Ds	4.613	6.31 ± 2.14	67.20 ± 10.05	27.19 ± 12.27
$^{277}_{111}$Rg	1.916	6.74 ± 2.33	70.80 ± 25.15	27.24 ± 11.95
$^{279}_{112}$Cn	0.5028	6.40 ± 1.72	75.02 ± 24.00	26.62 ± 12.30
$^{282}_{113}$Nh	1.858	5.80 ± 1.75	63.97 ± 5.25	27.23 ± 11.80
$^{284}_{114}$Fl	6.695	5.38 ± 1.49	62.84 ± 4.07	27.53 ± 11.70
$^{286}_{115}$Mc	7.435	4.47 ± 1.32	67.15 ± 3.17	29.23 ± 11.38

6.2.2 ^{40}Ca+^{250}Cm

Fig. 6.8 contains the angular distributions of primary SHE ICF products of the reaction ^{40}Ca+^{250}Cm. At all studied incident energies, all differential cross-sections are found between 0-33 degrees. The closer the incident energy is to the Coulomb barrier, the more dominant the lighter SHE ICF products, such as ^{266}Rf and ^{267}Db, are, maintaining among the highest cross-sections at all three incident energies. At $E_{0_{c.m.}}/V_{CB} = 1.05$, ^{273}Bh and ^{274}Hs have the highest peaks, and at $E_{0_{c.m.}}/V_{CB} = 1.10$ they have similar peak heights to ^{264}Rf and ^{265}Db, with ^{288}Mc and ^{286}Fl narrowly overtaking all other primary SHE ICF products.

Table 6.8 contains the total cross-sections and the means of the angular, excitation energy and angular momentum distributions of those same ICF products. The total cross-sections of the ICF products follow the same trend as the angular distributions in Fig. 6.8, in that ^{266}Rf and ^{267}Db have among the highest yields at all three incident energies, with ^{288}Mc and ^{286}Fl contending with them at 10% above the barrier. Similar general trends of the table are observed here as with the previous reaction, namely that the heavier the ICF product the more forward the angle and the higher the angular momentum, and the lower the total cross-section with exceptions for the heaviest two ICF products at higher energies.

Comparing like ICF products from different reactions, ^{266}Rf, ^{267}Db, ^{270}Sg and ^{274}Hs yield far lower total cross-sections, and with higher excitation energies, here than from the studied ^{20}Ne-induced reactions, further confirming that the ^{20}Ne-induced reactions are the preferable choices for production of more stable SHE ICF products that are shared with the ^{40}Ca-induced reactions.

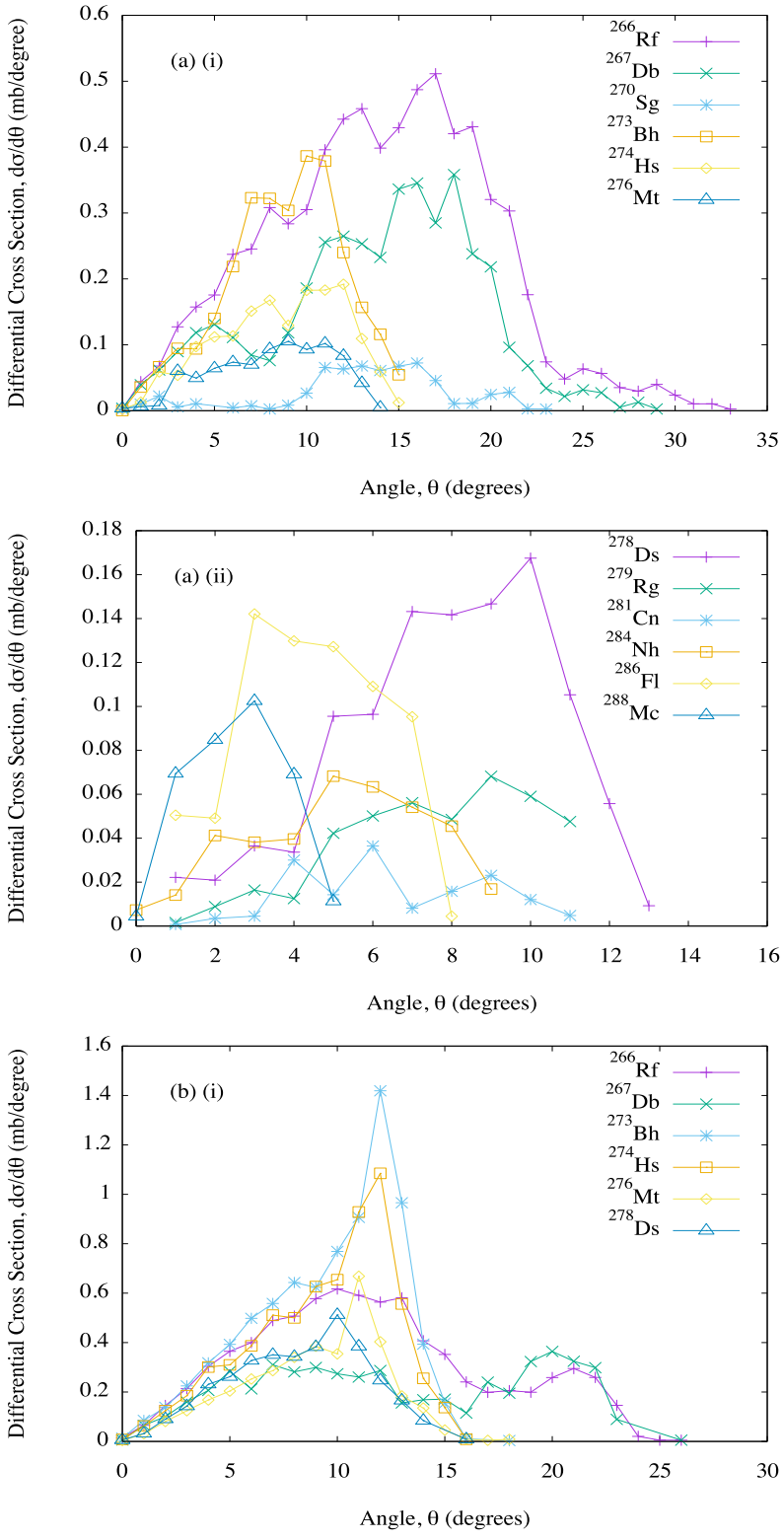

Figure 6.8: The same results as in Fig. 6.7, but for the reaction ^{40}Ca+^{250}Cm, with: (a) $E_{0_{c.m.}}/V_{CB} = 1.00$, (b) $E_{0_{c.m.}}/V_{CB} = 1.05$, and (c) $E_{0_{c.m.}}/V_{CB} = 1.10$. Subfigures are further separated into parts (i) and (ii) to enhance readability.

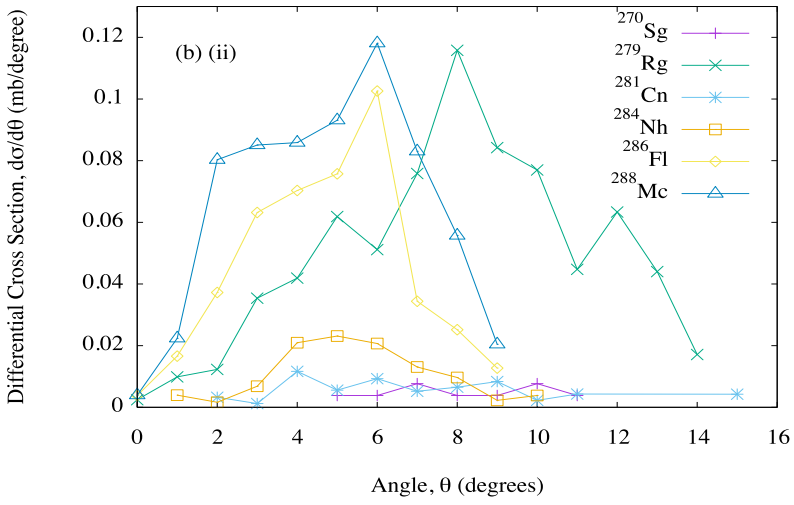

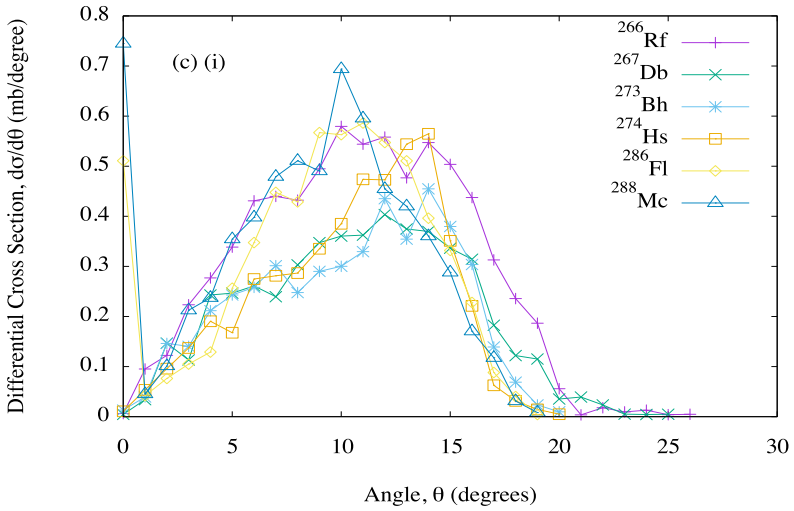

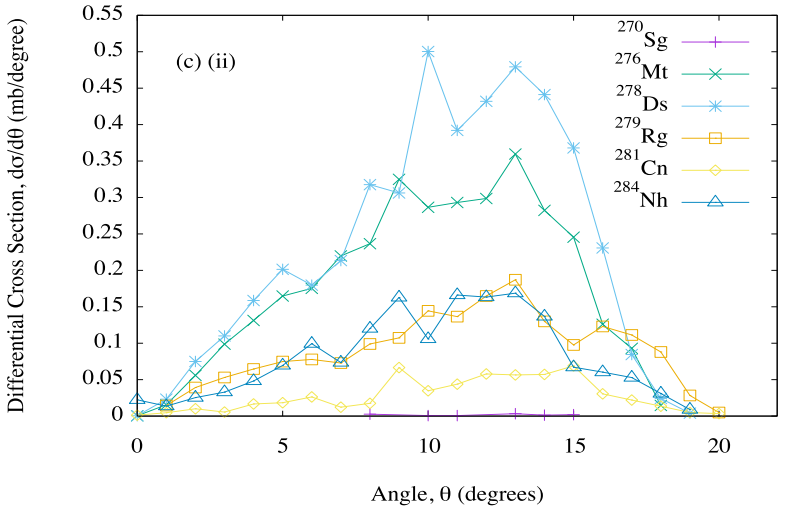

Continuation of Fig. 6.8.

Table 6.8: The same results as in Table 6.7, but for the reaction ^{40}Ca+^{250}Cm.

ICF product	Total cross section (mb)	Mean angle (degrees)	Mean exc. energy (MeV)	Mean angular momentum ($\hbar$)
$E_{0_{c.m.}}/V_{CB}$=1.00				
$^{266}_{104}$Rf	7.122	14.06 ± 5.83	52.21 ± 14.14	17.81 ± 11.37
$^{267}_{105}$Db	4.108	13.77 ± 5.46	81.15 ± 22.61	19.02 ± 11.73
$^{270}_{106}$Sg	0.6241	13.35 ± 4.57	54.28 ± 9.22	17.73 ± 8.98
$^{273}_{107}$Bh	2.932	8.80 ± 3.12	38.90 ± 23.93	27.53 ± 15.08
$^{274}_{108}$Hs	1.637	8.59 ± 3.30	72.95 ± 12.07	32.24 ± 14.45
$^{276}_{109}$Mt	0.8593	8.16 ± 3.05	80.14 ± 6.82	35.05 ± 13.51
$^{278}_{110}$Ds	1.074	7.86 ± 2.65	74.50 ± 4.96	37.24 ± 12.47
$^{279}_{111}$Rg	0.4114	7.63 ± 2.38	75.29 ± 23.11	34.91 ± 12.56
$^{281}_{112}$Cn	0.1535	6.50 ± 2.29	78.74 ± 24.31	33.35 ± 11.88
$^{284}_{113}$Nh	0.3885	5.11 ± 2.23	71.51 ± 2.94	30.90 ± 11.98
$^{286}_{114}$Fl	0.7076	4.36 ± 1.76	66.34 ± 2.31	25.37 ± 10.49
$^{288}_{115}$Mc	0.3415	2.58 ± 1.15	65.40 ± 1.15	19.16 ± 7.31
$E_{0_{c.m.}}/V_{CB}$=1.05				
$^{266}_{104}$Rf	8.027	11.58 ± 5.48	52.14 ± 6.49	21.06 ± 7.95
$^{267}_{105}$Db	5.197	12.66 ± 6.28	83.82 ± 17.66	20.30 ± 8.31
$^{270}_{106}$Sg	0.03834	8.11 ± 1.91	67.90 ± 5.37	21.20 ± 6.98
$^{273}_{107}$Bh	8.119	9.51 ± 3.32	36.06 ± 22.84	20.66 ± 9.37
$^{274}_{108}$Hs	6.641	9.33 ± 3.25	69.84 ± 7.03	20.50 ± 8.95
$^{276}_{109}$Mt	3.689	8.96 ± 3.21	72.52 ± 7.68	20.65 ± 8.82
$^{278}_{110}$Ds	3.571	8.20 ± 3.08	65.88 ± 9.49	20.48 ± 8.41
$^{279}_{111}$Rg	0.7370	8.11 ± 3.08	72.76 ± 23.26	19.63 ± 8.13
$^{281}_{112}$Cn	0.06187	7.08 ± 3.21	73.61 ± 22.30	18.10 ± 9.08
$^{284}_{113}$Nh	0.1060	5.46 ± 1.93	63.86 ± 2.44	17.37 ± 9.45
$^{286}_{114}$Fl	0.4418	4.78 ± 1.94	62.72 ± 2.36	18.42 ± 8.25
$^{288}_{115}$Mc	0.6479	4.89 ± 2.11	65.06 ± 1.95	18.24 ± 8.82

Continuation of Table 6.8.

ICF product	Total cross section (mb)	Mean angle (degrees)	Mean exc. energy (MeV)	Mean angular momentum ($\hbar$)
$E_{0_{c.m.}}/V_{CB}$=1.10				
$^{266}_{104}$Rf	7.351	10.85 ± 4.64	55.80 ± 6.88	25.94 ± 9.49
$^{267}_{105}$Db	4.993	10.83 ± 4.67	85.65 ± 18.20	24.78 ± 9.61
$^{270}_{106}$Sg	0.01043	11.94 ± 2.61	68.63 ± 6.33	30.75 ± 5.79
$^{273}_{107}$Bh	4.690	10.38 ± 4.35	38.83 ± 24.08	26.02 ± 11.29
$^{274}_{108}$Hs	4.960	10.43 ± 3.93	74.38 ± 10.32	26.34 ± 11.10
$^{276}_{109}$Mt	3.422	10.23 ± 3.82	77.36 ± 10.65	27.30 ± 11.79
$^{278}_{110}$Ds	4.542	10.59 ± 3.77	68.65 ± 10.09	27.09 ± 12.02
$^{279}_{111}$Rg	1.819	11.18 ± 4.43	70.65 ± 22.84	26.85 ± 12.79
$^{281}_{112}$Cn	0.5721	11.43 ± 4.00	76.94 ± 22.62	25.99 ± 12.07
$^{284}_{113}$Nh	1.628	10.31 ± 4.03	66.65 ± 5.13	27.07 ± 11.74
$^{286}_{114}$Fl	6.206	9.32 ± 4.43	65.68 ± 4.14	27.48 ± 11.92
$^{288}_{115}$Mc	6.714	8.50 ± 4.64	70.24 ± 3.06	28.90 ± 11.50

6.2.3 ^{40}Ca+^{252}Cf

Fig. 6.9 contains the angular distributions of primary SHE ICF products of the reaction ^{40}Ca+^{252}Cf. At all studied incident energies, all differential cross-sections are found between 0-34 degrees. The closer the incident energy is to the Coulomb barrier, the more dominant the lighter SHE ICF products, such as ^{268}Sg and ^{269}Bh, are, maintaining among the highest cross-sections at $E_{0_{c.m.}}/V_{CB} = 1.00$ and 1.05. At $E_{0_{c.m.}}/V_{CB} = 1.05$, ^{264}Rf and ^{275}Mt have the highest peaks along with ^{268}Sg and ^{269}Bh, however at $E_{0_{c.m.}}/V_{CB} = 1.10$ ^{288}Lv and ^{290}Ts dominate with over double the peak height of all other primary SHE ICF products.

Table 6.9 contains the total cross-sections and the means of the angular, excitation energy and angular momentum distributions of those same ICF products. The total cross-sections of the ICF products follow a similar trend to the angular distributions in Fig. 6.9, in that ^{264}Rf, ^{266}Db, ^{268}Sg and ^{269}Bh have among the highest yields at all three incident energies, with ^{288}Lv and ^{290}Ts contending with them at 5% above the barrier and exceeding them at 10% above the barrier. The same general trends of the table are observed here as with the previous two reactions.

Comparing like ICF products from different ^{40}Ca-induced reactions, ^{264}Rf, ^{272}Hs and ^{286}Mc have smaller total cross-sections, and ^{268}Sg and ^{276}Ds have larger total cross-sections from this reaction than from ^{40}Ca+^{248}Cm, whilst ^{264}Rf, ^{268}Sg, ^{272}Hs and ^{286}Mc have lower excitation energies, and ^{276}Ds has higher excitation energies from this reaction than from ^{40}Ca+^{248}Cm, making this reaction firmly preferable to ^{40}Ca+^{248}Cm for the production of colder ^{268}Sg.

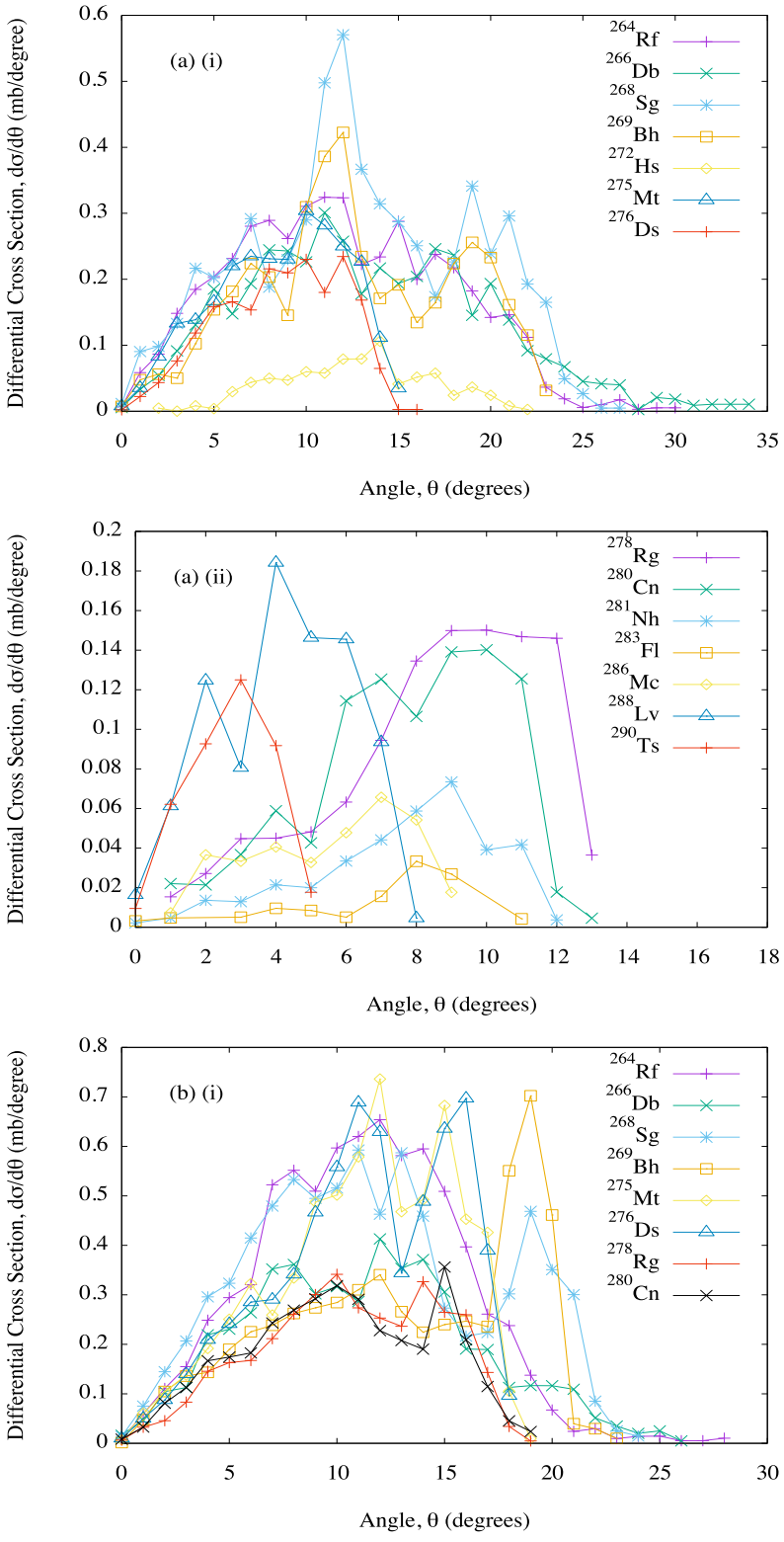

Figure 6.9: The same results as in Fig. 6.7, but for the reaction ^{40}Ca+^{252}Cf, with: (a) $E_{0_{c.m.}}/V_{CB} = 1.00$, (b) $E_{0_{c.m.}}/V_{CB} = 1.05$, and (c) $E_{0_{c.m.}}/V_{CB} = 1.10$. Subfigures are further separated into parts (i) and (ii) to enhance readability.

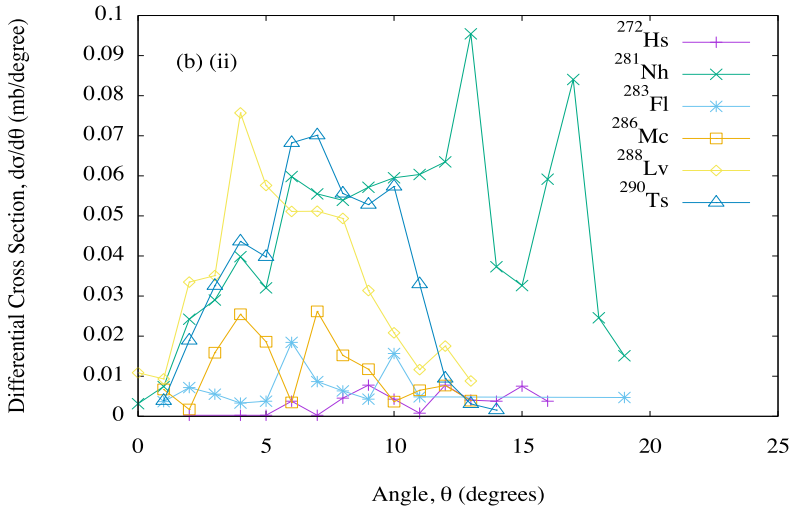

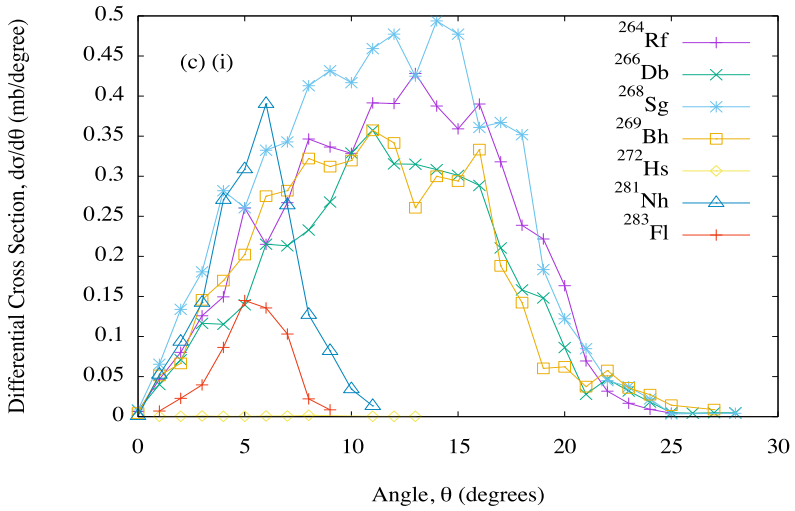

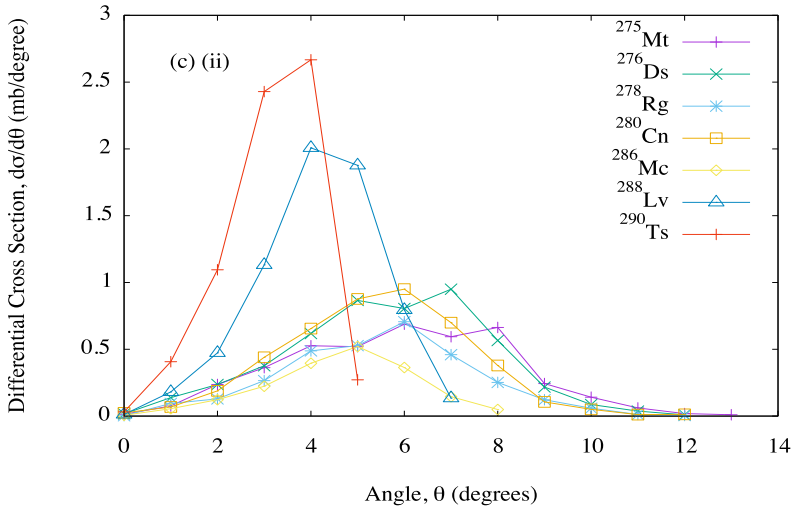

Continuation of Fig. 6.9.

Table 6.9: The same results as in Table 6.7, but for the reaction ^{40}Ca+^{252}Cf.

ICF product	Total cross section (mb)	Mean angle (degrees)	Mean exc. energy (MeV)	Mean angular momentum ($\hbar$)
$E_{0_{c.m.}}/V_{CB}$=1.00				
$^{264}_{104}$Rf	4.793	11.90 ± 5.67	42.11 ± 13.18	17.59 ± 9.56
$^{266}_{105}$Db	4.314	13.38 ± 6.44	50.45 ± 14.32	18.41 ± 10.65
$^{268}_{106}$Sg	5.982	12.85 ± 5.84	50.19 ± 14.23	18.35 ± 11.44
$^{269}_{107}$Bh	4.207	12.59 ± 5.35	79.24 ± 22.86	17.86 ± 11.34
$^{272}_{108}$Hs	0.8163	12.67 ± 3.96	52.35 ± 7.46	17.81 ± 7.72
$^{275}_{109}$Mt	2.688	8.57 ± 3.44	38.43 ± 24.59	28.11 ± 15.71
$^{276}_{110}$Ds	2.049	8.57 ± 3.24	68.15 ± 12.44	29.74 ± 15.28
$^{278}_{111}$Rg	1.102	8.56 ± 2.91	72.48 ± 10.95	33.26 ± 13.69
$^{280}_{112}$Cn	0.9552	7.69 ± 2.67	70.91 ± 5.08	38.40 ± 11.95
$^{281}_{113}$Nh	0.3692	7.56 ± 2.59	73.46 ± 24.47	35.18 ± 11.34
$^{283}_{114}$Fl	0.1162	6.85 ± 2.52	84.11 ± 21.09	33.07 ± 12.04
$^{286}_{115}$Mc	0.3358	5.49 ± 2.20	67.33 ± 3.22	29.14 ± 10.92
$^{288}_{116}$Lv	0.8570	4.18 ± 1.87	61.92 ± 2.36	26.18 ± 11.92
$^{290}_{117}$Ts	0.3988	2.70 ± 1.18	60.11 ± 1.25	20.81 ± 8.82
$E_{0_{c.m.}}/V_{CB}$=1.05				
$^{264}_{104}$Rf	7.550	11.08 ± 4.49	40.28 ± 6.04	19.93 ± 7.36
$^{266}_{105}$Db	5.027	11.19 ± 5.16	49.50 ± 6.39	20.42 ± 7.94
$^{268}_{106}$Sg	7.860	11.64 ± 5.37	51.14 ± 6.81	21.09 ± 8.10
$^{269}_{107}$Bh	5.565	13.02 ± 5.47	83.56 ± 18.93	20.24 ± 8.26
$^{272}_{108}$Hs	0.04901	11.35 ± 3.14	60.42 ± 9.91	19.49 ± 7.95
$^{275}_{109}$Mt	6.610	11.12 ± 4.09	33.62 ± 23.01	21.49 ± 9.35
$^{276}_{110}$Ds	6.648	11.19 ± 4.09	67.67 ± 7.30	21.16 ± 9.32

Continuation of Table 6.9.

ICF product	Total cross section (mb)	Mean angle (degrees)	Mean exc. energy (MeV)	Mean angular momentum ($\hbar$)
$E_{0_{c.m.}}/V_{CB}$=1.05				
$^{278}_{111}$Rg	3.554	10.53 ± 4.06	69.55 ± 7.37	21.26 ± 9.23
$^{280}_{112}$Cn	3.547	10.16 ± 4.25	62.63 ± 7.61	21.93 ± 9.18
$^{281}_{113}$Nh	0.8936	10.67 ± 4.62	68.69 ± 23.58	21.48 ± 9.35
$^{283}_{114}$Fl	0.08631	7.25 ± 3.99	65.54 ± 21.60	21.15 ± 8.77
$^{286}_{115}$Mc	0.1467	6.37 ± 3.00	61.66 ± 2.62	22.30 ± 10.67
$^{288}_{116}$Lv	0.4639	5.98 ± 2.96	58.53 ± 2.35	20.42 ± 9.96
$^{290}_{117}$Ts	0.4899	7.03 ± 2.67	60.15 ± 1.93	19.74 ± 9.20
$E_{0_{c.m.}}/V_{CB}$=1.10				
$^{264}_{104}$Rf	5.583	11.89 ± 4.90	47.13 ± 6.77	24.27 ± 8.17
$^{266}_{105}$Db	4.381	11.77 ± 4.95	54.47 ± 6.42	25.22 ± 8.87
$^{268}_{106}$Sg	6.782	11.51 ± 5.03	55.17 ± 7.17	25.87 ± 9.73
$^{269}_{107}$Bh	4.672	11.16 ± 5.01	86.05 ± 19.01	25.52 ± 9.39
$^{272}_{108}$Hs	0.007968	6.59 ± 3.31	71.83 ± 5.53	22.41 ± 10.94
$^{275}_{109}$Mt	4.154	5.91 ± 2.32	36.70 ± 23.80	26.73 ± 11.58
$^{276}_{110}$Ds	4.922	5.67 ± 2.11	71.07 ± 10.41	27.16 ± 11.36
$^{278}_{111}$Rg	3.123	5.47 ± 2.00	73.90 ± 10.33	26.90 ± 11.44
$^{280}_{112}$Cn	4.462	5.41 ± 1.91	64.65 ± 9.80	27.42 ± 11.73
$^{281}_{113}$Nh	1.780	5.47 ± 2.04	66.83 ± 24.69	27.15 ± 12.30
$^{283}_{114}$Fl	0.5706	5.32 ± 1.56	76.44 ± 23.42	27.78 ± 12.40
$^{286}_{115}$Mc	1.881	4.65 ± 1.56	63.68 ± 4.87	28.14 ± 12.33
$^{288}_{116}$Lv	6.614	4.18 ± 1.28	61.85 ± 4.12	27.54 ± 11.50
$^{290}_{117}$Ts	6.902	3.17 ± 0.97	65.80 ± 3.26	29.40 ± 11.33

6.2.4 ^{40}Ca+^{254}Cf

Fig. 6.10 contains the angular distributions of primary SHE ICF products of the reaction ^{40}Ca+^{254}Cf. At all studied incident energies, all differential cross-sections are found between 0-32 degrees. At $E_{0_{c.m.}}/V_{CB} = 1.00$, ^{266}Rf, ^{270}Sg and ^{271}Bh have the highest differential cross-sections, located in the ∼9-17 degree region. At $E_{0_{c.m.}}/V_{CB} = 1.05$, ^{266}Rf, ^{270}Sg, ^{277}Mt and ^{278}Ds have the highest differential cross-sections, located in the ∼9-16 degree region. At $E_{0_{c.m.}}/V_{CB} = 1.10$, ^{290}Lv and ^{292}Ts overtake the lighter SHE ICF products to have the highest differential cross-sections, located in the ∼5-13 degree region.

Table 6.10 contains the total cross-sections and the means of the angular, excitation energy and angular momentum distributions of those same ICF products. The total cross-sections of the ICF products follow a similar trend to the angular distributions in Fig. 6.10, in that ^{266}Rf, ^{268}Db, ^{270}Sg and ^{271}Bh have among the highest yields at all three incident energies, with ^{277}Mt and ^{278}Ds contending with them at 5% above the barrier and with ^{288}Lv and ^{290}Ts exceeding almost all of them at 10% above the barrier. The same general trends of the table are observed here as with the previous three reactions.

Comparing like ICF products from different ^{40}Ca-induced reactions, ^{266}Rf, ^{274}Hs and ^{288}Mc have smaller total cross-sections, and ^{270}Sg and ^{278}Ds have larger total cross-sections from this reaction than from ^{40}Ca+^{250}Cm, whilst ^{266}Rf, ^{270}Sg, ^{274}Hs, ^{278}Ds and ^{288}Mc all have lower excitation energies from this reaction than from ^{40}Ca+^{250}Cm, making this reaction firmly preferable to ^{40}Ca+^{250}Cm for the production of colder ^{270}Sg and ^{278}Ds.

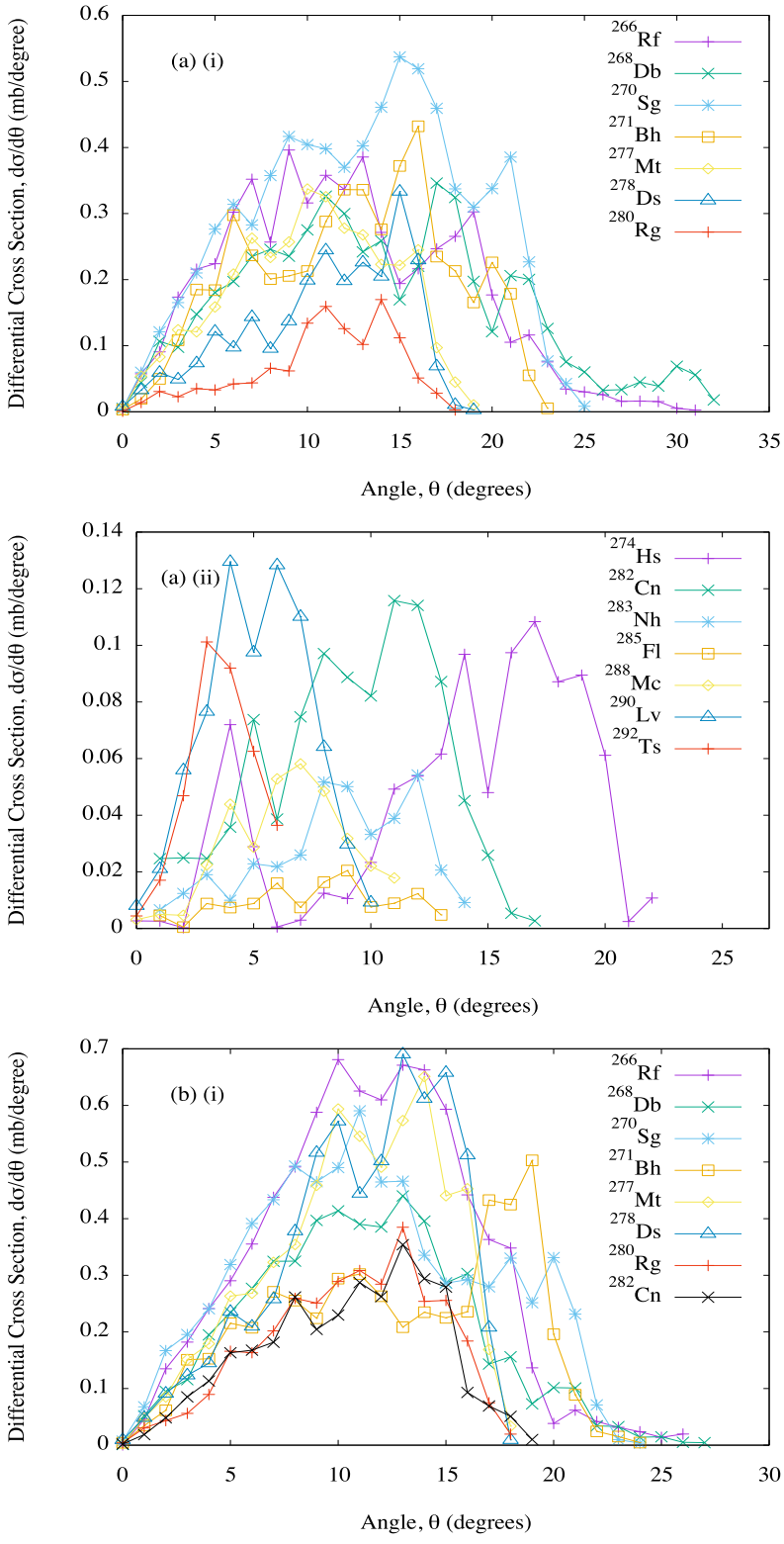

Figure 6.10: The same results as in Fig. 6.7, but for the reaction ^{40}Ca+^{254}Cf, with: (a) $E_{0_{c.m.}}/V_{CB} = 1.00$, (b) $E_{0_{c.m.}}/V_{CB} = 1.05$, and (c) $E_{0_{c.m.}}/V_{CB} = 1.10$. Subfigures are further separated into parts (i) and (ii) to enhance readability.

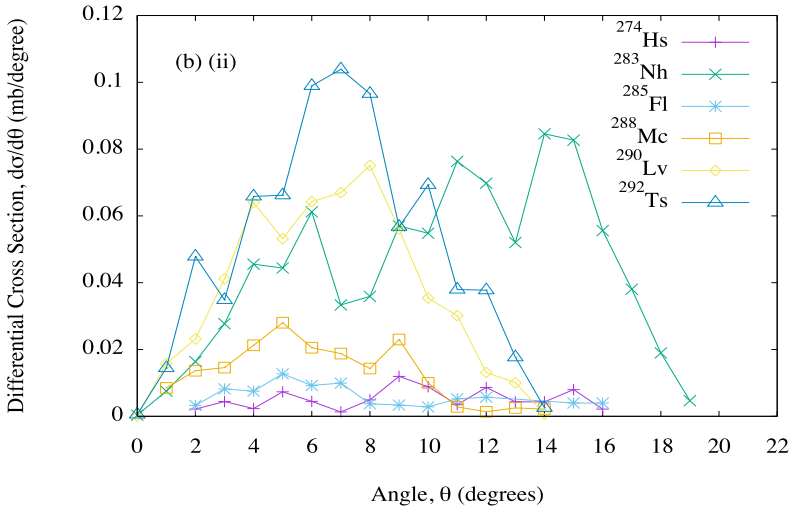

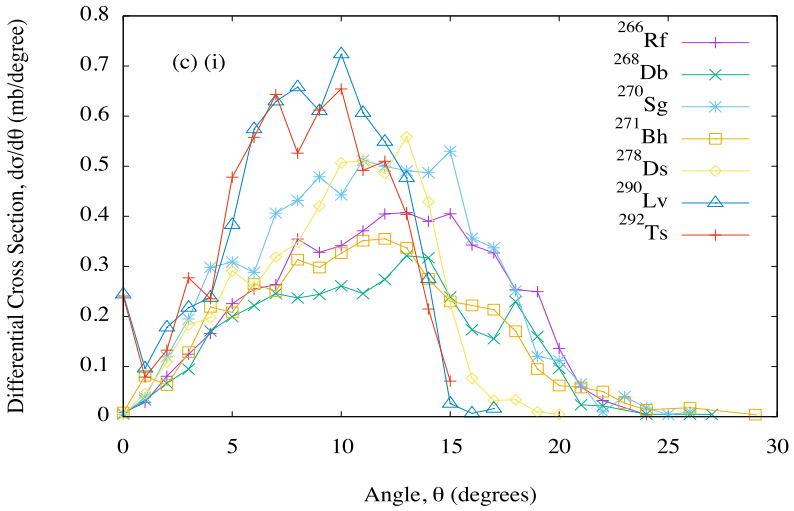

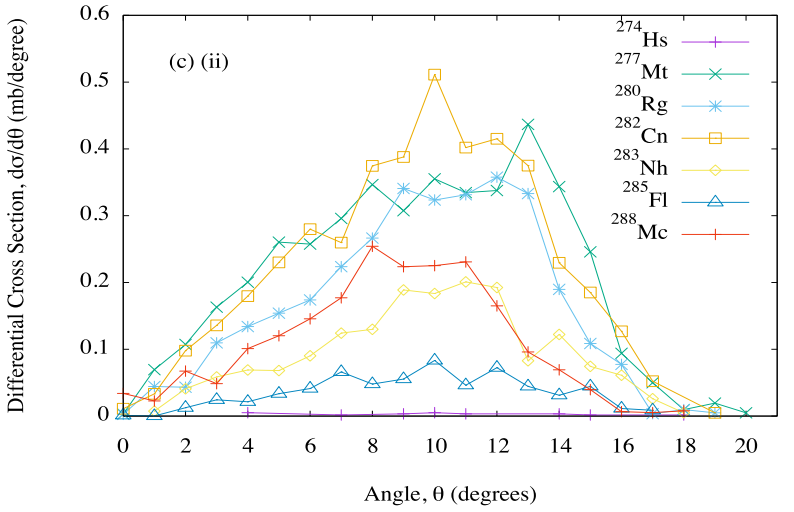

Continuation of Fig. 6.10.

Table 6.10: The same results as in Table 6.7, but for the reaction ^{40}Ca+^{254}Cf.

ICF product	Total cross section (mb)	Mean angle (degrees)	Mean exc. energy (MeV)	Mean angular momentum ($\hbar$)
$E_{0_{c.m.}}/V_{CB}$=1.00				
$^{266}_{104}$Rf	5.584	12.09 ± 5.86	37.54 ± 13.04	17.85 ± 9.56
$^{268}_{105}$Db	5.238	13.96 ± 6.87	44.13 ± 13.77	17.73 ± 9.84
$^{270}_{106}$Sg	7.485	12.96 ± 5.54	46.50 ± 13.33	17.17 ± 10.60
$^{271}_{107}$Bh	4.823	12.37 ± 5.15	74.82 ± 21.41	17.89 ± 11.35
$^{274}_{108}$Hs	0.9225	14.24 ± 4.72	50.96 ± 8.10	18.63 ± 8.26
$^{277}_{109}$Mt	3.556	10.11 ± 4.16	35.21 ± 22.78	26.13 ± 14.73
$^{278}_{110}$Ds	2.534	10.94 ± 4.15	62.19 ± 12.00	29.08 ± 13.84
$^{280}_{111}$Rg	1.235	10.87 ± 3.74	66.78 ± 11.48	31.14 ± 12.87
$^{282}_{112}$Cn	0.9614	9.09 ± 3.53	67.60 ± 7.98	37.29 ± 12.42
$^{283}_{113}$Nh	0.3765	8.57 ± 3.20	74.40 ± 22.88	35.92 ± 12.36
$^{285}_{114}$Fl	0.1239	7.69 ± 3.07	83.62 ± 22.75	33.18 ± 10.37
$^{288}_{115}$Mc	0.3389	6.54 ± 2.40	65.97 ± 2.96	32.31 ± 11.98
$^{290}_{116}$Lv	0.7299	5.18 ± 2.13	60.41 ± 2.26	28.01 ± 11.15
$^{292}_{117}$Ts	0.3605	3.64 ± 1.37	58.56 ± 1.25	19.66 ± 8.27
$E_{0_{c.m.}}/V_{CB}$=1.05				
$^{266}_{104}$Rf	8.130	11.42 ± 4.57	37.26 ± 6.10	19.81 ± 7.20
$^{268}_{105}$Db	5.312	11.18 ± 4.86	44.02 ± 6.20	20.79 ± 7.83
$^{270}_{106}$Sg	7.214	11.45 ± 5.25	47.27 ± 6.95	21.09 ± 8.15
$^{271}_{107}$Bh	5.030	12.61 ± 5.38	78.90 ± 18.96	20.02 ± 8.30
$^{274}_{108}$Hs	0.07861	9.51 ± 3.81	59.73 ± 4.56	22.08 ± 8.16
$^{277}_{109}$Mt	6.085	10.73 ± 3.88	31.30 ± 21.76	21.27 ± 9.43
$^{278}_{110}$Ds	6.221	11.09 ± 3.85	63.90 ± 7.19	20.90 ± 9.30

Continuation of Table 6.10.

ICF product	Total cross section (mb)	Mean angle (degrees)	Mean exc. energy (MeV)	Mean angular momentum ($\hbar$)
		$E_{0_{c.m.}}/V_{CB}$=1.05		
$^{280}_{111}$Rg	3.320	10.50 ± 3.79	67.13 ± 7.51	21.15 ± 9.23
$^{282}_{112}$Cn	3.176	10.43 ± 3.93	60.98 ± 7.55	21.63 ± 8.97
$^{283}_{113}$Nh	0.8670	10.64 ± 4.38	67.03 ± 23.47	20.98 ± 9.09
$^{285}_{114}$Fl	0.07971	7.37 ± 3.84	77.49 ± 19.81	19.90 ± 10.32
$^{288}_{115}$Mc	0.1815	6.01 ± 2.87	59.74 ± 2.78	18.50 ± 10.07
$^{290}_{116}$Lv	0.5491	6.65 ± 2.84	57.17 ± 2.56	19.72 ± 9.53
$^{292}_{117}$Ts	0.7512	6.98 ± 2.95	58.84 ± 2.06	19.03 ± 9.30
		$E_{0_{c.m.}}/V_{CB}$=1.10		
$^{266}_{104}$Rf	5.558	11.84 ± 4.81	43.82 ± 6.33	24.36 ± 8.10
$^{268}_{105}$Db	4.054	11.33 ± 4.94	49.88 ± 6.58	25.69 ± 8.92
$^{270}_{106}$Sg	6.856	11.22 ± 4.78	51.63 ± 6.97	26.48 ± 9.50
$^{271}_{107}$Bh	4.646	11.04 ± 5.08	82.65 ± 19.20	26.05 ± 9.59
$^{274}_{108}$Hs	0.02517	10.00 ± 4.02	68.27 ± 5.09	25.27 ± 9.24
$^{277}_{109}$Mt	4.242	9.54 ± 4.00	33.80 ± 22.26	25.95 ± 11.43
$^{278}_{110}$Ds	5.053	9.75 ± 3.75	66.37 ± 10.30	26.81 ± 11.28
$^{280}_{111}$Rg	3.232	9.57 ± 3.55	69.55 ± 10.47	26.45 ± 11.44
$^{282}_{112}$Cn	4.292	9.53 ± 3.67	62.33 ± 9.04	27.43 ± 11.43
$^{283}_{113}$Nh	1.726	9.73 ± 3.63	63.84 ± 24.07	27.78 ± 12.13
$^{285}_{114}$Fl	0.6459	9.55 ± 3.58	72.87 ± 23.78	25.70 ± 11.93
$^{288}_{115}$Mc	2.040	8.52 ± 3.44	62.45 ± 4.75	26.66 ± 11.84
$^{290}_{116}$Lv	6.507	8.28 ± 3.60	60.49 ± 4.14	27.59 ± 11.63
$^{292}_{117}$Ts	6.128	8.07 ± 3.59	64.20 ± 2.99	29.09 ± 11.31

6.2.5 ^{40}Ca+^{254}Es

Fig. 6.11 contains the angular distributions of primary SHE ICF products of the reaction ^{40}Ca+^{254}Es. At all studied incident energies, all differential cross-sections are found between 0-34 degrees. At $E_{0_{c.m.}}/V_{CB}$ = 1.00, ^{266}Db, ^{268}Sg, ^{270}Bh and ^{271}Hs have the highest differential cross-sections, located in the ∼9-17 degree region. At $E_{0_{c.m.}}/V_{CB}$ = 1.05, ^{266}Db, ^{277}Ds and ^{278}Rg have the highest differential cross-sections, located in the ∼8-14 degree region. At $E_{0_{c.m.}}/V_{CB}$ = 1.10, ^{290}Ts and ^{292}Og overtake the lighter SHE ICF products to have the highest differential cross-sections, located at 0 degrees, and elsewhere matching the peak height and shape of other SHE ICF products in the ∼5-15 degree region.

Table 6.11 contains the total cross-sections and the means of the angular, excitation energy and angular momentum distributions of those same ICF products. The total cross-sections of the ICF products follow a similar trend to the angular distributions in Fig. 6.11, in that ^{266}Db, ^{268}Sg, ^{270}Bh and ^{271}Hs have among the highest yields at all three incident energies, with ^{277}Ds and ^{278}Rg contending with them at 5% above the barrier and with ^{288}Lv and ^{290}Ts exceeding almost all of them at 10% above the barrier. The same general trends of the table are observed here as with the previous four reactions.

Comparing like ICF products from the reaction ^{40}Ca+^{248}Cm, ^{268}Sg and ^{282}Nh have larger total cross-sections and ^{274}Mt has a smaller total cross from this reaction. ^{268}Sg and ^{274}Mt have lower excitation energies and ^{282}Nh has higher excitation energies from this reaction. This suggests that the reaction ^{40}Ca+^{254}Es is preferable to the reaction ^{40}Ca+^{248}Cm for the production of colder ^{268}Sg.

Comparing like ICF products from the reaction ^{40}Ca+^{252}Cf, ^{280}Cn and ^{288}Lv have smaller total cross-sections, and ^{266}Db, ^{278}Rg, ^{283}Fl and ^{290}Ts have larger total cross-sections from this reaction, whilst ^{266}Db, ^{278}Rg, ^{283}Fl, ^{290}Ts have lower excitation energies and ^{280}Cn and ^{288}Lv have higher excitation energies from this reaction. This suggests that the reaction ^{40}Ca+^{254}Es is preferable to the reaction ^{40}Ca+^{252}Cf for the production of colder ^{266}Db, ^{278}Rg, ^{283}Fl and ^{290}Ts, whilst the inverse is true for the production of colder ^{280}Cn and ^{288}Lv.

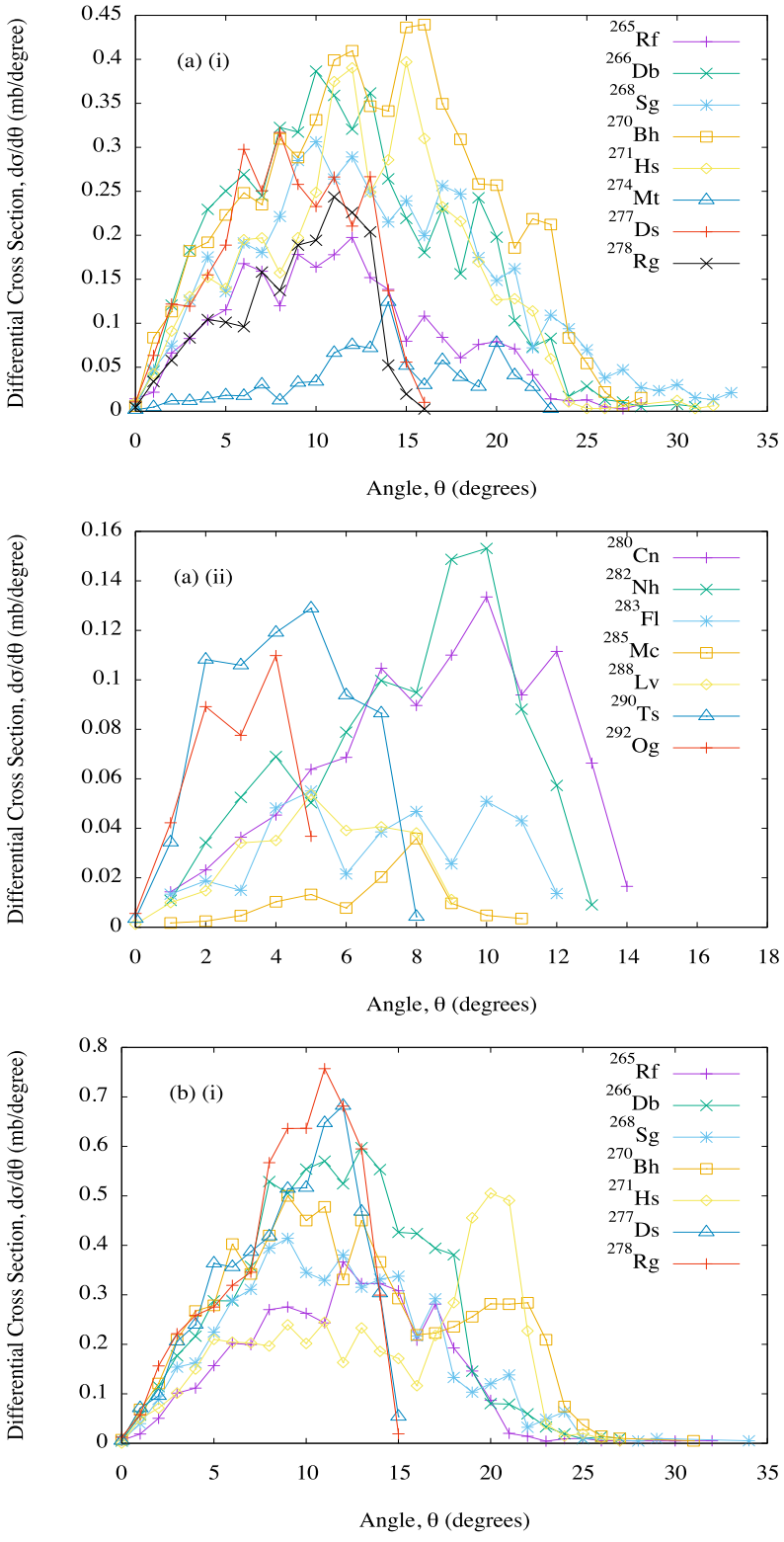

Figure 6.11: The same results as in Fig. 6.7, but for the reaction ^{40}Ca+^{254}Es, with: (a) $E_{0_{c.m.}}/V_{CB} = 1.00$, (b) $E_{0_{c.m.}}/V_{CB} = 1.05$, and (c) $E_{0_{c.m.}}/V_{CB} = 1.10$. Subfigures are further separated into parts (i) and (ii) to enhance readability.

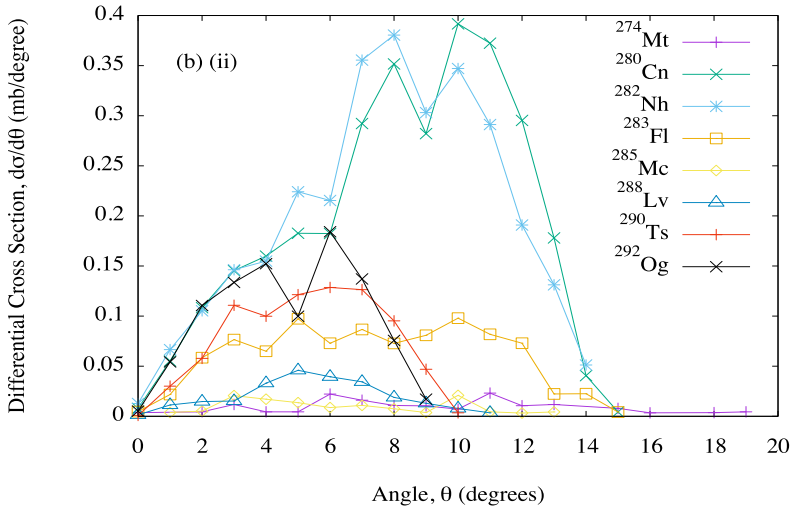

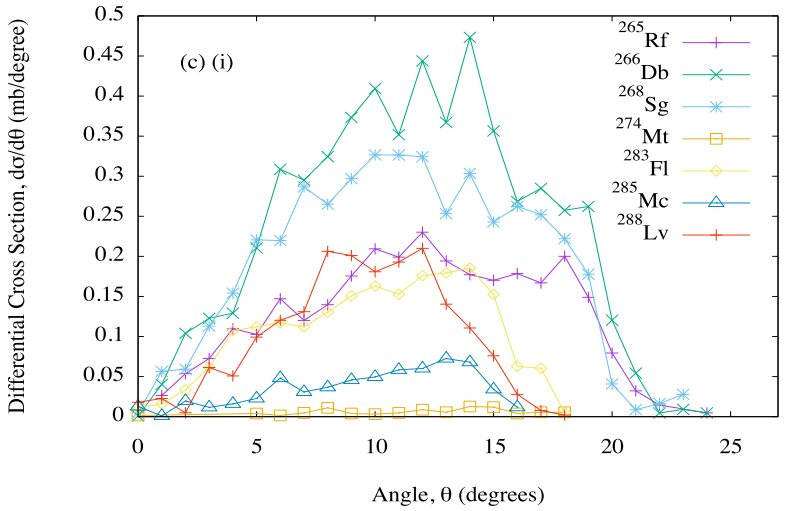

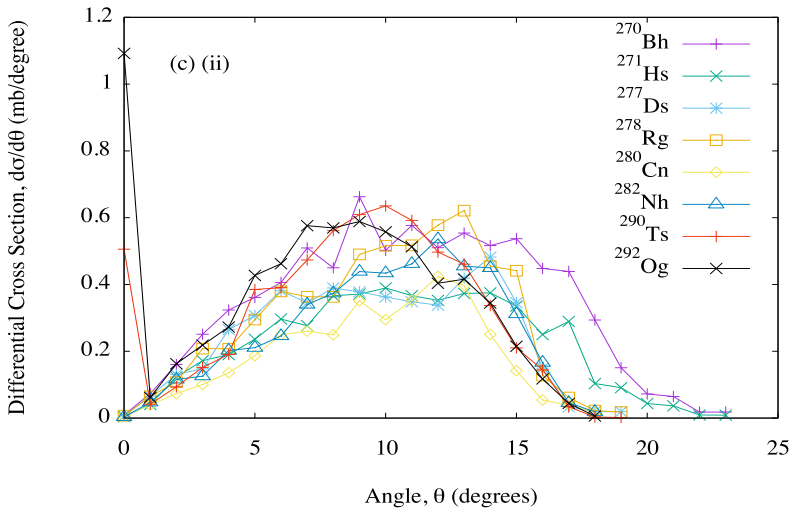

Continuation of Fig. 6.11.

Table 6.11: The same results as in Table 6.7, but for the reaction ^{40}Ca+^{254}Es.

ICF product	Total cross section (mb)	Mean angle (degrees)	Mean exc. energy (MeV)	Mean angular momentum ($\hbar$)
$E_{0_{c.m.}}/V_{CB}$=1.00				
$^{265}_{104}$Rf	2.512	11.21 ± 5.58	35.73 ± 23.32	18.57 ± 9.40
$^{266}_{105}$Db	5.254	11.66 ± 5.71	43.80 ± 13.46	17.90 ± 9.68
$^{268}_{106}$Sg	4.754	13.45 ± 6.67	53.17 ± 12.80	17.50 ± 9.92
$^{270}_{107}$Bh	6.556	13.13 ± 5.94	50.05 ± 14.21	17.77 ± 10.86
$^{271}_{108}$Hs	4.653	12.50 ± 5.46	77.88 ± 22.94	17.20 ± 10.56
$^{274}_{109}$Mt	0.8832	13.74 ± 4.92	53.95 ± 5.77	19.25 ± 7.72
$^{277}_{110}$Ds	2.961	8.37 ± 3.60	35.92 ± 23.17	26.72 ± 14.95
$^{278}_{111}$Rg	1.907	8.84 ± 3.45	65.57 ± 12.43	29.42 ± 14.35
$^{280}_{112}$Cn	0.9777	8.51 ± 3.10	74.03 ± 10.73	33.39 ± 13.87
$^{282}_{113}$Nh	0.9466	7.75 ± 2.85	69.94 ± 6.43	36.19 ± 13.25
$^{283}_{114}$Fl	0.3904	6.95 ± 2.99	73.10 ± 25.48	34.18 ± 14.59
$^{285}_{115}$Mc	0.1145	6.80 ± 2.14	80.82 ± 22.95	30.07 ± 15.13
$^{288}_{116}$Lv	0.2778	5.31 ± 2.07	69.74 ± 3.36	31.11 ± 12.92
$^{290}_{117}$Ts	0.6845	4.22 ± 1.80	61.46 ± 2.43	25.11 ± 10.70
$^{292}_{118}$Og	0.3612	2.98 ± 1.25	61.38 ± 1.29	18.89 ± 8.52
$E_{0_{c.m.}}/V_{CB}$=1.05				
$^{265}_{104}$Rf	4.211	11.85 ± 4.83	35.42 ± 20.16	20.47 ± 7.33
$^{266}_{105}$Db	7.411	11.59 ± 4.79	41.29 ± 6.82	20.21 ± 7.39
$^{268}_{106}$Sg	5.301	11.50 ± 5.28	53.17 ± 7.12	20.71 ± 8.15
$^{270}_{107}$Bh	7.115	12.32 ± 6.02	51.49 ± 7.19	21.22 ± 8.46
$^{271}_{108}$Hs	5.011	14.02 ± 6.16	84.22 ± 19.78	19.48 ± 8.08
$^{274}_{109}$Mt	0.1604	8.98 ± 4.31	66.27 ± 5.15	23.50 ± 8.88
$^{277}_{110}$Ds	5.329	9.02 ± 3.36	33.23 ± 22.40	21.81 ± 9.49
$^{278}_{111}$Rg	5.838	9.10 ± 3.30	65.97 ± 8.35	21.51 ± 9.01

Continuation of Table 6.11.

ICF product	Total cross section (mb)	Mean angle (degrees)	Mean exc. energy (MeV)	Mean angular momentum ($\hbar$)
		$E_{0_{c.m.}}/V_{CB}$=1.05		
$^{280}_{112}$Cn	3.050	8.28 ± 3.23	71.97 ± 7.21	21.53 ± 9.69
$^{282}_{113}$Nh	2.976	7.86 ± 3.16	63.66 ± 7.40	21.66 ± 9.45
$^{283}_{114}$Fl	0.9389	7.34 ± 3.46	68.78 ± 24.45	21.17 ± 9.43
$^{285}_{115}$Mc	0.1240	6.35 ± 3.21	73.79 ± 26.99	20.10 ± 11.19
$^{288}_{116}$Lv	0.2387	5.49 ± 2.30	64.03 ± 2.57	23.84 ± 9.75
$^{290}_{117}$Ts	0.8215	5.31 ± 2.16	58.85 ± 2.78	23.60 ± 10.26
$^{292}_{118}$Og	0.9700	4.75 ± 2.11	62.73 ± 2.56	22.62 ± 10.14
		$E_{0_{c.m.}}/V_{CB}$=1.10		
$^{265}_{104}$Rf	2.953	11.90 ± 4.99	42.17 ± 19.00	23.75 ± 7.50
$^{266}_{105}$Db	5.577	11.62 ± 4.74	47.98 ± 6.04	24.04 ± 8.02
$^{268}_{106}$Sg	4.462	11.24 ± 4.82	58.54 ± 5.93	25.32 ± 8.88
$^{270}_{107}$Bh	7.908	10.90 ± 4.72	55.13 ± 5.74	25.33 ± 9.46
$^{271}_{108}$Hs	5.101	10.70 ± 4.59	86.55 ± 19.54	24.88 ± 9.44
$^{274}_{109}$Mt	0.08882	11.96 ± 3.96	67.87 ± 9.11	25.26 ± 9.90
$^{277}_{110}$Ds	4.933	9.56 ± 4.04	35.20 ± 23.42	26.21 ± 11.32
$^{278}_{111}$Rg	5.843	9.93 ± 3.85	68.02 ± 11.42	26.88 ± 11.75
$^{280}_{112}$Cn	3.624	9.66 ± 3.65	74.47 ± 11.23	27.06 ± 11.59
$^{282}_{113}$Nh	4.981	10.00 ± 3.76	64.93 ± 10.35	27.38 ± 12.25
$^{283}_{114}$Fl	1.989	10.01 ± 4.05	66.37 ± 25.42	28.36 ± 12.42
$^{285}_{115}$Mc	0.6001	9.87 ± 3.85	75.19 ± 25.40	26.77 ± 13.16
$^{288}_{116}$Lv	1.864	9.44 ± 3.46	65.58 ± 5.19	27.61 ± 12.37
$^{290}_{117}$Ts	6.317	8.65 ± 4.18	61.01 ± 4.34	27.63 ± 12.18
$^{292}_{118}$Og	7.048	7.55 ± 4.65	66.89 ± 3.35	28.70 ± 11.46

6.2.6 ^{40}Ca+^{256}Es

Fig. 6.12 contains the angular distributions of primary SHE ICF products of the reaction ^{40}Ca+^{256}Es. At all studied incident energies, all differential cross-sections are found between 0-30 degrees. At $E_{0_{c.m.}}/V_{CB} = 1.00$, ^{268}Db, ^{270}Sg, ^{272}Bh and ^{273}Hs have the highest differential cross-sections, located in the ∼5-13 degree region. At $E_{0_{c.m.}}/V_{CB} = 1.05$, ^{268}Db, ^{279}Ds and ^{280}Rg have the highest differential cross-sections, located in the ∼6-12 degree region. At $E_{0_{c.m.}}/V_{CB} = 1.10$, ^{292}Ts and ^{294}Og overtake the lighter SHE ICF products to have the highest differential cross-sections in the ∼4-11 degree region.

Table 6.12 contains the total cross-sections and the means of the angular, excitation energy and angular momentum distributions of those same ICF products. The total cross-sections of the ICF products follow a similar trend to the angular distributions in Fig. 6.12, in that ^{268}Db, ^{270}Sg, ^{272}Bh and ^{273}Hs have among the highest yields at all three incident energies, with ^{279}Ds and ^{280}Rg contending with them at 5% above the barrier and with ^{292}Ts and ^{294}Og exceeding almost all of them at 10% above the barrier. The same general trends of the table are observed here as with the previous five reactions.

Comparing like ICF products from the reaction ^{40}Ca+^{250}Cm, ^{270}Sg and ^{284}Nh have larger total cross-sections and ^{276}Mt has a smaller total cross from this reaction. ^{270}Sg and ^{276}Mt have lower excitation energies and ^{284}Nh has higher excitation energies from this reaction. This suggests that the reaction ^{40}Ca+^{256}Es is preferable to the reaction ^{40}Ca+^{250}Cm for the production of colder ^{270}Sg.

Comparing like ICF products from the reaction ^{40}Ca+^{254}Cf, ^{282}Cn and ^{290}Lv have smaller total cross-sections, and ^{268}Db, ^{280}Rg, ^{285}Fl and ^{292}Ts have larger total cross-sections from this reaction, whilst ^{268}Db and ^{285}Fl have lower excitation energies and ^{280}Rg, ^{282}Cn, ^{290}Lv and ^{292}Ts have higher excitation energies from this reaction. This suggests that the reaction ^{40}Ca+^{256}Es is preferable to the reaction ^{40}Ca+^{254}Cf for the production of colder ^{268}Db and ^{285}Fl, whilst the inverse is true for the production of colder ^{282}Cn and ^{290}Lv.

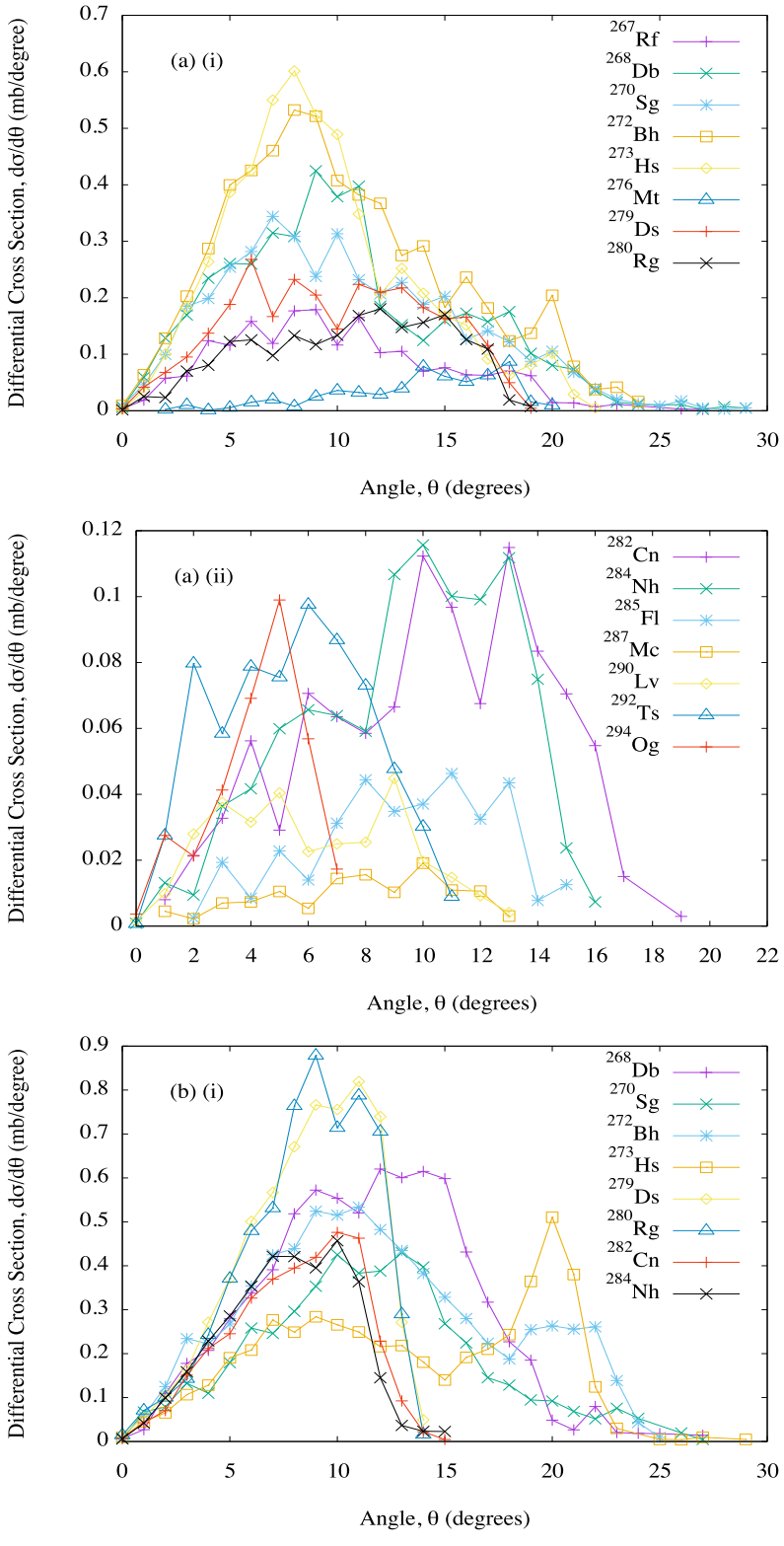

Figure 6.12: The same results as in Fig. 6.7, but for the reaction ^{40}Ca+^{256}Es, with: (a) $E_{0_{c.m.}}/V_{CB} = 1.00$, (b) $E_{0_{c.m.}}/V_{CB} = 1.05$, and (c) $E_{0_{c.m.}}/V_{CB} = 1.10$. Subfigures are further separated into parts (i) and (ii) to enhance readability.

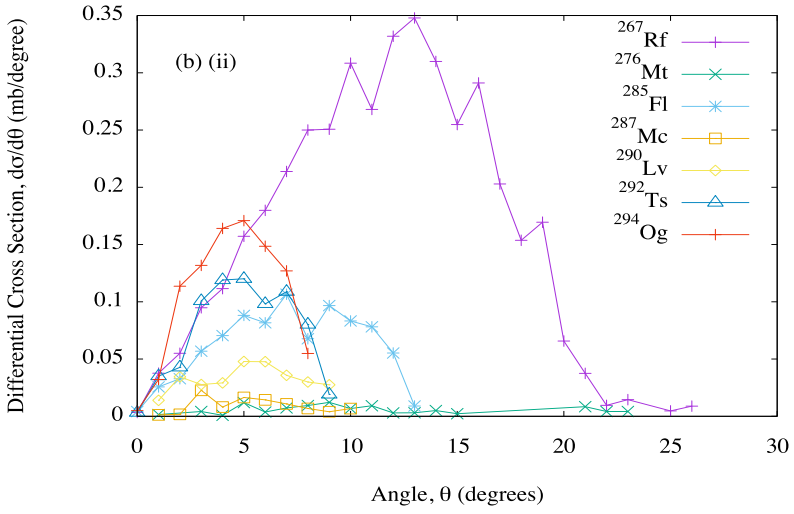

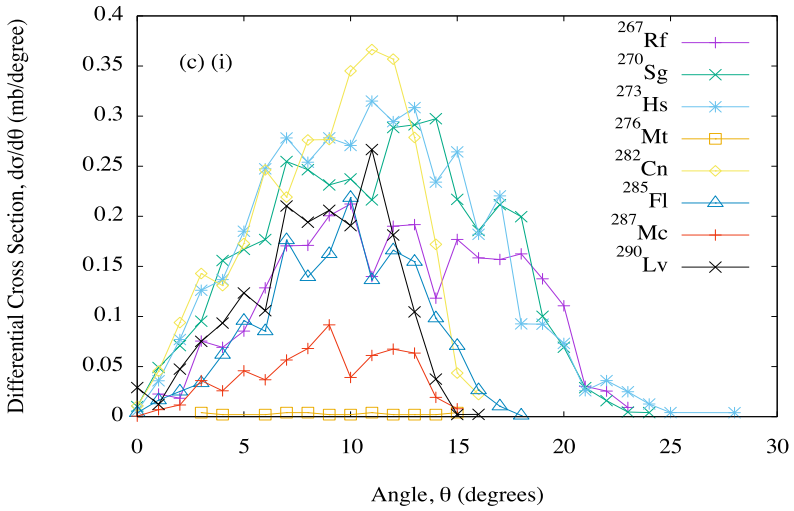

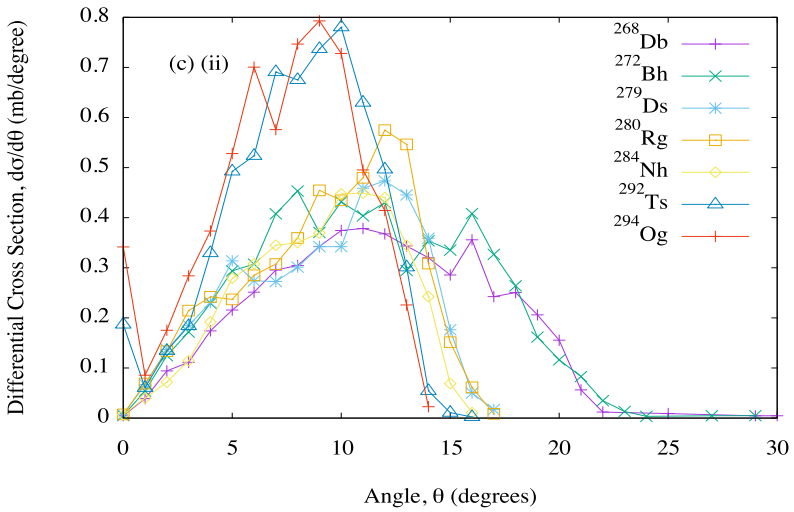

Continuation of Fig. 6.12.

Table 6.12: The same results as in Table 6.7, but for the reaction ^{40}Ca+^{256}Es.

ICF product	Total cross section (mb)	Mean angle (degrees)	Mean exc. energy (MeV)	Mean angular momentum ($\hbar$)
$E_{0_{c.m.}}/V_{CB}$=1.00				
$^{267}_{104}$Rf	1.960	9.98 ± 4.91	36.12 ± 23.11	18.30 ± 9.11
$^{268}_{105}$Db	4.412	10.29 ± 5.25	43.75 ± 13.60	17.86 ± 9.62
$^{270}_{106}$Sg	4.095	10.46 ± 5.41	55.52 ± 12.48	18.07 ± 9.96
$^{272}_{107}$Bh	5.994	10.26 ± 5.06	52.97 ± 13.31	18.78 ± 11.19
$^{273}_{108}$Hs	5.265	9.31 ± 4.26	82.19 ± 22.33	16.78 ± 10.44
$^{276}_{109}$Mt	0.5882	13.78 ± 3.88	55.25 ± 8.84	19.28 ± 8.84
$^{279}_{110}$Ds	2.882	9.81 ± 4.34	40.58 ± 24.27	28.34 ± 15.82
$^{280}_{111}$Rg	2.014	10.49 ± 4.27	69.82 ± 11.82	30.54 ± 15.69
$^{282}_{112}$Cn	1.025	10.11 ± 3.93	80.32 ± 9.70	35.31 ± 14.07
$^{284}_{113}$Nh	0.9895	9.40 ± 3.44	74.81 ± 6.62	37.21 ± 12.73
$^{285}_{114}$Fl	0.3573	9.28 ± 3.14	77.25 ± 22.88	32.99 ± 12.03
$^{287}_{115}$Mc	0.1211	7.78 ± 3.08	77.14 ± 24.75	31.30 ± 12.04
$^{290}_{116}$Lv	0.3145	6.19 ± 3.08	74.04 ± 3.46	30.36 ± 13.13
$^{292}_{117}$Ts	0.6648	5.51 ± 2.53	64.57 ± 2.65	26.41 ± 10.81
$^{294}_{118}$Og	0.3360	4.25 ± 1.63	64.44 ± 1.33	19.52 ± 7.39
$E_{0_{c.m.}}/V_{CB}$=1.05				
$^{267}_{104}$Rf	4.133	11.68 ± 4.72	34.74 ± 19.50	20.43 ± 7.09
$^{268}_{105}$Db	7.521	11.45 ± 4.57	40.56 ± 6.36	20.25 ± 7.35
$^{270}_{106}$Sg	4.977	11.51 ± 5.05	53.64 ± 6.74	20.53 ± 7.99
$^{272}_{107}$Bh	7.254	11.94 ± 5.60	52.21 ± 6.88	20.82 ± 8.43
$^{273}_{108}$Hs	4.910	13.30 ± 5.97	86.71 ± 20.31	19.56 ± 8.19
$^{276}_{109}$Mt	0.09734	10.79 ± 5.81	65.14 ± 5.62	24.96 ± 7.17
$^{279}_{110}$Ds	6.120	8.59 ± 2.89	35.97 ± 23.30	21.25 ± 9.55
$^{280}_{111}$Rg	6.108	8.58 ± 2.84	68.60 ± 7.89	20.99 ± 9.15

Continuation of Table 6.12.

ICF product	Total cross section (mb)	Mean angle (degrees)	Mean exc. energy (MeV)	Mean angular momentum ($\hbar$)
$E_{0_{c.m.}}/V_{CB}$=1.05				
$^{282}_{112}$Cn	3.525	8.05 ± 2.90	75.41 ± 7.84	21.07 ± 9.32
$^{284}_{113}$Nh	3.460	7.66 ± 2.86	67.34 ± 8.55	22.19 ± 9.51
$^{285}_{114}$Fl	0.8564	7.13 ± 3.07	71.21 ± 24.17	21.90 ± 9.24
$^{287}_{115}$Mc	0.09284	5.46 ± 2.24	72.64 ± 25.44	22.39 ± 8.81
$^{290}_{116}$Lv	0.2940	5.26 ± 2.30	67.90 ± 2.62	22.93 ± 9.90
$^{292}_{117}$Ts	0.7270	5.04 ± 2.07	62.12 ± 2.93	21.39 ± 10.08
$^{294}_{118}$Og	0.9479	4.63 ± 1.89	65.68 ± 2.42	20.88 ± 10.31
$E_{0_{c.m.}}/V_{CB}$=1.10				
$^{267}_{104}$Rf	2.762	12.03 ± 4.97	43.72 ± 19.82	25.12 ± 8.28
$^{268}_{105}$Db	5.199	11.59 ± 4.92	47.64 ± 6.94	24.81 ± 8.27
$^{270}_{106}$Sg	3.826	11.21 ± 4.88	59.67 ± 7.26	25.31 ± 9.24
$^{272}_{107}$Bh	6.087	11.17 ± 4.99	56.25 ± 7.25	25.88 ± 9.89
$^{273}_{108}$Hs	4.080	11.01 ± 4.89	89.18 ± 19.77	25.66 ± 9.56
$^{276}_{109}$Mt	0.03444	9.18 ± 3.81	73.24 ± 4.67	27.59 ± 8.68
$^{279}_{110}$Ds	4.452	9.24 ± 3.82	37.58 ± 23.99	25.43 ± 11.42
$^{280}_{111}$Rg	4.875	9.29 ± 3.67	71.02 ± 10.25	25.99 ± 11.69
$^{282}_{112}$Cn	3.199	8.93 ± 3.51	77.68 ± 10.19	26.90 ± 11.81
$^{284}_{113}$Nh	4.079	9.03 ± 3.33	69.14 ± 9.29	26.86 ± 11.92
$^{285}_{114}$Fl	1.683	9.49 ± 3.44	69.51 ± 24.08	26.83 ± 12.26
$^{287}_{115}$Mc	0.6382	8.69 ± 3.30	78.97 ± 24.12	27.79 ± 11.81
$^{290}_{116}$Lv	1.882	8.40 ± 3.22	70.24 ± 5.08	26.58 ± 12.11
$^{292}_{117}$Ts	6.288	7.99 ± 3.20	65.26 ± 4.18	27.66 ± 11.96
$^{294}_{118}$Og	6.489	7.35 ± 3.33	70.66 ± 3.17	28.93 ± 11.56

6.3 ^{48}Ca-induced incomplete fusion reactions

Total integrated cross-sections, angular, excitation energy and angular momentum distributions and their associated standard deviations were calculated for the primary ICF products of ^{48}Ca-induced incomplete fusion reactions with chains of Cm, Cf and Es targets at varying incident energies. The same targets were chosen here as with the ^{20}Ne- and ^{40}Ca- induced reactions: ^{248}Cm (Table 6.13), ^{250}Cm (Table 6.14), ^{252}Cf (Table 6.15), ^{254}Cf (Table 6.16), ^{254}Es (Table 6.17) and ^{256}Es (Table 6.18). The maximal orbital angular momentum between projectile and target considered here is $L_{TP} = 50\hbar$, with 1000 sampled fragmentations per orbital angular momentum. Results have been shown only for SHE primary ICF products. Also presented are the angular distributions of all tabulated primary ICF products (Figs. 6.13-6.18).

6.3.1 ^{48}Ca+^{248}Cm

Fig. 6.13 contains the angular distributions of primary SHE ICF products of the reaction ^{40}Ca+^{248}Cm. At all studied incident energies, all differential cross-sections are found between 0-27 degrees. The further above the Coulomb barrier the incident energy is, the more dominant the heaviest SHE ICF products, ^{292}Fl and ^{294}Mc, are, maintaining the highest cross-sections at all three incident energies, with peaks in the ∼1-4 degree region.

Table 6.13 contains the total cross-sections and the means of the angular, excitation energy and angular momentum distributions of those same ICF products. The total cross-sections of the ICF products follow a similar trend to the angular distributions in Fig. 6.13, in that ^{292}Fl and ^{294}Mc have the highest yields at all three incident energies, save for ^{294}Mc at the Coulomb barrier. Similar general trends of the table are observed here as with the ^{20}Ne- and ^{40}Ca-induced reactions, namely that the heavier the ICF product the more forward the angle and the higher the angular momentum, and the lower the total cross-section with exceptions for the heaviest two ICF products at higher energies. As was the case for the ^{20}Ne- and ^{40}Ca-induced reactions, the two heaviest ICF products have the highest cross-sections. The one common factor in all these reactions

is the transfer of the remaining fragments ^{2}H and ^{4}He, indicating that there may be a connection between them and the relatively higher ICF product cross-sections that result from the fusion of their respective heavier fragment counterparts and targets.

Comparing like ICF products from ^{40}Ca-induced reactions, ^{273}Bh has much smaller total cross-sections and much lower excitation energies at all studied incident energies here than from the reaction ^{40}Ca+^{250}Cm.

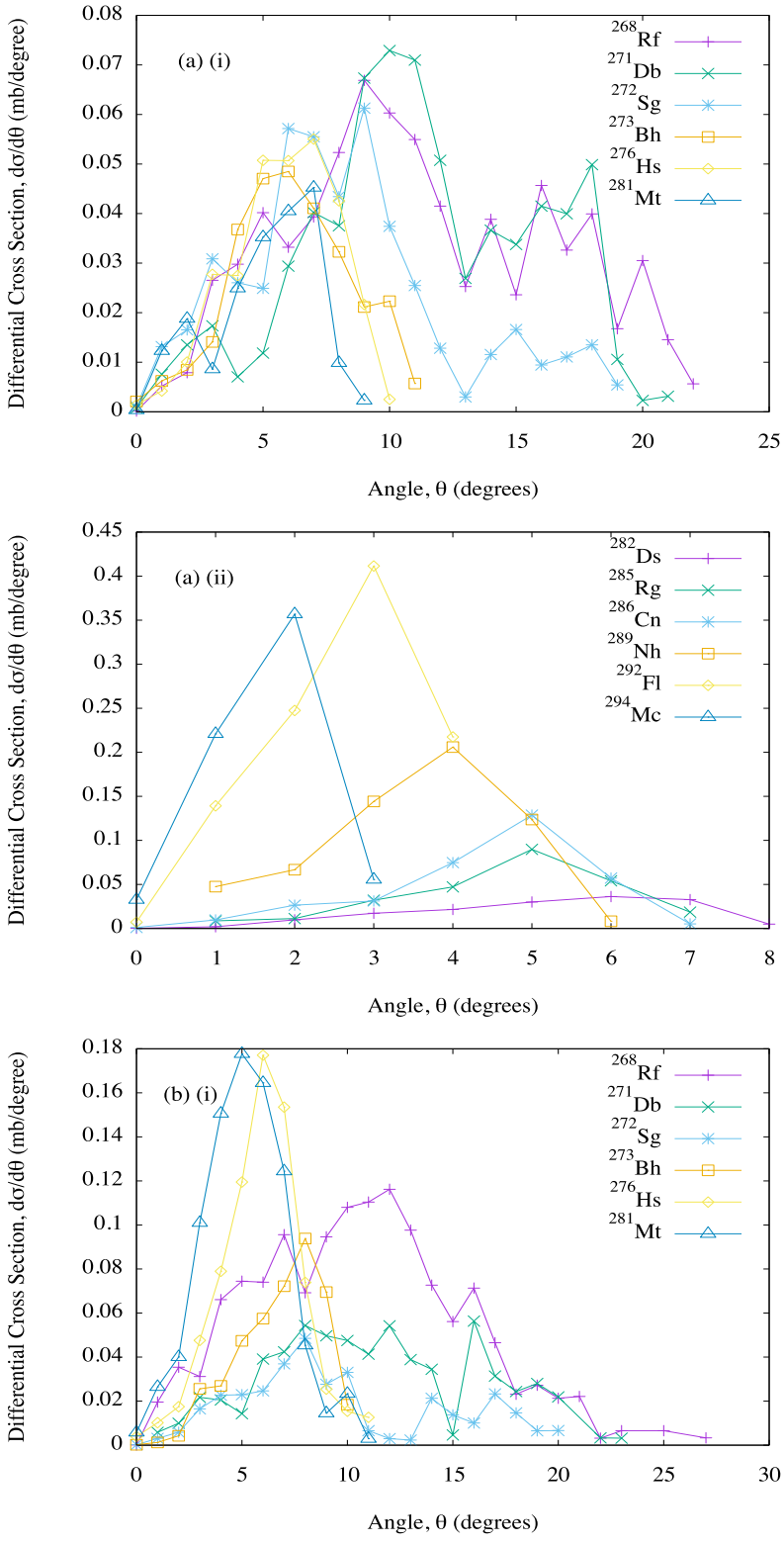

Figure 6.13: The same results as in Fig. 6.7, but for the reaction ^{48}Ca+^{248}Cm, with: (a) $E_{0_{c.m.}}/V_{CB} = 1.00$, (b) $E_{0_{c.m.}}/V_{CB} = 1.05$, and (c) $E_{0_{c.m.}}/V_{CB} = 1.10$. Subfigures are further separated into parts (i) and (ii) to enhance readability.

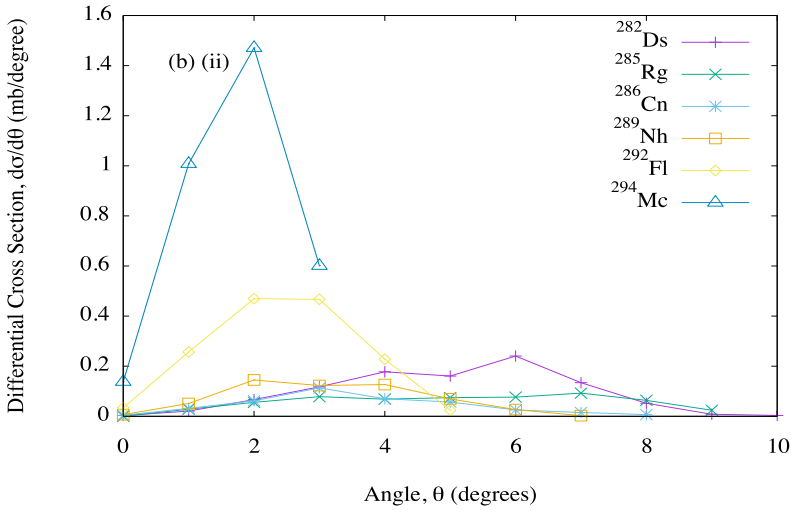

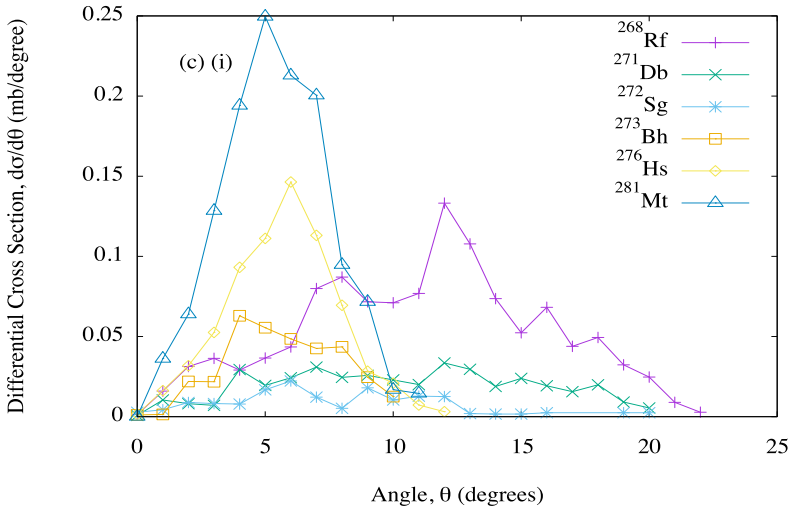

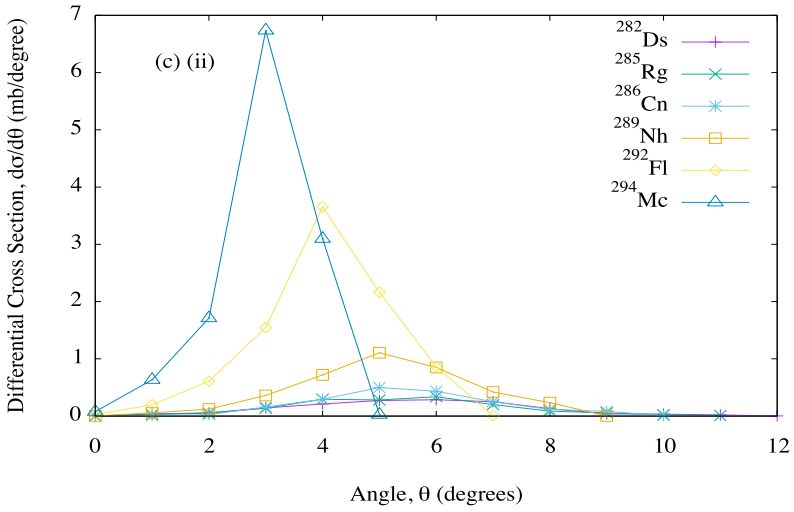

Continuation of Fig. 6.13.

Table 6.13: The same results as in Table 6.7, but for the reaction ^{48}Ca+^{248}Cm.

ICF product	Total cross section (mb)	Mean angle (degrees)	Mean exc. energy (MeV)	Mean angular momentum ($\hbar$)
$E_{0_{c.m.}}/V_{CB}$=1.00				
$^{268}_{104}$Rf	0.7316	11.22 ± 5.07	65.69 ± 13.26	22.47 ± 11.69
$^{271}_{105}$Db	0.6719	11.28 ± 4.39	104.07 ± 20.53	23.59 ± 13.47
$^{272}_{106}$Sg	0.4763	8.28 ± 4.21	55.27 ± 22.06	22.41 ± 13.10
$^{273}_{107}$Bh	0.2857	6.16 ± 2.32	10.43 ± 16.12	21.68 ± 13.17
$^{276}_{108}$Hs	0.2941	5.85 ± 2.00	37.30 ± 8.27	28.20 ± 14.76
$^{281}_{109}$Mt	0.1981	5.10 ± 1.98	30.01 ± 25.08	35.10 ± 15.36
$^{282}_{110}$Ds	0.1548	5.15 ± 1.65	31.77 ± 5.29	38.06 ± 13.09
$^{285}_{111}$Rg	0.2617	4.66 ± 1.40	42.36 ± 27.35	36.74 ± 13.25
$^{286}_{112}$Cn	0.3344	4.42 ± 1.33	22.11 ± 3.75	33.86 ± 12.49
$^{289}_{113}$Nh	0.5962	3.53 ± 1.20	50.52 ± 24.28	31.98 ± 12.56
$^{292}_{114}$Fl	1.023	2.68 ± 0.98	55.87 ± 24.65	27.10 ± 11.96
$^{294}_{115}$Mc	0.6659	1.65 ± 0.70	64.06 ± 25.83	19.20 ± 9.08
$E_{0_{c.m.}}/V_{CB}$=1.05				
$^{268}_{104}$Rf	1.353	10.64 ± 4.93	61.88 ± 8.17	26.43 ± 9.01
$^{271}_{105}$Db	0.6474	11.25 ± 4.88	101.07 ± 18.75	24.82 ± 10.18
$^{272}_{106}$Sg	0.3502	9.61 ± 4.81	55.92 ± 22.38	21.52 ± 9.85
$^{273}_{107}$Bh	0.4170	6.81 ± 1.95	12.59 ± 16.81	23.57 ± 10.12
$^{276}_{108}$Hs	0.7357	5.92 ± 1.94	41.43 ± 6.31	23.98 ± 10.05
$^{281}_{109}$Mt	0.8765	5.15 ± 1.98	20.80 ± 19.78	24.66 ± 11.05
$^{282}_{110}$Ds	0.9848	5.00 ± 1.78	27.02 ± 7.78	24.62 ± 10.87
$^{285}_{111}$Rg	0.5624	5.08 ± 2.21	25.67 ± 20.93	24.35 ± 11.36
$^{286}_{112}$Cn	0.3853	3.56 ± 1.64	15.18 ± 4.40	22.37 ± 9.66
$^{289}_{113}$Nh	0.5513	3.16 ± 1.40	41.09 ± 22.31	22.63 ± 11.14
$^{292}_{114}$Fl	1.479	2.45 ± 1.07	49.80 ± 21.69	19.77 ± 10.60
$^{294}_{115}$Mc	3.218	1.79 ± 0.79	57.68 ± 20.60	19.08 ± 9.85

Continuation of Table 6.13.

ICF product	Total cross section (mb)	Mean angle (degrees)	Mean exc. energy (MeV)	Mean angular momentum ($\hbar$)
$E_{0_{c.m.}}/V_{CB}$=1.10				
$^{268}_{104}$Rf	1.178	11.13 ± 4.69	67.11 ± 8.25	30.69 ± 10.34
$^{271}_{105}$Db	0.3990	10.34 ± 4.86	103.12 ± 18.45	29.63 ± 11.63
$^{272}_{106}$Sg	0.1549	7.68 ± 4.14	55.55 ± 22.20	28.33 ± 9.64
$^{273}_{107}$Bh	0.3367	5.72 ± 2.14	8.77 ± 14.96	29.49 ± 11.54
$^{276}_{108}$Hs	0.6952	5.72 ± 2.13	42.68 ± 12.56	29.27 ± 11.37
$^{281}_{109}$Mt	1.284	5.44 ± 2.08	20.29 ± 19.30	30.91 ± 12.70
$^{282}_{110}$Ds	1.484	5.56 ± 2.06	27.52 ± 11.06	30.57 ± 12.67
$^{285}_{111}$Rg	1.508	5.36 ± 1.89	26.36 ± 20.75	30.73 ± 13.17
$^{286}_{112}$Cn	1.874	5.50 ± 1.60	15.89 ± 4.96	29.83 ± 13.54
$^{289}_{113}$Nh	3.875	5.09 ± 1.52	44.31 ± 21.02	29.77 ± 13.02
$^{292}_{114}$Fl	9.065	4.05 ± 1.14	53.88 ± 20.36	28.34 ± 12.38
$^{294}_{115}$Mc	12.28	2.99 ± 0.81	64.50 ± 19.78	28.61 ± 11.47

6.3.2 ^{48}Ca+^{250}Cm

Fig. 6.14 contains the angular distributions of primary SHE ICF products of the reaction ^{48}Ca+^{250}Cm. At all studied incident energies, all differential cross-sections are found between 0-25 degrees. The further above the Coulomb barrier the incident energy is, the more dominant the heaviest SHE ICF products, ^{294}Fl and ^{296}Mc, are, maintaining the highest cross-sections at all three incident energies, with peaks in the ∼1-4 degree region at the Coulomb barrier and in the ∼2-7 degree region above the barrier.

Table 6.14 contains the total cross-sections and the means of the angular, excitation energy and angular momentum distributions of those same ICF products. The total cross-sections of the ICF products follow a similar trend to the angular distributions in Fig. 6.14, in that ^{294}Fl and ^{296}Mc have the highest yields at all three incident energies, save for ^{296}Mc at the Coulomb barrier and ^{294}Fl at 5% above the barrier. Similar general trends of the table are observed here as with the previous reaction, namely that the heavier the ICF product the more forward the angle and the higher the angular momentum, and the lower the total cross-section with exceptions for the three heaviest ICF products.

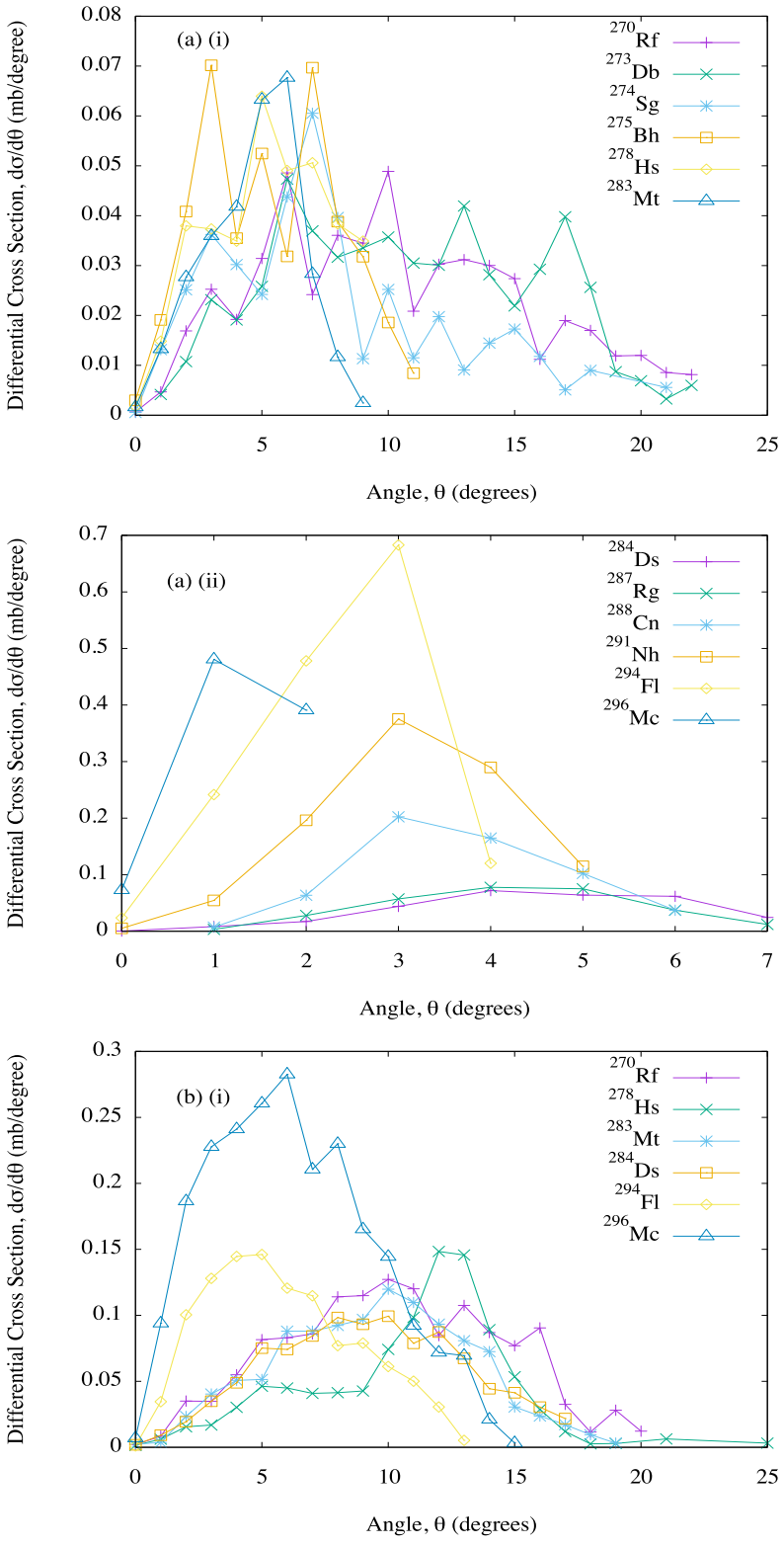

Figure 6.14: The same results as in Fig. 6.7, but for the reaction ^{48}Ca+^{250}Cm, with: (a) $E_{0_{c.m.}}/V_{CB} = 1.00$, (b) $E_{0_{c.m.}}/V_{CB} = 1.05$, and (c) $E_{0_{c.m.}}/V_{CB} = 1.10$. Subfigures are further separated into parts (i) and (ii) to enhance readability.

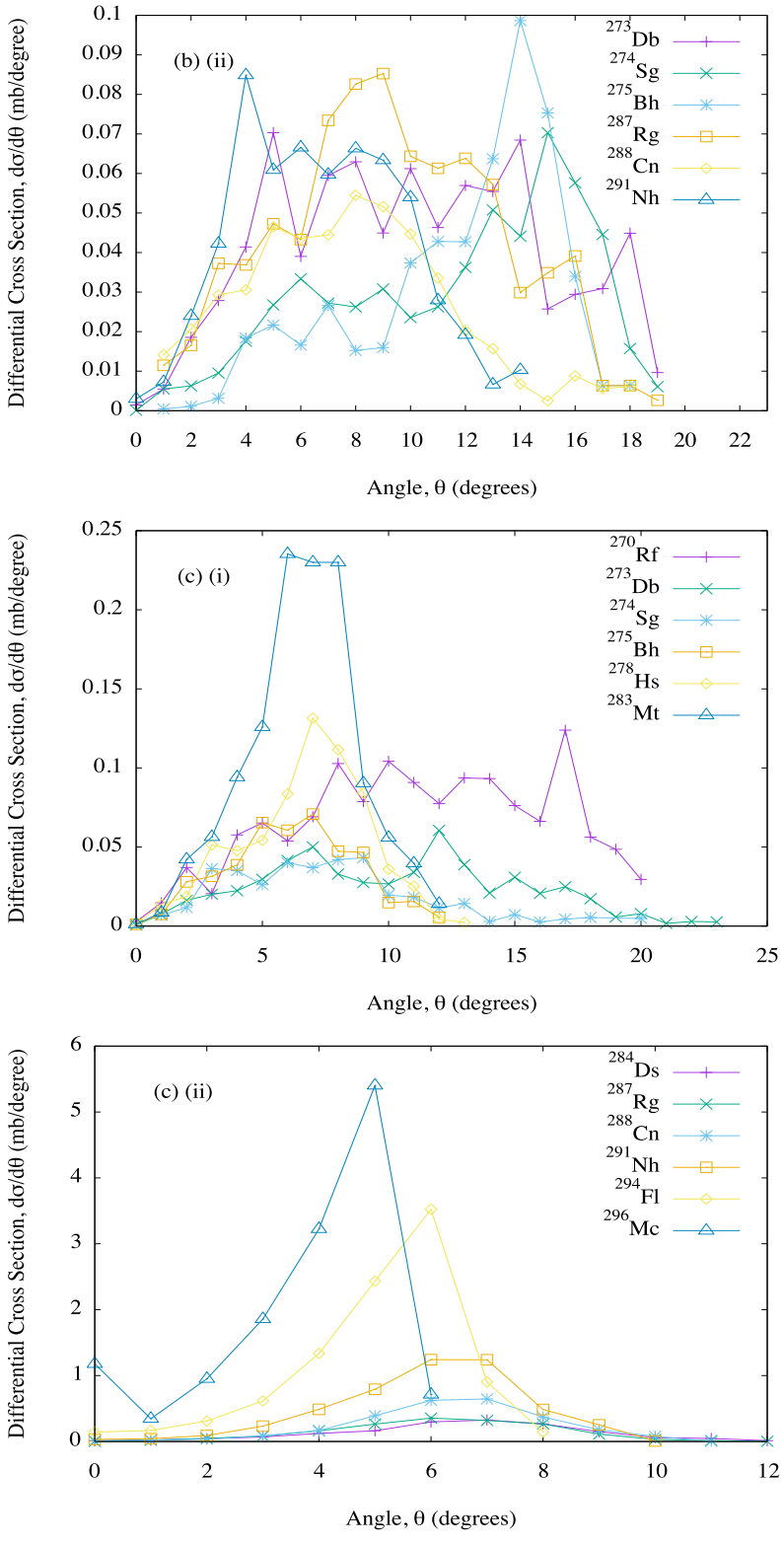

Continuation of Fig. 6.14.

Table 6.14: The same results as in Table 6.7, but for the reaction ^{48}Ca+^{250}Cm.

ICF product	Total cross section (mb)	Mean angle (degrees)	Mean exc. energy (MeV)	Mean angular momentum ($\hbar$)
$E_{0_{c.m.}}/V_{CB}$=1.00				
$^{270}_{104}$Rf	0.5178	10.35 ± 5.15	72.95 ± 14.89	26.80 ± 13.45
$^{273}_{105}$Db	0.5404	10.79 ± 4.95	110.98 ± 19.60	28.27 ± 13.79
$^{274}_{106}$Sg	0.4135	7.90 ± 4.55	58.33 ± 22.89	25.40 ± 14.12
$^{275}_{107}$Bh	0.4201	5.40 ± 2.64	9.60 ± 16.49	26.17 ± 15.03
$^{278}_{108}$Hs	0.3637	5.31 ± 2.30	40.38 ± 7.39	30.25 ± 15.45
$^{283}_{109}$Mt	0.2937	4.70 ± 1.83	26.95 ± 26.45	35.40 ± 15.93
$^{284}_{110}$Ds	0.2920	4.53 ± 1.48	33.19 ± 5.12	37.56 ± 14.10
$^{287}_{111}$Rg	0.2906	4.22 ± 1.34	38.42 ± 24.30	37.56 ± 12.61
$^{288}_{112}$Cn	0.5774	3.70 ± 1.12	23.31 ± 3.47	36.13 ± 12.54
$^{291}_{113}$Nh	1.036	3.19 ± 1.06	48.10 ± 24.02	31.66 ± 12.57
$^{294}_{114}$Fl	1.547	2.41 ± 0.90	57.08 ± 24.92	26.71 ± 11.67
$^{296}_{115}$Mc	0.9447	1.34 ± 0.61	63.96 ± 24.32	21.76 ± 8.94
$E_{0_{c.m.}}/V_{CB}$=1.05				
$^{270}_{104}$Rf	1.393	10.21 ± 4.26	63.41 ± 7.73	25.13 ± 9.22
$^{273}_{105}$Db	0.8005	10.07 ± 4.55	96.20 ± 19.35	24.88 ± 10.27
$^{274}_{106}$Sg	0.5587	11.63 ± 4.42	55.71 ± 21.61	22.43 ± 9.41
$^{275}_{107}$Bh	0.5265	11.79 ± 3.53	15.11 ± 17.71	22.07 ± 10.39
$^{278}_{108}$Hs	0.9514	10.76 ± 3.80	40.36 ± 8.40	24.12 ± 10.20
$^{283}_{109}$Mt	1.097	9.42 ± 3.71	20.57 ± 20.59	24.76 ± 10.22
$^{284}_{110}$Ds	1.010	9.17 ± 3.75	26.91 ± 8.69	24.08 ± 10.24
$^{287}_{111}$Rg	0.7999	9.26 ± 3.90	26.12 ± 20.80	23.10 ± 10.29
$^{288}_{112}$Cn	0.4793	7.75 ± 3.68	16.08 ± 5.58	19.97 ± 9.32
$^{291}_{113}$Nh	0.5964	6.80 ± 2.96	42.13 ± 23.60	22.22 ± 10.22
$^{294}_{114}$Fl	1.093	5.84 ± 2.88	54.03 ± 24.38	22.12 ± 10.24
$^{296}_{115}$Mc	2.307	6.28 ± 3.19	60.15 ± 22.34	19.82 ± 9.62

Continuation of Table 6.14.

ICF product	Total cross section (mb)	Mean angle (degrees)	Mean exc. energy (MeV)	Mean angular momentum ($\hbar$)
$E_{0_{c.m.}}/V_{CB}$=1.10				
$^{270}_{104}$Rf	1.362	11.28 ± 4.84	66.85 ± 6.56	28.26 ± 9.78
$^{273}_{105}$Db	0.5441	10.23 ± 4.82	100.33 ± 18.81	25.28 ± 10.91
$^{274}_{106}$Sg	0.3707	7.60 ± 3.93	55.50 ± 23.07	27.21 ± 11.48
$^{275}_{107}$Bh	0.4336	6.19 ± 2.48	10.35 ± 16.16	29.72 ± 11.57
$^{278}_{108}$Hs	0.6661	6.69 ± 2.42	41.06 ± 11.99	29.83 ± 11.72
$^{283}_{109}$Mt	1.224	6.63 ± 2.18	21.25 ± 20.39	30.35 ± 13.35
$^{284}_{110}$Ds	1.585	6.56 ± 2.20	27.49 ± 10.20	30.87 ± 13.24
$^{287}_{111}$Rg	1.679	6.16 ± 1.93	28.56 ± 22.34	30.16 ± 12.82
$^{288}_{112}$Cn	2.614	6.36 ± 1.77	18.24 ± 5.39	30.20 ± 12.83
$^{291}_{113}$Nh	4.904	5.95 ± 1.69	47.22 ± 23.05	28.72 ± 13.04
$^{294}_{114}$Fl	9.576	5.09 ± 1.49	56.86 ± 22.21	27.57 ± 12.50
$^{296}_{115}$Mc	13.67	3.80 ± 1.61	66.89 ± 21.42	28.37 ± 11.60

6.3.3 ^{48}Ca+^{252}Cf

Fig. 6.15 contains the angular distributions of primary SHE ICF products of the reaction ^{48}Ca+^{252}Cf. At all studied incident energies, all differential cross-sections are found between 0-26 degrees. The further above the Coulomb barrier the incident energy is, the more dominant the heaviest SHE ICF products, ^{296}Lv and ^{298}Ts, are, maintaining the highest cross-sections at all three incident energies, with peaks in the ∼1-4 degree region at the Coulomb barrier and 5% above it, and in the ∼4-10 degree region at 10% above the barrier.

Table 6.15 contains the total cross-sections and the means of the angular, excitation energy and angular momentum distributions of those same ICF products. The total cross-sections of the ICF products follow a similar trend to the angular distributions in Fig. 6.15, in that ^{296}Lv and ^{298}Ts have the highest yields at all three incident energies. Similar general trends of the table are observed here as with the previous two reactions, namely that the heavier the ICF product the more forward the angle and the higher the angular momentum, and the lower the total cross-section with exceptions for the heaviest three ICF products.

Comparing like ICF products from ^{20}Ne-induced reactions, ^{266}Rf has much smaller total cross-sections and much higher excitation energies at all studied incident energies here than from the reaction ^{20}Ne+^{250}Cm, suggesting ^{20}Ne+^{250}Cm is the preferable reaction for producing more stable ^{266}Rf. ^{266}Rf and ^{267}Db have much smaller total cross-sections and much higher excitation energies at all studied incident energies here than from the reaction ^{20}Ne+^{254}Cf, suggesting ^{20}Ne+^{254}Cf is the preferable reaction for producing more stable ^{266}Rf and ^{267}Db.

Comparing like ICF products from ^{40}Ca-induced reactions, ^{266}Rf and ^{267}Db have smaller total cross-sections and lower excitation energies at all studied incident energies here than from the reaction ^{40}Ca+^{250}Cm. ^{266}Rf and ^{277}Mt have smaller total cross-sections, with ^{266}Rf having higher excitation energies and ^{277}Mt having much lower excitation energies at all studied incident energies here than from the reaction ^{40}Ca+^{254}Cf.

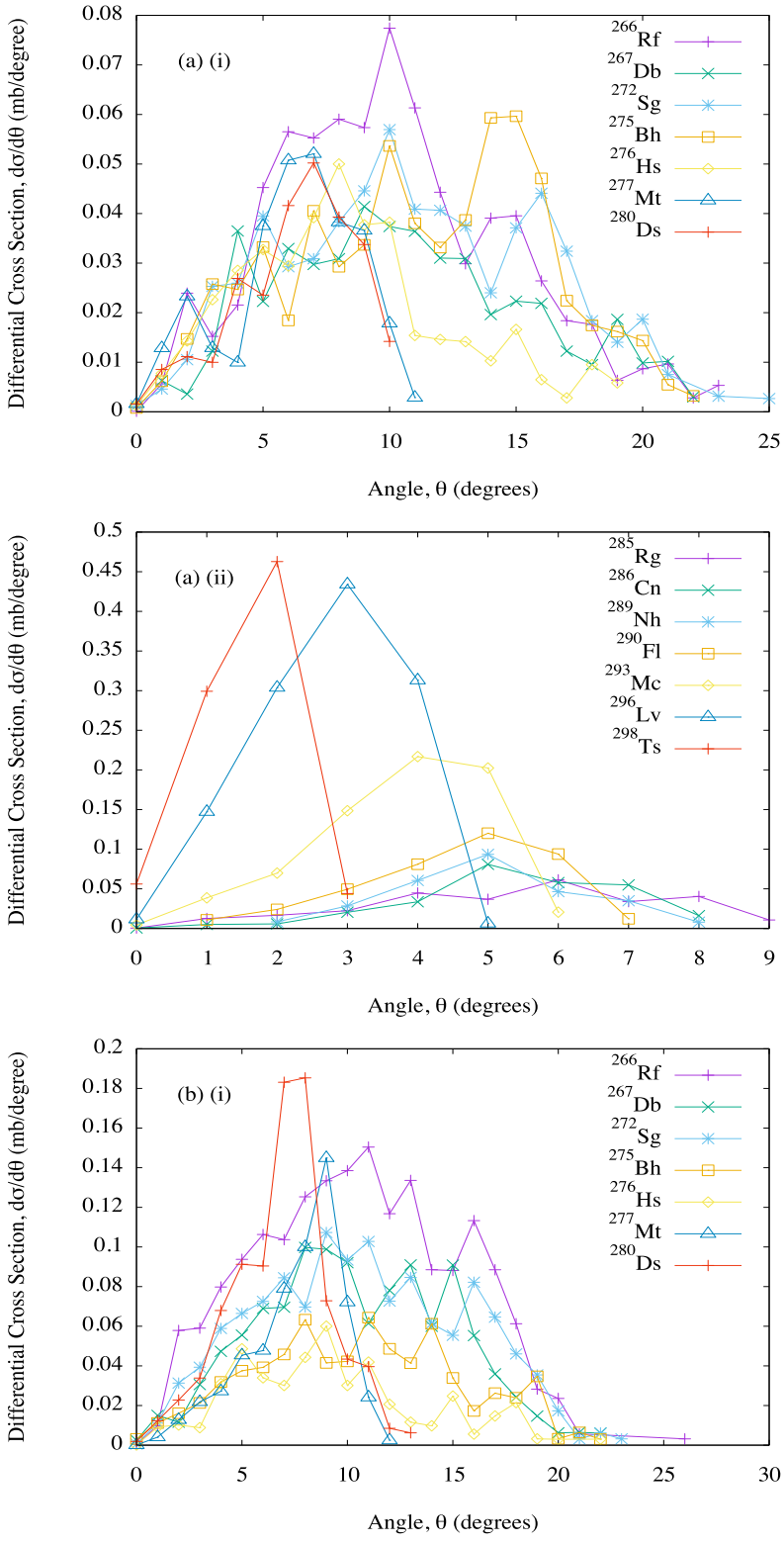

Figure 6.15: The same results as in Fig. 6.7, but for the reaction ^{48}Ca+^{252}Cf, with: (a) $E_{0_{c.m.}}/V_{CB} = 1.00$, (b) $E_{0_{c.m.}}/V_{CB} = 1.05$, and (c) $E_{0_{c.m.}}/V_{CB} = 1.10$. Subfigures are further separated into parts (i) and (ii) to enhance readability.

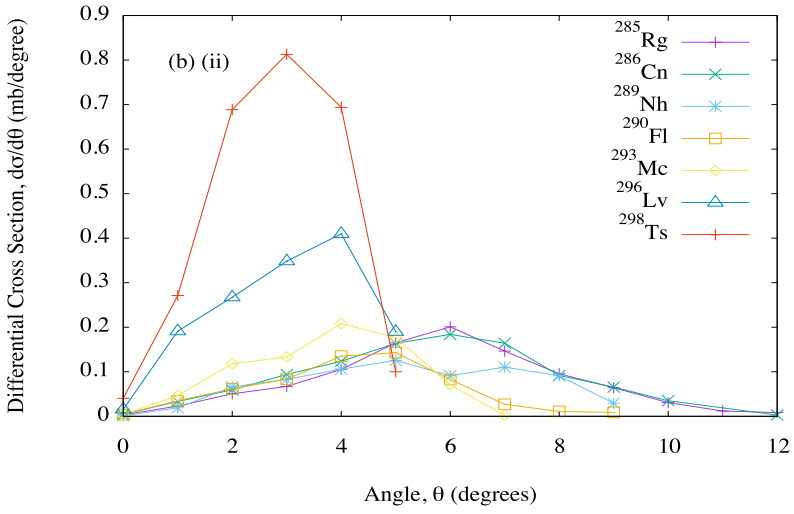

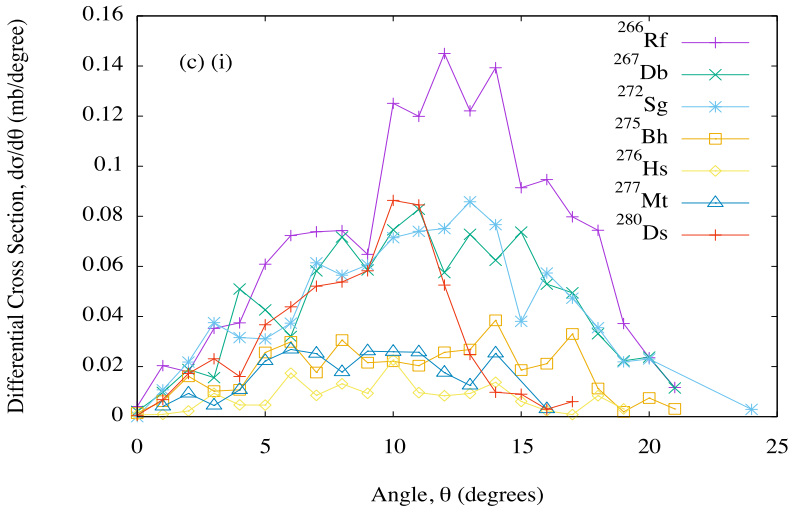

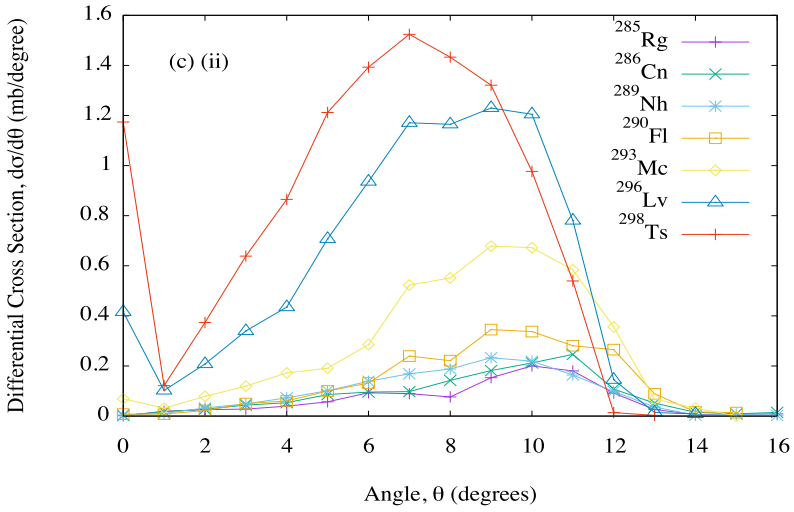

Continuation of Fig. 6.15.

Table 6.15: The same results as in Table 6.7, but for the reaction ^{48}Ca+^{252}Cf.

ICF product	Total cross section (mb)	Mean angle (degrees)	Mean exc. energy (MeV)	Mean angular momentum ($\hbar$)
$E_{0_{c.m.}}/V_{CB}$=1.00				
$^{266}_{104}$Rf	0.7266	10.14 ± 4.59	72.29 ± 14.17	21.96 ± 10.91
$^{267}_{105}$Db	0.4789	10.55 ± 4.90	78.71 ± 21.19	21.42 ± 11.00
$^{272}_{106}$Sg	0.6282	11.01 ± 5.03	70.62 ± 14.35	23.59 ± 13.60
$^{275}_{107}$Bh	0.6360	11.19 ± 4.88	106.90 ± 21.37	26.80 ± 14.84
$^{276}_{108}$Hs	0.3974	8.33 ± 4.14	54.19 ± 25.22	29.37 ± 15.45
$^{277}_{109}$Mt	0.2964	6.21 ± 2.48	11.04 ± 16.65	25.08 ± 13.88
$^{280}_{110}$Ds	0.2607	6.32 ± 2.30	41.40 ± 7.48	35.57 ± 14.55
$^{285}_{111}$Rg	0.2800	5.36 ± 2.07	25.99 ± 25.98	38.28 ± 13.89
$^{286}_{112}$Cn	0.2754	5.37 ± 1.54	32.11 ± 5.07	39.75 ± 12.40
$^{289}_{113}$Nh	0.2803	4.99 ± 1.35	42.51 ± 27.67	39.38 ± 12.43
$^{290}_{114}$Fl	0.3916	4.55 ± 1.37	19.63 ± 4.16	34.76 ± 12.75
$^{293}_{115}$Mc	0.7011	3.75 ± 1.24	51.92 ± 26.91	31.61 ± 13.42
$^{296}_{116}$Lv	1.216	2.75 ± 1.02	58.98 ± 26.99	27.85 ± 12.55
$^{298}_{117}$Ts	0.8622	1.57 ± 0.69	63.71 ± 24.95	21.87 ± 9.04
$E_{0_{c.m.}}/V_{CB}$=1.05				
$^{266}_{104}$Rf	1.809	10.52 ± 4.66	65.33 ± 6.68	22.98 ± 8.00
$^{267}_{105}$Db	1.122	10.44 ± 4.43	71.64 ± 17.69	22.57 ± 7.93
$^{272}_{106}$Sg	1.270	10.69 ± 4.81	64.92 ± 8.21	25.80 ± 9.72
$^{275}_{107}$Bh	0.7177	10.53 ± 4.83	99.81 ± 18.39	25.19 ± 10.56
$^{276}_{108}$Hs	0.4663	9.26 ± 4.46	53.61 ± 22.68	24.34 ± 10.33
$^{277}_{109}$Mt	0.5817	7.55 ± 2.23	12.47 ± 16.27	22.37 ± 10.27
$^{280}_{110}$Ds	0.8595	6.87 ± 2.32	38.25 ± 8.75	24.01 ± 10.61

Continuation of Table 6.15.

ICF product	Total cross section (mb)	Mean angle (degrees)	Mean exc. energy (MeV)	Mean angular momentum ($\hbar$)
$E_{0_{c.m.}}/V_{CB}$=1.05				
$^{285}_{111}$Rg	0.9722	5.84 ± 2.24	18.72 ± 19.69	23.62 ± 10.81
$^{286}_{112}$Cn	1.022	5.59 ± 2.23	23.20 ± 10.44	24.31 ± 10.83
$^{289}_{113}$Nh	0.7222	5.21 ± 2.09	23.99 ± 23.06	23.32 ± 9.91
$^{290}_{114}$Fl	0.5910	4.25 ± 1.73	11.69 ± 4.55	21.34 ± 9.81
$^{293}_{115}$Mc	0.7595	3.74 ± 1.41	38.80 ± 24.88	23.03 ± 10.23
$^{296}_{116}$Lv	1.422	3.07 ± 1.28	49.47 ± 25.17	22.72 ± 9.77
$^{298}_{117}$Ts	2.607	2.82 ± 1.10	56.66 ± 23.98	21.70 ± 9.25
$E_{0_{c.m.}}/V_{CB}$=1.10				
$^{266}_{104}$Rf	1.525	11.54 ± 4.55	71.96 ± 7.33	27.82 ± 8.69
$^{267}_{105}$Db	0.9774	11.16 ± 4.72	80.20 ± 16.07	27.99 ± 8.80
$^{272}_{106}$Sg	0.9578	11.06 ± 4.68	68.19 ± 7.46	30.59 ± 10.93
$^{275}_{107}$Bh	0.3999	10.64 ± 4.91	105.77 ± 17.48	29.80 ± 10.76
$^{276}_{108}$Hs	0.1552	9.83 ± 4.29	58.59 ± 23.85	25.05 ± 12.15
$^{277}_{109}$Mt	0.2568	8.66 ± 3.47	9.25 ± 15.08	26.99 ± 12.20
$^{280}_{110}$Ds	0.5844	8.74 ± 3.25	41.08 ± 11.79	30.48 ± 11.42
$^{285}_{111}$Rg	1.096	8.60 ± 2.92	17.58 ± 18.70	29.96 ± 12.82
$^{286}_{112}$Cn	1.405	8.73 ± 3.00	25.31 ± 9.80	30.66 ± 13.14
$^{289}_{113}$Nh	1.531	8.16 ± 2.77	25.37 ± 21.66	30.18 ± 13.49
$^{290}_{114}$Fl	2.189	8.92 ± 2.68	14.62 ± 5.52	29.28 ± 13.00
$^{293}_{115}$Mc	4.414	8.35 ± 2.80	43.46 ± 22.15	29.10 ± 13.01
$^{296}_{116}$Lv	8.865	7.19 ± 2.93	53.52 ± 21.69	28.32 ± 12.59
$^{298}_{117}$Ts	11.59	6.09 ± 3.09	63.91 ± 21.22	28.21 ± 11.32

6.3.4 ^{48}Ca+^{254}Cf

Fig. 6.16 contains the angular distributions of primary SHE ICF products of the reaction ^{48}Ca+^{254}Cf. At all studied incident energies, all differential cross-sections are found between 0-29 degrees. The further above the Coulomb barrier the incident energy is, the more dominant the heaviest SHE ICF products, ^{298}Lv and ^{300}Ts, are, maintaining the highest cross-sections at all three incident energies, with peaks in the ∼1-3 degree region at the Coulomb barrier, in the ∼1-6 degree region and 5% above the barrier, and in the ∼2-5 degree region at 10% above the barrier.

Table 6.16 contains the total cross-sections and the means of the angular, excitation energy and angular momentum distributions of those same ICF products. The total cross-sections of the ICF products follow a similar trend to the angular distributions in Fig. 6.16, in that ^{298}Lv and ^{300}Ts have the highest yields at all three incident energies, save for ^{298}Lv at 5% above the Coulomb barrier. Similar general trends of the table are observed here as with the previous three reactions, namely that the heavier the ICF product the more forward the angle and the higher the angular momentum, and the lower the total cross-section with exceptions for the heaviest four ICF products.

Comparing like ICF products from the reaction ^{48}Ca+^{248}Cm, ^{268}Rf has a slightly smaller total cross-section at the Coulomb barrier and slightly larger total cross-sections above the barrier here, with slightly higher excitation energies, suggesting ^{48}Ca+^{248}Cm is the preferable reaction for producing more stable ^{268}Rf. ^{282}Ds has a slightly larger total cross-section at the Coulomb barrier and slightly smaller total cross-sections above the barrier here, with higher excitation energies, suggesting ^{48}Ca+^{248}Cm is the preferable reaction for producing more stable ^{282}Ds at the Coulomb barrier. ^{292}Fl has lower total cross-sections at all studied incident energies here than from the reaction ^{48}Ca+^{248}Cm, but with drastically lower excitation energies.

Comparing like ICF products from the reaction ^{48}Ca+^{250}Cm,^{274}Sg has higher total cross-sections and excitation energies here. ^{278}Hs has a slightly larger total cross-section at the Coulomb barrier and smaller total cross-sections above the barrier here, with higher excitation energies all-round, suggesting ^{48}Ca+^{250}Cm is the preferable reaction for producing more stable ^{278}Hs above the Coulomb barrier. ^{287}Rg has a slightly smaller

total cross-section at the Coulomb barrier and larger total cross-sections above the barrier here, with lower excitation energies all-round, suggesting ^{48}Ca+^{254}Cf is the preferable reaction for producing more stable ^{287}Rg above the Coulomb barrier. ^{288}Cn has smaller total cross-sections at the Coulomb barrier and at 10% above the barrier and a larger total cross-section at 5% above the barrier here, with higher excitation energies all-round, suggesting ^{48}Ca+^{250}Cm is the preferable reaction for producing more stable ^{288}Cn at the Coulomb barrier and at 10% above the barrier. ^{291}Nh has smaller total cross-sections and lower excitation energies at all studied incident energies here.

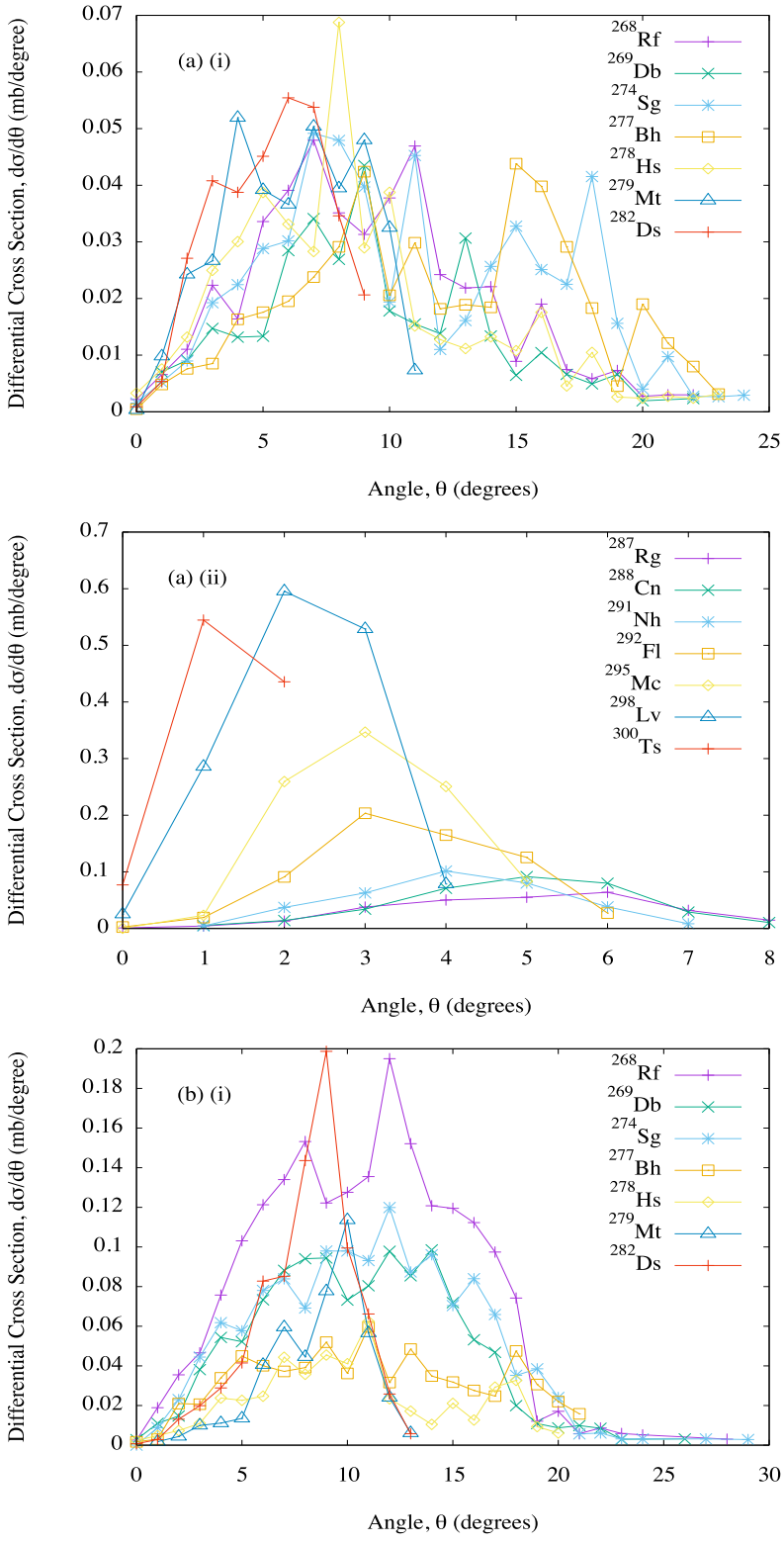

Figure 6.16: The same results as in Fig. 6.7, but for the reaction ^{48}Ca+^{254}Cf, with: (a) $E_{0_{c.m.}}/V_{CB} = 1.00$, (b) $E_{0_{c.m.}}/V_{CB} = 1.05$, and (c) $E_{0_{c.m.}}/V_{CB} = 1.10$. Subfigures are further separated into parts (i) and (ii) to enhance readability.

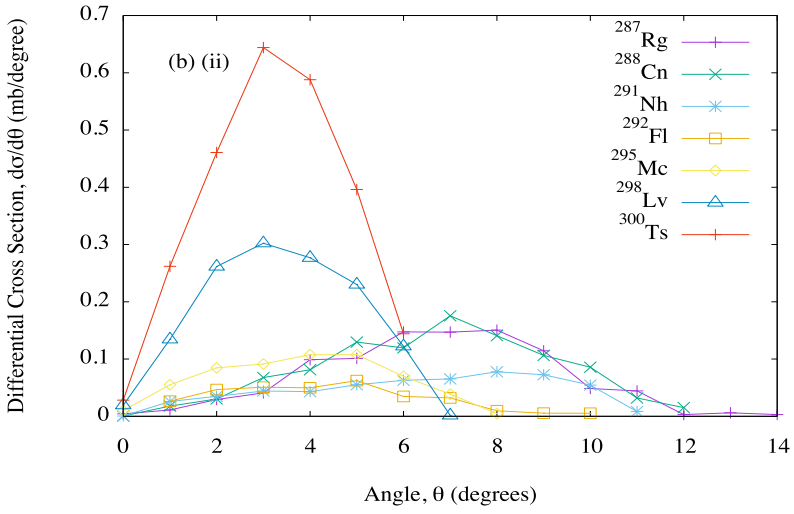

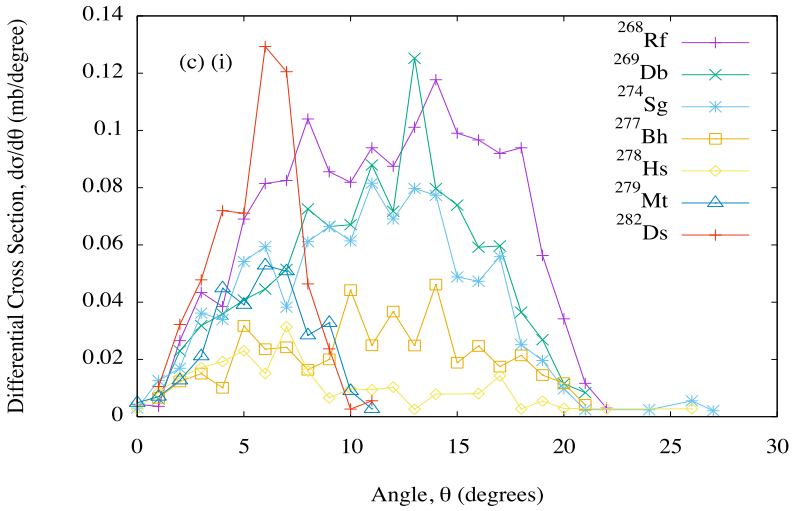

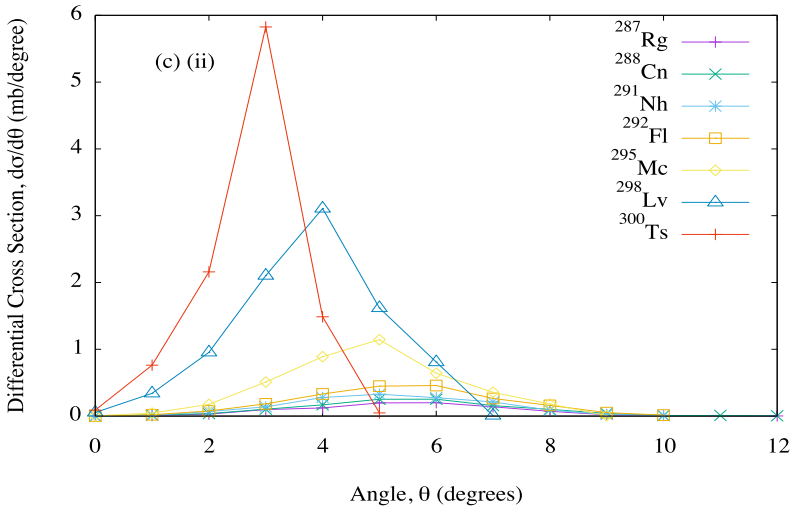

Continuation of Fig. 6.16.

Table 6.16: The same results as in Table 6.7, but for the reaction ^{48}Ca+^{254}Cf.

ICF product	Total cross section (mb)	Mean angle (degrees)	Mean exc. energy (MeV)	Mean angular momentum ($\hbar$)
$E_{0_{c.m.}}/V_{CB}$=1.00				
$^{268}_{104}$Rf	0.4557	9.29 ± 4.44	68.05 ± 15.79	23.00 ± 11.30
$^{269}_{105}$Db	0.3208	9.31 ± 4.41	74.60 ± 20.82	20.93 ± 10.53
$^{274}_{106}$Sg	0.5302	10.88 ± 5.28	72.05 ± 14.98	27.04 ± 13.98
$^{277}_{107}$Bh	0.4539	11.99 ± 5.22	107.14 ± 21.10	32.02 ± 15.51
$^{278}_{108}$Hs	0.4245	8.61 ± 4.64	56.92 ± 22.73	30.11 ± 14.58
$^{279}_{109}$Mt	0.3664	6.19 ± 2.59	10.05 ± 15.90	29.88 ± 15.85
$^{282}_{110}$Ds	0.3225	5.38 ± 2.10	37.05 ± 8.33	34.46 ± 14.98
$^{287}_{111}$Rg	0.2722	4.94 ± 1.64	22.90 ± 25.12	38.75 ± 14.45
$^{288}_{112}$Cn	0.3355	4.90 ± 1.45	27.52 ± 5.12	39.99 ± 12.31
$^{291}_{113}$Nh	0.3325	4.09 ± 1.29	35.56 ± 25.86	39.45 ± 12.17
$^{292}_{114}$Fl	0.6340	3.57 ± 1.19	16.49 ± 3.55	35.52 ± 12.32
$^{295}_{115}$Mc	0.9638	3.11 ± 0.98	45.97 ± 26.25	32.84 ± 13.08
$^{298}_{116}$Lv	1.514	2.23 ± 0.87	51.04 ± 26.21	29.11 ± 12.56
$^{300}_{117}$Ts	1.057	1.34 ± 0.61	59.58 ± 25.93	21.49 ± 8.92
$E_{0_{c.m.}}/V_{CB}$=1.05				
$^{268}_{104}$Rf	2.005	10.78 ± 4.61	61.41 ± 6.87	23.71 ± 7.97
$^{269}_{105}$Db	1.195	10.53 ± 4.57	69.12 ± 17.87	23.62 ± 8.35
$^{274}_{106}$Sg	1.362	11.07 ± 4.86	59.93 ± 7.80	25.96 ± 9.88
$^{277}_{107}$Bh	0.7047	11.09 ± 5.23	95.00 ± 19.62	25.19 ± 9.57
$^{278}_{108}$Hs	0.4880	10.39 ± 4.60	53.14 ± 22.24	23.04 ± 9.67
$^{279}_{109}$Mt	0.4635	8.62 ± 2.28	10.97 ± 16.19	22.64 ± 9.49
$^{282}_{110}$Ds	0.8146	8.04 ± 2.26	37.56 ± 7.00	23.93 ± 10.65

Continuation of Table 6.16.

ICF product	Total cross section (mb)	Mean angle (degrees)	Mean exc. energy (MeV)	Mean angular momentum ($\hbar$)
$E_{0_{c.m.}}/V_{CB}$=1.05				
$^{287}_{111}$Rg	0.9498	6.71 ± 2.42	16.48 ± 19.98	24.22 ± 10.58
$^{288}_{112}$Cn	1.002	6.66 ± 2.44	23.81 ± 8.25	24.34 ± 10.34
$^{291}_{113}$Nh	0.5448	6.28 ± 2.68	25.43 ± 22.49	22.39 ± 9.78
$^{292}_{114}$Fl	0.3231	4.32 ± 2.09	8.07 ± 3.65	19.57 ± 8.62
$^{295}_{115}$Mc	0.5697	3.85 ± 1.82	40.41 ± 25.97	18.71 ± 8.54
$^{298}_{116}$Lv	1.349	3.39 ± 1.51	47.28 ± 23.94	18.27 ± 8.25
$^{300}_{117}$Ts	2.523	3.29 ± 1.41	55.23 ± 24.04	16.55 ± 7.53
$E_{0_{c.m.}}/V_{CB}$=1.10				
$^{268}_{104}$Rf	1.508	11.65 ± 4.86	67.42 ± 7.22	28.06 ± 9.22
$^{269}_{105}$Db	1.080	11.28 ± 4.51	76.48 ± 16.88	27.80 ± 9.19
$^{274}_{106}$Sg	0.9702	10.82 ± 4.83	63.80 ± 8.52	31.58 ± 11.27
$^{277}_{107}$Bh	0.4497	11.08 ± 4.93	100.65 ± 18.59	29.86 ± 11.65
$^{278}_{108}$Hs	0.2320	8.43 ± 5.55	50.11 ± 21.30	28.22 ± 12.52
$^{279}_{109}$Mt	0.3063	5.83 ± 2.30	7.36 ± 13.74	27.96 ± 11.23
$^{282}_{110}$Ds	0.5617	5.61 ± 1.97	38.35 ± 10.88	31.68 ± 11.03
$^{287}_{111}$Rg	0.8996	5.43 ± 1.79	16.50 ± 19.27	29.86 ± 12.18
$^{288}_{112}$Cn	1.146	5.52 ± 1.87	22.48 ± 9.68	30.69 ± 13.23
$^{291}_{113}$Nh	1.435	5.22 ± 1.71	23.52 ± 22.10	29.54 ± 12.88
$^{292}_{114}$Fl	2.008	5.36 ± 1.73	11.04 ± 5.17	29.72 ± 13.10
$^{295}_{115}$Mc	3.950	4.82 ± 1.51	40.91 ± 22.79	28.81 ± 12.75
$^{298}_{116}$Lv	8.995	3.78 ± 1.26	51.53 ± 22.26	29.21 ± 12.20
$^{300}_{117}$Ts	10.37	2.77 ± 0.83	62.09 ± 22.04	28.86 ± 11.30

6.3.5 ^{48}Ca+^{254}Es

Fig. 6.17 contains the angular distributions of primary SHE ICF products of the reaction ^{48}Ca+^{254}Es. At all studied incident energies, all differential cross-sections are found between 0-28 degrees. The further above the Coulomb barrier the incident energy is, the more dominant the heaviest SHE ICF products, ^{298}Ts and ^{300}Og, are, maintaining the highest cross-sections at all three incident energies, with peaks in the ∼1-3 degree region at the Coulomb barrier, in the ∼2-8 degree region and 5% above the barrier, and in the ∼3-10 degree region at 10% above the barrier.

Table 6.17 contains the total cross-sections and the means of the angular, excitation energy and angular momentum distributions of those same ICF products. The total cross-sections of the ICF products follow a similar trend to the angular distributions in Fig. 6.17, in that ^{298}Ts and ^{300}Og have the highest yields at all three incident energies, save for ^{298}Ts at 5% above the Coulomb barrier. Similar general trends of the table are observed here as with the previous four reactions, namely that the heavier the ICF product the more forward the angle and the higher the angular momentum, and the lower the total cross-section with exceptions for the heaviest four ICF products.

Comparing like ICF products from ^{20}Ne-induced reactions, ^{265}Rf and ^{266}Db have smaller total cross-sections and higher excitation energies at all three studied incident energies here than from the reaction ^{20}Ne+^{254}Es. ^{266}Db has smaller total cross-sections and higher excitation energies at all three studied incident energies here than from the reaction ^{20}Ne+^{248}Cm. ^{269}Sg has smaller total cross-sections and higher excitation energies at all three studied incident energies here than from the reaction ^{20}Ne+^{256}Es. These comparisons all suggest that ^{20}Ne-induced reactions are generally the preferable choice over ^{48}Ca-induced reactions for producing more stable shared SHE ICF products.

Comparing like ICF products from ^{40}Ca-induced reactions, ^{268}Db has smaller total cross-sections and higher excitation energies at all three studied incident energies here than from the reaction ^{40}Ca+^{254}Cf. ^{265}Rf has smaller total cross-sections and higher excitation energies at all three studied incident energies here than from the reaction ^{40}Ca+^{254}Es. ^{268}Db has smaller total cross-sections and higher excitation energies at all three studied incident energies here than from the reaction ^{40}Ca+^{256}Es. ^{279}Ds has

smaller total cross-sections and lower excitation energies at all three studied incident energies here than from the reaction ^{40}Ca+^{256}Es. These comparisons suggest that ^{40}Ca-induced reactions are generally the preferable choice over ^{48}Ca-induced reactions for producing more stable shared SHE ICF products.

Comparing like ICF products from the reaction ^{48}Ca+^{252}Cf, ^{298}Ts has a higher total cross-section at the Coulomb barrier and lower total cross-sections above the barrier here, with lower excitation energies all-round. This suggests that at the Coulomb barrier, ^{48}Ca+^{254}Es is the preferable reaction for producing more stable ^{298}Ts.

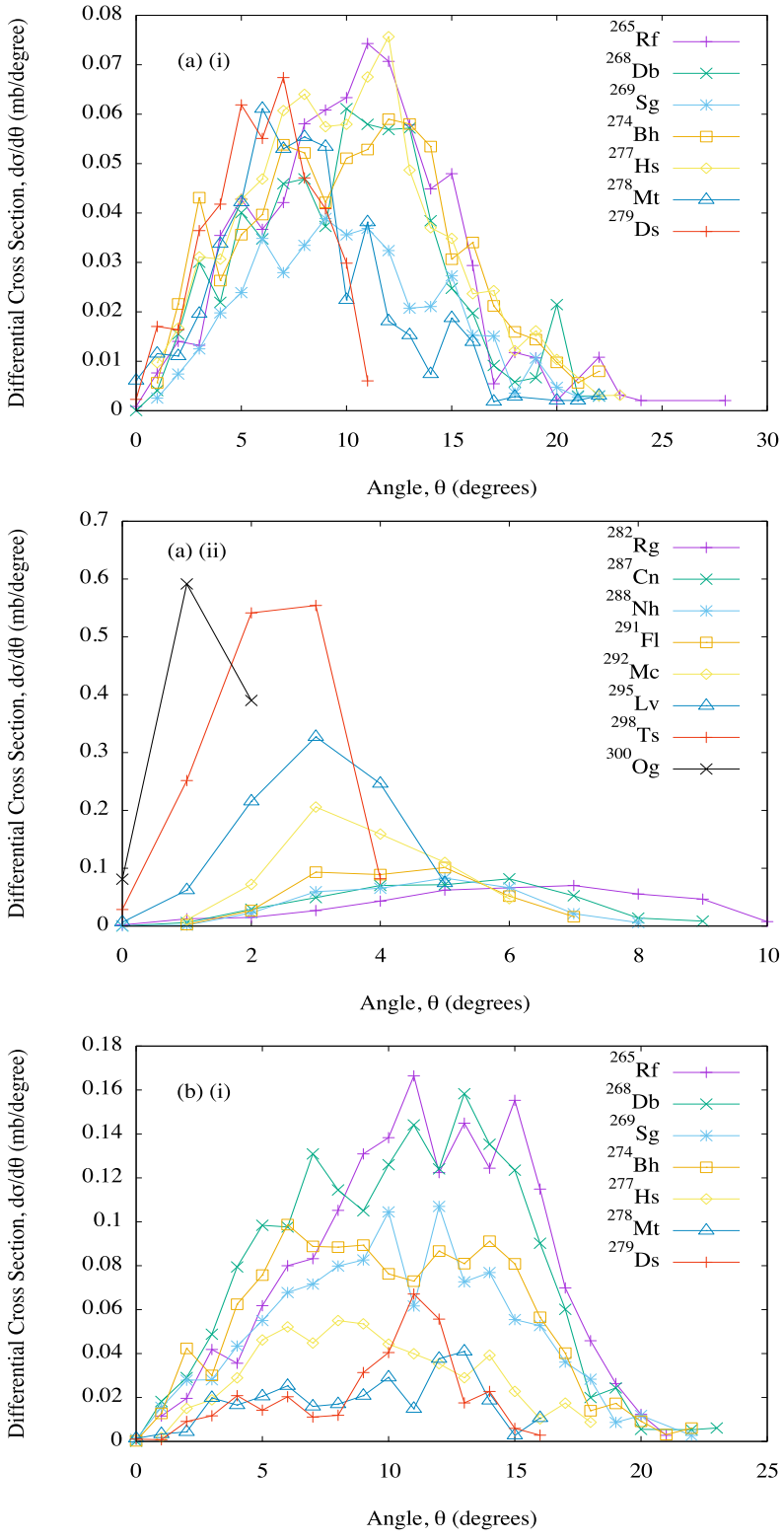

Figure 6.17: The same results as in Fig. 6.7, but for the reaction ^{48}Ca+^{254}Es, with: (a) $E_{0_{c.m.}}/V_{CB} = 1.00$, (b) $E_{0_{c.m.}}/V_{CB} = 1.05$, and (c) $E_{0_{c.m.}}/V_{CB} = 1.10$. Subfigures are further separated into parts (i) and (ii) to enhance readability.

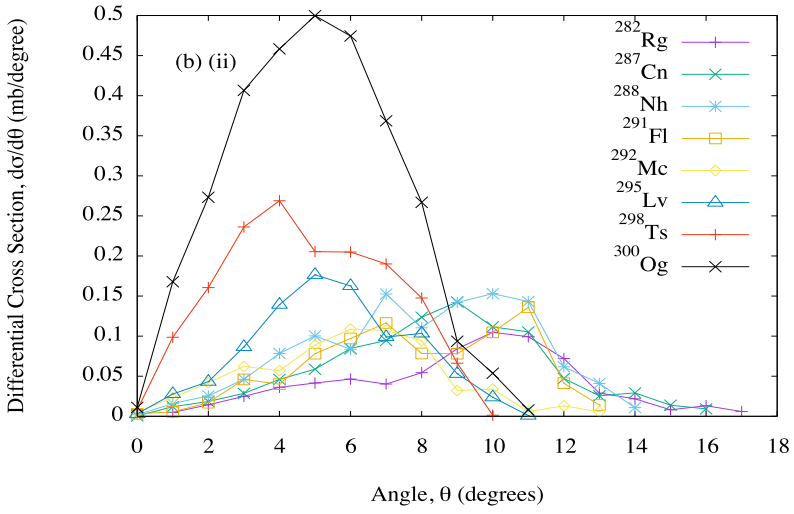

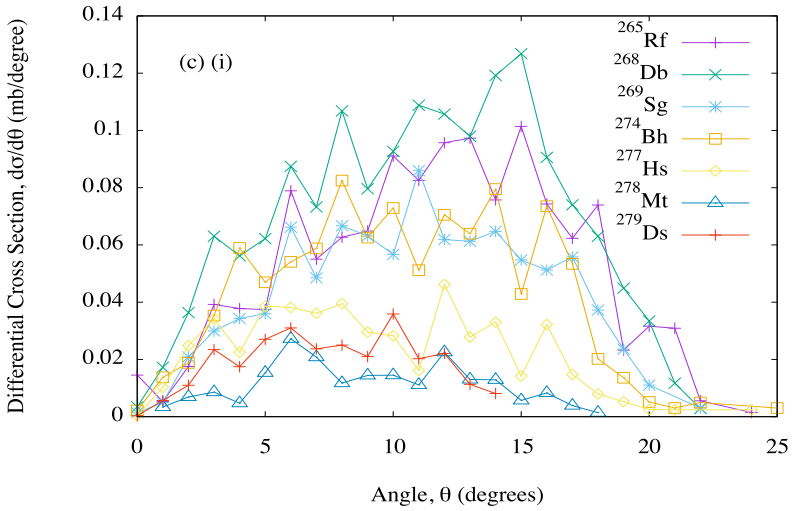

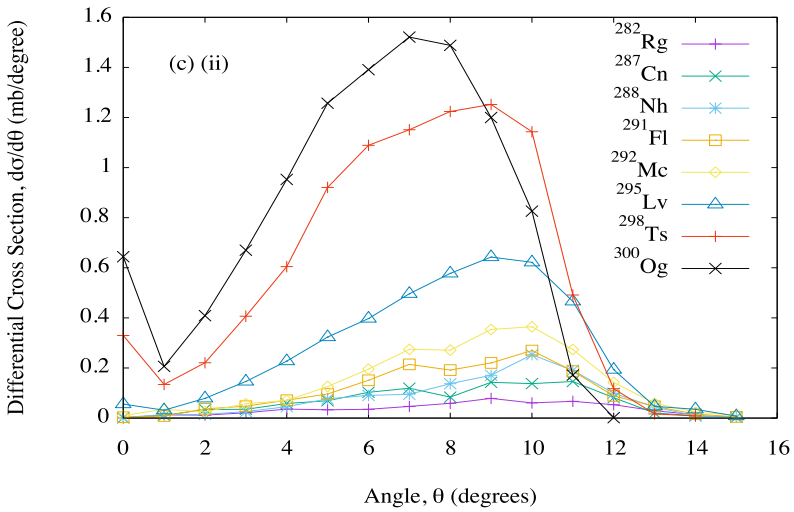

Continuation of Fig. 6.17.

Table 6.17: The same results as in Table 6.7, but for the reaction ^{48}Ca+^{254}Es.

ICF product	Total cross section (mb)	Mean angle (degrees)	Mean exc. energy (MeV)	Mean angular momentum ($\hbar$)
$E_{0_{c.m.}}/V_{CB}$=1.00				
$^{265}_{104}$Rf	0.7482	10.42 ± 4.45	55.80 ± 23.70	17.78 ± 8.53
$^{268}_{105}$Db	0.6417	10.13 ± 4.47	74.36 ± 14.67	22.73 ± 10.84
$^{269}_{106}$Sg	0.4303	10.19 ± 4.46	79.33 ± 23.07	19.60 ± 10.64
$^{274}_{107}$Bh	0.7341	10.34 ± 4.78	71.88 ± 14.55	27.68 ± 13.02
$^{277}_{108}$Hs	0.7746	10.04 ± 4.48	107.81 ± 22.29	26.99 ± 14.07
$^{278}_{109}$Mt	0.4931	8.12 ± 4.02	62.82 ± 21.70	28.11 ± 14.00
$^{279}_{110}$Ds	0.4222	6.03 ± 2.47	10.94 ± 16.12	29.23 ± 14.92
$^{282}_{111}$Rg	0.4077	5.97 ± 2.18	40.63 ± 8.59	34.80 ± 14.98
$^{287}_{112}$Cn	0.3829	4.95 ± 1.76	26.43 ± 24.26	38.79 ± 13.65
$^{288}_{113}$Nh	0.3262	4.59 ± 1.46	31.27 ± 6.55	37.33 ± 14.03
$^{291}_{114}$Fl	0.3809	4.26 ± 1.31	36.75 ± 26.01	38.33 ± 12.85
$^{292}_{115}$Mc	0.6049	3.71 ± 1.18	20.89 ± 4.04	35.99 ± 12.98
$^{295}_{116}$Lv	0.9322	3.04 ± 1.07	48.86 ± 24.90	32.68 ± 11.97
$^{298}_{117}$Ts	1.458	2.28 ± 0.88	57.69 ± 25.54	27.99 ± 12.11
$^{300}_{118}$Og	1.063	1.29 ± 0.60	66.01 ± 25.10	20.99 ± 9.05
$E_{0_{c.m.}}/V_{CB}$=1.05				
$^{265}_{104}$Rf	1.693	11.22 ± 4.15	53.91 ± 16.57	19.78 ± 6.96
$^{268}_{105}$Db	1.745	10.42 ± 4.36	68.54 ± 7.57	22.95 ± 8.46
$^{269}_{106}$Sg	1.091	10.25 ± 4.39	77.18 ± 18.01	23.99 ± 7.71
$^{274}_{107}$Bh	1.224	10.00 ± 4.55	63.38 ± 6.04	26.57 ± 9.67
$^{277}_{108}$Hs	0.5636	9.19 ± 3.95	99.76 ± 19.32	25.03 ± 9.56
$^{278}_{109}$Mt	0.2999	9.14 ± 3.86	56.59 ± 20.84	21.73 ± 10.54
$^{279}_{110}$Ds	0.3447	9.51 ± 3.37	9.97 ± 14.74	21.88 ± 10.57
$^{282}_{111}$Rg	0.7012	9.03 ± 3.29	38.61 ± 9.61	24.05 ± 10.70

Continuation of Table 6.17.

ICF product	Total cross section (mb)	Mean angle (degrees)	Mean exc. energy (MeV)	Mean angular momentum ($\hbar$)
$E_{0_{c.m.}}/V_{CB}$=1.05				
$^{287}_{112}$Cn	0.9518	8.40 ± 3.04	19.09 ± 20.03	24.24 ± 10.97
$^{288}_{113}$Nh	1.167	7.96 ± 2.94	25.28 ± 9.73	24.05 ± 11.12
$^{291}_{114}$Fl	0.8561	7.80 ± 2.82	25.31 ± 21.57	23.07 ± 10.11
$^{292}_{115}$Mc	0.6794	5.96 ± 2.58	13.23 ± 4.27	22.89 ± 10.16
$^{295}_{116}$Lv	0.9194	5.48 ± 2.13	41.59 ± 25.97	22.44 ± 10.23
$^{298}_{117}$Ts	1.588	4.77 ± 2.21	48.92 ± 24.02	21.03 ± 10.53
$^{300}_{118}$Og	3.082	4.96 ± 2.20	57.83 ± 23.65	20.29 ± 9.69
$E_{0_{c.m.}}/V_{CB}$=1.10				
$^{265}_{104}$Rf	1.260	11.67 ± 4.97	63.37 ± 17.25	25.45 ± 8.01
$^{268}_{105}$Db	1.557	11.13 ± 4.91	74.84 ± 7.97	27.73 ± 9.85
$^{269}_{106}$Sg	0.9392	10.91 ± 4.64	83.59 ± 17.05	27.77 ± 9.29
$^{274}_{107}$Bh	0.9916	10.46 ± 4.74	69.95 ± 8.01	30.55 ± 10.87
$^{277}_{108}$Hs	0.5072	9.32 ± 4.86	108.27 ± 21.11	28.18 ± 12.24
$^{278}_{109}$Mt	0.2064	9.05 ± 4.02	53.49 ± 21.79	25.76 ± 10.87
$^{279}_{110}$Ds	0.2832	7.59 ± 3.35	9.41 ± 14.50	27.44 ± 11.42
$^{282}_{111}$Rg	0.5580	8.38 ± 3.16	40.76 ± 11.93	28.96 ± 11.54
$^{287}_{112}$Cn	1.055	8.12 ± 2.93	18.40 ± 20.09	31.26 ± 13.60
$^{288}_{113}$Nh	1.271	8.72 ± 2.70	26.44 ± 9.45	30.21 ± 12.96
$^{291}_{114}$Fl	1.655	8.25 ± 2.72	25.85 ± 21.23	30.23 ± 13.35
$^{292}_{115}$Mc	2.294	8.40 ± 2.73	16.86 ± 5.39	29.78 ± 12.59
$^{295}_{116}$Lv	4.349	7.89 ± 2.77	44.86 ± 22.11	28.37 ± 12.49
$^{298}_{117}$Ts	9.110	6.92 ± 2.80	54.98 ± 21.74	28.52 ± 12.36
$^{300}_{118}$Og	10.74	6.05 ± 2.76	66.58 ± 21.38	28.59 ± 11.37

6.3.6 ^{48}Ca+^{256}Es

Fig. 6.18 contains the angular distributions of primary SHE ICF products of the reaction ^{48}Ca+^{256}Es. At all studied incident energies, all differential cross-sections are found between 0-28 degrees. The further above the Coulomb barrier the incident energy is, the more dominant the heaviest SHE ICF products, ^{300}Ts and ^{302}Og, are, maintaining the highest cross-sections at all three incident energies, with peaks in the ∼1-4 degree region at the Coulomb barrier, in the ∼1-7 degree region and 5% above the barrier, and in the ∼2-5 degree region at 10% above the barrier.

Table 6.18 contains the total cross-sections and the means of the angular, excitation energy and angular momentum distributions of those same ICF products. The total cross-sections of the ICF products follow a similar trend to the angular distributions in Fig. 6.18, in that ^{300}Ts and ^{302}Og have the highest yields at all three incident energies, save for ^{300}Ts at 5% above the Coulomb barrier. Similar general trends of the table are observed here as with the previous five reactions, namely that the heavier the ICF product the more forward the angle and the higher the angular momentum, and the lower the total cross-section with exceptions for the heaviest four ICF products.

Comparing like ICF products from ^{20}Ne-induced reactions, ^{267}Rf has smaller total cross-sections and higher excitation energies at all three studied incident energies here than from the reaction ^{20}Ne+^{256}Es, suggesting ^{20}Ne+^{256}Es is the preferable reaction for producing more stable ^{267}Rf.

Comparing like ICF products from the reaction ^{48}Ca+^{254}Cf, ^{300}Ts has a higher total cross-section at the Coulomb barrier and lower total cross-sections above the barrier here, with lower excitation energies all-round. This suggests that at the Coulomb barrier, ^{48}Ca+^{256}Es is the preferable reaction for producing more stable ^{300}Ts.

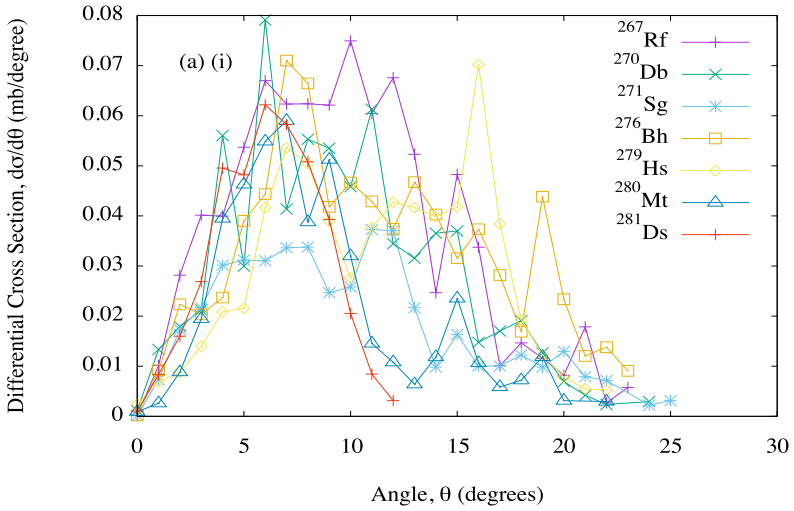

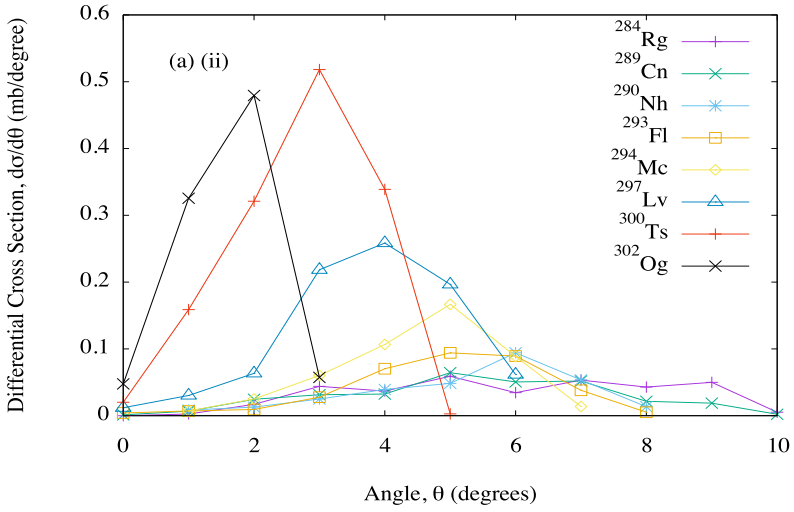

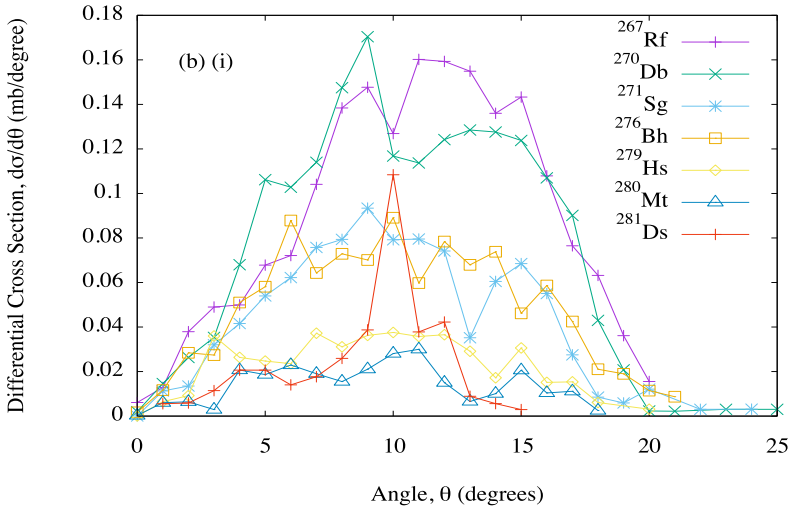

Figure 6.18: The same results as in Fig. 6.7, but for the reaction ^{48}Ca+^{256}Es, with: (a) $E_{0_{c.m.}}/V_{CB} = 1.00$, (b) $E_{0_{c.m.}}/V_{CB} = 1.05$, and (c) $E_{0_{c.m.}}/V_{CB} = 1.10$. Subfigures are further separated into parts (i) and (ii) to enhance readability.

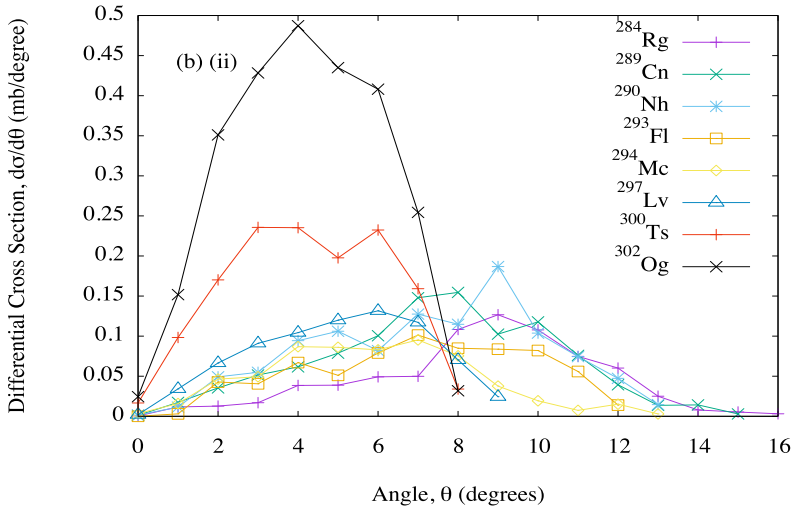

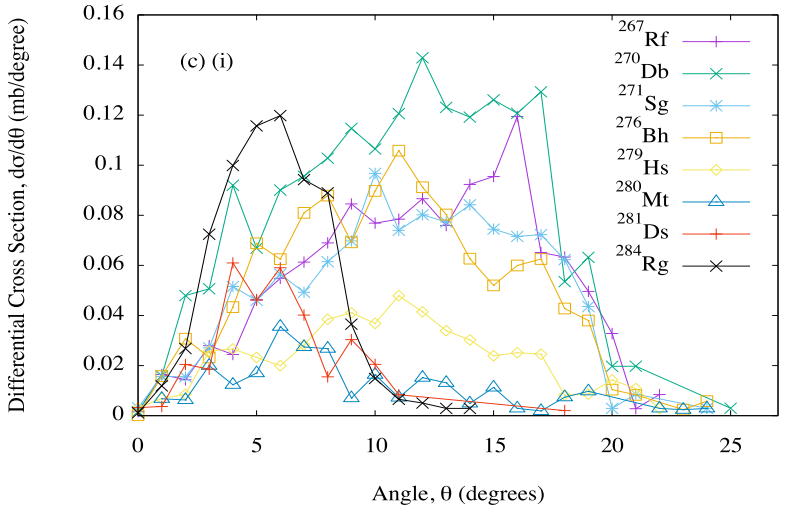

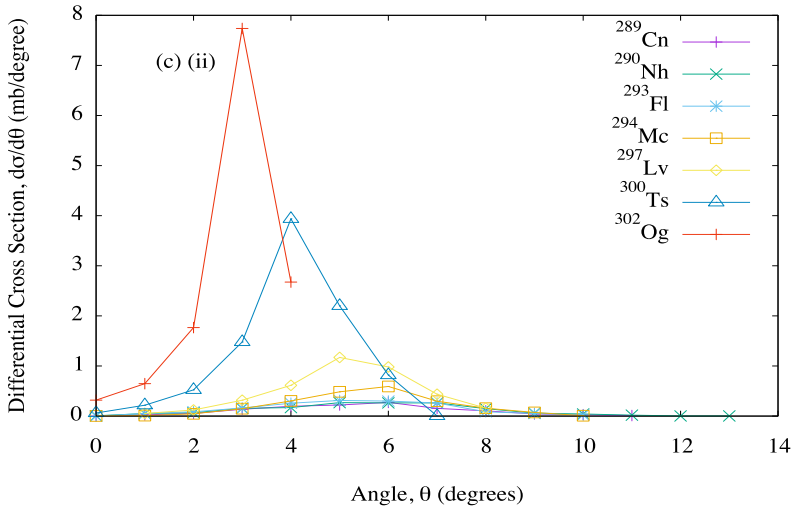

Continuation of Fig. 6.18.

Table 6.18: The same results as in Table 6.7, but for the reaction ^{48}Ca+^{256}Es.

ICF product	Total cross section (mb)	Mean angle (degrees)	Mean exc. energy (MeV)	Mean angular momentum ($\hbar$)
$E_{0_{c.m.}}/V_{CB}$=1.00				
$^{267}_{104}$Rf	0.8589	9.79 ± 4.78	56.13 ± 22.36	20.12 ± 9.48
$^{270}_{105}$Db	0.6956	9.57 ± 4.74	73.68 ± 14.92	22.07 ± 10.83
$^{271}_{106}$Sg	0.4544	9.96 ± 5.43	81.65 ± 24.41	23.40 ± 11.69
$^{276}_{107}$Bh	0.7685	11.13 ± 5.40	72.66 ± 14.74	26.20 ± 14.09
$^{279}_{108}$Hs	0.6490	11.26 ± 4.77	110.67 ± 22.97	29.12 ± 15.35
$^{280}_{109}$Mt	0.4621	8.53 ± 4.35	59.76 ± 22.09	26.91 ± 14.74
$^{281}_{110}$Ds	0.3926	6.21 ± 2.39	11.49 ± 16.76	25.80 ± 14.15
$^{284}_{111}$Rg	0.3454	5.90 ± 2.21	42.92 ± 8.38	33.57 ± 15.56
$^{289}_{112}$Cn	0.3059	5.33 ± 2.06	26.39 ± 24.45	35.80 ± 15.77
$^{290}_{113}$Nh	0.2952	5.27 ± 1.65	34.16 ± 5.25	41.12 ± 11.94
$^{293}_{114}$Fl	0.3451	4.94 ± 1.49	43.94 ± 26.71	40.70 ± 11.08
$^{294}_{115}$Mc	0.4680	4.54 ± 1.25	22.26 ± 3.44	34.38 ± 12.80
$^{297}_{116}$Lv	0.8407	3.80 ± 1.27	50.68 ± 25.98	33.09 ± 13.42
$^{300}_{117}$Ts	1.360	2.74 ± 1.01	59.39 ± 25.85	29.51 ± 11.97
$^{302}_{118}$Og	0.9100	1.60 ± 0.69	67.41 ± 26.39	21.95 ± 8.92
$E_{0_{c.m.}}/V_{CB}$=1.05				
$^{267}_{104}$Rf	1.866	11.01 ± 4.33	52.97 ± 17.62	19.99 ± 7.08
$^{270}_{105}$Db	1.793	10.58 ± 4.36	68.22 ± 6.97	23.55 ± 7.96
$^{271}_{106}$Sg	0.9754	10.08 ± 4.33	75.93 ± 17.87	23.78 ± 7.89
$^{276}_{107}$Bh	1.050	10.23 ± 4.62	65.15 ± 8.54	26.51 ± 9.13
$^{279}_{108}$Hs	0.4574	9.40 ± 4.35	102.58 ± 20.49	25.27 ± 10.28
$^{280}_{109}$Mt	0.2679	9.39 ± 4.19	54.93 ± 22.32	22.55 ± 9.88
$^{281}_{110}$Ds	0.3664	8.86 ± 2.93	12.00 ± 16.35	23.20 ± 10.72
$^{284}_{111}$Rg	0.7376	8.51 ± 2.87	41.49 ± 8.20	23.44 ± 10.04

Continuation of Table 6.18.

ICF product	Total cross section (mb)	Mean angle (degrees)	Mean exc. energy (MeV)	Mean angular momentum ($\hbar$)
		$E_{0_{c.m.}}/V_{CB}$=1.05		
$^{289}_{112}$Cn	1.015	7.47 ± 2.87	18.21 ± 19.68	24.30 ± 11.13
$^{290}_{113}$Nh	1.069	7.28 ± 2.83	27.57 ± 8.43	24.19 ± 11.27
$^{293}_{114}$Fl	0.7053	7.02 ± 2.69	24.98 ± 21.88	23.67 ± 10.99
$^{294}_{115}$Mc	0.6241	5.83 ± 2.54	14.06 ± 4.94	22.00 ± 10.81
$^{297}_{116}$Lv	0.7617	5.05 ± 2.08	41.06 ± 23.72	23.20 ± 11.49
$^{300}_{117}$Ts	1.379	4.25 ± 1.92	51.53 ± 24.34	21.41 ± 10.69
$^{302}_{118}$Og	2.572	4.18 ± 1.80	59.21 ± 23.80	20.58 ± 10.90
		$E_{0_{c.m.}}/V_{CB}$=1.10		
$^{267}_{104}$Rf	1.248	11.95 ± 4.76	62.35 ± 16.79	23.35 ± 7.36
$^{270}_{105}$Db	1.826	11.21 ± 4.87	74.93 ± 7.21	26.78 ± 8.52
$^{271}_{106}$Sg	1.147	11.37 ± 4.78	83.17 ± 16.52	26.70 ± 8.35
$^{276}_{107}$Bh	1.195	10.78 ± 4.77	68.19 ± 6.69	28.93 ± 9.73
$^{279}_{108}$Hs	0.5308	10.63 ± 4.92	105.50 ± 20.24	27.44 ± 10.84
$^{280}_{109}$Mt	0.2573	9.00 ± 5.16	55.00 ± 21.94	27.37 ± 12.03
$^{281}_{110}$Ds	0.3291	5.90 ± 2.58	10.27 ± 14.92	29.96 ± 11.86
$^{284}_{111}$Rg	0.6997	5.77 ± 2.26	41.61 ± 12.87	29.16 ± 12.19
$^{289}_{112}$Cn	1.246	5.42 ± 2.02	20.60 ± 21.50	31.00 ± 12.91
$^{290}_{113}$Nh	1.516	5.60 ± 2.21	27.46 ± 11.05	31.30 ± 13.32
$^{293}_{114}$Fl	1.591	5.22 ± 1.94	27.34 ± 21.98	30.43 ± 13.76
$^{294}_{115}$Mc	2.116	5.56 ± 1.59	15.29 ± 5.58	29.43 ± 13.51
$^{297}_{116}$Lv	3.853	5.13 ± 1.43	46.26 ± 23.06	30.34 ± 13.31
$^{300}_{117}$Ts	9.240	4.05 ± 1.14	56.69 ± 23.13	29.18 ± 12.86
$^{302}_{118}$Og	13.14	2.90 ± 0.86	67.30 ± 22.19	28.97 ± 11.43

6.4 Results Summary

The following are observed general trends across the 18 studied reactions in this chapter, save for a few exceptions:

- The higher the projectile incident energy is, the higher the ICF product mean angle, mean excitation energy, and mean angular momentum are.
- The heavier the ICF product is, the more forward the mean angle is and the lower the associated standard deviation is.
- The heavier the ICF product is, the higher the mean excitation energy is (^{20}Ne-induced only).
- The heavier the ICF product is, the lower the mean angular momentum and associated standard deviations are (^{20}Ne-induced only).
- The total cross-sections for the heaviest two ICF products of any given reaction increase significantly more with incident energy above the Coulomb barrier than cross-sections for other ICF products do.
- The studied ^{20}Ne-induced reactions are universally preferable to the studied ^{40,48}Ca-induced reactions for the production of more stable like ICF products.
- It is preferable to use ^{20}Ne projectiles with incident energy $E_{0_{c.m.}}/V_{CB}$=1.00 and ^{40,48}Ca projectiles with incident energy $E_{0_{c.m.}}/V_{CB}$=1.05 to maximise the stability of the ICF products, at the expense of total production cross-sections.

The following are the orders of preference for producing the most stable like ICF products in ^{20}Ne-induced reactions, from most to least preferable (left to right):

- $^{263}_{103}$Lr: ^{20}Ne+^{252}Cf > ^{20}Ne+^{250}Cm.
- $^{264}_{104}$Rf: ^{20}Ne+^{252}Cf > ^{20}Ne+^{248}Cm.
- $^{265}_{104}$Rf: ^{20}Ne+^{254}Es > ^{20}Ne+^{256}Es.
- $^{266}_{104}$Rf: ^{20}Ne+^{254}Cf > ^{20}Ne+^{250}Cm.

- $^{266}_{105}$Db: ^{20}Ne+^{254}Es > ^{20}Ne+^{250}Cm.
- $^{270}_{107}$Bh: ^{20}Ne+^{254}Es > ^{20}Ne+^{252}Cf.
- $^{272}_{107}$Bh: ^{20}Ne+^{256}Es > ^{20}Ne+^{254}Cf.

The following are the orders of preference for producing the most stable like ICF products in ^{40,48}Ca-induced reactions, from most to least preferable (left to right):

- $^{264}_{104}$Rf: ^{40}Ca+^{252}Cf > ^{40}Ca+^{248}Cm.
- $^{265}_{104}$Rf: ^{40}Ca+^{254}Es > ^{48}Ca+^{254}Es.
- $^{266}_{104}$Rf: ^{40}Ca+^{254}Cf > ^{48}Ca+^{252}Cf > ^{40}Ca+^{250}Cm.
- $^{268}_{104}$Rf: ^{48}Ca+^{248}Cm > ^{48}Ca+^{254}Cf.
- $^{266}_{105}$Db: ^{40}Ca+^{254}Es > ^{40}Ca+^{252}Cf.
- $^{267}_{105}$Db: ^{48}Ca+^{252}Cf > ^{40}Ca+^{250}Cm.
- $^{268}_{105}$Db: ^{40}Ca+^{256}Es > ^{40}Ca+^{254}Cf > ^{48}Ca+^{254}Es.
- $^{268}_{106}$Sg: ^{40}Ca+^{252}Cf > ^{40}Ca+^{254}Es > ^{40}Ca+^{248}Cm.
- $^{270}_{106}$Sg: ^{40}Ca+^{254}Cf > ^{40}Ca+^{256}Es > ^{40}Ca+^{250}Cm.
- $^{274}_{106}$Sg: ^{48}Ca+^{250}Cm > ^{48}Ca+^{254}Cf.
- $^{273}_{107}$Bh: ^{48}Ca+^{248}Cm > ^{40}Ca+^{250}Cm.
- $^{272}_{108}$Hs: ^{40}Ca+^{252}Cf > ^{40}Ca+^{248}Cm.
- $^{274}_{108}$Hs: ^{40}Ca+^{254}Cf > ^{40}Ca+^{250}Cm.
- $^{278}_{108}$Hs: ^{48}Ca+^{250}Cm > ^{48}Ca+^{254}Cf.
- $^{277}_{109}$Mt: ^{48}Ca+^{252}Cf > ^{40}Ca+^{254}Cf.
- $^{276}_{110}$Ds: ^{40}Ca+^{248}Cm > ^{40}Ca+^{252}Cf.
- $^{278}_{110}$Ds: ^{40}Ca+^{254}Cf > ^{40}Ca+^{250}Cm.

- $^{279}_{110}$Ds: ^{48}Ca+^{254}Es > ^{40}Ca+^{256}Es.
- $^{282}_{110}$Ds: ^{48}Ca+^{248}Cm > ^{48}Ca+^{254}Cf.
- $^{278}_{111}$Rg: ^{40}Ca+^{254}Es > ^{40}Ca+^{252}Cf.
- $^{287}_{111}$Rg: ^{48}Ca+^{254}Cf > ^{48}Ca+^{250}Cm.
- $^{280}_{112}$Cn: ^{40}Ca+^{252}Cf > ^{40}Ca+^{254}Es.
- $^{282}_{112}$Cn: ^{40}Ca+^{254}Cf > ^{40}Ca+^{256}Es.
- $^{288}_{112}$Cn: ^{48}Ca+^{250}Cm > ^{48}Ca+^{254}Cf.
- $^{291}_{113}$Nh: ^{48}Ca+^{254}Cf > ^{48}Ca+^{250}Cm.
- $^{283}_{114}$Fl: ^{40}Ca+^{254}Es > ^{40}Ca+^{252}Cf.
- $^{285}_{114}$Fl: ^{40}Ca+^{256}Es > ^{40}Ca+^{254}Cf.
- $^{292}_{114}$Fl: ^{48}Ca+^{254}Cf > ^{48}Ca+^{248}Cm.
- $^{286}_{115}$Mc: ^{40}Ca+^{252}Cf > ^{40}Ca+^{248}Cm.
- $^{288}_{115}$Mc: ^{40}Ca+^{254}Cf > ^{40}Ca+^{250}Cm.
- $^{288}_{116}$Lv: ^{40}Ca+^{252}Cf > ^{40}Ca+^{254}Es.
- $^{290}_{116}$Lv: ^{40}Ca+^{254}Cf > ^{40}Ca+^{256}Es.
- $^{290}_{117}$Ts: ^{40}Ca+^{254}Es > ^{40}Ca+^{252}Cf.
- $^{298}_{117}$Ts: ^{48}Ca+^{254}Es > ^{48}Ca+^{252}Cf.
- $^{300}_{117}$Ts: ^{48}Ca+^{256}Es > ^{48}Ca+^{254}Cf.

Of all the primary SHE products presented here, many have not been directly synthesised before, though occur in decay chains of heavier nuclides. The following 53 primary SHE products predicted here have not been observed before: ^{269,271,273}Db, ^{272,274}Sg, ^{273,275,276,277}Bh, ^{276,278,279}Hs, ^{279,280,281,283}Mt, ^{276,282,284}Ds, ^{277,284,285,287}Rg, ^{279,280,287,288,289}Cn, ^{281,288,289,291}Nh, ^{283,291,293,294}Fl, ^{285,286,292,293,294,295,296}Mc, ^{288,295,297,298}Lv, ^{290,298,300}Ts and ^{292,300,302}Og.

In this chapter, ICF predictions of the model have been presented and discussed for SHE formation in 18 different reactions, at three different incident energies each. Chapter 7 contains resultant EVR cross-sections for the two most dominant SHE primary ICF products of each of the 18 reactions.

Chapter 7

Evaporation Residues

With model predictions for SHE production via the ICF mechanism presented in Chapter 6, it follows that fusion-evaporation is subsequently addressed for the benefit of planning experiments. Tables 7.1-7.12 contain evaporation residue (EVR) cross-sections of the two most prevalent SHE primary ICF products of each of the six ^{20}Ne-induced reactions: ^{264,266}Rf, ^{266,268}Db, ^{268,270}Sg, ^{270,272}Bh and ^{272,274}Hs. EVR cross-sections of the two most prevalent SHE primary ICF products of each of the twelve ^{40,48}Ca-induced reactions are discussed in Chapter 7.2. These EVR cross-sections were calculated using the fusion-evaporation code PACE4 (Projection Angular momentum Coupled Evaporation) [100–102], a modified version of the JULIAN code (the Hillman-Eyal evaporation code using a Monte Carlo code coupling angular momentum) and uses the Bass model [103], which was derived by using a Monte-Carlo approach to determine the decay of the compound system in the framework of Hauser-Feshbach formalism [104] combined with a geometric interpretation of available experimental data. The Bass model potential provides an overall excellent description for the fusion cross sections at energies at or above the Coulomb barrier [83]. The calculated mean excitation energies and angular momentum distributions presented in Chapter 6 are used as inputs for the presented PACE4 results. Fission barrier parameters were sourced from calculations in the macroscopic-microscopic finite-range liquid-drop model [105]. A Fermi gas level density parameter of $a = A/12$ MeV^{-1} was used, with the ratio of this parameter at the saddle point to the ground state value being taken from Ref. [106], wherein a two-step

approach for level calculation is applied involving (i) the macroscopic-microscopic (MM) method to determine all necessary minima and saddle points (the minima are calculated by using multidimensional minimisation while the saddle points are calculated by applying the imaginary water flow technique (IWF) on multidimensional energy grids), and (ii) a statistical formalism allowing the estimation of the level-density parameters at these extreme points by employing the deformed single-particle spectra. The shell and pairing effects were found to decrease with excitation energy and the ratios reached asymptotic values more or less equal to 1.1 [106].

7.1 ^{20}Ne-induced primary incomplete fusion products

7.1.1 ^{20}Ne+^{248}Cm primary incomplete fusion products

Table 7.1 shows that for the primary ICF product ^{264}Rf (from the reaction ^{20}Ne+^{248}Cm), the main EVR at $E_{0_{c.m.}}/V_{CB} = 1.00$ is ^{257}No, with a percentage yield of over 58%, followed by ^{256}No with a percentage yield of 12%. At $E_{0_{c.m.}}/V_{CB} = 1.05$, the main EVR is still ^{257}No with a percentage yield of 48%, followed by ^{256}No with a percentage yield of 23%. At $E_{0_{c.m.}}/V_{CB} = 1.10$, the main EVR is ^{256}No with a percentage yield of 43%, followed by ^{257}No with a percentage yield of 27%. The percentage total fission of the primary ICF product ^{264}Rf increases with incident energy: 16%, 19% and 23% at $E_{0_{c.m.}}/V_{CB} = 1.00$, 1.05 and 1.10 respectively. In Ref. [97], the heaviest observed multinucleon transfer (MNT) products so far in the reaction ^{20}Ne+^{248}Cm are ^{256}Md and ^{256}Fm [107], which are notably lighter than the heaviest predicted ICF products here. This suggests that it would be possible to produce and detect new isotopes with the ICF mechanism.

Table 7.2 shows that for the primary ICF product ^{266}Db (from the reaction ^{20}Ne+^{248}Cm), the main EVR at $E_{0_{c.m.}}/V_{CB} = 1.00$ is ^{258}Lr, with a percentage yield of 58%, followed by ^{259}Lr with a percentage yield of 10%. At $E_{0_{c.m.}}/V_{CB} = 1.05$, the main EVR is still ^{258}Lr with a percentage yield of 59%, followed by ^{257}Lr with a percentage yield of 9%. At $E_{0_{c.m.}}/V_{CB} = 1.10$, the main EVR remains ^{258}Lr with a percentage yield of 43%, foll1lowed by ^{257}Lr with a percentage yield of 27%. The percentage total fission of the primary ICF product ^{264}Rf does not appear to vary greatly with incident energy: 28%, 26% and 28% at $E_{0_{c.m.}}/V_{CB} = 1.00$, 1.05 and 1.10 respectively.

Table 7.1: Evaporation residue (EVR) cross-sections for the primary ICF product ^{264}Rf, from the reaction ^{20}Ne+^{248}Cm. The total combined cross-sections over 100,000 cascades are 18.75 mb, 194.6 mb and 1.161×10^3 mb at $E_{0_{c.m.}}/V_{CB} = 1.00$, 1.05 and 1.10 respectively.

EVR	Percentage yield		
$E_{0_{C.M.}}/V_{CB}$	1.00	1.05	1.10
$^{262}_{103}$Lr	0.002 %	-	-
$^{261}_{103}$Lr	0.881 %	0.274 %	0.053 %
$^{261}_{102}$No	0.002 %	-	0.001 %
$^{260}_{103}$Lr	8.243 %	6.676 %	3.439 %
$^{260}_{102}$No	-	0.001 %	0.005 %
$^{259}_{103}$Lr	0.495 %	1.328 %	3.602 %
$^{259}_{102}$No	0.001 %	-	-
$^{259}_{101}$Md	0.001 %	0.001 %	-
$^{258}_{102}$No	4.104 %	1.595 %	0.414 %
$^{258}_{101}$Md	0.006 %	0.007 %	0.003 %
$^{257}_{102}$No	58.528 %	47.979 %	26.554 %
$^{257}_{101}$Md	0.009 %	0.009 %	0.026 %
$^{256}_{102}$No	12.051 %	23.256 %	42.974 %
$^{256}_{101}$Md	-	0.001 %	0.001 %
$^{255}_{102}$No	-	0.005 %	0.100 %
$^{255}_{100}$Fm	0.021 %	0.022 %	0.011 %
$^{254}_{100}$Fm	0.084 %	0.113 %	0.156 %
$^{253}_{100}$Fm	0.003 %	0.003 %	0.056 %
Total fission	15.569 %	18.730 %	22.605 %
TOTAL	100.000 %	100.000 %	100.000 %

Table 7.2: The same results as in Table 7.1, but for the primary ICF product ^{266}Db, from the reaction ^{20}Ne+^{248}Cm. The total combined cross-sections over 100,000 cascades are 4.346 mb, 185.6 mb and 962.3 mb at $E_{0_{c.m.}}/V_{CB}$ = 1.00, 1.05 and 1.10 respectively.

EVR	Percentage yield		
$E_{0_{C.M.}}/V_{CB}$	1.00	1.05	1.10
$^{260}_{103}$Lr	0.017 %	0.007 %	0.003 %
$^{260}_{102}$No	0.001 %	0.001 %	-
$^{259}_{103}$Lr	10.350 %	5.288 %	1.506 %
$^{259}_{102}$No	0.037 %	0.040 %	0.012 %
$^{258}_{103}$Lr	57.849 %	58.979 %	42.219 %
$^{258}_{102}$No	0.085 %	0.105 %	0.187 %
$^{257}_{103}$Lr	3.651 %	8.832 %	27.132 %
$^{257}_{102}$No	-	0.001 %	0.020 %
$^{257}_{101}$Md	0.004 %	0.002 %	0.001 %
$^{256}_{103}$Lr	-	-	0.053 %
$^{256}_{102}$No	-	-	0.001 %
$^{256}_{101}$Md	0.106 %	0.074 %	0.046 %
$^{255}_{101}$Md	0.214 %	0.308 %	0.439 %
$^{254}_{101}$Md	0.005 %	0.024 %	0.098 %
Total fission	27.681 %	26.339 %	28.283 %
TOTAL	100.000 %	100.000 %	100.000 %

7.1.2 ^{20}Ne+^{250}Cm primary incomplete fusion products

Table 7.3 shows that for the primary ICF product ^{266}Rf (from the reaction ^{20}Ne+^{250}Cm), the main EVR at $E_{0_{c.m.}}/V_{CB} = 1.00$ is ^{259}No, with a percentage yield of 49%, followed by ^{258}No with a percentage yield of 34%. At $E_{0_{c.m.}}/V_{CB} = 1.05$, the main EVR is ^{258}No with a percentage yield of 56%, followed by ^{259}No with a percentage yield of 28%. At $E_{0_{c.m.}}/V_{CB} = 1.10$, the main EVR is ^{258}No with a percentage yield of 69%, followed by ^{258}No with a percentage yield of 14%. The percentage total fission of the primary ICF product ^{266}Rf increases with incident energy at a much more hampered rate than with ^{264}Rf: 1.4%, 1.8% and 2.9% at $E_{0_{c.m.}}/V_{CB} = 1.00$, 1.05 and 1.10 respectively.

Table 7.4 shows that for the primary ICF product ^{268}Db (from the reaction ^{20}Ne+^{250}Cm), the main EVR at $E_{0_{c.m.}}/V_{CB} = 1.00$ is ^{260}Lr, with a percentage yield of 58%, followed by ^{259}Lr with a percentage yield of 32%. At $E_{0_{c.m.}}/V_{CB} = 1.05$, the main EVR is ^{259}Lr with a percentage yield of 49%, followed closely by ^{260}Lr with a percentage yield of 42%. At $E_{0_{c.m.}}/V_{CB} = 1.10$, the main EVR remains ^{259}Lr with a percentage yield of 66%, followed by ^{260}Lr with a percentage yield of 21%. The percentage total fission of the primary ICF product ^{268}Db increases with incident energy: 5.6%, 6.7% and 10.4% at $E_{0_{c.m.}}/V_{CB} = 1.00$, 1.05 and 1.10 respectively.

Table 7.3: The same results as in Table 7.1, but for the primary ICF product ^{266}Rf, from the reaction ^{20}Ne+^{250}Cm. The total combined cross-sections over 100,000 cascades are 6.721 mb, 291.8 mb and 1.058×10^3 mb at $E_{0_{c.m.}}/V_{CB} = 1.00$, 1.05 and 1.10 respectively.

EVR	Percentage yield		
$E_{0_{C.M.}}/V_{CB}$	1.00	1.05	1.10
$^{263}_{103}$Lr	0.495 %	0.116 %	0.022 %
$^{263}_{102}$No	0.002 %	0.001 %	-
$^{262}_{103}$Lr	10.005 %	6.434 %	2.994 %
$^{262}_{102}$No	0.002 %	0.005 %	0.003 %
$^{261}_{103}$Lr	2.952 %	6.638 %	9.169 %
$^{261}_{102}$No	-	0.001 %	0.002 %
$^{260}_{103}$Lr	-	-	0.022 %
$^{260}_{102}$No	1.375 %	0.459 %	0.178 %
$^{260}_{101}$Md	0.001 %	-	0.003 %
$^{259}_{102}$No	49.304 %	28.035 %	14.045 %
$^{259}_{101}$Md	0.012 %	0.011 %	0.014 %
$^{258}_{102}$No	34.328 %	56.238 %	68.837 %
$^{258}_{101}$Md	-	0.002 %	0.003 %
$^{257}_{102}$No	0.018 %	0.193 %	1.694 %
$^{257}_{100}$Fm	0.011 %	0.004 %	0.005 %
$^{256}_{100}$Fm	0.053 %	0.083 %	0.087 %
$^{255}_{100}$Fm	0.006 %	0.013 %	0.042 %
$^{254}_{100}$Fm	-	-	0.001 %
Total fission	1.436 %	1.767 %	2.879 %
TOTAL	100.000 %	100.000 %	100.000 %

Table 7.4: The same results as in Table 7.1, but for the primary ICF product ^{268}Db, from the reaction ^{20}Ne+^{250}Cm. The total combined cross-sections over 100,000 cascades are 1.576 mb, 218.9 mb and 1.009×10^3 mb at $E_{0_{c.m.}}/V_{CB} = 1.00$, 1.05 and 1.10 respectively.

EVR	Percentage yield		
$E_{0_{C.M.}}/V_{CB}$	1.00	1.05	1.10
$^{262}_{103}$Lr	0.001 %	0.002 %	0.001 %
$^{261}_{103}$Lr	4.387 %	1.857 %	0.559 %
$^{261}_{102}$No	0.013 %	0.007 %	0.004 %
$^{260}_{103}$Lr	58.007 %	42.113 %	20.812 %
$^{260}_{102}$No	0.071 %	0.082 %	0.083 %
$^{259}_{103}$Lr	31.713 %	48.866 %	65.969 %
$^{259}_{102}$No	0.004 %	0.009 %	0.039 %
$^{259}_{101}$Md	0.001 %	-	-
$^{258}_{103}$Lr	0.015 %	0.144 %	1.795 %
$^{258}_{101}$Md	0.036 %	0.025 %	0.015 %
$^{257}_{101}$Md	0.157 %	0.155 %	0.188 %
$^{256}_{101}$Md	0.011 %	0.040 %	0.128 %
$^{255}_{101}$Md	-	0.001 %	0.003 %
Total fission	5.584 %	6.699 %	10.404 %
TOTAL	100.000 %	100.000 %	100.000 %

7.1.3 ^{20}Ne+^{252}Cf primary incomplete fusion products

Table 7.5: The same results as in Table 7.1, but for the primary ICF product ^{268}Sg, from the reaction ^{20}Ne+^{252}Cf. The total combined cross-sections over 100,000 cascades are 16.77 mb, 307.5 mb and 1.145×10^3 mb at $E_{0_{c.m.}}/V_{CB} = 1.00$, 1.05 and 1.10 respectively.

EVR	Percentage yield		
$E_{0_{C.M.}}/V_{CB}$	1.00	1.05	1.10
$^{264}_{106}$Sg	0.004 %	0.001 %	0.001 %
$^{263}_{106}$Sg	-	-	0.002 %
Total fission	99.996 %	99.999 %	99.997 %
TOTAL	100.000 %	100.000 %	100.000 %

Tables 7.5-7.6 show that for the primary ICF products ^{268}Sg and ^{270}Bh (from the reaction ^{20}Ne+^{252}Cf), almost all EVRs are lost to fission, with only a small handful of lighter Sg and Bh isotope yields. Fission likely dominates because the fission barriers of the primary ICF products should be significantly smaller than the barriers involved in n-, p-, and α-decay modes. All the barriers are affected by the angular momenta of the rotating ICF products due to centrifugal effects. For a given angular momentum, the smaller the moment of inertia associated with a decay mode, the larger the corresponding centrifugal barrier. The moments of inertia associated with n-, p-, and α-emissions are smaller than that for fission because the moment of inertia is proportional to the corresponding reduced mass.

Table 7.6: The same results as in Table 7.1, but for the primary ICF product ^{270}Bh, from the reaction ^{20}Ne+^{252}Cf. The total combined cross-sections over 100,000 cascades are 2.922 mb, 252.6 mb and 947.2 mb at $E_{0_{c.m.}}/V_{CB} = 1.00$, 1.05 and 1.10 respectively.

EVR	Percentage yield		
$E_{0_{C.M.}}/V_{CB}$	1.00	1.05	1.10
$^{265}_{107}$Bh	0.001 %	-	-
$^{265}_{106}$Sg	0.001 %	-	-
Total fission	99.998 %	100.000 %	100.000 %
TOTAL	100.000 %	100.000 %	100.000 %

7.1.4 ^{20}Ne+^{254}Cf primary incomplete fusion products

Table 7.7: The same results as in Table 7.1, but for the primary ICF product ^{270}Sg, from the reaction ^{20}Ne+^{254}Cf. The total combined cross-sections over 100,000 cascades are 17.50 mb, 228.2 mb and 1.117×10^3 mb at $E_{0_{c.m.}}/V_{CB} = 1.00$, 1.05 and 1.10 respectively.

EVR	Percentage yield		
$E_{0_{C.M.}}/V_{CB}$	1.00	1.05	1.10
$^{266}_{106}$Sg	0.053 %	0.028 %	0.009 %
$^{265}_{106}$Sg	-	0.002 %	0.003 %
Total fission	99.947 %	99.970 %	99.988 %
TOTAL	100.000 %	100.000 %	100.000 %

Tables 7.7-7.8 show that for the primary ICF products ^{270}Sg and ^{272}Bh (from the reaction ^{20}Ne+^{254}Cf), EVRs are similarly suppressed as with their lighter counterparts in Tables 7.5-7.6, however there is a noticeable increase in Sg EVRs from the primary ICF product ^{270}Sg over those of ^{268}Sg, likely due to the lower fission barrier of ^{270}Sg. For ^{272}Bh, all EVRs are lost to fission.

Table 7.8: The same results as in Table 7.1, but for the primary ICF product ^{272}Bh, from the reaction ^{20}Ne+^{254}Cf. The total combined cross-sections over 100,000 cascades are 2.442 mb, 204.2 mb and 986.4 mb at $E_{0_{c.m.}}/V_{CB} = 1.00$, 1.05 and 1.10 respectively.

EVR	Percentage yield		
$E_{0_{C.M.}}/V_{CB}$	1.00	1.05	1.10
Total fission	100.000 %	100.000 %	100.000 %
TOTAL	100.000 %	100.000 %	100.000 %

7.1.5 ^{20}Ne+^{254}Es primary incomplete fusion products

Table 7.9: The same results as in Table 7.1, but for the primary ICF product ^{270}Bh, from the reaction ^{20}Ne+^{254}Es. The total combined cross-sections over 100,000 cascades are 33.91 mb, 395.8 mb and 1.148×10^3 mb at $E_{0_{c.m.}}/V_{CB} = 1.00$, 1.05 and 1.10 respectively.

EVR	Percentage yield		
$E_{0_{C.M.}}/V_{CB}$	1.00	1.05	1.10
$^{266}_{107}$Bh	0.001 %	-	-
$^{266}_{106}$Sg	0.001 %	0.001 %	-
$^{265}_{107}$Bh	-	-	0.002 %
Total fission	99.998 %	99.999 %	99.998 %
TOTAL	100.000 %	100.000 %	100.000 %

Tables 7.9-7.10 show that for the primary ICF products ^{270}Bh and ^{272}Hs (from the reaction ^{20}Ne+^{254}Es), virtually all EVRs are again lost to fission in a similar fashion. The tiny amount of Sg and Bh produced results from n-, p- and γ-emission from the primary ^{270}Bh.

Table 7.10: The same results as in Table 7.1, but for the primary ICF product ^{272}Hs, from the reaction ^{20}Ne+^{254}Es. The total combined cross-sections over 100,000 cascades are 7.280 mb, 301.5 mb and 993.4 mb at $E_{0_{c.m.}}/V_{CB} = 1.00$, 1.05 and 1.10 respectively.

EVR	Percentage yield		
$E_{0_{C.M.}}/V_{CB}$	1.00	1.05	1.10
Total fission	100.000 %	100.000 %	100.000 %
TOTAL	100.000 %	100.000 %	100.000 %

7.1.6 ^{20}Ne+^{256}Es primary incomplete fusion products

Table 7.11: The same results as in Table 7.1, but for the primary ICF product ^{272}Bh, from the reaction ^{20}Ne+^{256}Es. The total combined cross-sections over 100,000 cascades are 40.23 mb, 260.5 mb and 1.174×10^3 mb at $E_{0_{c.m.}}/V_{CB} = 1.00$, 1.05 and 1.10 respectively.

EVR	Percentage yield		
$E_{0_{C.M.}}/V_{CB}$	1.00	1.05	1.10
$^{267}_{106}$Sg	0.001 %	0.001 %	0.001 %
Total fission	99.999 %	99.999 %	99.999 %
TOTAL	100.000 %	100.000 %	100.000 %

Tables 7.11-7.12 show that for the primary ICF products ^{272}Bh and ^{274}Hs (from the reaction ^{20}Ne+^{256}Es), virtually all EVRs are again lost to fission in a similar fashion. The tiny amount of ^{267}Sg and ^{268}Hs produced results from n-, p- and γ-emission from the primary ^{272}Bh and ^{274}Hs respectively.

Table 7.12: The same results as in Table 7.1, but for the primary ICF product ^{274}Hs, from the reaction ^{20}Ne+^{256}Es. The total combined cross-sections over 100,000 cascades are 6.000 mb, 256.6 mb and 953.3 mb at $E_{0_{c.m.}}/V_{CB} = 1.00$, 1.05 and 1.10 respectively.

EVR	Percentage yield		
$E_{0_{C.M.}}/V_{CB}$	1.00	1.05	1.10
$^{268}_{108}$Hs	-	0.001 %	-
Total fission	100.000 %	99.999 %	100.000 %
TOTAL	100.000 %	100.000 %	100.000 %

7.2 ^{40,48}Ca-induced primary incomplete fusion products

The following listed products are the two heaviest SHE primary ICF products of each of the twelve Ca-induced reactions studied:

- ^{40}Ca+^{248}Cm: $^{284}_{114}$Fl and $^{286}_{115}$Mc.
- ^{40}Ca+^{250}Cm: $^{286}_{114}$Fl and $^{288}_{115}$Mc.
- ^{40}Ca+^{252}Cf: $^{288}_{116}$Lv and $^{290}_{117}$Ts.
- ^{40}Ca+^{254}Cf: $^{290}_{116}$Lv and $^{292}_{117}$Ts.
- ^{40}Ca+^{254}Es: $^{290}_{117}$Ts and $^{292}_{118}$Og.
- ^{40}Ca+^{256}Es: $^{292}_{117}$Ts and $^{294}_{118}$Og.
- ^{48}Ca+^{248}Cm: $^{292}_{114}$Fl and $^{294}_{115}$Mc.
- ^{48}Ca+^{250}Cm: $^{294}_{114}$Fl and $^{296}_{115}$Mc.
- ^{48}Ca+^{252}Cf: $^{296}_{116}$Lv and $^{298}_{117}$Ts.
- ^{48}Ca+^{254}Cf: $^{298}_{116}$Lv and $^{300}_{117}$Ts.
- ^{48}Ca+^{254}Es: $^{298}_{117}$Ts and $^{300}_{118}$Og.

- ^{48}Ca+^{256}Es: $^{300}_{117}$Ts and $^{302}_{118}$Og.

For all 24 of these primary ICF products, 100% of EVRs are lost to fission. In lieu of more detailed information on these heavier and more abundant SHE primary ICF products, EVRs of primary ICF products from ^{40,48}Ca-induced reactions are presented in Tables 7.13-7.34 for direct comparison with like primary ICF products from ^{20}Ne-induced reactions in Tables 7.1-7.12.

7.2.1 ^{40}Ca+^{248}Cm primary incomplete fusion products

Table 7.13 shows that for the primary ICF product ^{264}Rf (from the reaction ^{40}Ca+^{248}Cm), the main EVR at $E_{0_{c.m.}}/V_{CB} = 1.00$ is ^{257}No, with a percentage yield of 51%, followed by ^{256}No with a percentage yield of 20%. At $E_{0_{c.m.}}/V_{CB} = 1.05$, the main EVR is ^{256}No with a percentage yield of 41%, followed by ^{257}No with a percentage yield of 28%. At $E_{0_{c.m.}}/V_{CB} = 1.10$, the main EVR is ^{256}No with a percentage yield of 52%, followed by ^{257}No with a percentage yield of 9%. The percentage total fission of the primary ICF product ^{264}Rf increases with incident energy at an increased rate here than from the reaction ^{20}Ne+^{248}Cm (Table 7.1): 19%, 24% and 31% at $E_{0_{c.m.}}/V_{CB} = 1.00$, 1.05 and 1.10 respectively. On the whole, ^{264}Rf produced in the reaction ^{20}Ne+^{248}Cm results in higher percentages of heavier EVRs, and lower percentages of fission, than ^{264}Rf produced in the reaction ^{40}Ca+^{248}Cm. ^{264}Rf produced in the reaction ^{20}Ne+^{248}Cm has higher production cross-sections, lower mean excitation energies and lower mean angular momenta at all three studied incident energies.

Tables 7.14-7.15 show that for the primary ICF products ^{268}Sg and ^{272}Hs (from the reaction ^{40}Ca+^{248}Cm), almost all EVRs are lost to fission, as with their counterparts produced in ^{20}Ne-induced reactions (Tables 7.5 and 7.10 respectively). A notable difference here is that the ^{262}Sg EVRs shown in Table 7.14 are lighter than the ^{263,264}Sg shown in Table 7.5. ^{268}Sg produced in the reaction ^{20}Ne+^{252}Cf has higher production cross-sections, lower mean excitation energies and lower mean angular momenta at all three studied incident energies. In the case of ^{272}Hs all EVRs are again lost to fission (Tables 7.10 and 7.15).

Table 7.13: The same results as in Table 7.1, but for the primary ICF product ^{264}Rf, from the reaction ^{40}Ca+^{248}Cm. The total combined cross-sections over 100,000 cascades are 9.218 mb, 8.464 mb and 7.542 mb at $E_{0_{c.m.}}/V_{CB}$ = 1.00, 1.05 and 1.10 respectively.

EVR	Percentage yield		
$E_{0_{C.M.}}/V_{CB}$	1.00	1.05	1.10
$^{261}_{103}$Lr	0.355 %	0.055 %	0.005 %
$^{260}_{103}$Lr	6.689 %	3.365 %	1.004 %
$^{260}_{102}$No	0.002 %	0.006 %	0.009 %
$^{259}_{103}$Lr	0.988 %	3.322 %	4.937 %
$^{259}_{102}$No	0.001 %	0.002 %	0.002 %
$^{259}_{101}$Md	0.001 %	-	-
$^{258}_{103}$Lr	-	-	0.027 %
$^{258}_{102}$No	2.025 %	0.430 %	0.073 %
$^{258}_{101}$Md	0.009 %	0.005 %	0.002 %
$^{257}_{102}$No	51.166 %	27.560 %	8.936 %
$^{257}_{101}$Md	0.019 %	0.026 %	0.022 %
$^{256}_{102}$No	19.652 %	41.020 %	51.743 %
$^{256}_{101}$Md	0.001 %	0.006 %	0.015 %
$^{255}_{102}$No	-	0.073 %	1.526 %
$^{255}_{100}$Fm	0.022 %	0.012 %	0.006 %
$^{254}_{100}$Fm	0.091 %	0.151 %	0.143 %
$^{253}_{100}$Fm	0.012 %	0.042 %	0.132 %
$^{252}_{100}$Fm	-	-	0.004 %
Total fission	18.967 %	23.925 %	31.414 %
TOTAL	100.000 %	100.000 %	100.000 %

Table 7.14: The same results as in Table 7.1, but for the primary ICF product ^{268}Sg, from the reaction ^{40}Ca+^{248}Cm. The total combined cross-sections over 100,000 cascades are 1.406 mb, 1.221×10^{-1} mb and 1.198×10^{-1} mb at $E_{0_{c.m.}}/V_{CB}$ = 1.00, 1.05 and 1.10 respectively.

EVR	Percentage yield		
$E_{0_{C.M.}}/V_{CB}$	1.00	1.05	1.10
$^{262}_{106}$Sg	-	0.002 %	-
Total fission	100.000 %	99.998 %	100.000 %
TOTAL	100.000 %	100.000 %	100.000 %

Table 7.15: The same results as in Table 7.1, but for the primary ICF product ^{272}Hs, from the reaction ^{40}Ca+^{248}Cm. The total combined cross-sections over 100,000 cascades are 1.900 mb, 6.135 mb and 5.534 mb at $E_{0_{c.m.}}/V_{CB}$ = 1.00, 1.05 and 1.10 respectively.

EVR	Percentage yield		
$E_{0_{C.M.}}/V_{CB}$	1.00	1.05	1.10
Total fission	100.000 %	100.000 %	100.000 %
TOTAL	100.000 %	100.000 %	100.000 %

7.2.2 ^{40}Ca+^{250}Cm primary incomplete fusion products

Table 7.16 shows that for the primary ICF product ^{266}Rf (from the reaction ^{40}Ca+^{250}Cm), the main EVR at $E_{0_{c.m.}}/V_{CB} = 1.00$ is ^{258}No, with a percentage yield of 70%, followed by ^{259}No with a percentage yield of 13%. At $E_{0_{c.m.}}/V_{CB} = 1.05$, the main EVR is also ^{258}No with a percentage yield of 65%, followed by ^{259}No with a percentage yield of 18%. At $E_{0_{c.m.}}/V_{CB} = 1.10$, the main EVR remains ^{258}No with a percentage yield of 66%, followed by ^{261}Lr with a percentage yield of 9%. The percentage total fission of the primary ICF product ^{266}Rf increases with incident energy at a slightly increased rate here than from the reaction ^{20}Ne+^{250}Cm (Table 7.3): 2.3%, 3.7% and 7.8% at $E_{0_{c.m.}}/V_{CB} = 1.00$, 1.05 and 1.10 respectively. On the whole, ^{266}Rf produced in the reaction ^{20}Ne+^{250}Cm results in higher percentages of heavier EVRs, and lower percentages of fission, than ^{266}Rf produced in the reaction ^{40}Ca+^{250}Cm. ^{264}Rf produced in the reaction ^{20}Ne+^{248}Cm has higher production cross-sections, lower mean excitation energies and lower mean angular momenta at all three studied incident energies.

Tables 7.17-7.18 show that for the primary ICF products ^{270}Sg and ^{274}Hs (from the reaction ^{40}Ca+^{250}Cm), almost all EVRs are lost to fission, as with their counterparts produced in ^{20}Ne-induced reactions (Tables 7.7 and 7.12 respectively). The notable differences here are that the ^{264}Sg EVRs shown in Table 7.17 are lighter and far fewer than the ^{265,266}Sg shown in Table 7.7. ^{270}Sg produced in the reaction ^{20}Ne+^{254}Cf has higher production cross-sections, lower mean excitation energies and lower mean angular momenta at all three studied incident energies. In the case of ^{274}Hs all EVRs are lost to fission (Table 7.18).

Table 7.16: The same results as in Table 7.1, but for the primary ICF product ^{266}Rf, from the reaction ^{40}Ca+^{250}Cm. The total combined cross-sections over 100,000 cascades are 7.122 mb, 8.027 mb and 7.351 mb at $E_{0_{c.m.}}/V_{CB} = 1.00$, 1.05 and 1.10 respectively.

EVR	Percentage yield		
$E_{0_{C.M.}}/V_{CB}$	1.00	1.05	1.10
$^{263}_{103}$Lr	0.045 %	0.039 %	0.012 %
$^{262}_{103}$Lr	3.280 %	3.487 %	1.269 %
$^{262}_{102}$No	0.001 %	0.004 %	0.005 %
$^{261}_{103}$Lr	9.712 %	7.687 %	8.830 %
$^{261}_{102}$No	-	0.002 %	0.001 %
$^{260}_{103}$Lr	0.016 %	0.018 %	0.481 %
$^{260}_{102}$No	0.134 %	0.258 %	0.060 %
$^{260}_{101}$Md	-	0.001 %	0.001 %
$^{259}_{102}$No	13.101 %	18.278 %	6.422 %
$^{259}_{101}$Md	0.017 %	0.012 %	0.022 %
$^{258}_{102}$No	69.711 %	65.253 %	66.390 %
$^{258}_{101}$Md	0.003 %	0.002 %	0.013 %
$^{257}_{102}$No	1.502 %	1.132 %	8.545 %
$^{257}_{100}$Fm	0.004 %	0.007 %	0.002 %
$^{256}_{102}$No	-	-	0.022 %
$^{256}_{100}$Fm	0.101 %	0.089 %	0.071 %
$^{255}_{100}$Fm	0.038 %	0.032 %	0.089 %
$^{254}_{100}$Fm	0.001 %	-	0.005 %
Total fission	2.334 %	3.699 %	7.760 %
TOTAL	100.000 %	100.000 %	100.000 %

Table 7.17: The same results as in Table 7.1, but for the primary ICF product ^{270}Sg, from the reaction ^{40}Ca+^{250}Cm. The total combined cross-sections over 100,000 cascades are 6.241×10^{-1} mb, 3.834×10^{-2} mb and 1.043×10^{-2} mb at $E_{0_{c.m.}}/V_{CB}$ = 1.00, 1.05 and 1.10 respectively.

EVR	Percentage yield		
$E_{0_{C.M.}}/V_{CB}$	1.00	1.05	1.10
$^{264}_{106}$Sg	0.004 %	-	-
Total fission	99.996 %	100.000 %	100.000 %
TOTAL	100.000 %	100.000 %	100.000 %

Table 7.18: The same results as in Table 7.1, but for the primary ICF product ^{274}Hs, from the reaction ^{40}Ca+^{250}Cm. The total combined cross-sections over 100,000 cascades are 1.637 mb, 6.641 mb and 4.960 mb at $E_{0_{c.m.}}/V_{CB}$ = 1.00, 1.05 and 1.10 respectively.

EVR	Percentage yield		
$E_{0_{C.M.}}/V_{CB}$	1.00	1.05	1.10
Total fission	100.000 %	100.000 %	100.000 %
TOTAL	100.000 %	100.000 %	100.000 %

7.2.3 ^{40}Ca+^{252}Cf primary incomplete fusion products

Table 7.19 shows that for the primary ICF product ^{264}Rf (from the reaction ^{40}Ca+^{252}Cf), the main EVR at $E_{0_{c.m.}}/V_{CB} = 1.00$ is ^{257}No, with a percentage yield of 49%, followed by ^{258}No with a percentage yield of 19%. At $E_{0_{c.m.}}/V_{CB} = 1.05$, the main EVR is ^{258}No with a percentage yield of 36%, followed by ^{257}No with a percentage yield of 30%. At $E_{0_{c.m.}}/V_{CB} = 1.10$, the main EVR is ^{257}No with a percentage yield of 44%, followed by ^{256}No with a percentage yield of 14%. The percentage total fission of the primary ICF product ^{264}Rf increases with incident energy at a more steady rate here than from the reaction ^{20}Ne+^{248}Cm (Table 7.1): 24%, 28% and 33% at $E_{0_{c.m.}}/V_{CB} = 1.00$, 1.05 and 1.10 respectively. On the whole, ^{264}Rf produced in the reaction ^{20}Ne+^{248}Cm results in lower percentages of heavier EVRs, and lower percentages of fission, than ^{264}Rf produced in the reaction ^{40}Ca+^{252}Cf. ^{264}Rf produced in the reaction ^{20}Ne+^{248}Cm has higher production cross-sections, higher mean excitation energies and lower mean angular momenta at all three studied incident energies.

Table 7.20 shows that for the primary ICF product ^{266}Db (from the reaction ^{40}Ca+^{252}Cf), the main EVR at $E_{0_{c.m.}}/V_{CB} = 1.00$ is ^{259}Lr, with a percentage yield of 34.7%, followed very closely by ^{258}Lr with a percentage yield of 34.6%. At $E_{0_{c.m.}}/V_{CB} = 1.05$, the main EVR is ^{259}Lr with a percentage yield of 45%, followed by ^{258}Lr with a percentage yield of 24%. At $E_{0_{c.m.}}/V_{CB} = 1.10$, the roles are reversed and the main EVR is ^{258}Lr with a percentage yield of 46%, followed by ^{259}Lr with a percentage yield of 14%. The percentage total fission of the primary ICF product ^{266}Db increases with incident energy at a more consistent rate here than from the reaction ^{20}Ne+^{248}Cm (Table 7.2): 29.9%, 30.0% and 37% at $E_{0_{c.m.}}/V_{CB} = 1.00$, 1.05 and 1.10 respectively. On the whole, ^{266}Db produced in the reaction ^{20}Ne+^{248}Cm results in lower percentages of heavier EVRs, and lower percentages of fission, than ^{266}Db produced in the reaction ^{40}Ca+^{252}Cf. ^{266}Db produced in the reaction ^{20}Ne+^{248}Cm has higher production cross-sections, higher mean excitation energies and lower mean angular momenta at all three studied incident energies.

Tables 7.21-7.22 show that for the primary ICF products ^{268}Sg and ^{272}Hs (from the reaction ^{40}Ca+^{252}Cf), almost all EVRs are lost to fission, as with their counterparts produced in ^{20}Ne-induced reactions (Tables 7.5 and 7.10 respectively). A notable dif-

ference here is that the ^{263,264}Sg EVRs shown in Table 7.21 are slightly fewer than those shown in Table 7.5. ^{268}Sg produced in the reaction ^{20}Ne+^{252}Cf has higher production cross-sections, lower mean excitation energies and lower mean angular momenta at all three studied incident energies. In the case of ^{272}Hs all EVRs are again lost to fission (Tables 7.10 and7.22).

Table 7.19: The same results as in Table 7.1, but for the primary ICF product ^{264}Rf, from the reaction ^{40}Ca+^{252}Cf. The total combined cross-sections over 100,000 cascades are 4.793 mb, 7.550 mb and 5.583 mb at $E_{0_{c.m.}}/V_{CB} = 1.00$, 1.05 and 1.10 respectively.

EVR	Percentage yield		
$E_{0_{C.M.}}/V_{CB}$	1.00	1.05	1.10
$^{262}_{103}$Lr	0.003 %	0.025 %	-
$^{261}_{103}$Lr	2.578 %	3.874 %	0.277 %
$^{261}_{102}$No	0.001 %	0.001 %	0.001 %
$^{260}_{103}$Lr	3.729 %	1.399 %	4.189 %
$^{259}_{103}$Lr	0.007 %	-	0.534 %
$^{259}_{102}$No	0.021 %	0.171 %	0.004 %
$^{259}_{101}$Md	-	0.001 %	-
$^{258}_{102}$No	18.614 %	36.318 %	3.495 %
$^{258}_{101}$Md	0.004 %	0.003 %	0.006 %
$^{257}_{102}$No	49.403 %	29.968 %	44.398 %
$^{257}_{101}$Md	-	0.001 %	0.010 %
$^{256}_{102}$No	1.194 %	0.181 %	13.799 %
$^{256}_{100}$Fm	0.001 %	0.001 %	-
$^{255}_{102}$No	-	-	0.001 %
$^{255}_{100}$Fm	0.038 %	0.048 %	0.027 %
$^{254}_{100}$Fm	0.021 %	0.013 %	0.087 %
$^{253}_{100}$Fm	0.001 %	-	0.010 %
Total fission	24.385 %	27.996 %	33.162 %
TOTAL	100.000 %	100.000 %	100.000 %

Table 7.20: The same results as in Table 7.1, but for the primary ICF product ^{266}Db, from the reaction ^{40}Ca+^{252}Cf. The total combined cross-sections over 100,000 cascades are 4.314 mb, 5.027 mb and 4.381 mb at $E_{0_{c.m.}}/V_{CB} = 1.00$, 1.05 and 1.10 respectively.

EVR	Percentage yield		
$E_{0_{C.M.}}/V_{CB}$	1.00	1.05	1.10
$^{261}_{103}$Lr	0.001 %	0.001 %	-
$^{260}_{103}$Lr	0.311 %	0.701 %	0.047 %
$^{260}_{102}$No	0.004 %	0.003 %	0.001 %
$^{259}_{103}$Lr	34.709 %	44.886 %	13.640 %
$^{259}_{102}$No	0.049 %	0.036 %	0.046 %
$^{258}_{103}$Lr	34.588 %	24.112 %	45.946 %
$^{258}_{102}$No	0.022 %	0.006 %	0.060 %
$^{257}_{103}$Lr	0.170 %	0.050 %	2.471 %
$^{257}_{101}$Md	0.007 %	0.013 %	0.002 %
$^{256}_{101}$Md	0.157 %	0.130 %	0.122 %
$^{255}_{101}$Md	0.068 %	0.043 %	0.198 %
$^{254}_{101}$Md	0.001 %	-	0.011 %
Total fission	29.913 %	30.019 %	37.456 %
TOTAL	100.000 %	100.000 %	100.000 %

Table 7.21: The same results as in Table 7.1, but for the primary ICF product ^{268}Sg, from the reaction ^{40}Ca+^{252}Cf. The total combined cross-sections over 100,000 cascades are 5.982 mb, 7.860 mb and 6.782 mb at $E_{0_{c.m.}}/V_{CB} = 1.00$, 1.05 and 1.10 respectively.

EVR	Percentage yield		
$E_{0_{C.M.}}/V_{CB}$	1.00	1.05	1.10
$^{264}_{106}$Sg	0.001 %	-	-
$^{263}_{106}$Sg	0.001 %	-	-
Total fission	99.998 %	100.000 %	100.000 %
TOTAL	100.000 %	100.000 %	100.000 %

Table 7.22: The same results as in Table 7.1, but for the primary ICF product ^{272}Hs, from the reaction ^{40}Ca+^{252}Cf. The total combined cross-sections over 100,000 cascades are 8.163×10^{-1} mb, 4.901×10^{-2} mb and 7.968×10^{-3} mb at $E_{0_{c.m.}}/V_{CB} = 1.00$, 1.05 and 1.10 respectively.

EVR	Percentage yield		
$E_{0_{C.M.}}/V_{CB}$	1.00	1.05	1.10
Total fission	100.000 %	100.000 %	100.000 %
TOTAL	100.000 %	100.000 %	100.000 %

7.2.4 ^{40}Ca+^{254}Cf primary incomplete fusion products

Table 7.23 shows that for the primary ICF product ^{266}Rf (from the reaction ^{40}Ca+^{254}Cf), the main EVR at $E_{0_{c.m.}}/V_{CB} = 1.00$ is ^{260}No, with a percentage yield of 69%, followed by ^{259}No with a percentage yield of 20%. At $E_{0_{c.m.}}/V_{CB} = 1.05$, the main EVR is also ^{260}No with a percentage yield of 74%, followed by ^{259}No with a percentage yield of 15%. At $E_{0_{c.m.}}/V_{CB} = 1.10$, the roles are reversed and the main EVR is ^{259}No with a percentage yield of 62%, followed by ^{260}No with a percentage yield of 20%. The percentage total fission of the primary ICF product ^{266}Rf increases with incident energy at an increased rate here than from the reaction ^{20}Ne+^{250}Cm (Table 7.3): 1.1%, 1.5% and 5.0% at $E_{0_{c.m.}}/V_{CB} = 1.00$, 1.05 and 1.10 respectively. On the whole, ^{266}Rf produced in the reaction ^{20}Ne+^{250}Cm results in lower percentages of heavier EVRs, and on average lower percentages of fission, than ^{266}Rf produced in the reaction ^{40}Ca+^{254}Cf. ^{266}Rf produced in the reaction ^{20}Ne+^{250}Cm has higher production cross-sections, higher mean excitation energies and lower mean angular momenta at all three studied incident energies.

Table 7.24 shows that for the primary ICF product ^{268}Db (from the reaction ^{40}Ca+^{254}Cf), the main EVR at $E_{0_{c.m.}}/V_{CB} = 1.00$ is ^{261}Lr, with a percentage yield of 87%, followed by ^{260}Lr with a percentage yield of 6%. At $E_{0_{c.m.}}/V_{CB} = 1.05$, the main EVR is ^{261}Lr with a percentage yield of 85%, followed by ^{262}Lr with a percentage yield of 8%. At $E_{0_{c.m.}}/V_{CB} = 1.10$, the main EVR remains ^{261}Lr with a reduced percentage yield of 47%, followed closely by ^{260}Lr with a percentage yield of 41%. The percentage total fission of the primary ICF product ^{268}Db increases with incident energy at a more disjointed rate here than from the reaction ^{20}Ne+^{248}Cm (Table 7.2): 2.3%, 2.8% and 10.1% at $E_{0_{c.m.}}/V_{CB} = 1.00$, 1.05 and 1.10 respectively. On the whole, ^{268}Db produced in the reaction ^{20}Ne+^{250}Cm results in lower percentages of heavier EVRs, and higher percentages of fission, than ^{268}Db produced in the reaction ^{40}Ca+^{254}Cf. ^{268}Db produced in the reaction ^{20}Ne+^{250}Cm has higher production cross-sections above the Coulomb barrier, and higher mean excitation energies and lower mean angular momenta at all three studied incident energies.

Tables 7.25-7.26 show that for the primary ICF products ^{270}Sg and ^{274}Hs (from the

reaction ^{40}Ca+^{254}Cf), almost all EVRs are lost to fission, as with their counterparts produced in ^{20}Ne-induced reactions (Tables 7.7 and 7.12 respectively). Notable differences here are that the ^{266}Sg and ^{265}Sg EVRs shown in Table 7.25 are fewer and more, respectively, than the ^{266}Sg and ^{265}Sg shown in Table 7.7. ^{270}Sg produced in the reaction ^{20}Ne+^{254}Cf has higher production cross-sections, lower mean excitation energies and lower mean angular momenta at all three studied incident energies. In the case of ^{274}Hs virtually all EVRs are again lost to fission (Tables 7.12 and 7.26).

Table 7.23: The same results as in Table 7.1, but for the primary ICF product ^{266}Rf, from the reaction ^{40}Ca+^{254}Cf. The total combined cross-sections over 100,000 cascades are 5.584 mb, 8.130 mb and 5.558 mb at $E_{0_{c.m.}}/V_{CB} = 1.00$, 1.05 and 1.10 respectively.

EVR	Percentage yield		
$E_{0_{C.M.}}/V_{CB}$	1.00	1.05	1.10
$^{264}_{103}$Lr	0.202 %	0.300 %	0.010 %
$^{264}_{102}$No	-	0.001 %	-
$^{263}_{103}$Lr	8.254 %	7.155 %	2.538 %
$^{263}_{102}$No	-	-	0.001 %
$^{262}_{103}$Lr	0.582 %	0.308 %	5.572 %
$^{262}_{102}$No	0.002 %	0.002 %	-
$^{261}_{103}$Lr	-	-	0.060 %
$^{261}_{102}$No	1.001 %	1.964 %	0.050 %
$^{261}_{101}$Md	-	0.001 %	-
$^{260}_{102}$No	69.088 %	73.926 %	20.421 %
$^{260}_{101}$Md	0.001 %	-	0.001 %
$^{259}_{102}$No	19.729 %	14.844 %	61.978 %
$^{258}_{102}$No	0.007 %	0.003 %	4.328 %
$^{258}_{100}$Fm	0.005 %	0.003 %	-
$^{257}_{100}$Fm	0.012 %	0.013 %	0.027 %
$^{256}_{100}$Fm	-	0.002 %	0.012 %
Total fission	1.117 %	1.478 %	5.002 %
TOTAL	100.000 %	100.000 %	100.000 %

Table 7.24: The same results as in Table 7.1, but for the primary ICF product ^{268}Db, from the reaction ^{40}Ca+^{254}Cf. The total combined cross-sections over 100,000 cascades are 5.238 mb, 5.312 mb and 4.054 mb at $E_{0_{c.m.}}/V_{CB} = 1.00$, 1.05 and 1.10 respectively.

EVR	Percentage yield		
$E_{0_{C.M.}}/V_{CB}$	1.00	1.05	1.10
$^{263}_{103}$Lr	0.013 %	0.020 %	0.001 %
$^{262}_{103}$Lr	4.726 %	7.762 %	0.597 %
$^{262}_{102}$No	0.002 %	0.007 %	0.004 %
$^{261}_{103}$Lr	86.844 %	84.618 %	47.142 %
$^{261}_{102}$No	0.004 %	0.005 %	0.011 %
$^{260}_{103}$Lr	6.100 %	4.732 %	41.487 %
$^{260}_{102}$No	-	-	0.001 %
$^{260}_{101}$Md	-	0.002 %	-
$^{259}_{103}$Lr	0.001 %	-	0.611 %
$^{259}_{101}$Md	0.007 %	0.012 %	0.005 %
$^{258}_{101}$Md	0.023 %	0.018 %	0.058 %
$^{257}_{101}$Md	-	0.003 %	0.018 %
$^{256}_{101}$Md	-	-	0.001 %
Total fission	2.280 %	2.821 %	10.064 %
TOTAL	100.000 %	100.000 %	100.000 %

Table 7.25: The same results as in Table 7.1, but for the primary ICF product ^{270}Sg, from the reaction ^{40}Ca+^{254}Cf. The total combined cross-sections over 100,000 cascades are 7.485 mb, 7.214 mb and 6.856 mb at $E_{0_{c.m.}}/V_{CB}$ = 1.00, 1.05 and 1.10 respectively.

EVR	Percentage yield		
$E_{0_{C.M.}}/V_{CB}$	1.00	1.05	1.10
$^{266}_{106}$Sg	0.009 %	0.005 %	0.001 %
$^{265}_{106}$Sg	0.005 %	0.003 %	0.005 %
$^{264}_{106}$Sg	-	-	0.001 %
Total fission	99.986 %	99.992 %	99.993 %
TOTAL	100.000 %	100.000 %	100.000 %

Table 7.26: The same results as in Table 7.1, but for the primary ICF product ^{274}Hs, from the reaction ^{40}Ca+^{254}Cf. The total combined cross-sections over 100,000 cascades are 9.225×10^{-1} mb, 7.861×10^{-2} mb and 2.517×10^{-2} mb at $E_{0_{c.m.}}/V_{CB}$ = 1.00, 1.05 and 1.10 respectively.

EVR	Percentage yield		
$E_{0_{C.M.}}/V_{CB}$	1.00	1.05	1.10
$^{266}_{106}$Sg	-	0.001 %	-
Total fission	100.000 %	99.999 %	100.000 %
TOTAL	100.000 %	100.000 %	100.000 %

7.2.5 ^{40}Ca+^{254}Es primary incomplete fusion products

Table 7.27: The same results as in Table 7.1, but for the primary ICF product ^{266}Db, from the reaction ^{40}Ca+^{254}Es. The total combined cross-sections over 100,000 cascades are 5.254 mb, 7.411 mb and 5.577 mb at $E_{0_{c.m.}}/V_{CB} = 1.00$, 1.05 and 1.10 respectively.

EVR	Percentage yield		
$E_{0_{C.M.}}/V_{CB}$	1.00	1.05	1.10
$^{261}_{103}$Lr	0.029 %	0.148 %	0.003 %
$^{260}_{103}$Lr	9.638 %	28.856 %	2.182 %
$^{260}_{102}$No	0.011 %	0.010 %	0.007 %
$^{259}_{103}$Lr	77.759 %	58.770 %	58.544 %
$^{259}_{102}$No	0.015 %	0.004 %	0.035 %
$^{258}_{103}$Lr	1.551 %	0.120 %	10.622 %
$^{258}_{102}$No	-	-	0.004 %
$^{257}_{103}$Lr	-	-	0.005 %
$^{257}_{101}$Md	0.039 %	0.047 %	0.025 %
$^{256}_{101}$Md	0.064 %	0.025 %	0.113 %
$^{255}_{101}$Md	0.002 %	-	0.025 %
Total fission	10.892 %	12.020 %	28.435 %
TOTAL	100.000 %	100.000 %	100.000 %

Table 7.27 shows that for the primary ICF product ^{266}Db (from the reaction ^{40}Ca+^{254}Es), the main EVR at $E_{0_{c.m.}}/V_{CB} = 1.00$ is ^{259}Lr, with a percentage yield of 78%, followed by ^{260}Lr with a percentage yield of 10%. At $E_{0_{c.m.}}/V_{CB} = 1.05$, the main EVR is ^{259}Lr with a percentage yield of 59%, followed by ^{260}Lr with a percentage yield of 29%. At $E_{0_{c.m.}}/V_{CB} = 1.10$, the main EVR remains ^{259}Lr with a percentage yield of 59%, followed by ^{258}Lr with a percentage yield of 11%. The percentage total fission of the primary ICF product ^{266}Db increases with incident energy at a more pronounced rate here than from the reaction ^{20}Ne+^{248}Cm (Table 7.2): 11%, 12% and 28% at $E_{0_{c.m.}}/V_{CB} = 1.00$, 1.05 and 1.10 respectively. On the whole, ^{266}Db produced in the reaction ^{20}Ne+^{248}Cm re-

sults in lower percentages of heavier EVRs, and higher percentages of fission, than ^{266}Db produced in the reaction ^{40}Ca+^{254}Es. ^{266}Db produced in the reaction ^{20}Ne+^{248}Cm has higher production cross-sections above the Coulomb barrier, and higher mean excitation energies and lower mean angular momenta at all three studied incident energies.

Table 7.28: The same results as in Table 7.1, but for the primary ICF product ^{268}Sg, from the reaction ^{40}Ca+^{254}Es. The total combined cross-sections over 100,000 cascades are 4.754 mb, 5.301 mb and 4.462 mb at $E_{0_{c.m.}}/V_{CB} = 1.00$, 1.05 and 1.10 respectively.

EVR	Percentage yield		
$E_{0_{C.M.}}/V_{CB}$	1.00	1.05	1.10
$^{263}_{106}$Sg	-	0.001 %	0.001 %
$^{262}_{106}$Sg	0.001 %	-	0.001 %
Total fission	99.999 %	99.999 %	99.998 %
TOTAL	100.000 %	100.000 %	100.000 %

Tables 7.28-7.29 show that for the primary ICF products ^{268}Sg and ^{270}Bh (from the reaction ^{40}Ca+^{254}Es), almost all EVRs are lost to fission, as with their counterparts produced in ^{20}Ne-induced reactions (Table 7.5 for ^{268}Sg and Tables 7.6 and 7.9 for ^{270}Bh). Notable differences here are that the ^{262,263}Sg EVRs shown in Table 7.28 are lighter and slightly fewer than the ^{263,264}Sg EVRs shown in Table 7.5. ^{268}Sg produced in the reaction ^{20}Ne+^{252}Cf has higher production cross-sections, lower mean excitation energies and lower mean angular momenta at all three studied incident energies. In the case of ^{270}Bh the EVRs shown in Table 7.29 are slightly heavier and greater in number than the EVRs shown in Table 7.6, and are slightly lighter and slightly greater in number than the EVRs shown in Table 7.9. ^{270}Bh produced in the reaction ^{20}Ne+^{252}Cf has higher production cross-sections above the Coulomb barrier, higher mean excitation energies and lower mean angular momenta at all three studied incident energies, whilst ^{270}Bh produced in the reaction ^{20}Ne+^{254}Es has higher production cross-sections, lower mean excitation energies and lower mean angular momenta at all three studied incident energies.

Table 7.29: The same results as in Table 7.1, but for the primary ICF product ^{270}Bh, from the reaction ^{40}Ca+^{254}Es. The total combined cross-sections over 100,000 cascades are 6.556 mb, 7.115 mb and 7.908 mb at $E_{0_{c.m.}}/V_{CB} = 1.00$, 1.05 and 1.10 respectively.

EVR	Percentage yield		
$E_{0_{C.M.}}/V_{CB}$	1.00	1.05	1.10
$^{266}_{106}$Sg	-	0.001 %	-
$^{265}_{107}$Bh	0.001 %	0.004 %	-
$^{265}_{106}$Sg	-	0.001 %	-
Total fission	99.999 %	99.994 %	100.000 %
TOTAL	100.000 %	100.000 %	100.000 %

7.2.6 ^{40}Ca+^{256}Es primary incomplete fusion products

Table 7.30 shows that for the primary ICF product ^{268}Db (from the reaction ^{40}Ca+^{256}Es), the main EVR at $E_{0_{c.m.}}/V_{CB} = 1.00$ is ^{261}Lr, with a percentage yield of 87%, followed by ^{262}Lr with a percentage yield of 6%. At $E_{0_{c.m.}}/V_{CB} = 1.05$, the main EVR is ^{261}Lr with a percentage yield of 69%, followed by ^{262}Lr with a percentage yield of 29%. At $E_{0_{c.m.}}/V_{CB} = 1.10$, the main EVR remains ^{261}Lr with a reduced percentage yield of 68%, followed by ^{260}Lr with a percentage yield of 23%. The percentage total fission of the primary ICF product ^{268}Db varies with incident energy in a more disjointed fashion here than from the reaction ^{20}Ne+^{248}Cm (Table 7.2): 2.3%, 2.0% and 7.0% at $E_{0_{c.m.}}/V_{CB} = 1.00$, 1.05 and 1.10 respectively. On the whole, ^{268}Db produced in the reaction ^{20}Ne+^{250}Cm results in lower percentages of heavier EVRs, and higher percentages of fission, than ^{268}Db produced in the reaction ^{40}Ca+^{256}Es. ^{268}Db produced in the reaction ^{20}Ne+^{250}Cm has higher production cross-sections above the Coulomb barrier, and higher mean excitation energies and lower mean angular momenta at all three studied incident energies.

Tables 7.31-7.32 show that for the primary ICF products ^{270}Sg and ^{272}Bh (from the reaction ^{40}Ca+^{256}Es), almost all EVRs are lost to fission, as with their counterparts

Table 7.30: The same results as in Table 7.4, but for the primary ICF product ^{268}Db, from the reaction ^{40}Ca+^{256}Es. The total combined cross-sections over 100,000 cascades are 4.412 mb, 7.521 mb and 5.199 mb at $E_{0_{c.m.}}/V_{CB}$ = 1.00, 1.05 and 1.10 respectively.

EVR	Percentage yield		
$E_{0_{C.M.}}/V_{CB}$	1.00	1.05	1.10
$^{263}_{103}$Lr	0.014 %	0.230 %	0.003 %
$^{262}_{103}$Lr	6.477 %	28.828 %	2.023 %
$^{262}_{102}$No	0.005 %	0.001 %	0.005 %
$^{261}_{103}$Lr	86.779 %	68.735 %	67.825 %
$^{261}_{102}$No	0.005 %	0.001 %	0.007 %
$^{260}_{103}$Lr	4.405 %	0.215 %	22.949 %
$^{260}_{101}$Md	-	0.001 %	-
$^{259}_{103}$Lr	-	-	0.070 %
$^{259}_{101}$Md	0.023 %	0.013 %	0.010 %
$^{258}_{101}$Md	0.021 %	0.006 %	0.039 %
$^{257}_{101}$Md	0.002 %	-	0.007 %
Total fission	2.269 %	1.970 %	7.062 %
TOTAL	100.000 %	100.000 %	100.000 %

produced in ^{20}Ne-induced reactions (Table 7.7 for ^{270}Sg and Tables 7.8 and 7.11 for ^{272}Bh). Notable differences here are that the ^{264,265}Sg EVRs shown in Table 7.31 are lighter and fewer than the ^{265,266}Sg EVRs shown in Table 7.7. ^{270}Sg produced in the reaction ^{20}Ne+^{254}Cf has higher production cross-sections, lower mean excitation energies and lower mean angular momenta at all three studied incident energies. In the case of ^{272}Bh the EVRs shown in Table 7.32 are slightly heavier and slightly fewer than the EVRs shown in Table 7.11, whereas in Table 7.8 all EVRs are lost to fission. ^{272}Bh produced in the reaction ^{20}Ne+^{256}Es has higher production cross-sections above the Coulomb barrier, lower mean excitation energies and lower mean angular momenta at all three studied incident energies, save for a minusculely lower excitation energy at

$E_{0_{C.M.}}/V_{CB}$=1.05.

Table 7.31: The same results as in Table 7.1, but for the primary ICF product ^{270}Sg, from the reaction ^{40}Ca+^{256}Es. The total combined cross-sections over 100,000 cascades are 4.095 mb, 4.977 mb and 3.826 mb at $E_{0_{c.m.}}/V_{CB}$ = 1.00, 1.05 and 1.10 respectively.

EVR	Percentage yield		
$E_{0_{C.M.}}/V_{CB}$	1.00	1.05	1.10
$^{265}_{106}$Sg	0.004 %	0.001 %	0.001 %
$^{264}_{106}$Sg	0.005 %	-	0.002 %
Total fission	99.991 %	99.999 %	99.997 %
TOTAL	100.000 %	100.000 %	100.000 %

Table 7.32: The same results as in Table 7.1, but for the primary ICF product ^{272}Bh, from the reaction ^{40}Ca+^{256}Es. The total combined cross-sections over 100,000 cascades are 5.994 mb, 7.254 mb and 6.087 mb at $E_{0_{c.m.}}/V_{CB}$ = 1.00, 1.05 and 1.10 respectively.

EVR	Percentage yield		
$E_{0_{C.M.}}/V_{CB}$	1.00	1.05	1.10
$^{268}_{106}$Sg	-	0.001 %	-
Total fission	100.000 %	99.999 %	100.000 %
TOTAL	100.000 %	100.000 %	100.000 %

7.2.7 ^{48}Ca-induced primary incomplete fusion products

Table 7.33 shows that for the primary ICF product ^{266}Rf (from the reaction ^{48}Ca+^{252}Cf), the main EVR at $E_{0_{c.m.}}/V_{CB} = 1.00$ is ^{256}No, with a percentage yield of 52%, followed by ^{257}No with a percentage yield of 19%. At $E_{0_{c.m.}}/V_{CB} = 1.05$, the main EVR is ^{257}No with a percentage yield of 50%, followed by ^{256}No with a percentage yield of 13%. At $E_{0_{c.m.}}/V_{CB} = 1.10$, the the main EVR is ^{256}No with a percentage yield of 43%, followed by ^{257}No with a percentage yield of 24%. The percentage total fission of the primary ICF product ^{266}Rf increases with incident energy at an increased rate here than from the reactions ^{20}Ne+^{250}Cm (Table 7.3), ^{40}Ca+^{250}Cm (Table 7.16) and ^{40}Ca+^{254}Cf (Table 7.23): 12%, 14% and 20% at $E_{0_{c.m.}}/V_{CB} = 1.00$, 1.05 and 1.10 respectively. On the whole, ^{266}Rf produced in the reaction ^{48}Ca+^{252}Cf results in lower percentages of heavier EVRs than ^{266}Rf produced in the other three aforementioned reactions. ^{266}Rf produced in the reaction ^{48}Ca+^{252}Cf has lower production cross-sections, higher mean excitation energies and higher mean angular momenta at all three studied incident energies.

Table 7.34 shows that for the primary ICF product ^{268}Db (from the reaction ^{48}Ca+^{254}Es), the main EVR at $E_{0_{c.m.}}/V_{CB} = 1.00$ is ^{258}Lr, with a percentage yield of 51%, followed by ^{259}Lr with a percentage yield of 16%. At $E_{0_{c.m.}}/V_{CB} = 1.05$, the main EVR is ^{259}Lr with a percentage yield of 48%, followed by ^{258}Lr with a percentage yield of 27%. At $E_{0_{c.m.}}/V_{CB} = 1.10$, the the main EVR is ^{258}Lr with a percentage yield of 44%, followed by ^{259}Lr with a percentage yield of 15%. The percentage total fission of the primary ICF product ^{268}Db varies with incident energy in a more disjointed fashion here than from the reactions ^{20}Ne+^{250}Cm (Table 7.4), ^{40}Ca+^{254}Cf (Table 7.24) and ^{40}Ca+^{256}Es (Table 7.30): 23%, 21% and 31% at $E_{0_{c.m.}}/V_{CB} = 1.00$, 1.05 and 1.10 respectively. On the whole, ^{268}Db produced in the reaction ^{48}Ca+^{254}Es results in lower percentages of heavier EVRs a higher percentages of fission than ^{268}Db produced in the other three aforementioned reactions. ^{268}Db produced in the reaction ^{48}Ca+^{254}Es has lower production cross-sections, higher mean excitation energies and higher mean angular momenta at all three studied incident energies.

Table 7.33: The same results as in Table 7.1, but for the primary ICF product ^{266}Rf, from the reaction ^{48}Ca+^{252}Cf. The total combined cross-sections over 100,000 cascades are 7.266×10^{-1} mb, 1.809 mb and 1.525 mb at $E_{0_{c.m.}}/V_{CB}$ = 1.00, 1.05 and 1.10 respectively.

EVR	Percentage yield		
$E_{0_{C.M.}}/V_{CB}$	1.00	1.05	1.10
$^{262}_{103}$Lr	-	0.024 %	0.001 %
$^{262}_{102}$No	-	0.001 %	-
$^{261}_{103}$Lr	0.122 %	1.632 %	0.219 %
$^{261}_{102}$No	0.003 %	0.013 %	0.005 %
$^{260}_{103}$Lr	4.099 %	7.477 %	4.053 %
$^{260}_{102}$No	0.035 %	0.006 %	0.029 %
$^{259}_{103}$Lr	8.052 %	1.122 %	5.671 %
$^{259}_{102}$No	0.011 %	0.096 %	0.006 %
$^{259}_{101}$Md	0.001 %	0.004 %	-
$^{258}_{103}$Lr	0.153 %	0.001 %	0.055 %
$^{258}_{102}$No	0.995 %	11.990 %	1.489 %
$^{258}_{101}$Md	0.016 %	0.043 %	0.022 %
$^{258}_{100}$Fm	0.001 %	-	-
$^{257}_{102}$No	19.466 %	50.126 %	23.816 %
$^{257}_{101}$Md	0.123 %	0.037 %	0.086 %
$^{256}_{102}$No	51.619 %	13.290 %	43.068 %
$^{256}_{101}$Md	0.036 %	-	0.022 %
$^{256}_{100}$Fm	0.001 %	0.017 %	0.003 %
$^{255}_{102}$No	2.163 %	0.008 %	1.035 %
$^{255}_{101}$Md	0.001 %	-	-
$^{255}_{100}$Fm	0.040 %	0.202 %	0.074 %
$^{254}_{100}$Fm	0.412 %	0.202 %	0.449 %
$^{253}_{100}$Fm	0.223 %	0.009 %	0.139 %
$^{252}_{100}$Fm	0.006 %	-	0.002 %
Total fission	12.422 %	13.700 %	19.756 %
TOTAL	100.000 %	100.000 %	100.000 %

Table 7.34: The same results as in Table 7.1, but for the primary ICF product ^{268}Db, from the reaction ^{48}Ca+^{254}Es. The total combined cross-sections over 100,000 cascades are 6.417×10^{-1} mb, 1.745 mb and 1.557 mb at $E_{0_{c.m.}}/V_{CB}$ = 1.00, 1.05 and 1.10 respectively.

EVR	Percentage yield		
$E_{0_{C.M.}}/V_{CB}$	1.00	1.05	1.10
$^{261}_{103}$Lr	0.002 %	0.030 %	0.004 %
$^{261}_{102}$No	-	0.001 %	-
$^{260}_{103}$Lr	0.232 %	2.284 %	0.228 %
$^{260}_{102}$No	0.012 %	0.046 %	0.010 %
$^{259}_{103}$Lr	15.951 %	48.494 %	15.347 %
$^{259}_{102}$No	0.172 %	0.172 %	0.146 %
$^{258}_{103}$Lr	51.088 %	26.872 %	44.264 %
$^{258}_{102}$No	0.212 %	0.047 %	0.195 %
$^{258}_{101}$Md	0.001 %	0.002 %	-
$^{257}_{103}$Lr	8.326 %	0.330 %	8.037 %
$^{257}_{102}$No	0.002 %	-	0.002 %
$^{257}_{101}$Md	0.030 %	0.105 %	0.029 %
$^{256}_{103}$Lr	0.003 %	-	0.008 %
$^{256}_{101}$Md	0.323 %	0.358 %	0.323 %
$^{256}_{100}$Fm	0.002 %	-	0.001 %
$^{255}_{101}$Md	0.528 %	0.100 %	0.541 %
$^{254}_{101}$Md	0.024 %	0.001 %	0.033 %
$^{254}_{99}$Es	-	0.001 %	-
$^{253}_{99}$Es	-	-	0.002 %
Total fission	23.092 %	21.157 %	30.830 %
TOTAL	100.000 %	100.000 %	100.000 %

7.3 Evaporation residue summary

Throughout all the comparisons drawn between EVRs of like primary ICF products from ^{20}Ne- and ^{40,48}Ca-induced reactions, the overarching trend is that the primary ICF product with the lower mean excitation energy is the one that results in higher yields of the heavier EVRs. For the ten like primary ICF products compared in this chapter, the following reactions appear to be the preferred production method in terms of the highest percentage yields of the heaviest EVR products:

- $^{264}_{104}$Rf: ^{40}Ca+^{252}Cf.
- $^{266}_{104}$Rf: ^{40}Ca+^{254}Cf.
- $^{266}_{105}$Db: ^{40}Ca+^{254}Es.
- $^{268}_{105}$Db: ^{40}Ca+^{256}Es.
- $^{268}_{106}$Sg: ^{20}Ne+^{252}Cf.
- $^{270}_{106}$Sg: ^{20}Ne+^{254}Cf.
- $^{270}_{107}$Bh: ^{20}Ne+^{254}Es.
- $^{272}_{107}$Bh: ^{20}Ne+^{256}Es.
- $^{272}_{108}$Hs: Inconclusive.
- $^{274}_{108}$Hs: Inconclusive.

It should be noted that whilst the above concern the highest percentage yields of heavier EVRs, primary ICF products from ^{20}Ne-induced reactions universally have higher total production cross-sections at all three studied incident energies, save for a few instances at the Coulomb barrier. Comparisons of ^{272,274}Hs are deemed inconclusive as only one EVR per 100,000 cascades has been registered at most for these products. ^{270,272}Bh almost fall into this category too, with only a handful of EVRs registered per 100,000 cascades, making these marginally preferable reactions.

Interestingly, for the primary ICF products ^{264,266}Rf and ^{266,268}Db, the preferable reactions for the highest percentage yields of the heaviest EVR products have a notable trait in common: the formation of these primary ICF products from these reactions involve the transfer of ^{12}C to the target. Similarly, for the primary ICF products ^{268,270}Sg and ^{270,272}Bh, the preferable reactions for the highest percentage yields of the heaviest EVR products have the following trait in common: the formation of these primary ICF products from these reactions involve the transfer of ^{16}O to the target. It may well be the case that ^{16}O and ^{12}C fragments play a key role in the production of more stable SHE isotopes via the ICF mechanism. For example, in the case of a ^{20}Ne projectile fragmenting into ^{16}O and ^{4}He, the α-particle may be responsible for carrying away more of the projectile's excitation energy than other non-captured fragments would. The same could extend to the ^{28}Si fragment carrying away the bulk of the ^{40}Ca projectile's excitation after undergoing fragmentation with the resulting ^{12}C going on to fuse with the target. Another interesting link is that ^{16}O+^{4}He is the fragmentation pairing with the lowest driving potential in Table 4.1, and ^{12}C+^{28}Si is the fragmentation pairing with the second-lowest driving potential in Table 4.2 by a margin of fewer than 1.5 MeV. Extending this to the projectile ^{48}Ca in Table 4.3, the fragmentation pairing of ^{44}Ar+^{4}He has the lowest driving potential by a margin of almost 8 MeV, suggesting that ICF products involving this binary fragmentation could result in the highest percentage yields of the heaviest EVR products compared with like ICF products produced in different reactions.

In this chapter, ICF predictions of the model presented in Chapter 6 have been used to determine resultant EVR cross-sections for the two most dominant SHE primary ICF products of each of the 18 reactions, and additionally to draw comparisons between ^{20}Ne- and ^{40,48}Ca-induced reactions. Chapter 8 summarises the findings of this work and provides future outlooks for its continuation.

Chapter 8

Conclusions and Outlook

The goals of this work outlined at the end of Chapter 1, namely: (i) to develop a semi-classical dynamical model comprised of a classical trajectory model and the quantum-mechanical fragmentation theory, (ii) to test the resultant predictions of the aforementioned model against published experimental results in order to calibrate the model and validate its accuracy, and (iii) to use the calibrated model to make new predictions for SHE formation in ICF reactions at Coulomb energies, have all been met. A semi-classical dynamical model that combines the classical trajectory model with stochastic breakup from Chapter 2 with the dynamical fragmentation theory treatment of two-body clusterisation and decay of a projectile from Chapter 3 has been developed. Following projectile parameterisation in Chapter 4 and calibration via test cases in Chapter 5, results of this model have been presented in Chapter 6 for ^{20}Ne- and ^{40,48}Ca-induced ICF reactions for the production of SHE isotopes. Targets include ^{248,250}Cm, ^{252,254}Cf and ^{254,256}Es, and results include total integrated cross-sections, mean angles, mean excitation energies and mean angular momenta in addition angular distributions. Predictions have been made for over 50 as-of-yet unobserved nuclides, the majority of which are more neutron-rich than their discovered neighbours in the chart of nuclides. The results in Chapter 6 have shown that for ^{20}Ne-induced reactions heavier targets are preferred for the production of 'colder' and more stable primary SHE isotopes through the ICF mechanism, and that ^{20}Ne-induced reactions themselves are preferred to ^{40,48}Ca-induced reactions for the production of more stable like primary

ICF products. The results also suggest that in order to maximise the stability of the primary ICF products, an incident energy equal to the Coulomb barrier is preferable for ^{20}Ne-induced reactions, whilst an incident energy 5% above the Coulomb is preferable for ^{40,48}Ca-induced reactions. Also presented in Chapter 7 and useful for future experiments are EVR cross-sections for the dominant two primary ICF products of each of the 18 reactions, in addition to EVR cross-sections for relatively lighter SHE ICF products of ^{40,48}Ca-induced reactions to serve as comparisons with like products of ^{20}Ne-induced reactions. The results there suggest that the ^{20}Ne fragmentation of ^{16}O+^{4}He and the ^{40}Ca fragmentation of ^{12}C+^{28}Si (and by extrapolation, perhaps the ^{48}Ca fragmentation of ^{44}Ar+^{4}He) lead to the primary ICF products with the highest percentage yields of the heaviest EVR products.

The present model calculations are very useful for planning and interpreting new experiments for SHE research using the ICF reaction mechanism. The proof of this lies in the publication of two journal articles in *Physical Review C* [62, 63] during the development of this model, which in turn resulted in collaboration offers from researchers at the Grand Accélérateur National d'Ions Lourds (GANIL) in Caen, France [108] and at Argonne National Laboratory (ANL) in Illinois, USA [109]. At the time of writing these offers have resulted in the approval of a Letter of Intent (LoI) from the GANIL Program Advisory Committee (PAC) and in the submission of a research proposal to ANL-PAC. The GANIL LoI proposes to study the feasibility of the reactions induced by ^{238}U (6.5 MeV/A) on gaseous ^{40}Ar or ^{132,134}Xe filling the ACTAR TPC detector, a French project aiming at constructing a new-generation active target in order to study very rare nuclear processes and nuclei produced in very small quantities. Both experiments imply a rather low gas pressure such as to offer a display of the reaction and decay products over the whole length of TPC. The beam on/off function will be also tested in order to provide the possibility to study correlations between one reaction product and the decay of the other reaction product. The ANL proposal aims to start an initiative at ATLAS using the ^{9}Be+^{238}U and ^{12}C+^{238}U reactions at the Coulomb barrier to study the incomplete-fusion channels with the Gammasphere-Microball setup. This will be just the first round where the goals are: (i) to perform a systematic test of the calculated cross sections for the above reactions, obtained with the novel semiclassical model

presented in this thesis, and (ii) to test the target arrangement and its implications for spectroscopic studies.

Moving forward, this model could be developed further in several ways. Target deformation has been demonstrated to have an effect on ICF dynamics [110], so considering deformed fragments throughout the model would serve as an interesting comparison to the present results. The present model considers projectile fragmentation in the charge asymmetry co-ordinate, which does well to identify the charges of the projectile fragments, however considering fragmentation in the mass-asymmetry co-ordinate could serve as a good refinement as it would assign definite masses to the fragments, removing the assumption of a N/Z-equilibrium in the dinuclear system model [88–93] and offering a more realistic assortment of potential ICF products. Taking fragmentation theory even further, the model could potentially be extended beyond the single binary fragmentation of the projectile considered here, by considering that the projectile fragments may undergo binary fragmentation again, or even by considering the possibility of trinary fragmentation, though the scaling of calculation complexity would present its own challenges to overcome.

Appendix A

Classical breakup in overall centre-of-mass frame

(P = Projectile, T = Target, CM = Centre-of-Mass, $\perp$ = perpendicular)

Initially in the lab frame

Mass:

$$M = m_P + m_T. \tag{A.1}$$

Total energy:

$$E_0 = \frac{1}{2} m_P v^2. \tag{A.2}$$

Velocity:

$$v = \sqrt{2E_0/m_P}. \tag{A.3}$$

Total angular momentum ($\perp$ to plane):

$$|\overrightarrow{L}_0| = m_P v b_0. \tag{A.4}$$

Projectile, P, initially located at $\overrightarrow{R}_P(t = 0)$.

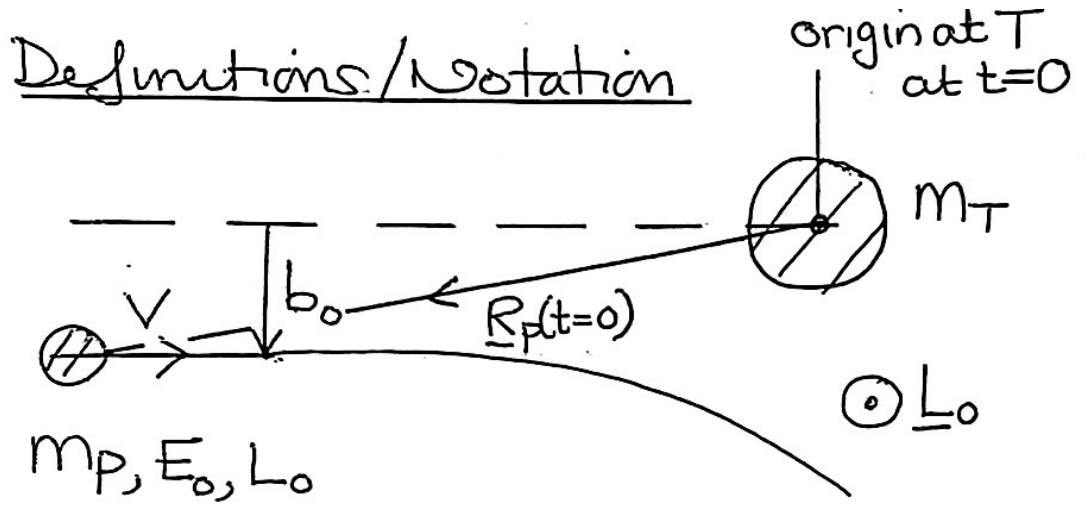

Figure A.1: Diagram of projectile and target definitions.

Overall CM moves with $\overrightarrow{V}_{CM}$ in beam direction

As $MV_{CM} = m_P v$ at $(t = 0)$, velocity in the CM frame can be written as:

$$V_{CM} = \frac{m_P}{M} v \tag{A.5}$$

in the beam direction. Similarly, energy and angular momentum ($\perp$ to plane) in the CM frame can be written as:

$$E_{CM} = \frac{1}{2} M V_{CM}^2 = \frac{1}{2} M \frac{m_P^2}{M^2} v^2 = \frac{m_P}{M} E_0, \tag{A.6}$$

$$L_{CM} = M V_{CM} \frac{m_P}{M} b_0 = m_P V_{CM} b_0. \tag{A.7}$$

These are all *conserved* quantities.

So V_{CM} forms basis of Galilean transformation of velocities back to lab frame, and for transforming radii and positions:

$$\overrightarrow{R}_{CM}(t) = \frac{m_P}{M} \overrightarrow{R}_P(t = 0) + \overrightarrow{V}_{CM} t. \tag{A.8}$$

So, available (conserved) *in* the overall CM frame are the total energy, momentum and angular momentum ($\perp$ to plane) respectively:

$$E_{tot} = \quad E_0 - E_{CM} = \tfrac{m_T}{M} E_0, \tag{A.9a}$$

$$\overrightarrow{P}_{tot} = \quad 0, \tag{A.9b}$$

$$L_{tot} = \quad m_P b_0 [v - v_{CM}]. \tag{A.9c}$$

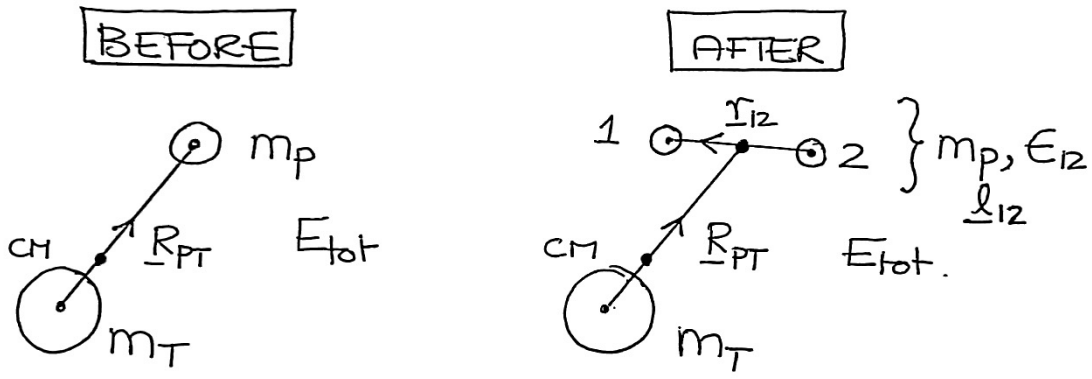

Figure A.2: Diagram of the system before and after projectile breakup.

Conservation of E, $\overrightarrow{P}$, $\overrightarrow{L}$ *in* overall CM frame at breakup

*Know *all* positions, 1, 2, P, T relative to CM and relative positions $\overrightarrow{r}_{12}$, $\overrightarrow{R}_{PT}$.

*Know excitation of the projectile, P, to a definite state $\varepsilon_{12}, \overrightarrow{\ell}_{12}, \overrightarrow{d}_{12}$ of mass m_P.

Conserved total energy:

$$E_{tot} = \varepsilon_{12} + U_{1T}(r_{1T}) + U_{2T}(r_{2T}) + P_{PT}^2/2\mu_{PT}, \tag{A.10}$$

hence we know the projectile-target momentum and velocity:

$$P_{PT}, V_{PT} = P_{PT}/\mu_{PT}. \tag{A.11}$$

Conserved total angular momentum:

$$\overrightarrow{L}_{tot} = \overrightarrow{\ell}_{12} + \overrightarrow{L}_{PT}, \tag{A.12}$$

where $\overrightarrow{L}_{PT}$ is the angular momentum associated with relative motion of P and T about CM, hence we know $\overrightarrow{L}_{PT}$.

Conserved total momentum:

$$\overrightarrow{P}_{tot} = 0 = \overrightarrow{P}_T + \overrightarrow{P}_1 + \overrightarrow{P}_2 = \overrightarrow{P}_T + \overrightarrow{P}_{P*}, \tag{A.13}$$

where $\overrightarrow{P}_T + \overrightarrow{P}_1 + \overrightarrow{P}_2$ are momenta of the target and projectile fragments relative to CM, and $\overrightarrow{P}_{P*}$ is the momentum of the centre of mass of the excited compound projectile, $P*$, relative to CM.

Acquiring $\overrightarrow{\tilde{v}}_T$ and $\overrightarrow{\tilde{v}}_{P*}$ relative to overall CM to complete initial conditions for subsequent time evolution

Clearly, from Eq. (A.13) $m_T \overrightarrow{\tilde{v}}_T + m_P \overrightarrow{\tilde{v}}_{P*} = 0$, therefore:

$$\overrightarrow{\tilde{v}}_T = -\frac{m_P}{m_T} \overrightarrow{\tilde{v}}_{P*}, \tag{A.14}$$

so we need $\overrightarrow{\tilde{v}}_{P*}$. We will drop *; $\overrightarrow{\tilde{v}}_{P*} \equiv \overrightarrow{\tilde{v}}_P$ = velocity of centre of mass of P relative to overall CM. Will need the velocity of P relative to T ($\equiv \overrightarrow{R}_{PT}$):

$$\overrightarrow{v}_{PT} = \overrightarrow{\tilde{v}}_P - \overrightarrow{\tilde{v}}_T, \tag{A.15}$$

and we know the magnitude of V_{PT} from Eq. (A.11).

The internal structure of $P*$ is no longer required. From overall CM:

$$\overrightarrow{R}_T = -\alpha \overrightarrow{R}_{PT} \tag{A.16a}$$

$$\overrightarrow{R}_P = \beta \overrightarrow{R}_{PT} \tag{A.16b}$$

$$\alpha + \beta = 1 \tag{A.16c}$$

$$\overrightarrow{L}_{PT} = m_T \overrightarrow{R}_T \times \overrightarrow{\tilde{v}}_T + m_P \overrightarrow{R}_P \times \overrightarrow{\tilde{v}}_P \tag{A.17a}$$

$$= m_T(-\alpha \overrightarrow{R}_{PT}) \times \overrightarrow{\tilde{v}}_T + m_P \beta \overrightarrow{R}_{PT} \times \overrightarrow{\tilde{v}}_P \tag{A.17b}$$

From Eq. (A.14) we know that:

$$\overrightarrow{\tilde{v}}_P = -\frac{m_T}{m_P} \overrightarrow{\tilde{v}}_T, \tag{A.18}$$

so the angular momentum as calculated from T is:

$$\overrightarrow{L}_{PT} = m_T(+\alpha \overrightarrow{R}_{PT}) \times \tfrac{m_P}{m_T} \overrightarrow{\tilde{v}}_P + m_P \beta \overrightarrow{R}_{PT} \times \overrightarrow{\tilde{v}}_P \tag{A.19a}$$

$$= m_P \overrightarrow{R}_{PT} \times \overrightarrow{\tilde{v}}_P \tag{A.19b}$$

or as calculated from P:

$$\overrightarrow{L}_{PT} = m_T(-\alpha \overrightarrow{R}_{PT}) \times \overrightarrow{\tilde{v}}_T + m_P \beta \overrightarrow{R}_{PT} \times (-\tfrac{m_T}{m_P} \overrightarrow{\tilde{v}}_T) \tag{A.20a}$$

$$= -m_T \overrightarrow{R}_{PT} \times \overrightarrow{\tilde{v}}_T \tag{A.20b}$$

The simplest to use for angular momentum associated with 'PT' is:

$$\overrightarrow{L}_{PT} = m_P \overrightarrow{R}_{PT} \times \overrightarrow{\widetilde{v}}_P, \tag{A.21}$$

in which we know $\overrightarrow{L}_{PT}$ and $\overrightarrow{R}_{PT}$.

Since $\overrightarrow{L}$ is $\perp$ to the plane defined by $\overrightarrow{R}_{PT}$ and $\overrightarrow{\widetilde{v}}_P$, we can define $\overrightarrow{\widetilde{v}}_P$ as the sum of the radial and transverse components of the projectile velocity:

$$\overrightarrow{\widetilde{v}}_P = \widetilde{v}_P^{(r)}\hat{r} + \widetilde{v}_P^{(q)}\hat{q}, \tag{A.22}$$

where:

$$\overrightarrow{R}_{PT} = \quad R_{PT}\hat{r}, \tag{A.23a}$$

$$\overrightarrow{L}_{PT} = \quad L_{PT}\hat{n}, \tag{A.23b}$$

$$\hat{q} = \quad \hat{n} \times \hat{r}. \tag{A.23c}$$

And so from Eq. (A.21):

$$L_{PT} = m_P R_{PT} \widetilde{v}_P^{(q)}, \tag{A.24}$$

$$\widetilde{v}_P^{(q)} = \frac{L_{PT}}{m_P R_{PT}}, \tag{A.25}$$

and of course:

$$\widetilde{v}_T^{(q)} = -\frac{L_{PT}}{m_T R_{PT}}. \tag{A.26}$$

The remaining unknown is $\widetilde{v}_P^{(r)}$, the radial component. From Eq. (A.15):

$$\overrightarrow{v}_{PT} = \left(\widetilde{v}_P^{(q)} - \widetilde{v}_T^{(q)}\right)\hat{q} + \left(\widetilde{v}_P^{(r)} - \widetilde{v}_T^{(r)}\right)\hat{r}, \tag{A.27}$$

but we know $|\overrightarrow{v}_{PT}| = V_{PT}$ from Eq. (A.11) and $\tilde{v}^{(q)}$ so:

$$\left[\widetilde{v}_P^{(r)} - \widetilde{v}_T^{(r)}\right] = \pm\left[V_{PT}^2 - \left[\widetilde{v}_P^{(q)} - \widetilde{v}_T^{(q)}\right]^2\right]^{1/2}, \tag{A.28}$$

and from Eq. (A.14):

$$\widetilde{v}_P^{()} - \widetilde{v}_T^{()} = \widetilde{v}_P^{()}\left[1 + \frac{m_P}{m_T}\right], \tag{A.29}$$

gives us:

$$\widetilde{v}_P^{(r)} = \pm\left[V_{PT}^2 - \left[\widetilde{v}_P^{(q)}\left(1 + \frac{m_P}{m_T}\right)\right]^2\right]^{1/2} \Big/ \left(1 + \frac{m_P}{m_T}\right). \tag{A.30}$$

Both roots are consistent with $\overrightarrow{L}_{tot}$, $\overrightarrow{P}_{tot}$ and $\overrightarrow{E}_{tot}$ conservation and so are sampled in equal measure.

Appendix B

Breakup probability function

If we define the probability of breakup between R and $R + dR$ as $\rho(R)dR$ [with $\rho(R)$ being a density of probability], and the probability of the weakly bound projectile's survival from ∞ to R as $S(R)$, then we can write the survival probability at $R + dR$, $S(R + dR)$, as follows:

$$S(R + dR) = S(R)[1 - \rho(R)dR], \tag{B.1}$$

which in turn allows us to write the differential equation for the survival probability $S(R)$ as:

$$\frac{dS(R)}{dR} = -S(R)\rho(R), \tag{B.2}$$

Taking $S(\infty) = 1$, the solution to Eq. (B.2) is:

$$S(R) = \exp\left(-\int_{\infty}^{R} \rho(R)dR\right). \tag{B.3}$$

The breakup probability at R, $B(R)$, is equal to $1 - S(R)$. Therefore, in the event that $\int_{\infty}^{R} \rho(R)dR \ll 1$, the breakup probability can be written using Eq. (B.3) as:

$$B(R) \approx \int_{\infty}^{R} \rho(R)dR. \tag{B.4}$$

Identifying $\rho(R)$ in Eq. (B.4) with $\mathcal{P}_{BU}^{L}(R)$ we derive Eq. (2.1) for the breakup probability integrated along a given classical orbit.

Appendix C

Finite-difference method

Fortran-90 code

```
MODULE fragmentation_theory
  USE nrutil, ONLY: nrerror,SPLINE,SPLINT,LOCATE
  IMPLICIT NONE

  ! Constant declarations
  REAL (rkind), PARAMETER :: HMC=0.04818696_rkind
   !HMC=2m/h^2 (MeV^-1fm^-2),
                             ! where m and h are the nucleon mass and
                             ! the planck constant divided by 2*pi,
                             ! respectively.

  INTEGER, PARAMETER ::    NPTS=2001,     NSTM=1000
  REAL (rkind), PARAMETER :: interval_length=2.d0
   !Length of the fragmentation interval
  REAL (rkind), PARAMETER :: xmin=-1.0_rkind,xmax=1.0_rkind

  REAL (rkind), DIMENSION(11) :: &
```

```
  BU1 = (/ 0.0, 11.688, -5.6664, 11.1503, -5.6522, &
    14.4476, -5.6522, 11.1503, -5.6664, 11.688, 0.0 /), &
  MASS1 = (/ 7292.8222, 15348.5485, 16078.4048, 16459.5914, &
   16665.2558, 16727.8784, 16665.2558, 16459.5914, &
   16078.4048, 15348.5485, 7292.8222 /), &
  ETAZ1 =(/ -1.0, -0.8, -0.6, -0.4, -0.2, 0.0, &
    0.2, 0.4, 0.6, 0.8, 1.0 /)  !CHARGE ASYMMETRY COORDINATE

  REAL(rkind) :: inv_mass = 1.E-6_rkind

  REAL(rkind), DIMENSION(11) :: x1,y1,d2y1,x2,y2,d2y2

  !Properties of compound nucleus
  !REAL (rkind) :: ACN=20.0_rkind, ZCN=10.0_rkind
  !REAL (rkind) :: U0=0.0_rkind !potential energy of the CN

  !Auxiliary variables
  integer ::   nst
  real (rkind) ::  dx,vmin,de,ss1,ss2,xx,const,inertia1,inertia2
  real(rkind), DIMENSION(NPTS,NPTS) :: A,ev1
  real (rkind), DIMENSION(NPTS) :: v,inertia,diag,subd,subd1,subd2,ee
  real (rkind), DIMENSION(NPTS,NSTM) ::  ev

  CONTAINS

SUBROUTINE fragmentation(U0)
  IMPLICIT NONE
  REAL (rkind), INTENT(IN)  :: U0

  integer :: i,j,n,nrot1
  integer :: m,info,lwork1,error
```

```
  real (rkind), DIMENSION(8*NPTS) :: work1
  integer, DIMENSION(5*NPTS) :: iwork
  integer, DIMENSION(NPTS) :: ifail
  real (rkind), DIMENSION(5*NPTS) :: work
  real(rkind) ::  abstol, dlamch
  real(rkind), DIMENSION(NPTS) :: ev1_tmp,ev2_tmp

  INTEGER, DIMENSION(1) :: maxim

      REAL(rkind) :: L = 2.0_rkind

!   ------------------------------------------------------------------
!   specify units:
!   rewrite Schroedinger equation: v(x)=2m*V(x)/hbar^2; ee=2m*E/hbar^2
!
!   [    d^2       2m        ]           2m*E
!   [ - -----  + ------ V(x) ] phi(x) = ------  phi(x)
!   [   d x^2    hbar^2      ]          hbar^2
!
!   ------------------------------------------------------------------

! discretization
dx=L/dble(NPTS-1)

! define inertia and potential

  MASS1 = MASS1*1.E-6_rkind
 !inv_mass = SUM(MASS1(1:SIZE(MASS1,1)))/SIZE(MASS1,1) !average inertia
  maxim = MAXLOC(MASS1(1:SIZE(MASS1,1)))
  inv_mass = MASS1(maxim(1))
  const = HMC/inv_mass
```

```
write(13,*)'Averaged inverse inertia in charge asymmetry is', inv_mass

BU1(1) = U0
BU1(SIZE(BU1,1)) = BU1(1)

x1 = ETAZ1
y1 = BU1

do i=1,SIZE(ETAZ1,1)
   WRITE(8,*) ETAZ1(i),BU1(i),MASS1(i)
enddo

CALL SPLINE(x1,y1,SIZE(x1,1),1.E+30_rkind,1.E+30_rkind,d2y1)

x2 = x1
y2 = MASS1

CALL SPLINE(x2,y2,SIZE(x2,1),1.E+30_rkind,1.E+30_rkind,d2y2)

write(13,*) "Interpolating driving potential and inertia"
nst=NSTM                              ! initial states included
do i=1,NPTS
   xx = xmin+(i-1)*dx
   !potential
   CALL SPLINT(x1,y1,d2y1,SIZE(x1,1),xx,ss1)
   v(i)= const*ss1
   !inertia
   CALL SPLINT(x2,y2,d2y2,SIZE(x2,1),xx,ss2)
   inertia(i)=ss2
   WRITE(9,*) xx,ss1,ss2
```

```
  enddo

! discretized form of kinetic energy operator (incl. boundary cond.)
!     f''(x_i) \approx (f(x_{i-1})-2*f(x_i)+f(x_{i+1}))/dx^2
! by dropping terms from outside the mesh, we have chosen boundary
! conditions such that the phi vanishes outside the mesh
  do i=1,NPTS

    if (i > 1 .and. i < NPTS) then
      inertia1 = 0.5_rkind*(inertia(i+1) + inertia(i))
      inertia2 = 0.5_rkind*(inertia(i) + inertia(i-1))
    else if (i == 1) then
      inertia1 = 0.5_rkind*(inertia(i+1) + inertia(i))
      inertia2 = 0.5_rkind*(inertia(i) + inertia(NPTS-1))
    else if (i == NPTS) then
      inertia1 = 0.5_rkind*(inertia(2) + inertia(i))
      inertia2 = 0.5_rkind*(inertia(i) + inertia(i-1))
    end if

    inertia1 = inertia1/inv_mass
    inertia2 = inertia2/inv_mass

    diag(i)=v(i)+(inertia1 + inertia2)/dx**2
    subd1(i)=-inertia1/dx**2
    subd2(i)=-inertia2/dx**2

    !symmetrizing the tridiagonal matrix, which should be
    !a good approximation if inertia1 is almost equal to inertia2.
    subd(i) = (subd1(i) + subd2(i))/2.0_rkind

  enddo
```

```
! Building the matrix A which is required for a non tridiagonal case,
! for instance, having periodic boundary conditions.
A=0.0_rkind
do i=1,NPTS

  A(i,i) = diag(i)

  ! Upper triangle of A
  if (i < NPTS) then
    A(i,i+1) = subd1(i)
    ! For periodic b.c.s
    if (i == 1) then
      A(1,NPTS) = subd(1)
    end if
  end if

  ! Lower triangle of A
  if (i > 1) then
    A(i,i-1) = subd2(i)
    ! For periodic b.c.s
    if (i == NPTS) then
      A(NPTS,1) = subd(1)
    end if
  end if

enddo
lwork1=SIZE(work1,1)

! call LAPACK to diagonalize tridiagonal matrix
if(nst.lt.1) nst=1
```

```
  if(nst.gt.NSTM) then
    write(*,'(">>> increase NSTM to get more states")')
    nst=NSTM
  endif
  abstol=2d0*dlamch('s')

  call DSYEVX('v','i', 'U', NPTS, A, NPTS, 0d0,1d0, 1,NSTM, abstol, &
              m,ee,ev,NPTS,work1,lwork1,iwork,ifail,info)

  if(info.ne.0) stop '>>> diagonalization failed'

! Determine number of states to include using projectile friction
DO n=1,nst
IF ((ee(n)/const).LE.((ee(1)/const)+EXCRANGE)) THEN
CYCLE
ELSE
nst=(n-1)
EXIT
END IF
END DO

  ! Normalising the eigenvectors
  do j=1,nst
    ev(:,j) = ev(:,j)/sqrt(dx*dot_product(ev(:,j),ev(:,j)))
    write(13,*) "Length of ev(",j,")=", dx*dot_product(ev(:,j),ev(:,j))
    write(13,*) "Orthogonality of ev(1) with ev(",j,")=", &
     dx*dot_product(ev(:,1),ev(:,j))
  end do

! Lowest symmetric and anti-symmetric states
ev1_tmp(:) = ev(:,1) + ev(:,2)
```

```
  ev2_tmp(:) = ev(:,1) - ev(:,2)
ev1_tmp = ev1_tmp/sqrt(dx*dot_product(ev1_tmp(:),ev1_tmp(:)))
  ev2_tmp = ev2_tmp/sqrt(dx*dot_product(ev2_tmp(:),ev2_tmp(:)))
write(13,*) "Length of ev1_tmp=", dx*dot_product(ev1_tmp(:),ev1_tmp(:))
write(13,*) "Length of ev2_tmp=", dx*dot_product(ev2_tmp(:),ev2_tmp(:))
write(13,*) "Orthogonality between ev1_tmp  and ev2_tmp=", &
dx*dot_product(ev1_tmp(:),ev2_tmp(:))

! symmetrized and anti-symmetrized states
do i=1,NPTS
write(16,'(I6,F20.10,3(E25.15E3))') i-1, xmin+(i-1)*dx, &
dx*ev1_tmp(i)**2, dx*ev2_tmp(i)**2, dx*(ev(i,1)**2 + ev(i,2)**2)
enddo

  ! write eigenenergies
  write(13,*) "eigenenergies:"
    do n=1,nst
      write(13,'(I4,F20.10,F20.10," MeV")') n,ee(n),ee(n)/const
  enddo

  ! output for gnuplot ---------------------------------------------
  ! minimum of potential for plotting range
  vmin=1d10
  do i=1,NPTS
    if(v(i).lt.vmin) vmin=v(i)
  enddo

  ! average spacing of energy levels (for adjusting scale of ev)
  de=(ee(nst)-ee(1))/dble(nst-1)
  open(10,file='1d_fragmentation.dat')
```

```
  write(10,'("eigenenergies:")')
    do n=1,nst
      write(10,'(I4,F20.10,F20.10," MeV")') n,ee(n),ee(n)/const
  enddo

  write(10,'("e")')
  do n=1,nst
    write(10,'("# eng=",F20.10,F20.10," MeV")') ee(n), ee(n)/const
    if (n <= 2) then  !For ground-state wave function
      write(15,'("#")')
      write(15,'("# eng=",F20.10," MeV"/)') ee(n)/const
    end if
    do i=1,NPTS
      write(10,'(I6,F20.10,E25.15E3)') i-1, xmin+(i-1)*dx,ev(i,n)
      if (n <= 2) then  !For ground-state wave function
        write(15,'(I6,F20.10,E25.15E3,E25.15E3)') &
        i-1, xmin+(i-1)*dx,ev(i,n), dx*ev(i,n)**2
      end if
    enddo
    write(10,'(I6,E25.15E3)') 0,ev(1,n)
    write(10,'("e")')
  enddo

  CLOSE(10, STATUS='KEEP')

    END SUBROUTINE fragmentation

END MODULE fragmentation_theory
```

Appendix D

Monte-Carlo sampling

D.1 Method

Following the implementation of the finite-difference method, the next step is to Monte-Carlo sample the fragmentation of the projectile numerous times for each partial wave of the computation via direct inversion of the cumulative distribution function (CDF) [111], as illustrated by Fig. D.1 below:

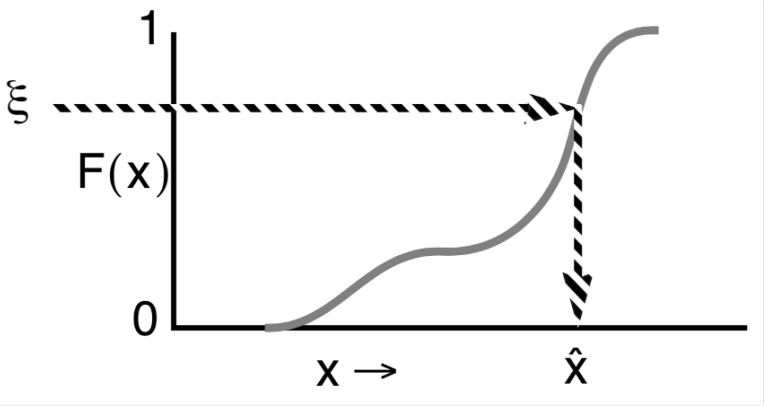

Figure D.1: Determining $\hat{x}$ from ξ using a cumulative distribution function [112].

The algorithm is implemented as follows:

- First the PDF ψ^2 is read in (lines 60-65 in the sample code provided below).
- Then the PDF is transformed into a CDF (denoted $F(x)$ in Fig. D.1) (lines 68-73).
- To make one sample ξ is randomly generated between 0 and 1 (line 79).
- ξ is then sorted into its appropriate bin from the PDF (lines 81-87).
- The corresponding η_Z value (denoted $\hat{x}$ in Fig. D.1) from the PDF is then returned (lines 89-91).
- This process is repeated 1,000,000 times in a 'do loop' (lines 76-93 in).
- This new array is then re-ordered (lines 96-101 in Appendix E).
- This array is then written out to a file for plotting (lines 104-110).

Fig. D.2 below is an example of that plot for the first eigenvalue of Neon-20 shown in Fig. 5a.

When comparing Fig. D.2 to Fig. 3.2a, the plots appear identical, indicating the correctness of this Monte-Carlo sampling algorithm.

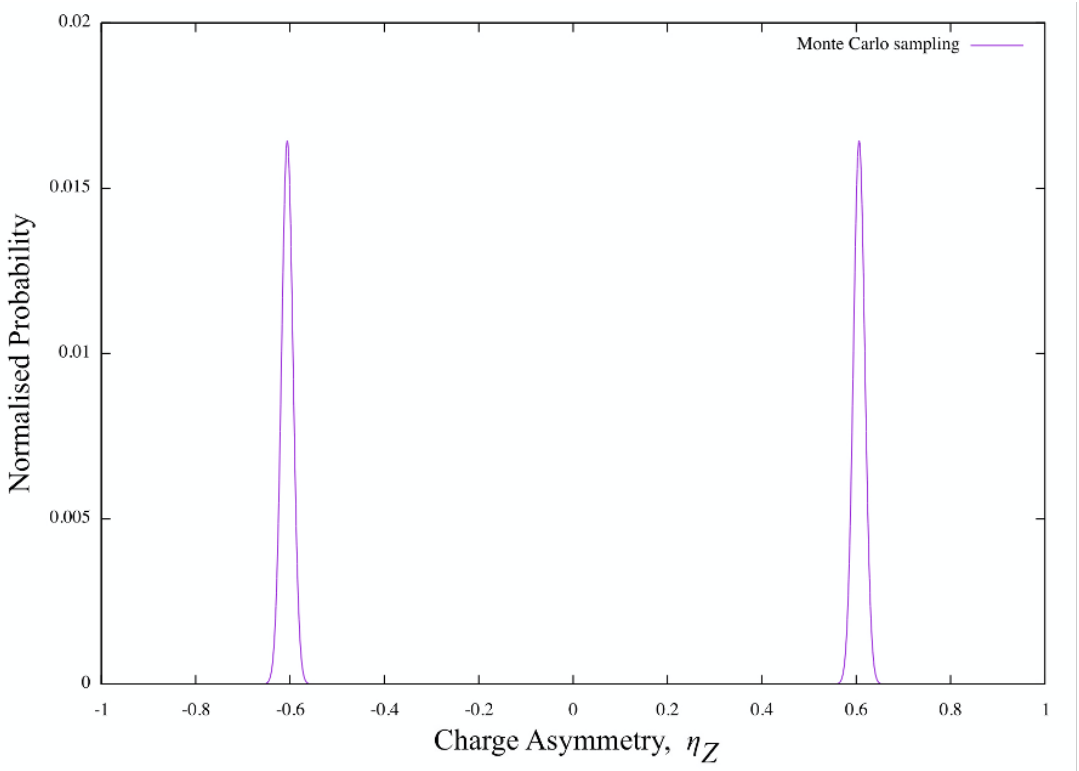

Figure D.2: Monte-Carlo sampling of the first eigenvalue of ^{20}Ne shown in Fig. 3.2a, indicating that this Monte-Carlo sampling technique is successful.

D.2 Fortran-90 code

```
MODULE random_number_generator

  IMPLICIT NONE

  PRIVATE

  INTEGER,  PARAMETER :: DP=SELECTED_REAL_KIND(12,60)
  REAL(DP), PARAMETER :: half=0.5_DP
  INTEGER,  SAVE      :: jz, jsr=123456789

  PUBLIC :: shr3, uni

  CONTAINS

    ! Generate random 32-bit integers
    FUNCTION shr3() RESULT(ival)
      INTEGER :: ival

      jz = jsr
      jsr = IEOR(jsr,ISHFT(jsr, 13))
      jsr = IEOR(jsr,ISHFT(jsr,-17))
      jsr = IEOR(jsr,ISHFT(jsr,  5))
      ival = jz+jsr

      RETURN
    END FUNCTION shr3

    ! Genrate uniformly distributed random numbers
    FUNCTION uni() RESULT(fn_val)
```

```
      REAL(DP) :: fn_val

      fn_val = half+0.2328306E-09_DP*shr3()

      RETURN
    END FUNCTION uni

END MODULE random_number_generator

!-----------------------------------------------------------------------

PROGRAM CDF
  USE random_number_generator
  IMPLICIT NONE

  INTEGER, PARAMETER      :: rkind=SELECTED_REAL_KIND(P=12), NPTS=2001
  INTEGER                 :: i, j, N, irow, krow
  REAL                    :: junk
  REAL (rkind), PARAMETER :: xmin=-1.0_rkind, L=2.d0
  REAL (rkind)            :: dx=L/dble(NPTS-1), xi
  REAL (rkind), SAVE, DIMENSION(NPTS)       :: z, psi, F
  REAL (rkind), ALLOCATABLE, DIMENSION(:,:) :: MC
  REAL (rkind), ALLOCATABLE, DIMENSION(:)   :: buf

  ! Number of random points to sample
  N = 1000000

  ALLOCATE(MC(N,2),buf(2))

  ! Read input file
  OPEN(11,FILE='psi_symmetrised.dat')
```

```
READ(11,*)
DO i=1,NPTS
  READ(11,*) z(i), junk, psi(i)
END DO
CLOSE(11)

! Construct CDF
OPEN(12,FILE='CDF.dat')
DO i=1,NPTS
  F(i) = SUM(psi(1:i))
  WRITE(12,*) xmin+(i-1)*dx, F(i)
END DO
CLOSE(12)

! Monte Carlo sampling
OPEN(13,FILE='MonteCarlo.dat')
DO i=1,N
  ! Generate random xi value between 0 and 1
  xi = uni()
  ! Sort xi value into appropriate bin from F(xi)
  DO j=1,NPTS
    IF (xi.GT.F(j)) THEN
      CYCLE
    ELSE
      EXIT
    END IF
  END DO
  ! Take corresponding X value [Eta(Z)]
  MC(i,1) = xmin+(j-1)*dx
  MC(i,2) = psi(j)
  WRITE(13,*) MC(i,1), MC(i,2)
```

```
  END DO
  CLOSE(13)

  ! Re-order array (for plotting)
  DO irow = 1,N
    krow = MINLOC(MC(irow:N,1),DIM=1)+irow-1
    buf(:)     = MC(irow,:)
    MC(irow,:) = MC(krow,:)
    MC(krow,:) = buf(:)
  END DO

  ! Write newly-ordered array to file
  OPEN(14,FILE='MonteCarlo2.dat')
  DO i=1,N
    WRITE(14,*) MC(i,1), MC(i,2)
  END DO
  CLOSE(14)

  WRITE(6,'(a,e9.2)') 'Average x value: ', SUM(MC(:,1))/N

  DEALLOCATE(MC)

END PROGRAM CDF
```

Appendix E

Inertia coefficient calculation Fortran-90 code

```
MODULE kinds
  INTEGER(KIND=8), parameter :: rkind  = SELECTED_REAL_KIND(P=12)
  real(rkind), parameter    :: zero_r = 0.0_rkind
  real(rkind), parameter    :: one_r  = 1.0_rkind
  real(rkind), parameter    :: half_r = 0.5_rkind
END MODULE kinds

MODULE global_data
   USE kinds
   IMPLICIT NONE
   SAVE

   ! Constant declarations
   REAL (rkind), PARAMETER :: HMC=0.04818696_rkind, &
                              charge_2=1.43997_rkind, m0= 1.0422_rkind
                              ! HMC=2m/h^2 (MeV^-1fm^-2),
                              ! where m and h are the nucleon mass and
```

```
                                ! the planck constant divided by 2*pi,
                                ! respectively.
                                ! charge^2=e^2 (MeV fm).
                                ! m0 is nucleon mass,938 MeV/c^2, or
                                ! 1.0422 x 10^{-44} MeV fm^{-2} s^{2}.

  ! Variable declarations

  REAL (rkind) :: PI
  ! Limits of integration in cylindrical coordinates
  REAL (rkind) :: Z_MIN,Z_MAX,R_MAX
  ! z-coordinate of the center of the fragments and the place where
  ! the densities are the same.
  REAL (rkind) :: Z0L,Z0H,Z0M
  ! Distance between the centers of the fragments, which is ZH - ZL.
  REAL (rkind) :: DISTANCE
  ! Variables used to search for different values of ETA-parameter.
  REAL (rkind) :: ETA_start=0.0_rkind, ETA_end=1.0_rkind, ETA_step=0.1_rkind

  ! Radius parameters (fm) for Light and Heavy fragments.
  REAL (rkind) :: r0L=1.1_rkind,r0H=1.1_rkind
  ! Diffuseness of the density (fm).
  REAL (rkind) :: a0L=0.5_rkind,a0H=0.5_rkind
  ! Density in the center of a nucleus (fm^{-3}).
  REAL (rkind) :: DEN0 = 0.16_rkind
  ! Neck parameter (fm).
  REAL (rkind) :: b0neck=0.45_rkind
  ! Mass and charge of the fragments.
  REAL (rkind) :: AL,AH,ZL,ZH
  ! Mass of the Compound Nucleus.
  REAL (rkind) :: ACN=48.0_rkind
```

```
   ! Charge of the Compound Nucleus.
   REAL (rkind) :: ZCN=20.0_rkind

END MODULE global_data

MODULE volume
   USE global_data
   IMPLICIT NONE
   PRIVATE
   PUBLIC :: Aneck

   CONTAINS

     SUBROUTINE Aneck(nu)

       ! Dummy arguments
       REAL (rkind), INTENT (OUT) :: nu

       ! Local variables
       INTEGER(KIND=8) :: i,INFO1,KEY,NF,IFAIL,NW,MAXPTS,MINPTS,NEVAL, &
                  NDIM,RESTAR,error
       REAL (rkind) :: pi,EPSABS,EPSREL
       REAL (rkind), ALLOCATABLE, DIMENSION(:), SAVE :: VOL,ABSERR
       ! VOL(NF),ABSERR(NF)
       REAL (rkind), ALLOCATABLE, DIMENSION (:), SAVE :: AA,BB
       ! AA(NDIM),BB(NDIM)
       REAL (rkind), ALLOCATABLE, DIMENSION (:), SAVE :: WRKSTR
       ! WRKSTR(NW)

   !  Here the subroutine DCUHRE from NETLIB is used to perform the
   !  multidimensional integration.
```

```
   NDIM=2
   NF=1
   MINPTS=0
   MAXPTS=200000000
   EPSABS=0.0_rkind
   EPSREL=1.E-8_rkind
   IFAIL=-1
   KEY=4
!   NW=(NDIM+2)*(1+MAXPTS/(2**NDIM+2*NDIM*NDIM+2*NDIM+1))
   NW=MAXPTS*(2*NDIM+2*NF+2) + 17*NF + 1
   RESTAR=0
   ALLOCATE(VOL(NF),ABSERR(NF),AA(NDIM),BB(NDIM),WRKSTR(NW), &
            STAT=error)
!   IF (error /= 0) CALL nrerror('Program could not allocate space &
!                                &for VOL,ABSERR,AA,BB and WRKSTR &
!                                &in volume')

   AA(1)=Z_MIN
   BB(1)=Z_MAX
   AA(2)=0.0_rkind
   BB(2)=R_MAX

   CALL DCUHRE(NDIM,NF,AA,BB,MINPTS,MAXPTS,FUNSUB,EPSABS,EPSREL, &
               KEY,NW,RESTAR,VOL,ABSERR,NEVAL,IFAIL,WRKSTR)

!   IF (IFAIL /= 0) PRINT *,"IN DCUHRE IFAIL=",IFAIL

!   PRINT *, "Volume=",VOL(NF)

   nu=VOL(NF)
```

```
 DEALLOCATE(VOL,ABSERR,AA,BB,WRKSTR)

 RETURN
 END SUBROUTINE Aneck

 SUBROUTINE FUNSUB(NDIM,VV,NUMFUN,FUNVLS)

!Dummy argument
 INTEGER(KIND=8), INTENT (IN) :: NDIM,NUMFUN
 REAL (rkind), DIMENSION (NDIM), INTENT (IN) :: VV
 REAL (rkind), DIMENSION (NUMFUN), INTENT (OUT) :: FUNVLS

!Local variables
 INTEGER(KIND=8) :: I
 REAL (rkind) :: SL,SH,ss,ss1,ssL,ssH,integrand


 ssL= (SQRT( VV(2)**2 + VV(1)**2 ) - Z0L)/a0L
 IF (ABS(ssL) < 299.0_rkind) THEN
    SL = EXP(ssL)
 ELSE
    SL = 0.0_rkind
 END IF

 ssH=(SQRT( VV(2)**2 + (DISTANCE-VV(1))**2 ) - Z0H)/a0H
 IF (ABS(ssH) < 299.0_rkind) THEN
    SH = EXP(ssH)
 ELSE
    SH = 0.0_rkind
 END IF
```

```
      ss = 1.0_rkind/(1.0_rkind + SL) + 1.0_rkind/(1.0_rkind + SH)

      ss1=((VV(1)-Z0M)/b0neck)**2
      IF (ss1 < 299.0_rkind) THEN
         integrand = VV(2)*ss*EXP(-ss1)
      ELSE
         integrand = 0.0_rkind
      END IF

      DO I=1,NUMFUN
         FUNVLS(I)=integrand
      END DO

      RETURN
      END SUBROUTINE FUNSUB

END MODULE volume

PROGRAM inertia_DNS
   USE global_data
   USE volume
   IMPLICIT NONE

   !This program calculates the mass parameters of a dinuclear system,
   !(ADT, April 2020).
   !See Adamian et al., NPA 584 (1995) 205-220.

   !Local variable declarations
   INTEGER(KIND=8) :: error,i,N_step
   REAL (rkind) :: aa,yy,xx,ss,ETA,invmass,invmass2
```

```
PI=acos(-1.0_rkind)
N_step=NINT((ETA_end - ETA_start)/ETA_step)

aa=a0L/a0H
yy = ZCN/ACN
!yy = 1.0_rkind

DO i=0,N_step,1

   ETA = ETA_start + ETA_step*i  !Different mass/charge asymmetries

   AL = 0.5_rkind*ACN*(1.0_rkind - ETA)
   AH = 0.5_rkind*ACN*(1.0_rkind + ETA)
   ZL = 0.5_rkind*ZCN*(1.0_rkind - ETA)
   ZH = 0.5_rkind*ZCN*(1.0_rkind + ETA)

   !b0neck = 0.479 - 0.019*ETA

   Z0L =   r0L*AL**(1.0_rkind/3.0_rkind)
   Z0H =   r0H*AH**(1.0_rkind/3.0_rkind)

   DISTANCE = Z0H + Z0L

   !Defining the point where the densities are the same
   !(origin of the z-coordinate).
   Z0M = (aa*(DISTANCE-Z0H) + Z0L)/(1.0_rkind + aa)

   Z_MIN = -10.0_rkind*Z0L
   Z_MAX = DISTANCE+10.0_rkind*Z0H
   R_MAX = 10.0_rkind*Z0H
```

```
        CALL Aneck(xx)

        ss=2.0_rkind*PI*DEN0*xx
        invmass = (1.0_rkind/yy/yy)*ss/ &
                  (2.0_rkind*SQRT(2.0_rkind*PI)*b0neck*b0neck*ACN*ACN)
        invmass2 = invmass/m0

        PRINT*,"ETA=", ETA, "Aneck=",ss, "invmass=",invmass, &
                "[m0^{-1} fm^{-2}]", " invmass2=", invmass2, &
                "[10^{-44} MeV^{-1} s^{-2}]"

    END DO

END PROGRAM inertia_DNS
```

Bibliography

[1] H. Kragh, *From Transuranic to Superheavy Elements* (Springer International Publishing, 2018), pp. 2–3.

[2] A. Sobiczewski, F. A. Gareev, and B. N. Kalinkin, Physics Letters **22**, 500 (1966).

[3] Y. T. Oganessian, V. K. Utyonkov, Y. V. Lobanov, F. S. Abdullin, A. N. Polyakov, I. V. Shirokovsky, Y. S. Tsyganov, G. G. Gulbekian, S. L. Bogomolov, B. N. Gikal, et al., Nuclear Physics A **734**, 109 (2004).

[4] G. T. Seaborg and W. D. Loveland, *The Elements Beyond Uranium* (Wiley-Interscience, 1990).

[5] S. Ćwiok, J. Dobaczewski, P.-H. Heenen, P. Magierski, and W. Nazarewicz, Nuclear Physics A **611**, 211 (1996).

[6] D. Seweryniak, *Recoil separators for studies of super-heavy nuclei*, "Przyszłość fizyki jądrowej w Polsce" Conference (2019). Available at: `http://slcj.uw.edu.pl/wp-content/uploads/konferencja_slcj2019/DSeweryniak_HIL2019_publish.pdf`, Accessed: 13/04/2021.

[7] S. G. Nilsson, C. F. Tsang, A. Sobiczewski, Z. Szymański, S. Wycech, C. Gustafson, I.-L. Lamm, P. Möller, and B. Nilsson, Nuclear Physics A **131**, 1 (1969).

[8] U. Mosel and W. Greiner, Zeitschrift für Physik A Hadrons and nuclei **217**, 256 (1968).

[9] U. Mosel and W. Greiner, Zeitschrift für Physik A Hadrons and nuclei **222**, 261 (1969).

[10] S. Hofmann and G. Münzenberg, Reviews of Modern Physics **72**, 733 (2000).

[11] H. C. Britt and A. R. Quinton, Physical Review **124**, 877 (1961).

[12] J. Galin, B. Gatty, D. Guerreau, C. Rousset, U. C. Schlotthauer-Voos, and X. Tarrago, Physical Review C **9**, 1126 (1974).

[13] T. Udagawa and T. Tamura, Physical Review Letters **45**, 1311 (1980).

[14] J. R. Wu and I. Y. Lee, Physical Review Letters **45**, 8 (1980).

[15] J. R. Wu, C. C. Chang, and H. D. Holmgren, Physical Review Letters **40**, 1013 (1978).

[16] J. Wilczyński, K. Siwek-Wilczyńska, J. van Driel, S. Gonggrijp, D. C.J. M. Hageman, R. V. F. Janssens, J. Łukasiak, and R. H. Siemssen, Physical Review Letters **45**, 606 (1980).

[17] I. M. Brâncuş, H. Rebel, J. Wentz, and V. Corcalciuc, Physical Review C **42**, 2157 (1990).

[18] J. P. Bondorf, J. N. De, G. Fái, A. O. T. Karvinen, B. Jakobsson, and J. Randrup, Nucl. Phys. A **333**, 285 (1980).

[19] D. H. E. Gross and J. Wilczyński, Physics Letters B **67**, 1 (1977).

[20] H. Tricoire, C. Gerschel, A. Gillibert, and N. Perrin, Zeitschrift für Physik A: Atomic Nuclei **323**, 163 (1986).

[21] T. C. Awes, G. Poggi, C. K. Gelbke, B. B. Back, B. G. Glagola, H. Breuer, and V. E. Viola, Physical Review C **24**, 89 (1981).

[22] M. Blann, Physical Review C **23**, 205 (1981).

[23] T. Otsuka and K. Harada, Physics Letters B **121**, 106 (1983).

[24] B. G. Harvey, Nuclear Physics A **444**, 498 (1985).

[25] M. H. Simbel and A. Y. Abul-Magd, Zeitschrift für Physik A: Atoms and Nuclei **294**, 277 (1980).

[26] W. Morison, S. Samaddar, D. Sperber, and M. Zielińska-Pfabé, Physics Letters B **99**, 205 (1981).

[27] K. Möhring, T. Srokowski, D. Gross, and H. Homeyer, Physics Letters B **203**, 210 (1988).

[28] H. Morgenstern, W. Bohen, W. Galster, K. Grabisch, and A. Kyanowski, Physical Review Letters **52**, 1104 (1984).

[29] U. Gupta, P. P. Singh, D. P. Singh, M. K. Sharma, A. Yadav, R. Kumar, B. Singh, and R. Prasad, Nuclear Physics A **811**, 77 (2008).

[30] P. P. Singh, B. P. Singh, M. K. Sharma, U. Gupta, D. P. Singh, R. Prasad, R. Kumar, and K. S. Golda, Physical Review C **77**, 014607 (2008).

[31] T. Inamura, M. Ishihara, T. Fukuda, T. Shimoda, and H. Hiruta, Physics Letters B **68**, 51 (1977).

[32] T. Inamura, T. Kojima, T. Nomura, T. Sugitate, and H. Utsunomiya, Physics Letters B **84**, 71 (1979).

[33] T. Inamura, A. C. Kahler, D. R. Zolnowski, U. Garg, T. T. Sugihara, and M. Wakai, Physical Review C **32**, 1539 (1985).

[34] D. R. Zolnowski, H. Yamada, S. E. Cala, A. C. Kahler, and T. T. Sugihara, Physical Review Letters **41**, 92 (1978).

[35] K. A. Geoffroy, D. G. Sarantites, M. L. Halbert, D. C. Hensley, R. A. Dayras, and J. H. Barker, Physical Review Letters **43**, 1303 (1979).

[36] W. Trautmann, O. Hansen, H. Tricoire, W. Hering, R. Ritzka, and W. Trombik, Physical Review Letters **53**, 1630 (1984).

[37] C. Gerschel, Nuclear Physics A **387**, 297 (1982).

[38] R. L. Robinson, R. L. Auble, I. Y. Lee, M. J. Martin, G. R. Young, J. G. del Campo, J. B. Ball, F. E. Bertrand, R. L. Ferguson, C. B. Fulmer, J. R. Wu, J. C. Wells, and H. Yamada, Physical Review C **24**, 2084 (1981).

[39] H. Utsunomiya, T. Nomura, M. Ishihara, T. Sugitate, K. Ieki, and S. Kohmoto, Physics Letters B **105**, 135 (1981).

[40] J. H. Barker, J. R. Beene, M. L. Halbert, D. C. Hensley, M. Jääskeläinen, D. G. Sarantites, and R. Woodward, Physical Review Letters **45**, 424 (1980).

[41] B. Back, H. Esbensen, C. Jiang, and K. Rehm, Reviews of Modern Physics **86**, 317 (2014).

[42] L. Canto, P. Gomes, R. Donangelo, J. Lubian, and M. Hussein, Physics Reports **596**, 1 (2015).

[43] M. Boselli and A. Diaz-Torres, Journal of Physics G: Nuclear and Particle Physics **41**, 094001 (2014).

[44] B. Carlson, T. Frederico, and M. Hussein, Physics Letters B **767**, 53 (2017).

[45] J. Lei and A. M. Moro, Physical Review Letters **122**, 042503 (2019).

[46] K. Yabana, Progress of Theoretical Physics **97**, 437 (1997).

[47] M. Boselli and A. Diaz-Torres, Physical Review C **92**, 044610 (2015).

[48] A. Diaz-Torres and I. J. Thompson, Physical Review C **65**, 024606 (2002).

[49] A. Diaz-Torres, I. J. Thompson, and C. Beck, Physical Review C **68**, 044607 (2003).

[50] I. J. Thompson and A. Diaz-Torres, Progress of Theoretical Physics Supplement **154**, 69 (2004).

[51] A. Diaz-Torres, D. J. Hinde, J. A. Tostevin, M. Dasgupta, and L. R. Gasques, Physical Review Letters **98**, 152701 (2007).

[52] A. Diaz-Torres, Journal of Physics G: Nuclear and Particle Physics **37**, 075109 (2010).

[53] A. Diaz-Torres, Computer Physics Communications **182**, 1100 (2011).

[54] A. Shrivastava, A. Navin, A. Diaz-Torres, V. Nanal, K. Ramachandran, M. Rejmund, S. Bhattacharyya, A. Chatterjee, S. Kailas, A. Lemasson, R. Palit, V. Parkar, R. Pillay, P. Rout, and Y. Sawant, Physics Letters B **718**, 931 (2013).

[55] C. Borcea, E. Gierlik, R. Kalpakchieva, Y. Oganessian, and Y. Penionzhkevich, Nuclear Physics A **351**, 312 (1981).

[56] C. Borcea, E. Gierlik, A. M. Kalinin, R. Kalpakchieva, Y. T. Oganessian, T. Pawlat, Y. E. Penionzhkevich, and A. V. Rykhlyuk, Nuclear Physics A **391**, 312 (1982).

[57] C. Borcea, E. Gierlik, R. Kalpakchieva, N. H. Chau, Y. Oganessian, T. Pawlat, and Y. Penionzhkevich, Nuclear Physics A **415**, 169 (1984).

[58] H. Homeyer, U. Jahnke, G. Ingold, M. Bürgel, H. Fuchs, and D. Hilscher, Zeitschrift für Physik A: Atoms and Nuclei **314**, 143 (1983).

[59] P. P. Singh, A. Yadav, D. P. Singh, U. Gupta, M. K. Sharma, R. Kumar, D. Singh, R. P. Singh, S. Muralithar, M. A. Ansari, B. P. Singh, R. Prasad, and R. K. Bhowmik, Physical Review C **80**, 064603 (2009).

[60] I. Stefan, B. Fornal, S. Leoni, F. Azaiez, C. Portail, J. Thomas, A. Karpov, D. Ackermann, P. Bednarczyk, Y. Blumenfeld, S. Calinescu, A. Chbihi, M. Ciemala, N. Cieplicka-Oryńczak, F. Crespi, S. Franchoo, F. Hammache, Ł. Iskra, B. Jacquot, R. Janssens, O. Kamalou, T. Lauritsen, M. Lewitowicz, L. Olivier, S. Lukyanov, M. Maccormick, A. Maj, P. Marini, I. Matea, M. Naumenko, F. de Oliveira Santos, C. Petrone, Y. Penionzhkevich, F. Rotaru, H. Savajols, O. Sorlin, M. Stanoiu, B. Szpak, O. Tarasov, and D. Verney, Physics Letters B **779**, 456 (2018).

[61] P. P. Singh, Y. Abhishek, V. R. Sharma, R. Kumar, B. P. Singh, R. K. Bhowmik, and R. P. and, EPJ Web of Conferences **21**, 10009 (2012).

[62] R. Van den Bossche and A. Diaz-Torres, Physical Review C **100**, 044604 (2019).

[63] R. Van den Bossche and A. Diaz-Torres, Physical Review C **102**, 064618 (2020).

[64] S. N. Kuklin, T. M. Shneidman, G. G. Adamian, and N. V. Antonenko, European Physical Journal A **48**, 112 (2012).

[65] P. Lichtner, D. Dreschsel, J. Maruhn, and W. Greiner, Physics Letters B **45**, 175 (1973).

[66] H. J. Fink, J. Maruhn, W. Scheid, and W. Greiner, Zeitschrift für Physik **268**, 321 (1974).

[67] O. Zohni, J. Maruhn, W. Scheid, and W. Greiner, Zeitschrift für Physik A: Atoms and Nuclei **275**, 235 (1975).

[68] W. Greiner, J. Y. Park, and W. Scheid, *Nuclear Molecules* (World Scientific Publishing Co Pte Ltd, 1994), p. 344.

[69] J. Maruhn and W. Greiner, Zeitschrift für Physik **251**, 431 (1972).

[70] J. Eisenberg and W. Greiner, *Nuclear Theory: Nuclear models* (North-Holland, 1987).

[71] R. Rafiei, R. d. Rietz, D. H. Luong, D. J. Hinde, M. Dasgupta, M. Evers, and A. Diaz-Torres, Phys. Rev. C **81**, 024601 (2010).

[72] D. J. Hinde, M. Dasgupta, B. R. Fulton, C. R. Morton, R. J. Wooliscroft, A. C. Berriman, and K. Hagino, Physical Review Letters **89**, 272701 (2002).

[73] K. J. Cook, E. C. Simpson, D. H. Luong, S. Kalkal, M. Dasgupta, and D. J. Hinde, Physical Review C **93**, 064604 (2016).

[74] S. Kalkal, E. C. Simpson, D. H. Luong, K. J. Cook, M. Dasgupta, D. J. Hinde, I. P. Carter, D. Y. Jeung, G. Mohanto, C. S. Palshetkar, E. Prasad, D. C. Rafferty, C. Simenel, K. Vo-Phuoc, E. Williams, L. R. Gasques, P. R. S. Gomes, and R. Linares, Physical Review C **93**, 044605 (2016).

[75] D. Gross and H. Kalinowski, Physics Reports **45**, 175 (1978).

[76] G. G. Adamian, N. V. Antonenko, and R. V. Jolos, Nuclear Physics A **584**, 205 (1995).

[77] I. S. Rogov, G. G. Adamian, and N. V. Antonenko, Physical Review C **100**, 024606 (2019).

[78] Y. Murayama, *Mesoscopic Systems: Fundamentals and Applications* (Wiley VCH, 2001), pp. 183–186.

[79] J. D. Cooper, A. Valavanis, Z. Ikonić, P. Harrison, and J. E. Cunningham, Journal of Applied Physics **108**, 113109 (2010).

[80] B. V. Svistunov, *Periodic Boundary Conditions. Classical Limit*, University of Massachusetts Amherst. Available at: `http://people.umass.edu/bvs/pbc.pdf`, Accessed: 02/10/2020.

[81] *LAPACK v3.8.0*, Available at: `www.netlib.org/lapack/`, Accessed: 2018.

[82] R. L. Harrison, C. Granja, and C. Leroy, AIP Conference Proceedings **1204**, 17 (2010).

[83] W Reisdorf, Journal of Physics G: Nuclear and Particle Physics **20**, 1297 (1994).

[84] G. Audi, A. Wapstra, and M. Dedieu, Nuclear Physics A **565**, 193 (1993).

[85] P. Möller, A. Sierk, T. Ichikawa, and H. Sagawa, Atomic Data and Nuclear Data Tables **109-110**, 1 (2016).

[86] G. G. Adamian, private communication (2018).

[87] J. Berntsen, T. O. Espelid, and A. Genz, ACM Trans. Math. Softw. **17**, 452 (1991).

[88] A. Diaz-Torres, G. Adamian, N. Antonenko, and W. Scheid, Nuclear Physics A **679**, 410 (2001).

[89] N. Antonenko, E. Cherepanov, A. Nasirov, V. Permjakov, and V. Volkov, Physics Letters B **319**, 425 (1993).

[90] G. Adamian, N. Antonenko, and W. Scheid, Nuclear Physics A **618**, 176 (1997).

[91] G. G. Adamian, N. V. Antonenko, A. Diaz-Torres, S. P. Ivanova, W. Scheid, and V. V. Volkov, Nuclear Physics A **633**, 409 (1998).

[92] R. Jolos, A. Muminov, and A. Nasirov, The European Physical Journal A **4**, 245 (1999).

[93] E. A. Cherepanov, Pramana - Journal of Physics **53**, 619 (1999).

[94] I. Strojek, W. Czarnacki, W. Gawlikowicz, N. Keeley, M. Kisieliński, S. Kliczewski, A. Kordyasz, E. Koshchiy, and M. K. et al., *HIL Annual Report 2010*, 37-38.

[95] E. Inopin and M. A. El-Moaty, Nuclear Physics **42**, 660 (1963).

[96] D. C. Hoffman, M. M. Fowler, W. R. Daniels, H. R. von Gunten, D. Lee, K. J. Moody, K. Gregorich, R. Welch, G. T. Seaborg, W. Brüchle, M. Brügger, H. Gaggeler, M. Schadel, K. Sümmerer, G. Wirth, T. Blaich, G. Herrmann, N. Hildebrand, J. V. Kratz, M. Lerch, and N. Trautmann, Physical Review C **31**, 1763 (1985).

[97] G. G. Adamian, N. V. Antonenko, A. Diaz-Torres, and S. Heinz, The European Physical Journal A **56**, 47 (2020).

[98] H. Diamond, L. B. Magnusson, J. F. Mech, C. M. Stevens, A. M. Friedman, M. H. Studier, P. R. Fields, and J. R. Huizenga, Physical Review **94**, 1083 (1954).

[99] G. Audi, O. Bersillon, J. Blachot, and A. Wapstra, Nuclear Physics A **729**, 3 (2003).

[100] O. Tarasov and D. Bazin, Nuclear Instruments and Methods in Physics Research Section B: Beam Interactions with Materials and Atoms **266**, 4657 (2008).

[101] A. Gavron, Physical Review C **21**, 230 (1980).

[102] *PACE4 fusion-evaporation code*, Available at: `http://lise.nscl.msu.edu/pace4`, Accessed: 02/08/2020.

[103] R. Bass, Physical Review Letters **39**, 265 (1977).

[104] W. Hauser and H. Feshbach, Physical Review **87**, 366 (1952).

[105] P. Möller, A. J. Sierk, T. Ichikawa, A. Iwamoto, and M. Mumpower, Physical Review C **91**, 024310 (2015).

[106] A. Rahmatinejad, A. N. Bezbakh, T. M. Shneidman, G. Adamian, N. V. Antonenko, P. Jachimowicz, and M. Kowal, Physical Review C **103**, 034309 (2021).

[107] D. Lee, H. von Gunten, B. Jacak, M. Nurmia, Y. fang Liu, C. Luo, G. T. Seaborg, and D. C. Hoffman, Physical Review C **25**, 286 (1982).

[108] C. Borcea and M. Stanoiu, private communication (2020).

[109] M. Siciliano and W. Reviol, private communication (2021).

[110] D. Singh, R. Ali, M. A. Ansari, R. Kumar, R. P. Singh, S. Muralither, and R. K. Bhowmik, EPJ Web of Conferences **86**, 00051 (2015).

[111] W. Hörmann, J. Leydold, and G. Derflinger, in *Automatic Nonuniform Random Variate Generation* (Springer Berlin Heidelberg, 2004), pp. 13–41.

[112] J. L. Vujic, *Monte Carlo Sampling Methods*, Nuclear Engineering Department, University of California, Berkeley, [Online]. Available at: `http://web.ist.utl.pt/~ist11038/acad/theo/simul/Vujic.pdf`, Accessed: 08/11/2020.